Table of Contents

Journal of Science and Technology in Civil Engineering, HUCE (NUCE), 2023, 17 (1): 1–15

AN ENHANCED SINGLE DAMAGE IDENTIFICATION IN BEAMS USING NATURAL FREQUENCY SHIFTS AND ANALYTIC MODAL CURVATURES

Duc-Tuan Ta[a,*], Thien-Phu Le[a], Michael Burman[a]

[a]*Université Paris-Saclay, Univ Evry, LMEE, 91020, Evry, France*

Article history:
Received 12/9/2022, Revised 12/12/2022, Accepted 16/12/2022

Abstract

This article presents an improved procedure for detecting single damage in beam-like structures. Many damage detection methods are based on the analysis of beam natural frequency shifts in damaged and intact states and its analytical modal curvatures. They identify the damage by constructing curves of damage coefficients along the beam and visually determining the point of their mutual intersection. However, for some cases, the absence of an unambiguous point of intersection of these curves or the low accuracy of its localization makes it difficult to use these methods. To accurately determine the mutual intersection of damage coefficient curves, this work proposes to use a subset of modes without one having its curvature close to zero at the site of the alleged damage. This approach greatly simplifies the determination of the point of intersection of the curves of damage coefficients. An enhanced procedure for the numerical determination of this intersection point is also proposed, rather than the visual one used in existing methods. The effectiveness of the proposed technique was confirmed by numerical simulation followed by experimental verification.

Keywords: beams; damage detection; natural frequency shift; mode shape curvature.

https://doi.org/10.31814/stce.nuce2023-17(1)-01

1. Introduction

Structural damage detection is essential, especially in the early damage state, to avoid sudden failures and improve the safety and longevity of structures [1]. Many of the vibration-based fault detection methods in mechanical systems are based on monitoring changes in the dynamic properties of these systems, such as natural frequencies, mode shapes, and damping ratios [2, 3]. These methods are well suited to real structures, especially when operational modal analysis is applied, due to their ability to continuously monitor structures without interrupting their normal functioning.

The great variety of these methods also results from the way in which the listed parameters are used. For example, the damping ratio is less frequently used than the system's natural frequencies and mode shape parameters because it is sensitive to environmental factors such as humidity and temperature. Also, from a technical point of view, the natural frequencies of a structure can be identified from signal measurements with only one sensor, however, multiple sensors are needed to determine the mode shapes.

Among other techniques that use the above parameters for damage identification, the following studies are of interest from the point of view of using and analyzing these parameters. Lee and Chung

*Corresponding author. *E-mail address:* ductuan.ta@univ-evry.fr (Ta, D.-T.)

[4] identified a single damage for a cantilever beam in which the approximate crack location is estimated using Armon's rank ordering method, which uses the first four frequencies of the damaged structure. Patil and Maiti [5] developed a crack detection technique that uses a rotational spring model to simulate the crack effect in a beam, with the damage index being an indicator of how much strain energy is stored in the spring. Gillich et al. [6] proposed a method to compare the measured frequency changes with the values obtained analytically and then use the pattern recognition problem to determine the location of the damage and its severity. The damaged zone was identified according to the classification of the first four frequencies of structures in [7]. Sha et al. [8] developed a damage detection method that combines relative numerical natural frequency variation and measured values using Bayesian inference. Surace et al. [9] used the ratios of natural frequencies of different modes for a characteristic of damage.

Many researchers have focused on changes in modal shapes and/or modal curvatures. Changes in mode shapes can directly provide information about the location of a damage [10]. The difference in modal curvatures between intact and damaged states was used to determine the location of damage [11, 12]. Gorgin [13] developed a damage localization method based on the analysis of the first mode shape of the structure. In general, these methods are mainly based on the change of mode shapes between a healthy state and a damaged one. However, they require a large number of measurements at different locations and are almost exclusively limited to damage localization.

The use of mode shapes (or their derivatives) is limited to the localization level. Therefore, combined methods for damage quantification using both natural frequencies and mode shapes (or their derivatives) are proposed. Dahak et al. [14] developed a damage detection method using curves intersection based on the curvature of the intact mode shape and the measured frequencies. The use of the relationship between natural frequency variation and modal curvature for damage detection was discussed in [15].

In addition, significant improvements in computing power and advances in sensor technology have made it possible to use machine learning techniques in damage detection applications. Lee [16] constructed a set of training patterns of a neural network for damage detection in pipe-type beams using changes in natural frequencies. Other methods such as genetic algorithm [17], hybrid optimization [18], particle swarm optimization [19] have been used for damage detection. These methods are generally effective but require a considerable computational resource to achieve the convergence of the algorithm and are therefore time consuming.

This work focuses on rapid damage identification methods which are effective at the stage of early damage detection in beam-like structures. Among the discussed above studies, methods using natural frequency shifts and analytical modal curvatures seem to be simple and easy to detect single cracks in beams [6, 14, 15]. First, from the shifts of natural frequencies and modal curvatures, curves are generated along the entire length of the beam. The mutual intersection of all these curves is then used to localize the damage. However, the intersection is not always evident, which complicates the method. To overcome this limitation, an improved procedure is proposed that uses a subset of modal curvatures to highlight the intersection, thereby simplifying identification of its location. Numerical examples and an experimental test are used to validate the proposed procedure.

2. Theoretical background and existing method

The relationship between natural frequency shift and damage at location x_0 is obtained as [20]:

$$\frac{\Delta f_i}{f_i} = \frac{f_i - \bar{f}_i}{f_i} \approx \delta_K \frac{\phi_i''^2(x_0)}{\left\|\phi_i''\right\|_2^2} + \delta_M \frac{\phi_i^2(x_0)}{\|\phi_i\|_2^2} \tag{1}$$

where f_i and $\bar{f}_i$ are the natural frequencies of the i^{th} mode of the intact and damaged states, respectively; $\delta_K = \dfrac{\Delta EI \Delta L}{2EI}$ and $\delta_M = -\dfrac{\Delta \mu \Delta L}{2\mu}$ are the relative local variation of bending stiffness and mass, respectively; ϕ_i and ϕ_i'' are the mode shape and the modal curvature of the i^{th} mode. The first five analytic mode shapes and the corresponding modal curvatures of a cantilever beam are presented in Fig. 1.

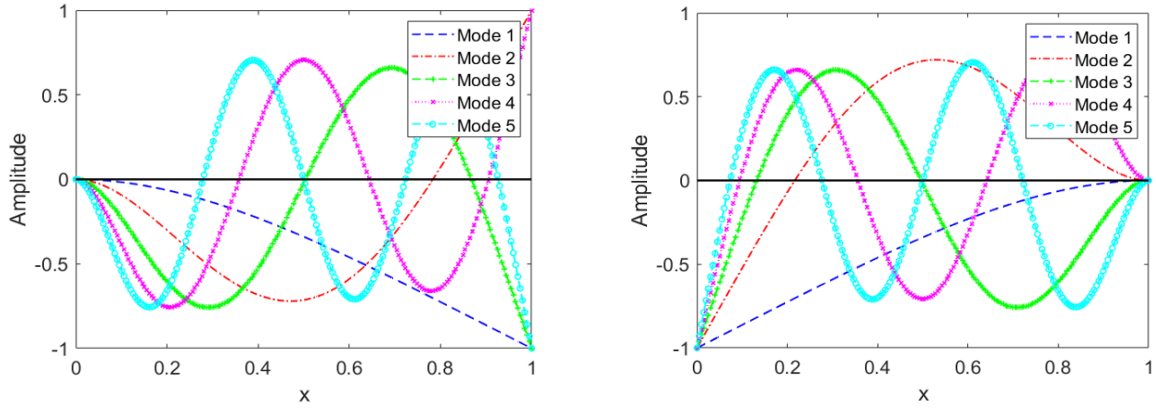

(a) Mode shapes (b) Modal curvatures

Figure 1. A cantilever beam

In the case of damage caused only by a change in bending stiffness and neglecting the effect of a change in mass, a simpler expression for the natural frequency variation can be represented as a function of squared modal curvature:

$$\frac{\Delta f_i}{f_i} \approx \zeta \phi_i''^2(x_0) \tag{2}$$

where ζ represents the damage coefficient and depends on the size of the damage.

The relative frequency shift is defined as:

$$\overline{\Delta f_i} = \frac{f_i - \bar{f}_i}{f_i} \tag{3}$$

Substituting Eq. (3) into Eq. (2), the relationship between damage coefficient and relative frequency shift is given as follows:

$$\zeta \approx \frac{\overline{\Delta f_i}}{\phi_i''^2(x_0)} \tag{4}$$

Thus, a curve of damage coefficients $\zeta_i(x)$ defined as follows:

$$\zeta_i(x) \approx \frac{\overline{\Delta f}_i}{\phi_i''^2(x)} \tag{5}$$

where x is the position on the beam and $\zeta_i(x)$ is the curve of damage coefficients for mode i.

Following Eq. (4), if $x = x_0$ then $\zeta_i(x) = \zeta_i(x_0) = \zeta\ \forall i$. Thus, the curves $\zeta_i(x)$ intersect at the point of coordinate (x_0, ζ) that gives the location $x_0$of the damage.

Eq. (5) has been applied to damage detection in many studies [6, 14, 15]. The intersection of these damage coefficient curves was used to determine the location and severity of damage. This method is simple and convenient for single crack detection in beams. An illustration of the mutual intersection of damage coefficient curves is given in Fig. 2.

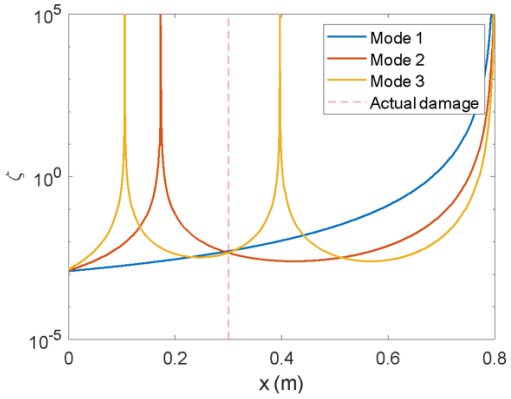

Figure 2. Example of the mutual intersection of damage coefficient curves

However, in some cases, the curves do not have a mutual intersection as presented in Fig. 3. To explain why the curves do not intersect, one can rewrite Eq. (5) as follows:

$$\overline{\Delta f}_i \approx \zeta_i(x)\phi_i''^2(x) \tag{6}$$

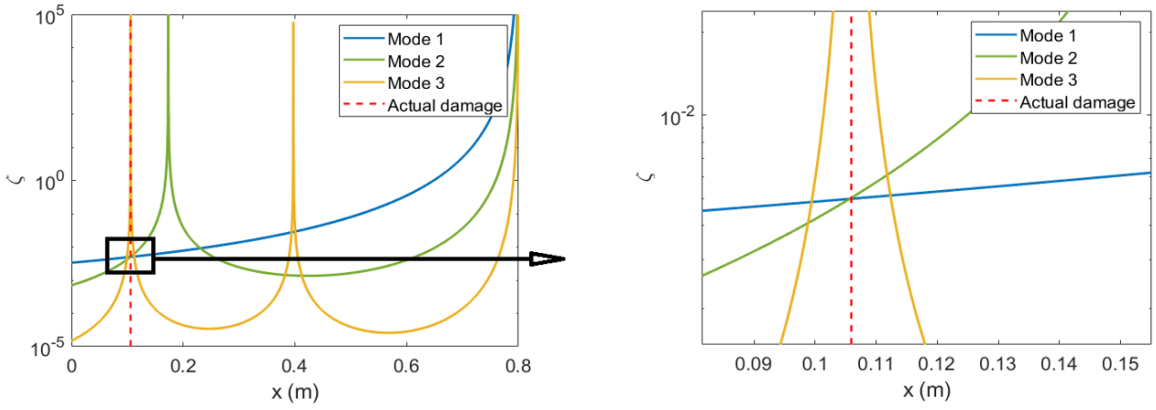

(a) Plot of curves

(b) Zoom of intersection zone

Figure 3. Damage at the location of zero modal curvature

It can be seen from Eq. (6) that when the damage location x_0 coincides with the location where the modal curvature of the i^{th} mode $\phi_i''^2(x_0)$ is zero, the natural frequency shift $\overline{\Delta f}_i$ should be zero. However, the natural frequency shift $\overline{\Delta f}_i$ can be non-zero due to numerical error or noise effect. Thus $\zeta_i(x_0)$ tends to be infinite as can be seen from Eq. (5). Therefore, in this particular case the mutual intersection does not exist, and the damage location cannot be detected using the intersection

of curves. Fig. 3 illustrates the case described above when damage occurs at the location where the curvature of the 3^{rd} mode is zero.

The absence of a single clear point of intersection of the damage coefficient curves (Fig. 3) does not allow one to unambiguously determine the location of the damage. However, visually it is possible to determine a certain area of intersection of these curves. Thus, it is necessary to establish a procedure that will allow one to uniquely identify the point of intersection of these curves using numerical methods in order to facilitate the application of the method described above.

3. Enhanced procedure

To overcome these shortcomings, it is proposed to use a subset of curves to highlight their mutual intersection, which will ensure its presence. Moreover, damage identification will be more accurate and systematic if a numerical procedure is used to determine this intersection of curves.

3.1. Selection of curves

As presented above, when damage site is close to a location where the modal curvature is close to zero, its curve $\zeta_i(x)$ gives a peak at damage location and does not intersect the other curves at the damage position. To select a subset of curves that will uniquely define the intersection, it is proposed to perform the following steps:

- Draw the curves $\zeta_i(x)$ for all available modes on the same graph.
- Eliminate a curve if it has a vertex with an abscissa which is close to the abscissa of the common point of intersection of other curves.

3.2. Finding the intersection from the singular value decomposition

To accurately calculate the position of the mutual intersection of the curves, a new approach is proposed as follows:

- Divide the length of the beam into n positions. For each mode $i$at each location x_j one gets: $\zeta_{i,j} \approx \dfrac{\overline{\Delta f}_i}{\phi_i''^2(x_j)}$ with $i = 1 : m$ and $j = 1 : n$ with $m << n$, where m is the number of modes.
- Define the following matrix $\mathbf{A}^{(j)}$ for each location x_j:

$$\mathbf{A}^{(j)}_{(m+1)\times m} = \begin{bmatrix} 1 & 1 & \cdots & 1 & \cdots & 1 \\ \dfrac{\zeta_{1,j}}{\zeta_{1,j}} & \dfrac{\zeta_{2,j}}{\zeta_{1,j}} & \cdots & \dfrac{\zeta_{i,j}}{\zeta_{1,j}} & \cdots & \dfrac{\zeta_{m,j}}{\zeta_{1,j}} \\ \dfrac{\zeta_{1,j}}{\zeta_{2,j}} & \dfrac{\zeta_{2,j}}{\zeta_{2,j}} & \cdots & \dfrac{\zeta_{i,j}}{\zeta_{2,j}} & \cdots & \dfrac{\zeta_{m,j}}{\zeta_{2,j}} \\ \vdots & \vdots & \cdots & \vdots & \cdots & \vdots \\ \dfrac{\zeta_{1,j}}{\zeta_{i,j}} & \dfrac{\zeta_{2,j}}{\zeta_{i,j}} & \cdots & \dfrac{\zeta_{i,j}}{\zeta_{i,j}} & \cdots & \dfrac{\zeta_{m,j}}{\zeta_{i,j}} \\ \vdots & \vdots & \cdots & \vdots & \cdots & \vdots \\ \dfrac{\zeta_{1,j}}{\zeta_{m,j}} & \dfrac{\zeta_{2,j}}{\zeta_{m,j}} & \cdots & \dfrac{\zeta_{i,j}}{\zeta_{m,j}} & \cdots & \dfrac{\zeta_{m,j}}{\zeta_{m,j}} \end{bmatrix} \tag{7}$$

- Take a singular value decomposition of matrix $\mathbf{A}^{(j)}$ to obtain m singular values for each location x_j:

$$s_1^{(j)} > s_2^{(j)} > \ldots > s_m^{(j)} > 0 \tag{8}$$

when $x \to x_0$, all elements in matrix $\mathbf{A}^{(j)}$ tend to be 1, and thus:

$$s_1^{(j)} > 0 \text{ and } s_2^{(j)}, s_3^{(j)}, \ldots, s_m^{(j)} \to 0 \tag{9}$$

- Plot the curve $p(x_j) = \dfrac{1}{s_2^{(j)}}$ over the length of the beam. Then, the peak at location $x = x_0$ is observed.

3.3. Enhanced procedure of single damage detection

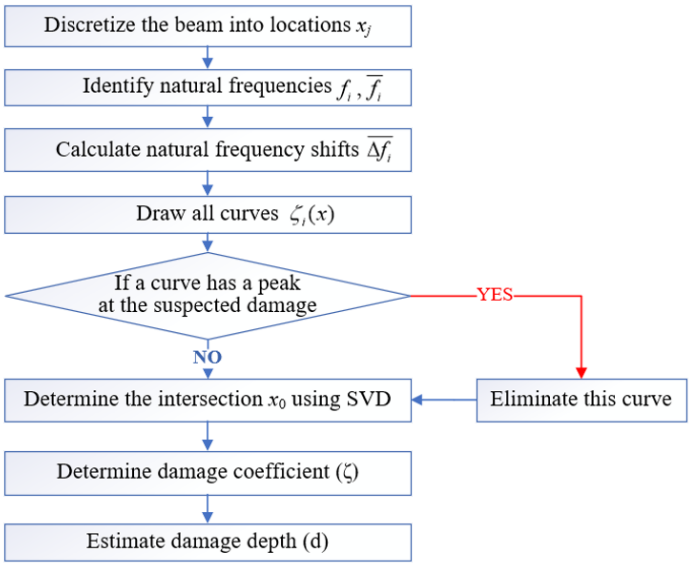

Figure 4. Enhanced procedure flowchart

Summarizing the above analysis, the following enhanced single damage identification procedure is proposed:

- Step 1. Discretize the beam into n positions x_j.
- Step 2. Identify natural frequencies f_i and $\overline{f_i}$ of the intact and the damaged beam.
- Step 3. Calculate the relative frequency shifts $\overline{\Delta f_i}$
- Step 4. Select curves by drawing all curves for the modes on the same graph and exclude the curve if its vertex abscissa is close to the intersection point abscissa.
- Step 5. Determine the intersection x_0 of the remaining curves (the peak of $p(x)$ as in Section 3.2).
- Step 6. Determine the damage coefficient (ζ) using Eq. (4).
- Step 7. Estimate the damage depth (d). In order to quantify the damage depth, an inverse method is used to estimate the relationship between the coefficient (ζ) and the damage depth (d). Since the damage coefficient (ζ) only depends on the change in stiffness and width, it can be calculated as a function of these parameters. To establish the relationship between the damage coefficient (ζ) and the

damage depth (d), a fixed position x_0 and the width ΔL of the damage are used while the damage depth changes (for this work ΔL = 2 mm is used for every case). The damage depth corresponding to any damage coefficient can then be interpolated from neighboring values using spline interpolation.

Fig. 4 shows a flowchart that summarizes the enhanced procedure for determining a single damage in a beam presented above.

4. Verification of proposed procedure by numerical investigation

In this section, the proposed procedure is validated by analyzing the model simulated in ANSYS Workbench which is presented in Fig. 5. The numerical tests were carried out for a steel beam of Young's modulus E = 200 GPa, and mass density ρ = 7850 kg/m^3. The beam of 800 mm long, 40 mm wide and 6 mm high was used for these simulations with different boundary conditions. All simulated damage sites are 2 mm wide.

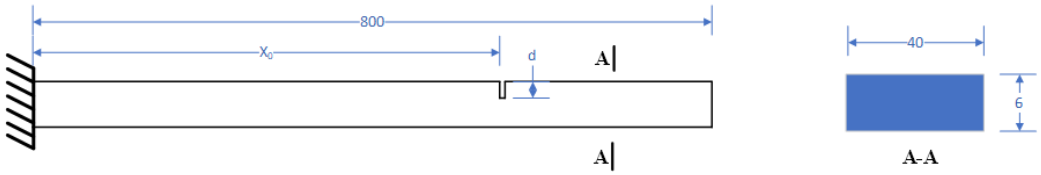

Figure 5. Cantilever beam

Six cases of damage are considered, which differ in their location and depth of the crack (see Table 1). Following the proposed procedure, the identified intersection point represents the damage location as shown in Figs. 6–11. In case 1, damage is modeled at the location where the modal curvature of the 4^{th} mode is zero. In case 2, damage is modeled at the point where the modal curvature of the 3^{rd} mode is zero. In case 3, damage is modeled at the location where the modal curvature of the 2^{nd} mode is zero. In case 5, damage is modeled at the point where the modal curvature of the 3^{rd} mode is zero. Thus, modes with a peak close to the intersection point are discarded from the damage identification process. However, for cases 4 and 6, the damage is modeled at the location where the modal curvature of all modes is nonzero, so all curves are used for the damage identification procedure.

Table 1. Damage scenarios of the numerical cantilever beam

Case	Damage		Natural frequency (Hz)			
	x_0 (mm)	d (mm)	Mode 1	Mode 2	Mode 3	Mode 4
Intact	-	-	7.6850	48.149	134.79	264.08
1	75.6	10	7.6233	47.986	134.67	264.07
2	105.9	15	7.5567	47.981	134.78	263.44
3	173.3	20	7.5134	48.148	133.58	259.52
4	300.0	15	7.6375	47.838	133.83	263.86
5	397.1	15	7.6629	47.579	134.77	261.06
6	600	20	7.6820	47.753	131.69	258.98

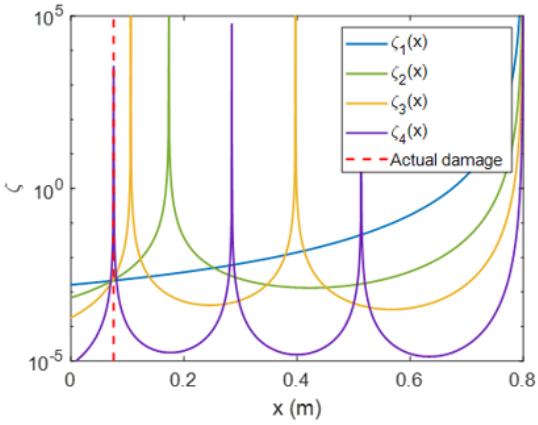

(a) Plot of all curves

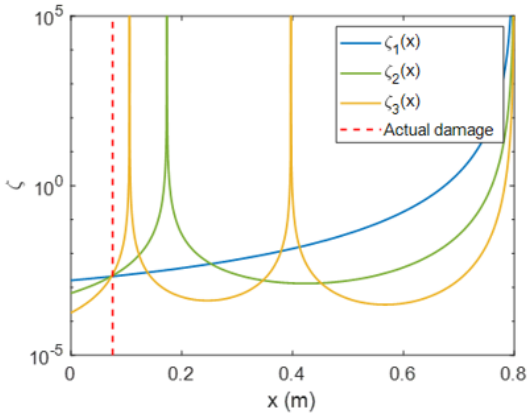

(b) Plot of a subset of curves

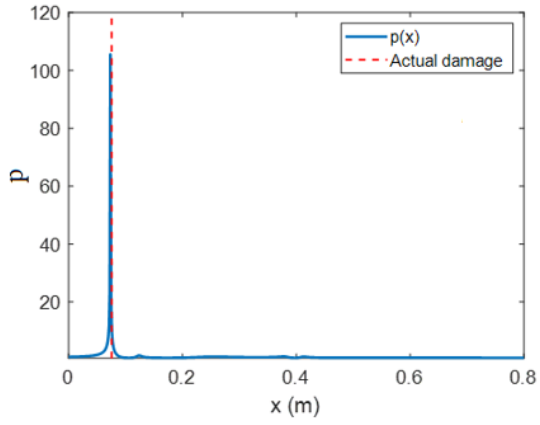

(c) Identified damage location

Figure 6. Damage detection for case 1

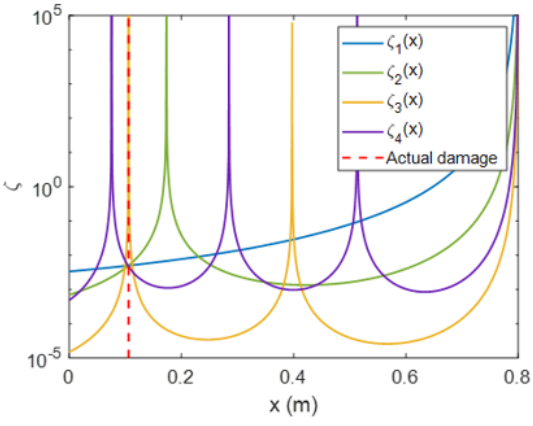

(a) Plot of all curves

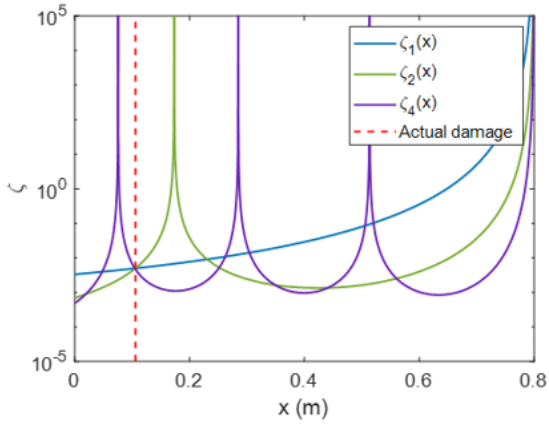

(b) Plot of a subset of curves

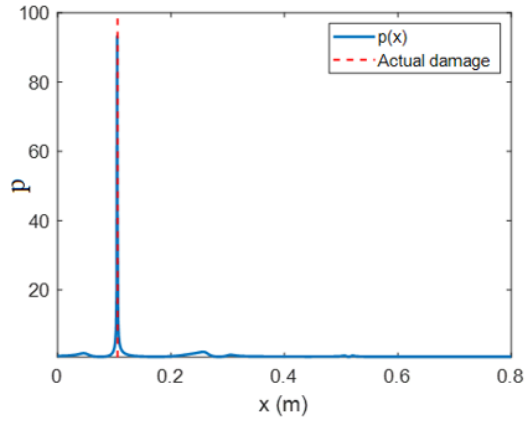

(c) Identified damage location

Figure 7. Damage detection for case 2

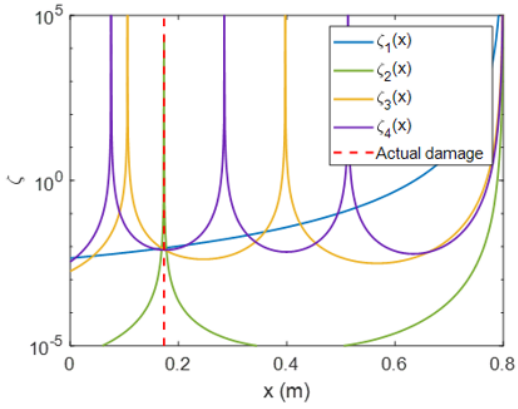

(a) Plot of all curves

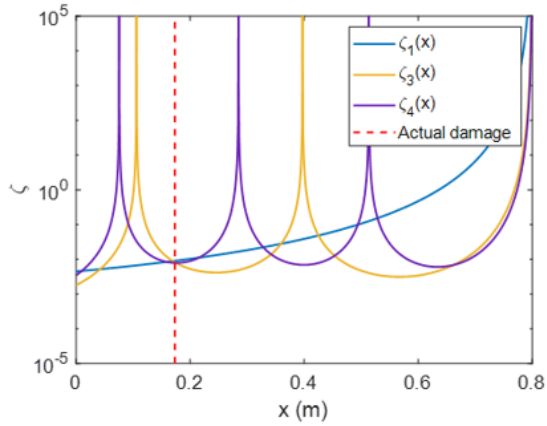

(b) Plot of a subset of curves

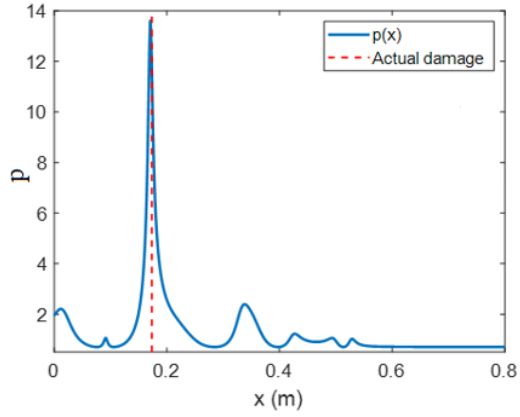

(c) Identified damage location

Figure 8. Damage detection for case 3

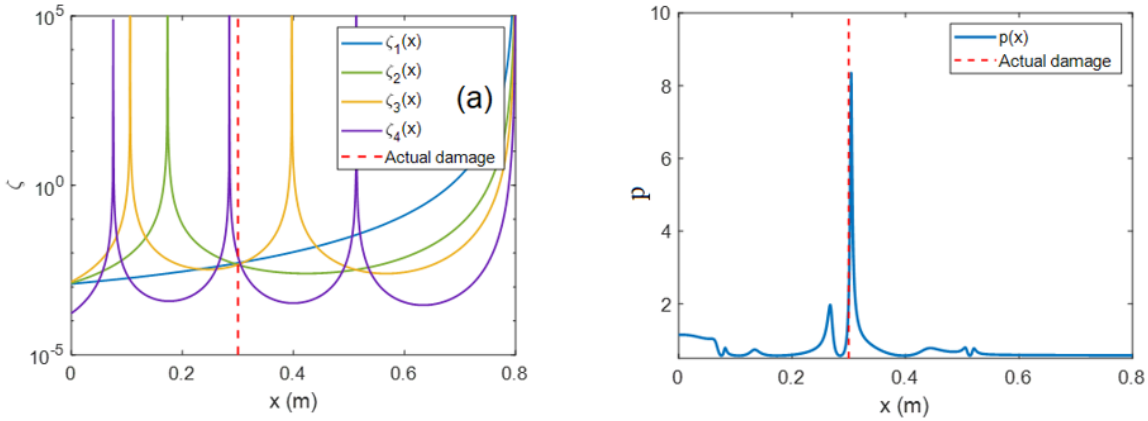

(a) Plot of all curves (b) Identified damage location

Figure 9. Damage detection for case 4

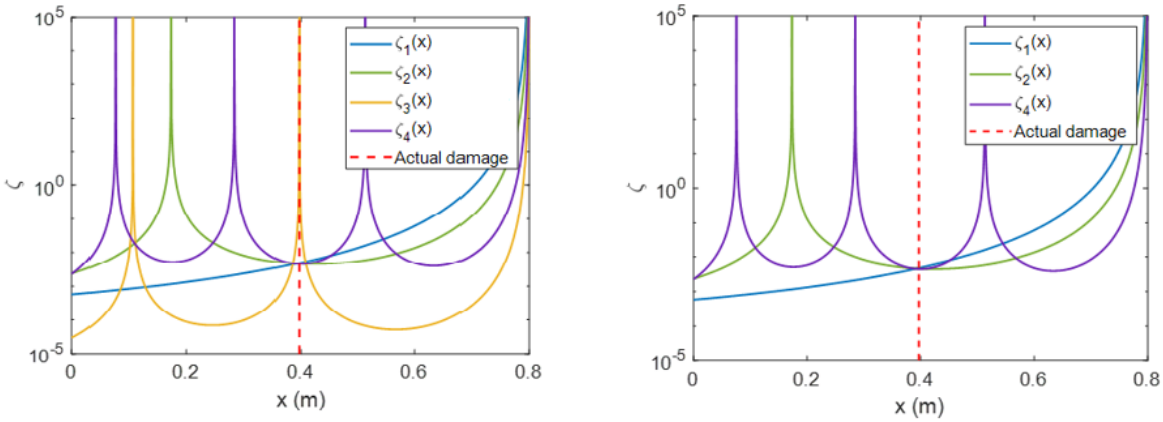

(a) Plot of all curves (b) Plot of a subset of curves

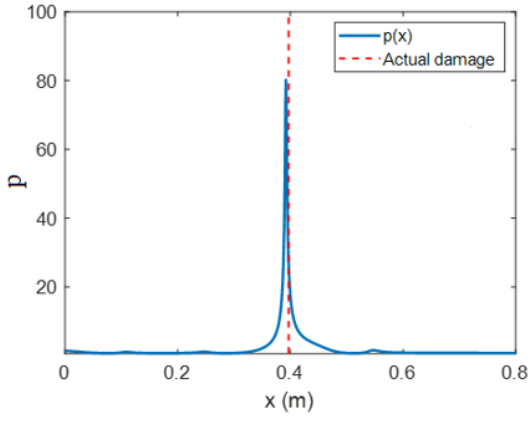

(c) Identified damage location

Figure 10. Damage detection for case 5

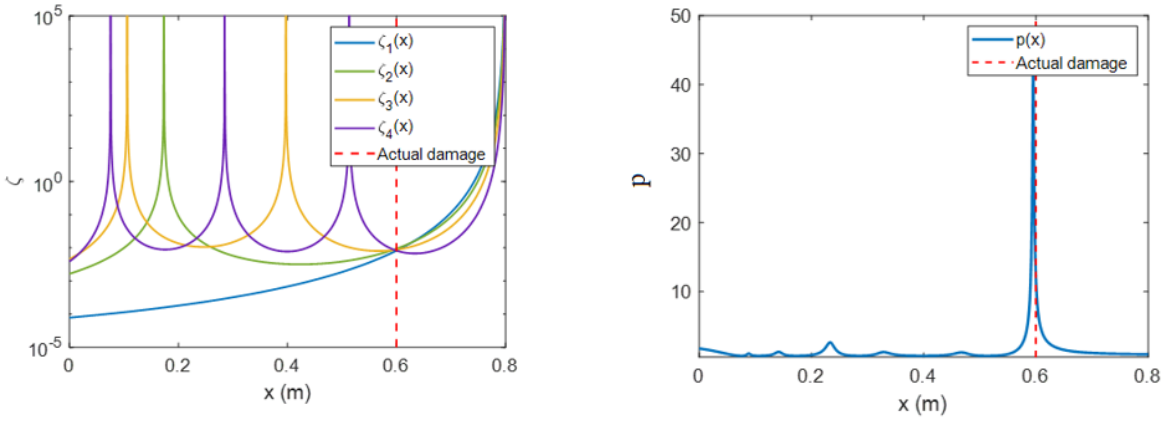

(a) Plot of all curves

(b) Identified damage location

Figure 11. Damage detection for case 6

To estimate the damage depth, numerical simulations are performed to establish a relationship between the depths and their damage coefficients for the cantilever beam. The curve for this relationship is shown in Fig. 12.

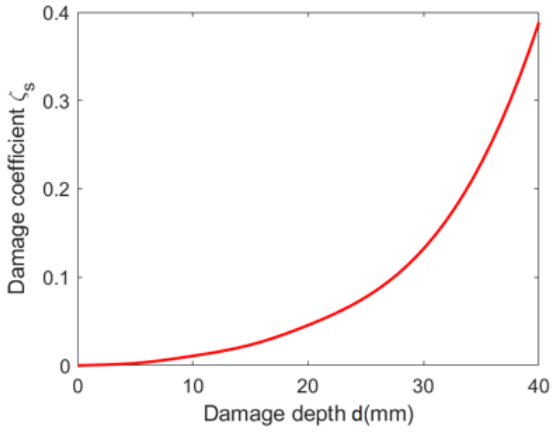

Figure 12. Damage coefficient vs. damage depth for the numerical test

Table 2. Results estimated from the numerical tests

No	x_0 (mm)	Error (%)	d (mm)	Error (%)
1	73.1	3.3	9.9	1.0
2	105.0	0.8	15.5	3.3
3	169.0	2.5	19.4	3.0
4	300.7	0.2	15.4	2.7
5	386.4	2.7	14.9	0.7
6	598.7	0.3	19.6	2.0

The results found are given in Table 2 indicating the location of the damage and the damage depth. It can be seen that they are close to real ones with an error in determining the location and the damage depth of less than 3.3%.

5. Verification of proposed procedure by experimental investigation

The beam used to perform the experimental studies presented in this article are steel cantilever beams. They have the following physical parameters: length L = 1005 mm, width B = 42 mm and height H = 10 mm. The material of the beam has Young's modulus E = 200 GPa, and density ρ = 7850 kg/m^3.

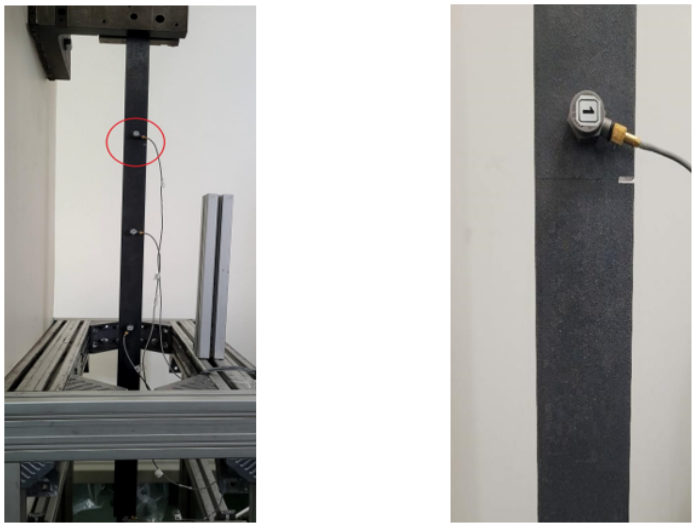

(a) A whole system view (b) Zoom of the damage area

Figure 13. Experimental setup for the cantilever beam

For this test scenario, a cut 2 mm wide and 5 mm deep was created by machining. It was located at a distance of 220 mm from the support. The damage of the beam is shown in Fig. 13. The damage site is created close to the place where the modal curvature of the 2^{nd} mode is equal to zero. Thus, this mode is excluded for damage identification procedure. To obtain the natural frequencies for the intact and damaged states of the beam, modal tests were carried out using an impact hammer. Time responses were recorded using five PCB piezoelectric accelerometers. Commercial B&K Connect^{TM} software was used to acquire the excitation and the beam responses. The modal parameters were determined using the Rational Fraction Polynomial (RFP) method implemented in the software. The measured frequencies of the beam are given in Table 3 while the identified location of the damage is shown in Fig. 14. The relationship between coefficient (ζ) and depth (d) is obtained by simulations (presented at Step 7 in Section 3.3) and shown in Fig. 15. The identified results are presented in Table 4. They are close to real values, which confirms the proposed method.

Table 3. Frequencies of the experimental test for the cantilever beam

No	Damage		Natural frequency (Hz)			
	x_0 (mm)	d (mm)	Mode 1	Mode 2	Mode 3	Mode 4
Intact	-	-	7.769	48.366	137.350	277.269
Damage	220	5	7.767	48.365	137.339	277.240

Table 4. Results estimated from the experimental test

No	x_0 (mm)	Error (%)	d (mm)
1	208	5.4	4.7

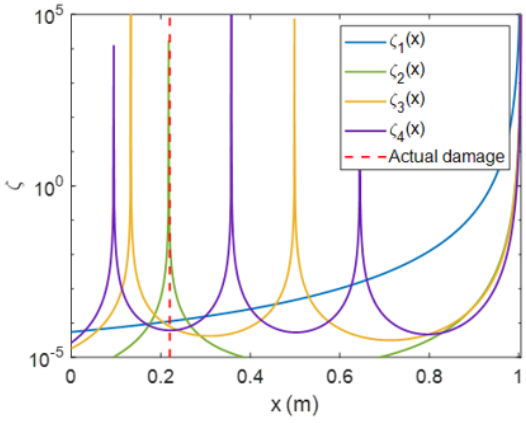

(a) Plot of all curves

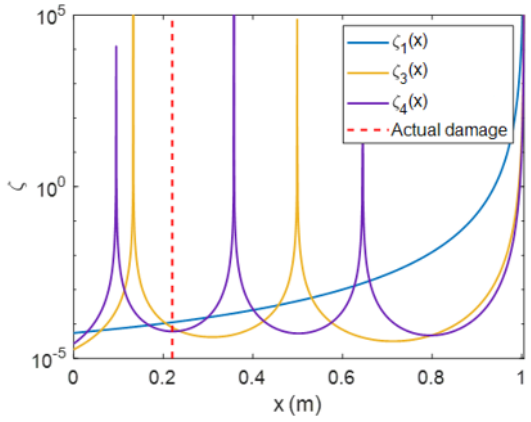

(b) Plot of a subset of curves

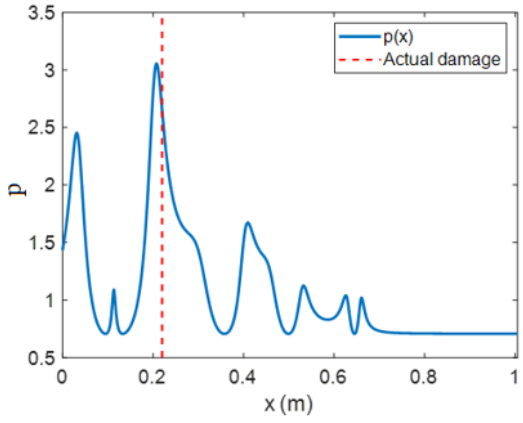

(c) Identified damage location

Figure 14. Damage detection for the experimental test

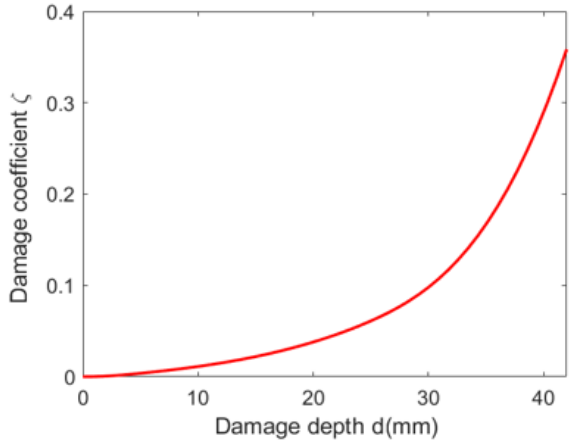

Figure 15. Damage coefficient vs. damage depth for the experimental test

6. Conclusions

This paper presents an improved procedure for detecting single damage in beam structures. First, curves of damage coefficients are constructed along the beam from natural frequency shifts and analytical modal curvatures. Then, the exact identification of the intersection of these curves gives the location of the damage. The numerical determination of the point of intersection of these curves is based on the singular value decomposition of matrices constructed from the ratios of the curves of damage coefficients. In consequence the degree of this damage is defined.

The proposed procedure was first applied to numerical examples. Good results of the identified damages (location and extent) were noted compared to exact ones on cantilever beams. Compared to the existing procedure, the proposed one makes the intersections more visual and simplifies their determination from the peaks of the inverse of the second singular value.

Finally, this procedure was tested on an experimental cantilever beam. The identified damage coincided well with the real one. This confirms the validity of the proposed method for detecting single damage in beam-like structures. The next step is to extend to multiple damages and first results can be seen in [20].

References

[1] Chen, H.-P., Ni, Y.-Q. (2018). *Structural Health Monitoring of Large Civil Engineering Structures*. Wiley.

[2] Doebling, S. W., Farrar, C. R., Prime, M. B., Shevitz, D. W. (1996). Damage identification and health monitoring of structural and mechanical systems from changes in their vibration characteristics: A literature review. Technical report.

[3] Avci, O., Abdeljaber, O., Kiranyaz, S., Hussein, M., Gabbouj, M., Inman, D. J. (2021). A review of vibration-based damage detection in civil structures: From traditional methods to Machine Learning and Deep Learning applications. *Mechanical Systems and Signal Processing*, 147:107077.

[4] Lee, Y.-S., Chung, M.-J. (2000). A study on crack detection using eigenfrequency test data. *Computers & Structures*, 77(3):327–342.

[5] Patil, D. P., Maiti, S. K. (2005). Experimental verification of a method of detection of multiple cracks in beams based on frequency measurements. *Journal of Sound and Vibration*, 281(1-2):439–451.

[6] Gillich, G.-R., Praisach, Z.-I. (2014). Modal identification and damage detection in beam-like structures using the power spectrum and time–frequency analysis. *Signal Processing*, 96:29–44.

[7] Dahak, M., Touat, N., Benseddiq, N. (2017). On the classification of normalized natural frequencies for damage detection in cantilever beam. *Journal of Sound and Vibration*, 402:70–84.

[8] Sha, G., Radzieński, M., Cao, M., Ostachowicz, W. (2019). A novel method for single and multiple damage detection in beams using relative natural frequency changes. *Mechanical Systems and Signal Processing*, 132:335–352.

[9] Surace, C., Bovsunovsky, A. (2020). The use of frequency ratios to diagnose structural damage in varying environmental conditions. *Mechanical Systems and Signal Processing*, 136:106523.

[10] Carden, E. P., Fanning, P. (2004). Vibration Based Condition Monitoring: A Review. *Structural Health Monitoring*, 3(4):355–377.

[11] Pandey, A. K., Biswas, M., Samman, M. M. (1991). Damage detection from changes in curvature mode shapes. *Journal of Sound and Vibration*, 145(2):321–332.

[12] Wahab, M. M. A., Roeck, G. D. (1999). Damage detection in bridges using modal curvatures: Application to a real damage scenario. *Journal of Sound and Vibration*, 226(2):217–235.

[13] Gorgin, R. (2020). Damage identification technique based on mode shape analysis of beam structures. *Structures*, 27:2300–2308.

[14] Dahak, M., Touat, N., Kharoubi, M. (2018). Damage detection in beam through change in measured frequency and undamaged curvature mode shape. *Inverse Problems in Science and Engineering*, 27(1): 89–114.

[15] Capecchi, D., Ciambella, J., Pau, A., Vestroni, F. (2016). Damage identification in a parabolic arch by means of natural frequencies, modal shapes and curvatures. *Meccanica*, 51(11):2847–2859.

[16] Lee, J.-W. (2016). Crack identification method for tapered cantilever pipe-type beam using natural frequencies. *International Journal of Steel Structures*, 16(2):467–476.

[17] Vakil-Baghmisheh, M.-T., Peimani, M., Sadeghi, M. H., Ettefagh, M. M. (2008). Crack detection in beam-like structures using genetic algorithms. *Applied Soft Computing*, 8(2):1150–1160.

[18] Moezi, S. A., Zakeri, E., Zare, A. (2018). Structural single and multiple crack detection in cantilever beams using a hybrid Cuckoo-Nelder-Mead optimization method. *Mechanical Systems and Signal Processing*, 99:805–831.

[19] Khatir, S., Dekemele, K., Loccufier, M., Khatir, T., Wahab, M. A. (2018). Crack identification method in beam-like structures using changes in experimentally measured frequencies and Particle Swarm Optimization. *Comptes Rendus Mécanique*, 346(2):110–120.

[20] Ta, D.-T. (2022). Structural health monitoring based on operational modal analysis. PhD thesis, Université Paris-Saclay.

Journal of Science and Technology in Civil Engineering, HUCE (NUCE), 2023, 17 (1): 16–25

PROBABILISTIC EVALUATION OF THE AXIS DISTANCE'S INFLUENCE ON THE FLEXURAL STRENGTH DETERIORATION OF REINFORCED CONCRETE BEAMS UNDER ISO 834 FIRE

Nguyen Truong Thang[a], Dang Viet Hung[a,*]

[a]*Faculty of Building and Industrial Construction, Hanoi University of Civil Engineering, 55 Giai Phong road, Hai Ba Trung district, Hanoi, Vietnam*

Article history:
Received 08/6/2022, Revised 31/8/2022, Accepted 06/9/2022

Abstract

The distance from the nearest concrete exposed surface to the centroidal axis of main longitudinal steel reinforcing bars, so-called axis distance, plays a critical role in ensuring the safety of reinforced concrete (RC) structures under fire, as it helps the rebars not being directly exposed to heating in a fire incident. However, a large axis distance value could reduce the effective height as well as the beam's flexural strength at ambient condition. In order to determine the appropriate values of axis distance, this article developes a data-driven method for predicting the flexural strength deterioration (FSD) of RC beams under ISO 834 standard fire based on the material and geometrical inputs. This method consists of two main stages: (i) Establishing a theoretical/experimental database by collecting experimental data from the literature; and (ii) Engineering a probabilistic model based on the Bayesian Neural Network. The results obtained show that the proposed approach is a practical tool that is capable of performing quick and reasonably accurate analysis such as degradation curves of FSD against exposure time. In addition, the uncertainty related to the prediction results is also evaluated, providing useful information for structural fire engineers to achieve conservative designs.

Keywords: reinforced concrete; structure, fire engineering; probabilistic; machine learning.

https://doi.org/10.31814/stce.nuce2023-17(1)-02

1. Introduction

Reinforced concrete (RC) is the most common structural material that is widely used in civil and industrial buildings, infrastructure systems and other subjects in construction field. Ensuring the safety of load-bearing RC structural members under fire conditions is of great importance, that helps save human life and valuable assets. For RC members, the fire safety is primarily considered by providing an appropriate covering concrete layer to protect the inner steel reinforcing bars (rebars), which can be characterized by the distance from the nearest concrete exposed surface to the rebars' centroidal axis, so-called axis distance. However, a relatively thick concrete covering layer will reduce the effective cross-section sizes, thus reducing the RC members' strength and stiffness. In the meantime, a thin concrete cover may not guarantee the particular fire resistance class that is required by

*Corresponding author. *E-mail address:* hungdv@huce.edu.vn (Hung, D. V.)

design standards. To determine the adequate values of the axis distance, it is necessary to accurately estimate their influences on the structural performances of the considered RC members.

In the literature, there are a number of research works using different approaches, including experimental, theoretical, and numerical methods, to study the behavior of structural members subjected to standard fire conditions such as ISO 834 under different perspectives. Kodur et al. [1, 2] built a numerical model to estimate the flexural behavior of RC beams from elastic until failure using moment-curvature relationships. Thanks to the numerical model, parametric studies were carried out, showing the effects of different materials, fire scenarios, and geometric configurations without requiring expensive and time-consuming full-scale experiments. Thanaraj et al. [3] performed a series of experiments to explore the responses of RC beams with various concrete grades under fires. Recently, Gedam [4] proposed a theoretical method to estimate the RC beam load-bearing capacity based on the materials' thermally-induced properties, stress-strain relationship, and heat transfer model. In [5], the corresponding author analytically investigated the flexural strength deterioration (FSD) of RC beams, showing that the cross-section dimension and axis distance having a positive correlation with the FSD coefficient. Moreover, the authors also developed a calculation sheet to quickly calculate the FSD coefficient, which is useful for design practice [5]. Later, the authors [6] extended the theory for computing the FSD of RC T-beams, interestingly highlighting that the dimension of the beam's web and flanges have a negative correlation with FSD coefficients. Sun et al. [7] proposed a hybrid numerical method combining a finite element model for simulating members' thermal behavior with a one-dimensional spectral model for modeling RC beams response. The method significantly reduces the computational time while still provides competing results with more complex Finite Element models. Ozbolt et al. [8] proposed a thermo-mechanic three-dimensional (3-D) model to simulate the behavior of RC members under fire loads according to ISO 834. The model was successfully validated through comparison with experimental data from 4-point tests on RC beams. In addition to technical contribution for building a high-fidelity 3-D numerical model, the study provided noteworthy observations about the reduction in flexural stiffness of cracked beams due to thermal load after one hour of fire exposure and the occurrence of flexural shear failure after 1.5 hour. Zhang et al. [9] carried out both experimental and numerical studies to fully investigate the fire resistance of RC T-beam equipped with high strength reinforcement. The obtained results demonstrated that the flexural failure mode dominated with the presence of plastic hinges; hence, the full plastic analysis method is applicable for the design of RC T-beams with high-strength rebars.

On the other aspect, in the past decade, machine learning (ML) algorithms have been increasingly adopted by fire scientists and engineers to predict the behaviors of concrete-based structural members thanks to their practical, fast calculation and acceptable accuracy [10–12]. Naser [13] investigated the applicability of nine ML algorithms in analyzing fire-induced spalling of RC columns. Though obtained results were promising, the author emphasized the need for collaboration and sharing of data between research groups to address the data scarcity caused by the complexity of fire testing. Panev et al. [14] proposed a support vector machine-based algorithm to predict the fire resistance of composite shallow floor systems subjected to the ISO 834 standard fire. The proposed model could provide highly accurate results (up to 96%) about insulation ratings of the shallow system floor; on the other hand, the author also pointed out the limited extrapolation capacity of the method, i.e., if data points are too different compared to training data, prediction results may not be physically reasonable. Fu [15] developed a ML-framework specially designed for assessing the progressive collapse resistance of steel frame structures under fire, showing that the neural network-based model achieved better results than the counterparts given a sufficiently large dataset. Kodur et al. [16] explored a data-driven

method to assess the fire hazard of bridges based on their geometric configurations (span, number of lanes), materials, and current operation states (damage, age). It was shown that the proposed method could be used as a low-budget tool to assess the fire vulnerability of bridges with similar patterns.

As pointed out by the aforementioned studies [10–16], a common major obstacle to the data-driven method is the scarcity of relevant data; this problem is more accentuated when studying structural members under fire compared to ambient condition. Even with data in hand, there exist unavoidable deviations between them because experiments and simulations were carried out by different authors in various conditions. Hence, the key contributions of this article are as follows:

- A probabilistic ML model on the basis of the Bayesian Neural Network rather than deterministic models introduced in the reviewed research works, is proposed for evaluating the effect of axis distance on the deterioration of RC beams' flexural strength. The advantage of such a probabilistic model is that it could not only predict quantities of interest, such as load, deformation, etc., but it is also able to estimate what amount of uncertainty is associated with prediction values; and

- With the help of the proposed ML model, the evolution curves of the FSD factors against exposure time can be computed for various values of axis distance, providing reference results for the subsequent studies.

The remainder of this article is organized as follows. Sections 2 and 3 respectively introduce the background and a database including both experimental and numerical data collected from the literature for RC beams' flexural strength deterioration under ISO 834 fire. After that, Section 4 describes the theoretical foundation and realization steps of the Bayesian Neural Network. Section 5 then demonstrates the calculation results obtained by BNN and resulting FSD curves for various axis distances. Finally, the conclusions and some ideas for future works are withdrawn in Section 6.

2. Flexural strength deterioration of RC beams exposed to ISO 834 fire

The European standard ISO-834 fire exposure [17] is one of the most common standards in the world, which describes in detail the temperature-time relation on the surface of the fire-exposed structural members, based on which the time-dependent temperature distribution and evolution within the cross-section of structural members can be further analyzed. According to the standard, the temperature at the beam's surface exposed to fire is determined by the following equation:

$$T = T_0 + 345 \log_{10}(8t + 1) \tag{1}$$

where t is time expressed in minutes, T is the temperature at time t in Celsius degree, and T_0 is the initial temperature, which is usually set to 20 °C.

In real situations, when a fire occurs, temperatures of any internal points within the beams' cross-sections will be lower than those of the points on the concrete surfaces which are directly exposed to fire, because heat requires a transfer process to reach these points. The transfer process is dependent on the materials' thermal properties. It is well known that the thermal conductivity of concrete is much lower than that of steel; therefore, it is reasonable to assume that the temperature in rebar is the same as that of the nearby concrete areas. As the temperature increases, the material strength will decrease accordingly, leading to the reduction in the beam flexural strength. This reduction is quantified through the FSD factor which is the ratio between the ultimate moment capacity at an elevated temperature T, i.e., $M_{u,T}$ with that at ambient temperature M_u as follows:

$$k_{FSD} = \frac{M_{u,T}}{M_u} \tag{2}$$

The value of $M_{u,T}$ could be experimentally determined indirectly through the ultimate load at failure or theoretically calculated using the 500 °C isotherm method as done in [5, 6].

3. Database on RC beams under ISO 834 fire

As a standard step when building any data-driven method, it is crucial to prepare a relevant database a priori, which would be used to train and validate the data-driven method later. The authors conducted a bibliography study from the literature and selected a number of published works which were directly related to the flexural behavior of beams at elevated temperatures. The criteria for selecting this database are the following three folds: (i) The considered concrete is ordinary Portland concrete (OPC), without any of other materials such as fly ash, geopolymer, fiber-reinforced polymer, etc.; (ii) Fire exposure is in conformity with the ISO 834 Standard; and (iii) The results should provide directly or indirectly information about the FSD of RC beams.

In summary, nine selected works are enumerated in Table 1, including the size of data, the cross-section of RC beams ($b \times h$), the tensile rebar ratio of the beam ($\mu_{A_{sbot}}$), the cube concrete strength (f_{cu}), duration (t) and axis distance (a).

It is noted that the tensile strength of the longitudinal reinforcement is not a variable of interest in the published research works since the reduction factors of hot-rolled reinforcing steel strength at elevated temperatures are identical between the steel classes [18]. However, in future this figure should be considered for the cold-worked reinforcing steel, which has different values of strength reduction at the same temperature compared to that of hot-rolled reinforcing steel.

Table 1. Summary of database on the flexural behavior of RC beams subjected to ISO 834 standard fire, collected from the literature

No	Study	Number of data	b (mm)	h (mm)	f_{cu} (MPa)	$\mu_{A_{sbot}}$ (%)	a (mm)	Time (min)
1	Kodur et al. [1]	9	300	500	37.5	0.63	50	0-240
2	Kodur and Dwaikat [2]	27	300	500	30	0.63	50	0-220
3	Thanaraj et al. [3]	35	200	200	20, 30, 40, 50	0.39	30	0-240
4	Gedam [4]	27	200	400	25	1.00	28, 48, 68	0-240
5	Nguyen et al. [5]	108	80, 160, 300, 500	150, 300, 600, 800	30	1.00	30	0-240
6	Nguyen et al. [6]	7	300	600	20	1.64	40	0-240
7	Sun et al. [7]	5	200	300	20	0.75	30	0-120
8	Ozbolt et al. [8]	5	200	300	20	0.75	30	0-120
9	Zhang et al. [9]	24	300	600	45	1.27	40, 60	0-220

For each work, one focused on the evolution of FSD against the temperature, relevant information is extracted and stored in a tabular format. These tabular data were concatenated together, forming a

final database with 7 columns of features and 244 lines of data. Moreover, Fig. 1 displays histograms of features, showing clear visualization of the range of values as well as their distributions. It can be seen from Table 1 and Fig. 1 that the compressive strength of concrete varies in the range [20- 50 mm], the rebar ratio in [0.4-1.7%], the beam width in [80-500 mm], beam height in [160-500 mm], axis distance in [28-60 mm]. Next, the database is split into three non-overlapping datasets, namely training, validation and testing dataset with a ratio of 60:20:20.

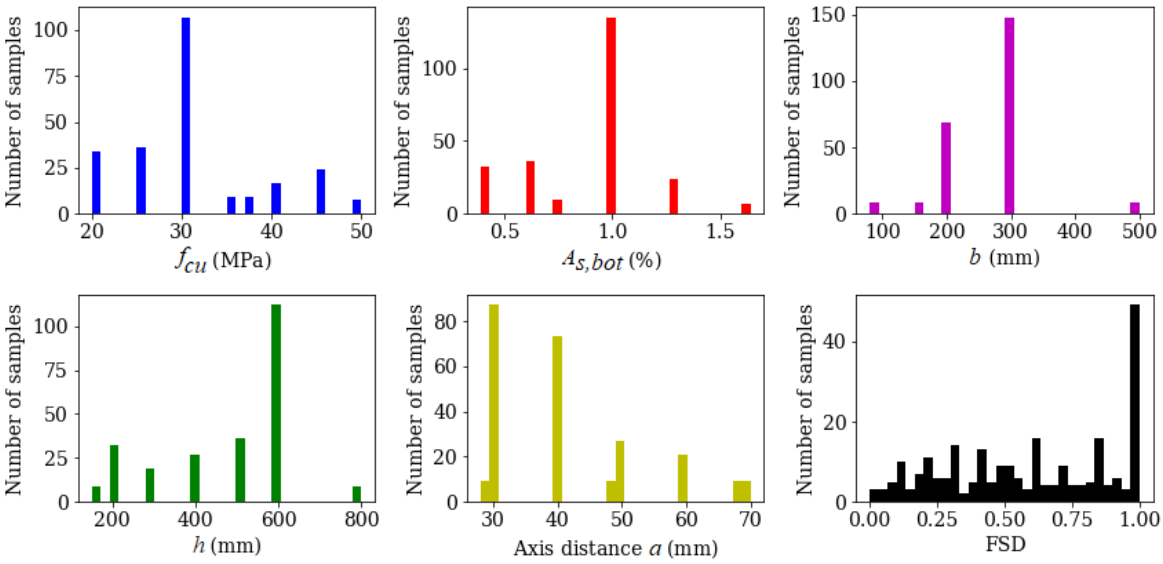

Figure 1. Statistical representation of database via histograms

4. Stochastic model using Bayesian Neural Network

Bayesian Neural Network (BNN) [19] is a probabilistic deep learning model that combines the high prediction performance of ANN with the ability to estimate uncertainty of the Bayes theory. In the authors' opinion, the model is especially suitable for working with not-so-abundant experimental data because two reasons: (i) In practice, similar series of experiments with identical input parameters still provide different results due to unavoidable uncertainty; and (ii) Fitting an ANN with many parameters to a limited database may cause the over-fitting problem, i.e., ANN is likely to yield low-accuracy results on new data despite being well trained. In other words, it is necessary to not only perform prediction of RC beam response but also to estimate how much confidence we have about the prediction results.

Specifically, the adopted architecture of the BNN in this study is 6/16/16/1, i.e., it consists of an input layer with 6 neurons, 2 hidden layers with 16 neurons and an output layer with 1 neuron corresponding to the FSD factor, as graphically illustrated in Fig. 2. For the input layer, there are six neurons corresponding to the concrete strength, beam width, beam height, rebar ratio, axis distance and exposure time. Because the data size is moderate, it is not reasonable to use either a too deep architecture of many hidden layers, or a wide layer with too many neurons, which could increase the number of parameters to determine significantly. On the other hand, as a rule of thumb, the number of neurons should be a power of 2 to be convenient with the binary memory structure of the computer; thus, one sets the number of neurons for the hidden layer as 16. Note that, for the BNN model, each

neuron has two parameters to be determined as discussed previously, characterizing the probability distribution of its weight. At the beginning of learning, they are initialized as a normal distribution with zero mean and unity standard deviation.

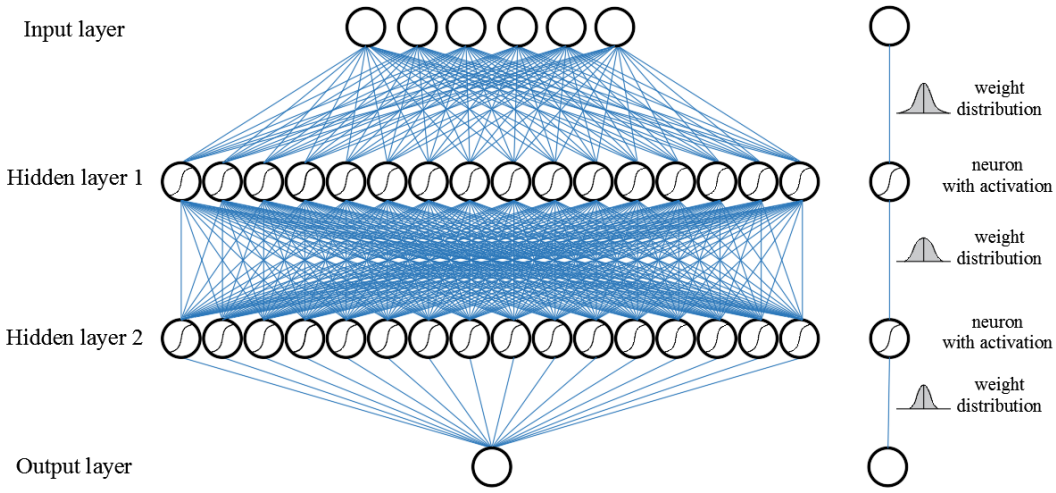

Figure 2. Graphical representation of Bayesian neural network whose weights are characterized by probability distributions

5. Calculation results on FSD factor using data-driven model

The updating of the model's weights is realized with the help of the optimization algorithm Adam belonging to the first-order gradient descent optimization family which gradually adapts the model's weights by a small amount after each iteration to reduce the loss function. The amount of updates is controlled through a hyper-parameter, a.k.a, learning rate, which is set equal to 0.001. This value was determined via a preliminary test to ensure the learning process is convergent within a reasonable learning time. Note that a small learning rate will unnecessarily increase learning time, while a large value could lead to premature results. On the other hand, to obviate the scale difference issue between different features with different physical meanings, the pre-processing standardization is adopted. The implementation of the proposed data-driven framework is realized by the authors with the aid of the deep learning library Pytorch for building the overall framework, the deep probabilistic library Pyro [20] for building the BNN-based data-driven model, Pandas for data management, scikit-learn library [21] for data standardization and Matplotlib for data visualization.

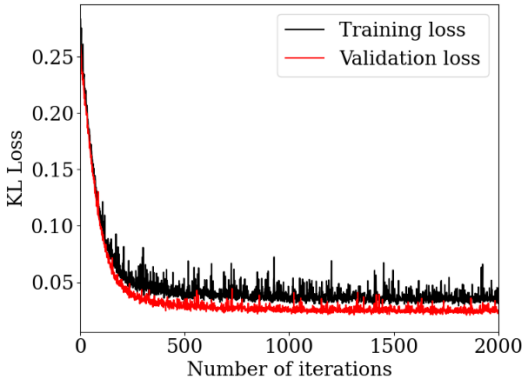

Figure 3. Evolution of KL loss function against number of iterations on training and validation datasets

Once the probabilistic model is built, it will be trained with the database prepared in the previous section associated with the aforementioned training setting. Fig. 3 depicts the learning curve of

the BNN model, showing how loss functions evolve versus the number of training iterations, a.k.a., epochs, on both training and validation datasets. Apparently, the KL loss function quickly drops for epochs from 0 to 200, before gradually decreasing to values around 0.04 and 0.03 on the training and validation datasets, respectively. After that, a steady trend is observed, i.e., no clear improvement is obtained, until the number of epochs reaches 2000. It is also noticed that for epochs from 1600 to 1800, there is less fluctuation in loss function than for other intervals; hence, one selected the configuration at iteration 1600 as the final configuration of the BNN model.

Next, the final performance of the trained model is evaluated on the test dataset, whose results are demonstrated in Fig. 4. It can be seen in Fig. 4 that each data point (shown in the cross symbol), its X-coordinate denotes true FSD values from the database, while Y-coordinate is a value predicted by the model. Ideally, a perfect model will provide the same results as those from the database, as highlighted by the solid 45-degree inclined line. It can be seen that, predicted points lie closely to the ideal line. Statistically, the average of relative errors is about 6.5%. These results qualitatively and quantitatively confirm the viability of the BNN model.

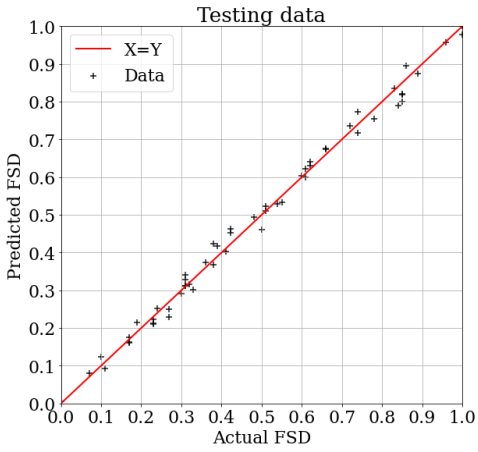

Figure 4. Comparison results between FSD values predicted by the data-driven models with true values from the testing dataset

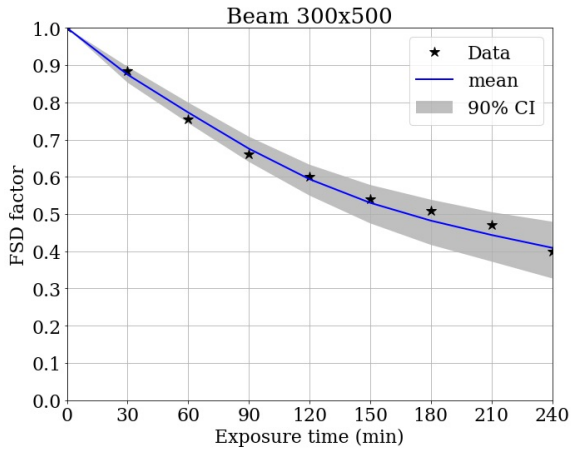

Figure 5. Representative example of FSD curve for a 300×500 beam with an axis distance of 30 mm and associated 90%-confidence interval, constructed by using the data-driven model

After that, the trained model is used to construct the FSD curve showing the evolution of the FSD factor against exposure time. Fig. 5 illustrates an example of computed FSD curves for a 300×500 (mm) beam with $\mu_{A_{sbot}} = 0.6\%$ and an axis distance of 50 mm. To obtain these results, the inference is repeated 100 times, then the average results (in solid blue line) and its 90% confidence interval (gray areas) are derived.

It is noted that for each inference, neurons' weights are randomly drawn from corresponding distributions; thus, they are not the same among inferences, leading to different prediction results. The 90% confidence interval (CI) area signifies that 90% of prediction results will fall within this area. Obviously, the CI area encompasses all data points (from the collected database). In other words, if there is any data point lying outside this CI area, it will be an anomaly uncorrelated with results from the literature, indicating potentially a miscalculation or an unexpected failure.

Next, the data-driven model is used to plot FSD curves for RC beams with $\mu_{A_{sbot}} = 1.0\%$ and with different values of axis distance as shown in Fig. 6 for beams of cross-sections 200×400, 350×500

and 400×600 (in mm). One can roughly divide a FSD curve into three parts. In the first part, the beam can still maintain its strength to some extent. After that, FSD decreases approximately linearly with a faster rate as curves shown in the leftmost subfigure. The third part corresponds to a short period before the failure occurs whose reduction rate is smaller than that of the second part. It is noted that with a low value of axis distance (a = 30 mm), the first part is nearly unnoticeable, i.e., the FSD drop quickly with exposure time; while for larger section and high values of a (a = 80 mm), it can maintain FSD values more than 90% for a period longer than 60 min as shown in the rightmost subfigure. Hence, it should apply adequate axis distance for RC beams to ensure required periods of fire resistance of structures.

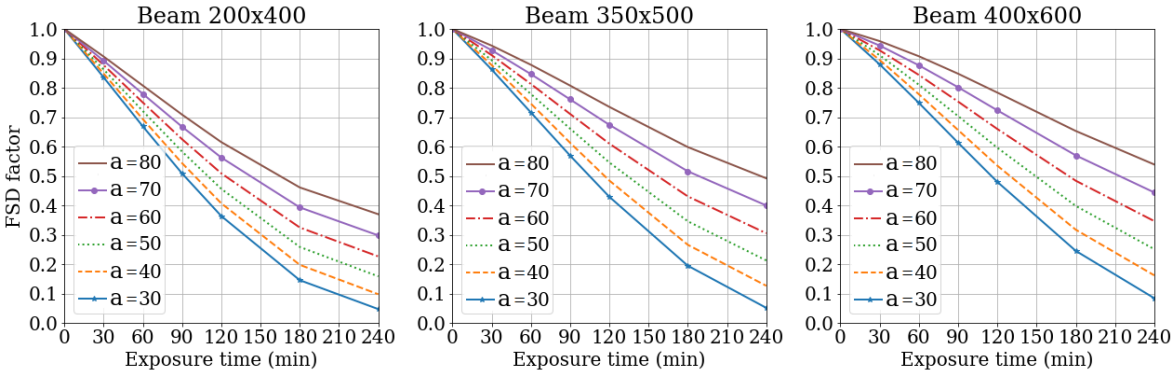

Figure 6. FSD curve for RC beams of various cross-section and different with axis distance values

In detail, the axis distance has a significant impact on the absolute value of the FSD factor, i.e., the larger the axis-distance, the larger the FSD factor. For example, for beam 200×400 (mm), FSD after 240 min for a = 30 mm and 80 mm are around 0.05, and 0.38, respectively. With larger cross-sections of beam (400×600 (mm)), after 240 min for a = 30 mm and 80 mm, FSD factor increases up to 0.1 and ~0.55. Besides, these subfigures placed side-by-side point out that the reduction rate of FSD factors of beams with large cross-sections is considerably lower than that of small beams.

It should be noted that although playing an active role on the FSD factor and the fire resistance of RC beams, the increment of axis distance requires some remarkable issues in the design as follows: (i) It reduces the effective height of the beam cross-section and leads to a reduction of the flexural strength of RC beams at ambient condition; thus the beams dimensions should be further increased for the ambient strength compensation and then influence to the designs of architecture, mechanical and plumping as well as the cost of the project; and (ii) With a relatively thick concrete cover, surface reinforcement mesh should be provided to avoid falling-off of the surface concrete layer when exposed to fire. For example, the Eurocode specifies that when the axis distance to the reinforcement is 70 mm or more, the surface reinforcement mesh should have a diameter not less than 4 mm and a spacing not greater than 100 mm [18].

6. Conclusions

The study presented in this article explores a data-driven method for assessing the flexural strength deterioration (FSD) of reinforced concrete (RC) beams subjected to ISO 834 fire exposure based on its geometric, material properties, and especially axis distance. The backbone of the proposed method is as follows: (i) An experimental and numerical database about the RC beams' flexural strength

selectively gathered from accredited works; and (ii) A probabilistic machine learning model based on the Bayesian Neural Network. Throughout the article, an overview of RC beam's behavior at elevated temperatures, the theoretical foundation of the model, collected database, and key parameters of the proposed approach are described.

As one of the main results, the proposed model helps plot the FSD curves of RC beams for different values of axis distance and provide the associated confidence interval accounting for unavoidable uncertainties of input data and/or the prediction model. In addition, the utilization of the data-driven model is straightforward as it is built based on open source libraries and the user-friendly programming language Python without requiring any specialized software; thus, it could be used as a complementary tool to perform preliminary checks for any theoretical method or experimental set up for fire testing of RC beams.

For the next step of the study, one can incorporate into the database more material/geometric properties and enlarge the BNN model to a more generalized framework accounting for more types of RC beams such as T-beam, fly ash concrete, recycled concrete, etc. Another interesting direction is to extend the proposed method for other structural members such as RC columns, shear walls, steel-concrete composite members, etc. This can be done by using a similar procedure presented in this study, though for members featuring more complex behaviors such as combined shear and flexural behavior, it is required to consider simultaneously different metrics rather than only the FSD factor.

Acknoweledgement

The research presented in this paper was funded by Ministry of Construction (MOC Vietnam) under Grant No. RD 19-21. The financial support of MOC is gratefully acknowledged.

References

[1] Kodur, V. K. R., Dwaikat, M. (2008). A numerical model for predicting the fire resistance of reinforced concrete beams. *Cement and Concrete Composites*, 30(5):431–443.

[2] Kodur, V. K. R., Dwaikat, M. (2008). Flexural response of reinforced concrete beams exposed to fire. *Structural Concrete*, 9(1):45–54.

[3] Thanaraj, D. P., N, A., Arulraj, P., Al-Jabri, K. (2020). Investigation on structural and thermal performance of reinforced concrete beams exposed to standard fire. *Journal of Building Engineering*, 32:101764.

[4] Gedam, B. A. (2021). Fire resistance design method for reinforced concrete beams to evaluate fire-resistance rating. *Structures*, 33:855–877.

[5] Thang, N. T., Trung, N. T. (2019). Investigation on flexural strength deterioration of reinforced concrete beams under fire exposure to the Eurocode. *Journal of Science and Technology in Civil Engineering (STCE) - HUCE*, 13(4V):22–34. (in Vietnamese).

[6] Thang, N. T., Viet, N. H. (2021). Simplified calculation of flexural strength deterioration of reinforced concrete T-beams exposed to ISO 834 standard fire. *Journal of Science and Technology in Civil Engineering (STCE) - HUCE*, 15(4):123–135.

[7] Sun, R., Xie, B., Perera, R., Pan, Y. (2018). Modeling of reinforced concrete beams exposed to fire by using a spectral approach. *Advances in Materials Science and Engineering*, 2018:1–12.

[8] Ožbolt, J., Bošnjak, J., Periškić, G., Sharma, A. (2014). 3D numerical analysis of reinforced concrete beams exposed to elevated temperature. *Engineering Structures*, 58:166–174.

[9] Zhang, G., He, S. H., Guo, H. J. (2012). Assessment of load carrying capacity for concrete rectangle section simple beam subjected to fire. *Applied Mechanics and Materials*, 204-208:2841–2845.

[10] Hung, D. V., Hung, H. M., Anh, P. H., Thang, N. T. (2020). Structural damage detection using hybrid deep learning algorithm. *Journal of Science and Technology in Civil Engineering (STCE) - HUCE*, 14 (2):53–64.

[11] Hung, D. V., Thang, N. T., Dat, P. X. (2021). Probabilistic pushover analysis of reinforced concrete frame structures using dropout neural network. *Journal of Science and Technology in Civil Engineering (STCE) - NUCE*, 15(1):30–40.

[12] Hung, D. V., Thang, N. T. (2022). Predicting dynamic responses of frame structures subjected to stochastic wind loads using temporal surrogate model. *Journal of Science and Technology in Civil Engineering (STCE) - HUCE*, 16(2):106–116.

[13] Naser, M. Z. (2021). Observational analysis of fire-induced spalling of concrete through ensemble machine learning and surrogate modeling. *Journal of Materials in Civil Engineering*, 33(1):04020428.

[14] Panev, Y., Kotsovinos, P., Deeny, S., Flint, G. (2021). The use of machine learning for the prediction of fire resistance of composite shallow floor systems. *Fire Technology*, 57(6):3079–3100.

[15] Fu, F. (2020). Fire induced progressive collapse potential assessment of steel framed buildings using machine learning. *Journal of Constructional Steel Research*, 166:105918.

[16] Kodur, V. K., Naser, M. Z. (2021). Classifying bridges for the risk of fire hazard via competitive machine learning. *Advances in Bridge Engineering*, 2(1).

[17] ISO 834 (1975). *Fire resistance tests - elements of building construction*. International Organization for Standardization.

[18] EN 1992-1-2:2004 (2004). *Eurocode 2: Design of concrete structures. Part 1-2: General rules - structural fire design*.

[19] Bishop, C. M. (1997). Bayesian Neural Networks. *Journal of the Brazilian Computer Society*, 4(1).

[20] Bingham, E., Chen, J. P., Jankowiak, M., Obermeyer, F., Pradhan, N., Karaletsos, T., Singh, R., Szerlip, P., Horsfall, P., Goodman, N. D. (2019). Pyro: Deep universal probabilistic programming. *The Journal of Machine Learning Research*, 20(1):973–978.

[21] Pedregosa, F., Varoquaux, G., Gramfort, A., Michel, V., Thirion, B., Grisel, O., Blondel, M., Prettenhofer, P., Weiss, R., Dubourg, V., Vanderplas, J. (2011). Scikit-learn: Machine learning in Python. *The Journal of Machine Learning Research*, 12:2825–2830.

Journal of Science and Technology in Civil Engineering, HUCE (NUCE), 2023, 17 (1): 26–40

GRAIN BOUNDARY STRENGTHENING OF MICROSTRUCTURE PHASES IN SS400 STRUCTURAL STEEL WELD ZONE

Nguyen Ngoc Vinh[a,*], Duong Hong Quan[a]

[a]*Faculty of Advanced Technology and Engineering, VNU Vietnam Japan University, Nam Tu Liem, Ha Noi, Viet Nam*

Article history:
Received 14/11/2022, Revised 17/12/2022, Accepted 20/12/2022

Abstract

Grain boundary strengthening is a method of strengthening materials by changing their average crystalize (grain) size, exhibiting the basic relationship between yield stress and the grain size of the materials. This methodology is based on the observation of grain boundaries that are insurmountable borders for dislocations and the number of dislocations located within a grain. Applying this methodology to the structural steel weld zone, the mechanical properties of each microstructural phase can be evaluated through the values of grain diameter. For structural steel weld zones, there are not many methods to directly determine the mechanical properties of microstructural phases. Thus, in this study, a methodology was created to evaluate the values of the yield stress of materials based on the grain boundary strengthening equation. This method was constructed by observing the average grain size and determining the mechanical properties of three microstructural phases in the weld zone (i.e. based metal, heat-affected zone, and weld metal). The results from this study provide an easy way for engineers, architects, and scientists to evaluate the values of mechanical properties of based metal, heat-affected zone, and weld metal in the SS400 structural steel weld zone.

Keywords: cyclic loading; dislocation cell; dislocation density; grain boundary strengthening; microstructure; indentation.

https://doi.org/10.31814/stce.nuce2023-17(1)-03

1. Introduction

Structural steel is applied in many different structural projects such as buildings, bridges, mines, the auto industry, and so on, because of its favorable physical properties, for example, high durability, toughness, and ductility [1–5]. The mechanical properties of structural steel are strongly dependent on both service conditions and metallurgical factors, which include temperature, environmental conditions, and especially the historical loading state [6, 7]. To connect the steel members, welding was attributed to being an efficient method since it is fast and simple in the design. Pham et al. [8] pointed out that the microstructure of the weld zone was complex and included three main microstructural phases such as based metal (BM), Heat-affected zone (HAZ), and weld metal (WM). This can lead to the microstructural inhomogeneous and variation of mechanical properties across the weld joint [3]. Furthermore, the weld joint was also considered to be the weakest link because of its microstructural inhomogeneous and the appearance of local stress concentration in the weld zone, leading to crack

*Corresponding author. *E-mail address:* nn.vinh@vju.ac.vn (Vinh, N. N.)

propagation. As mentioned before, the weld zone is mainly composed of three main microstructural phases, i.e., BM, HAZ, and WM. Among them, the microstructures formed in the WM and HAZ regions play an important role in controlling material properties. These properties consist of elastic modulus (E), yield strength (σ_y), strain hardening exponent (n), and indentation hardness (H). Due to the differences in microstructures in the region of HAZ and WM, mechanical properties of these regions are different when compared to the BM region in the weld zone. For the WM region, typical microstructures mainly include grain boundary ferrite, Widmanstatten ferrite, acicular ferrite, and a small amount of pearlite [9]. The HAZ contains Widmanstatten ferrite, large grains of ferrite, and colonies of pearlite [10–13]. It can be seen that the grain size of HAZ is relatively greater than those in the WM region, and the shape of the Ferrite grains is more uniform. Some researchers pointed out that the mechanical properties of materials depended on both metallurgical factors and operation conditions, including environment, load history, and temperature [6, 14]. During the service life, these conditions can cause the degradation of not only the material properties but also the crack propagation in the structural steel weld zone. Thus, there is a lot of attention on the studies on mechanical properties of microstructural phases as well as the influences of operating factors on the microstructural change in the structural weld zone [5, 7, 15–18].

In the late 1990s, Huang et al. [19] studied the inelastic properties of SS400 structural steel weld joints under cyclic gradient stress. The authors used different strength ranges to simulate the case of a sudden extreme earthquake and the results indicated that although weld connection doesn't influence the loading capacity and inelastic deformation capacity for the plain strength steels, weld connection dramatically reduces the inelastic deformation capacity for high-strength steels. An experimental investigation was carried out to determine the important factors that cause cracking and breakage of SS400 steel members under repeated and large deformation [20]. The experimental data showed that the energy dissipation capacity depended on the entire history of loading, the failure mode, the slenderness ratio, and the width-to-thickness ratio. Pham et al. [17] used the depth-sensing instrumented indentation experiment to estimate the microstructural composition of three microstructural phases in the structural steel weld zone. This research indicated that there is no influence of the size, shape, and grain orientation on the elastic modulus of both ferritic phases; however, these orientations have a significant influence on the stiffness of the ferritic phases [17]. Pham and Kim [21] conducted a series of experiments such as a room temperature low cyclic fatigue (LCF), indentation, tensile testing, optical microscopy examination, and finite element methodology (FEM) to investigate the microstructure and mechanical properties in SS400 structural weld zone under low-cycle fatigue. The results from Pham and Kim's study showed that mechanical properties of the WM region were higher than those in the BM region, while the other properties of HAZ decreased from the WM region to the BM region [21]. Recently, Nguyen et al. [5] employed the definition of strain rate sensitivity to investigate the influences of loading rate on mechanical properties of BM, HAZ, and WM subjected to fatigue conditions. Strain rate sensitivity is defined as the change in the mechanical properties to the change of strain rate ($\dot{\varepsilon}_I$) at a given temperature and is described as $m = dH/d\dot{\varepsilon}_I$. The experimental results showed that when the strain amplitude increased from 0.4% to 1.0%, strain rate sensitivity tended to decrease from 0.042 to 0.028, respectively. Moreover, the micromechanism was also proposed to further explain the variation of mechanical properties under different fatigue conditions by showing the relationship between the strain rate sensitivity and dislocation cell size (d') as $m = \dfrac{3\sqrt{3}K_bT}{\alpha\mu bcKV^*}d'$, where K_b and T are Boltzmann's constant and the absolute temperature; V^* is an activation volume; c is Tabor's factor; α, μ, b, and K are material constant.

However, there are not many methodologies to determine directly the mechanical properties of microstructural phases due to the small size of the structural steel weld zone. Furthermore, advanced instrumented machines, such as depth sensing nanoindentation, are not available, leading to the difficulty in the determination of mechanical properties of BM, HAZ, and WM regions. Since the limitation of mechanical properties of the weld zone, the engineers, architects, and designers ignored these properties of the weld zone in the hall structures. Therefore, it is necessary to have a comprehensive study to propose a methodology that allows determining the mechanical properties of microstructural phases based on the information of grain size and to characterize the variation of dislocation lines subjected to the cyclic loading for three main microstructural components.

2. Methodology

Nanoindentation technology is recently used to determine the mechanical properties of the materials based on the indentation responses, i.e., apply load-penetration depth curves as seen in Fig. 1 [4, 22–26]. Generally, Kick's law, $P = Ch^k$, is used to describe the loading part, while $P_u = B(h - h_r)^m$ is also employed to describe the unloading curve [22, 27–33], where C is the load curvature; h is the penetration depth of the indentation; P is the applied load, and k is the exponential factor ranging from 1.5 to 2; h_r is the final depth; B and m are constant coefficients. Based on the indentation responses, hardness and elastic modulus of the materials can be calculated using Eq. (1) and Eq. (2), respectively. For plastic properties of materials, the inverse algorithm and dimensionless function can be used to evaluate the values of yield stress σ_y, and strain hardening exponent n as illustrated in Eqs. (3) and (4) [17, 34].

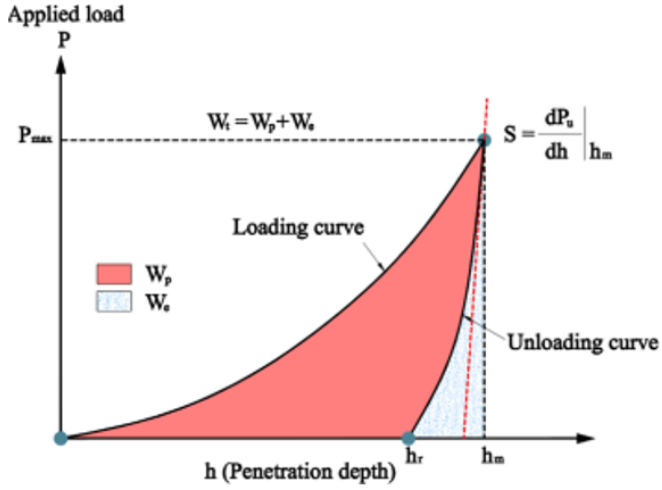

Figure 1. A typical load-displacement curve (P-h) of structural steel from nanoindentation experiment

$$H = \frac{P_m}{A_c} \tag{1}$$

$$E = \left(1 - \vartheta^2\right)\left[\frac{1}{E_r} - \frac{1 - \vartheta_i^2}{E_i}\right]^{-1} \tag{2}$$

$$\frac{E_r^*}{\sigma_y} = \Pi_1 = \sum_{i=1}^{4}\sum_{j=1}^{4}\sum_{k=1}^{3}\left[a_{ijk}n^{j-1}\alpha^{k-1}\left(\frac{E_r}{C}\right)^{i-1}\right] \tag{3}$$

$$\frac{S}{E_r^* h_m} = \Pi_2 = \sum_{i=1}^{4}\sum_{j=1}^{4}\sum_{k=1}^{3}\left[b_{ijk}n^{j-1}\alpha^{k-1}ln\left(\frac{E_r}{\sigma_y}\right)^{i-1}\right] \tag{4}$$

In Eqs. (1)–(4), h_c is contact depth; A_c is contact area; P_m is maximum applied load; ϑ and ϑ_i are Poisson's ratio of the indented material and indenter; E_i is the elastic modulus of the indenter; E_r is reduced modulus; S is the initial unloading slope described as $S = dP_u/dh|_{h_m}$; β is a correction factor for indenter shape; a_{ijk} and b_{ijk} are the coefficients; α is defined as the strain at the start of the stiff strain ε_{st} divided by the initial yield strain ε_y [17].

In this study, a methodology is proposed to determine the values of material properties in the weld zone based on the values of microstructural grain size d. Normally, the variation of microstructure can be observed by using the optical microscope examination. Based on the micro images from optical microscope examination, microstructural grain size of BM and HAZ can be determined using the straight-line method [35]. Since WM includes polymorphic ferrite (α), Widmanstatten ferrite (α_w), and lenticular ferrite (α_a) with different shapes and sizes [36], it is difficult to determine the grain size in this region. Therefore, the straight-line method does not seem to be appropriate to determine the grain size in the WM region. Fortunately, the appearance of the circle method [35] can overcome this challenge. As a result, the circle method was used to determine the average grain size in the WM region in this study. It should be noted that at least 3 circles can be used for each microimage to estimate the average diameter of the grain. The formula of this circle method can be described as $d = (C \times \pi)/(2 \times N \times M)$, where C is the diameter of the circle, N is the number of lines that intersect the circle, M is the scale of the microstructure [35]. The dislocation density (ρ) and dislocation cell size (d) can be calculated based on the micrographs and their sketches of the dislocation structure. Nguyen et al. [5] point out that dislocation density can be calculated using the following equation

$$\rho = \frac{N_{Intersection}}{A} \tag{5}$$

where A and $N_{Intersection}$ are a checked area and the intersection number of the dislocation lines to the surface plane, respectively. It should be noted that both values of $N_{Intersection}$ and A are directly obtained from micro-images.

3. Results and Discussion

3.1. Relationship between grain size and mechanical properties of the weld zone

Fig. 2 shows optical microscopy images of the microstructure of BM, containing ferrite grains and small regions of pearlite (α-ferrite + Fe_3C cement), in which a small amount of pearlite is located at the grain boundary edges or the corners of the ferrite grain [36]. Based on the microimages in Fig. 2, the average grain diameter of the BM region was well calculated using the straight-line method [35]. As a result, d = 12.83 μm ± 2.18 μm was reported for the BM region. Similarly, the HAZ region composes of polygonal ferrite (PF) grains with different degrees of reflected color brightness as seen in Fig. 3. It can be recognized that ferrite grains in the HAZ region are relatively smaller than those observed in the BM region. Furthermore, there are two types of phase changes that occur in the HAZ during the cooling process. The first one is the high-temperature conversion from $\delta - Fe$ to $\gamma - Fe$, and the second phase is the conversion from $\gamma - Fe$ to $\alpha - Fe$ [36]. The averaged grain size of the HAZ region was determined from the microimages using the straight-line method to be 9.3 μm ± 1.5 μm.

The microstructure of WM is completely different from other phases as observed in Fig. 4. It can be seen that WM mainly contains ferrite grains with different sizes and shapes and a certain small amount of pearlites. These Ferrite grains were divided into several types, for example, polymorphic ferrite (α), Widmanstatten ferrite (α_w), and lenticular ferrite (α_a) [36]. By using the circle method, the mean grain size of the WM region was well reported to be 2.99 μm ± 0.61 μm. It can be recognized from the variation of grain size crossing the weld joint that the mean grain size tends to decrease from the BM region to the WM region, while the value of the HAZ region gradually decreases from the BM region to the WM region. Another interesting feature of the microstructural evolution in the weld joint is that the variation of grain size in the region from HAZ to WM seems to be greater than that in the region from BM to HAZ.

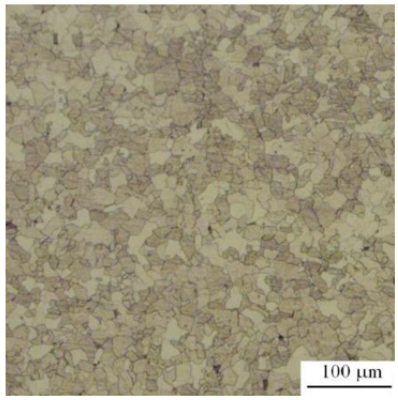

Figure 2. Optical microscopy images of microstructures of BM

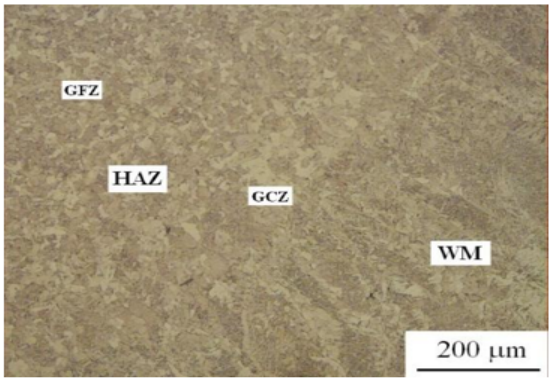

(a) Scale bar of 200 μm

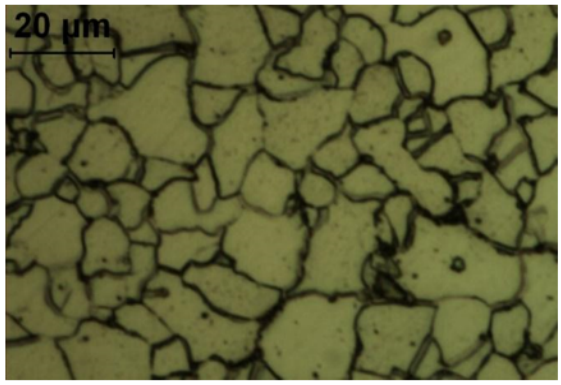

(b) Scale bar of 20 μm

Figure 3. Optical microscopy images of microstructures of HAZ

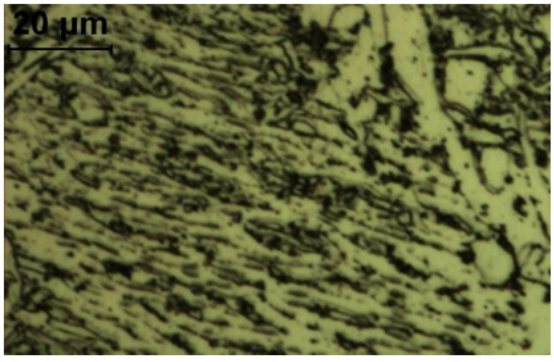

(a) Scale bar of 200 μm

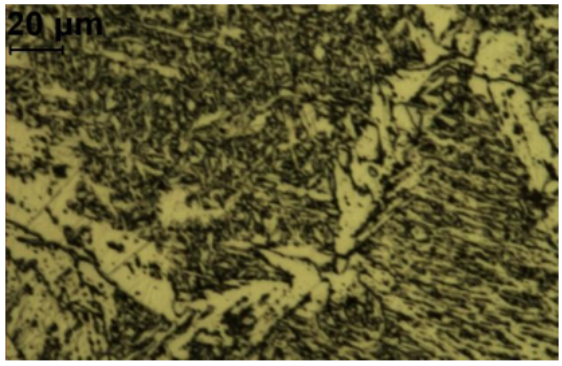

(b) Scale bar of 20 μm

Figure 4. Optical microscopy images of microstructures of WM

Table 1. Average data mechanical properties in the weld zone

Mechanical Properties	BM	HAZ	WM
E (GPa)	207.5	212.2	218.3
H (GPa)	2.0	2.2	2.7
σ_y (MPa)	302.6	331.2	403.4
n	0.191	0.196	0.204

To construct the grain boundary strengthening equation of the SS400 structural steel weld zone, the information on grain size and mechanical properties of each microstructural phase is necessary to build the relationship between the grain size and yield stress. For this purpose, depth-sensing instrumented experiments were conducted on three main regions in the weld zone, for example, BM, HAZ, and WM. Based on the indentation response, the mechanical properties of these microstructural phases were determined using Eqs. (1)–(4). As a result, the values of yield stress, hardness, elastic modulus, and work hardening were obtained as listed in Table 1. It can be seen that both H and σ_y of

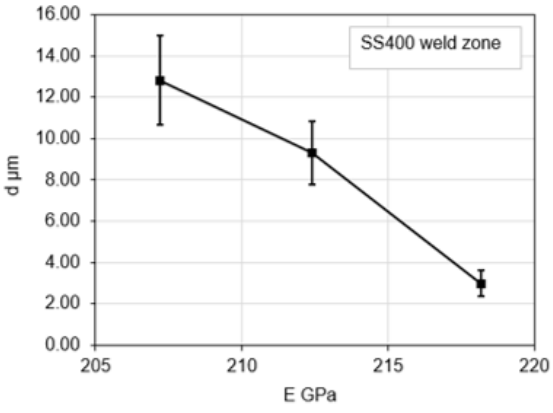

(a) Relationship between d and E

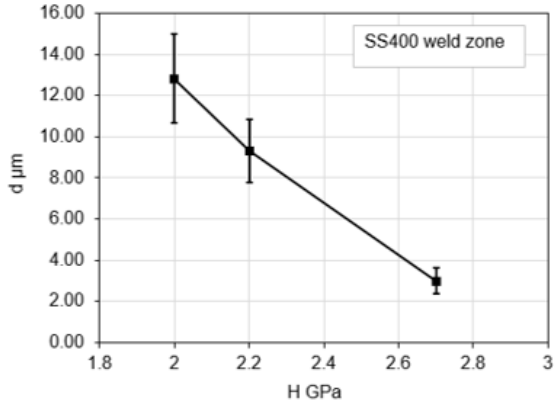

(b) Relationship between d and H

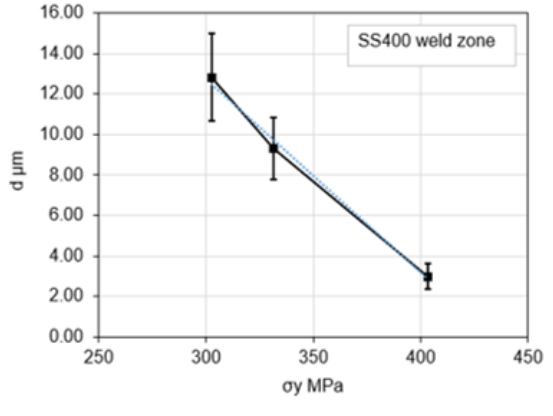

(c) Relationship between d and σ_y

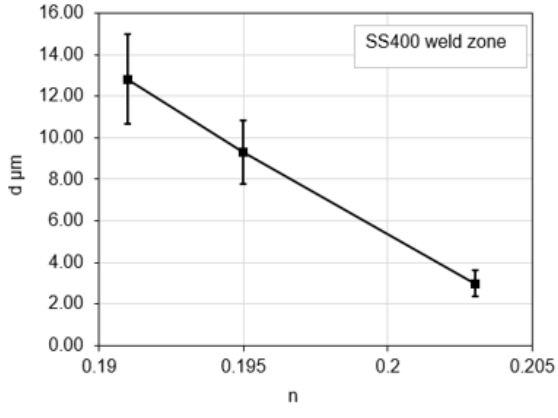

(d) Relationship between d and n

Figure 5. Relationship between the grain diameter and the mechanical properties

BM are the smallest, while the WM region has the highest values compared to other microstructural phases in the weld joint. This trend is in good agreement with the results reported in the literature [10, 37]. Combined with the variation of grain size in the weld zone, the relationship between mechanical properties and grain size was well constructed as shown in Fig. 5.

It can be observed that E decreases from 218.2 GPa to 207.2 GPa when the grain size increases from 2.99 μm ± 0.61 μm to 12.83μm ± 2.18 μm. It means that E is inverse-proportional to the grain size. Furthermore, the relationship between E and grain size seems to be nonlinear as seen in Fig. 5(a). A similar observation for the relationship between σ_y, H, n, and grain size can be seen in Figs. 5(b), 5(c), and 5(d), respectively. When the grain size increases in the range of 2.99–12.83 μm, H decreases from 2.7 GPa to 2 GPa, while σ_y decreases from 403.4 MPa to 302.6 MPa. Additionally, n tends to increase from 0.191 to 0.204 with the decrease of grain size from 12.83 μm ± 2.18 μm to 2.99 μm ± 0.61 μm. It can be deduced that mechanical properties of microstructural phases tend to increase when the grain size becomes smaller.

3.2. Grain boundary strengthening equation in the weld zone

Grain boundary strengthening (or Hall–Petch strengthening) is generally employed as a methodology to strengthen materials through a change in their mean grain (crystallite) size, in which the change of grain size can influence the number of dislocations piled up at the grain boundary and yield stress [38]. Thus, the yield stress-grain size relationship can be mathematically described by the Hall–Petch equation as follows [38, 39]:

$$\sigma_y = \sigma_0 + \frac{k_y}{\sqrt{d}} \tag{6}$$

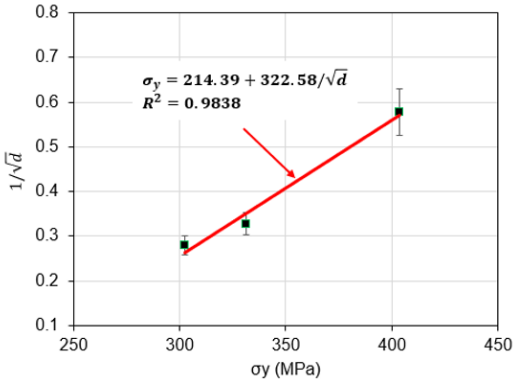

Figure 6. Plot of $1/\sqrt{d}$ versus yield stress to determine the Hall–Petch equation using regression analysis

In Eq. (6), σ_0 is a material constant for the starting stress for dislocation movement and k_y is the strengthening coefficient [38]. Since the main purpose of this study is to find out the relationship between mechanical properties and grain size, the regression analysis was employed to evaluate the parameters of Eq. (6), and the results were shown in Fig. 6. It should be noted that the correlation between σ_y and $1/\sqrt{d}$ was employed to reduce the complexity of the regression analysis. Thus, the linear relation of yield stress and $1/\sqrt{d}$ was employed instead of the original relation of grain boundary strengthening relation. As seen, the relationship between σ_y and $1/\sqrt{d}$ can be well described by using the following equation

$$y = 0.0031x - 0.6646 \tag{7}$$

As a result, the strengthening equation for weld joint was logically described as

$$\sigma_y = 214.39 + 322.58/\sqrt{d} \tag{8}$$

Eq. (8) describes well the experimental data in the weld zone with a standard deviation of 0.984. Furthermore, the values of material constant σ_0 and the strengthening coefficient k_y were determined via the regression analysis results as 214.39 and 322.58, respectively. Thus, Eq. (8) was recommended

to describe the grain boundary strengthening relationships in the SS400 structural steel weld zone. It can be observed from the variation of mean grain size (Figs. 2–5) and the variation of mechanical properties in the weld zone that yield stress tended to increase from the BM (302.6 MPa) to the WM (403.4 MPa), while means grain size showed a decrease from 12.83 μm ± 2.18 μm to 2.99 μm ± 0.61 μm, respectively. It means that the yield stress and mean grain size are inversely proportional to each other.

To confirm the accuracy of the present study, the strengthening equation for SS400 structural steel weld zone was compared to the results reported in the literature [36, 40]. The results indicated that the strengthening equation described well the correlation between yield stress and grain size with a maximum relative error of 3.82%. The maximum relative error being less than 5% ensures the high accuracy of the grain boundary strengthening equation of the SS400 structural steel weld zone in this study. Therefore, this equation can be used to predict the values of mechanical properties of microstructural phases based on the values of grain size, which can be easily obtained from the micro images of microstructure.

Table 2. Validation of present grain boundary strengthening equation

	d (μm)	σ_y (MPa)	Prediction of present study (MPa)	Relative error (%)
Pham et al. [36]	17.5	302.70	291.50	3.70
Nguyen et al. [40]	18	301.95	290.42	3.82

3.3. Variation of mechanical properties of SS400 structural steel weld zone under low-cycle fatigue

In this section, the variation of mechanical properties of SS400 structural steel weld zone was investigated by performing the nanoindentation experiments on the fatigue specimens at the strain amplitude of 0.4%, 0.6%, 0.8%, and 1.0%. It should be noted that all nanoindentation experiments were performed at the same loading rate of 0.04/s and these tests must be conducted as soon as finishing the polishing process to reduce the influence of oxidation. The results of indentation experiments were presented in Fig. 7. As seen, when the strain amplitude increases from 0.4% to 1%, the larger applied load and indentation depth can be observed. Indeed, at the strain amplitude of 0.4%, the maximum applied load can be observed to be 183.239 mN, and the maximum indentation depth can be obtained to be 2057.55 nm. Furthermore, at the strain amplitude of 0.6%, the maximum applied load

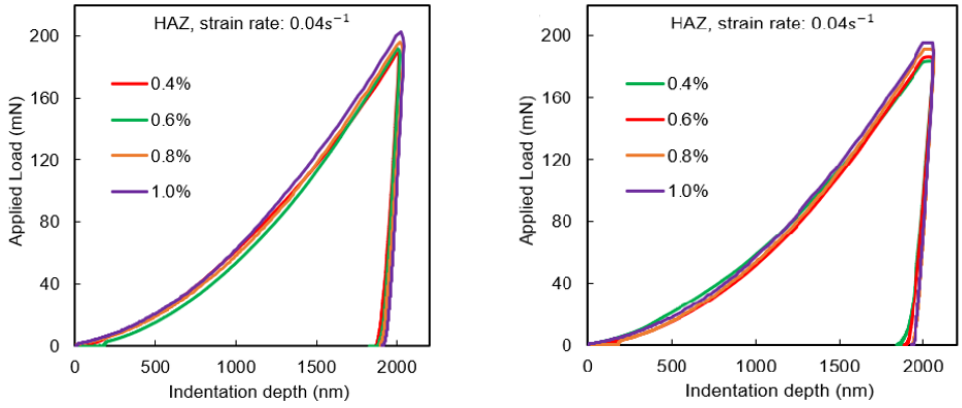

(a) Series #1 (b) Series #2

Figure 7. Indentation curves of microstructural phases in SS400 structural steel weld zone

is 186.133 mN, while the largest penetration depth can be obtained being 2054.65 nm. When the strain amplitude increase to 0.8%, the maximum applied load can maximum displacement can be recorded as 191.701 mN and 2047.36 nm, respectively. At the highest strain amplitude, the maximum applied load reaches 195.527 mN, corresponding to the maximum indentation depth of 2056.28 nm. From the experimental data, it can be inferred that the applied load and indentation depth both tend to increase with the increase of strain amplitude. The same behavior can be observed for series #2 of indentation curves presented in Fig. 7(b). Based on these indentation responses, mechanical properties of material can be determined using Eqs. (1)–(4), resulting in the relationship between mechanical properties and fatigue condition was well constructed in Figs. 8 and 9.

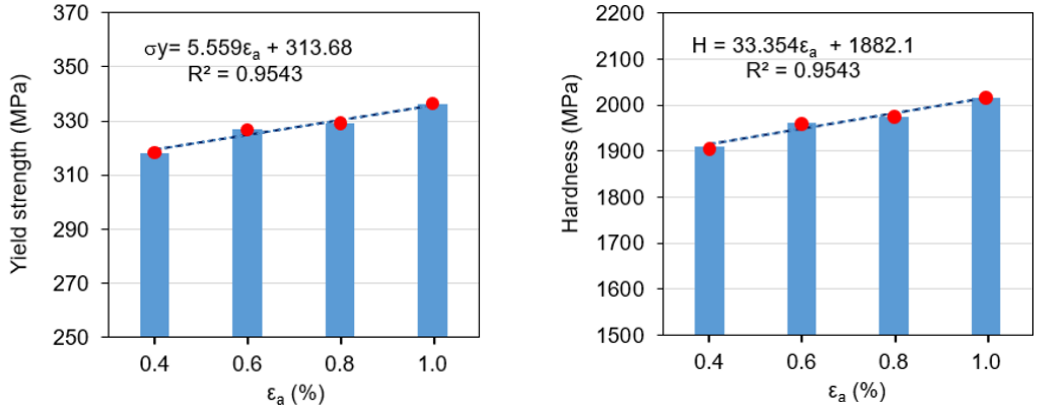

(a) Variation of yield strength

(b) Variation of hardness

Figure 8. The influences of cyclic loading on mechanical properties for series #1

It can be observed from Fig. 8(a) that σ_y tends to increase from 318.30 MPa to 336.15 MPa when the strain amplitude gradually increases from 0.4% to 1.0%. The variation of yield stress seems to be linear as illustrated in Fig. 8(a) and described in Eq. (10). Similarly, the same behavior of hardness can be observed in Fig. 8(b). Indeed, when the strain amplitude increases from 0.4% to 1.0%, H increases from 1909.80 MPa to 2016.91 MPa, respectively. The linear increase of hardness with the increase of strain amplitude can be described using the linear equation, Eq. (10), and the equation parameters can be obtained using the regression analysis. In Eqs. (9) and (10), ε_a is the strain amplitude of the low-cycle fatigue testing. It can be seen that Eq. (9) describes well the experimental data of yield stress of three main microstructural phases in the SS400 structural steel weld zone. Similarly, the observation for hardness can be found in Fig. 8(b).

$$\sigma_y = 5.559\varepsilon_a + 313.68 \tag{9}$$

$$H = 33.354\varepsilon_a + 1882.1 \tag{10}$$

From the data obtained in Fig. 7(b), Eqs. (1)–6 calculate the mechanical properties of the material under cyclic loading, and the results were shown in Fig. 9. It can be observed that the yield strength σ_y value also tends to increase from 342.37 MPa to 362.40 MPa when the strain amplitude gradually increases from 0.4% to 1.0%. This growth trend can also be seen in Fig. 9(b), indeed when the strain amplitude increases gradually from 0.4% to 1.0%, the trend of hardness H increases from 2054.20 MPa to 2174.42 MPa. The variation of yield stress and hardness under strain amplitude can

be described using the equations as follows

$$\sigma_y = 6.3645\varepsilon_a + 336 \tag{11}$$

$$H = 38.187\varepsilon_a + 2016 \tag{12}$$

Eqs. (11) and (12) describe well the experimental data in the weld zone with a standard deviation of 0.9742.

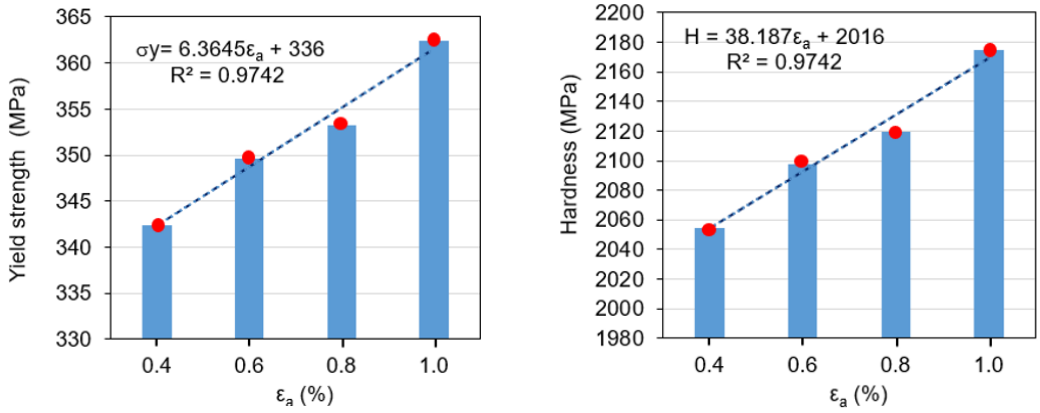

(a) Variation of yield strengt

(b) Variation of hardness

Figure 9. Influences of cyclic loading on mechanical properties for series #2

3.4. Microstructure evolution of SS400 weld zone under cyclic loading

The basic correlation between the damaged microstructure and the degradation of mechanical properties of the SS400 structural steel weld zone strongly depends on the strain amplitude of cyclic loading. Therefore, the dislocation structure of the damaged samples at different strain amplitude levels was observed and investigated by using optical microscopy examination. The results of optical microscope examination were illustrated as seen in Fig. 10.

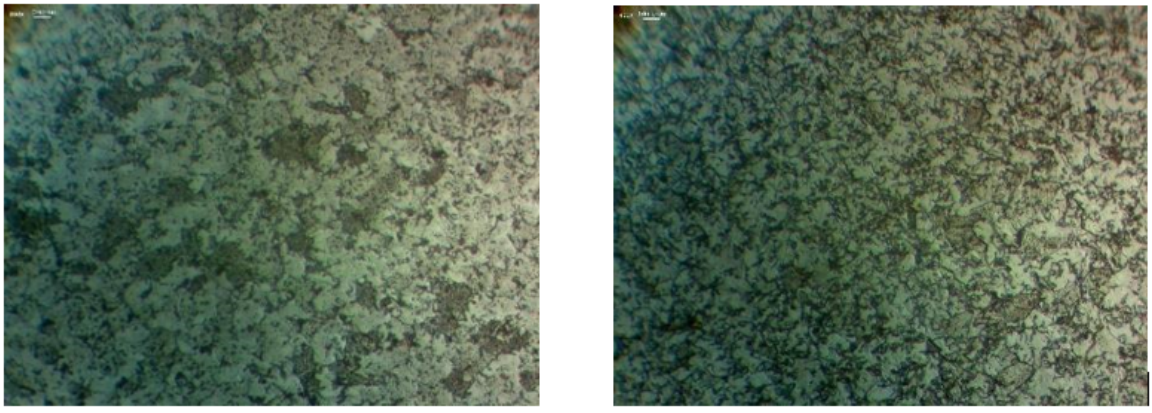

(a) Microstructure of BM region at a strain amplitude of 0.4%

(b) Microstructure of BM region at a strain amplitude of 1%

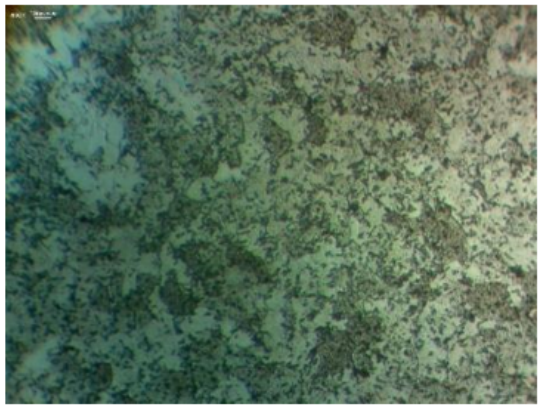

(c) Microstructure of HAZ region at a strain amplitude of 0.4%

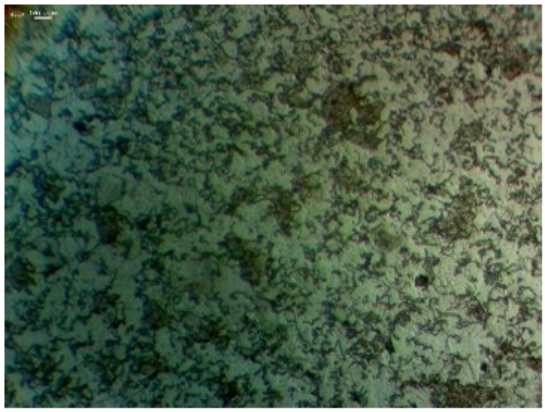

(d) Microstructure of HAZ region at a strain amplitude of 1%

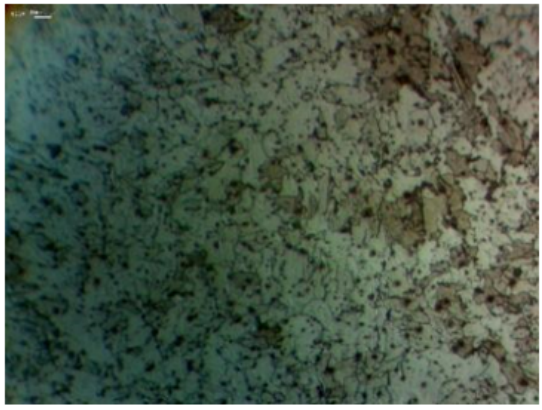

(e) Microstructure of WM region at a strain amplitude of 0.4%

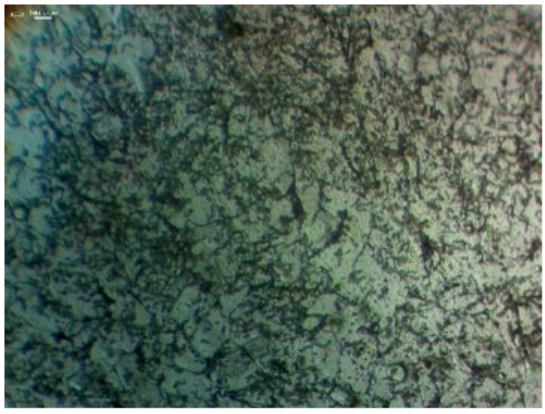

(f) Microstructure of the WM region at a strain amplitude of 1%

Figure 10. Dislocation structure of microstructural phases under cyclic loading

At a strain amplitude of 0.4%, as mentioned before, the grain size of the BM region is larger and the grain size of the WM region is smaller, while the grain size of the HAZ region gradually decreases from the BM region to the WM region. The dislocation density gradually increases from BM to WM as observed in Figs. 10(a), 10(c), and 10(e), respectively. The dislocation lines were developed with a random arrangement. Dislocation lines were detected in the sub-grains resulting in the formation of smaller grain size structures as demonstrated in Figs. 10(a), 10(c), and 10(e). When the strain amplitude increased from 0.4% to 1%, the dislocation structures of BM, HAZ, and WM regions were fully developed as seen in Figs. 10(b), 10(d), and 10(f). It can be seen that the density of dislocation lines at 1% strain amplitude was higher than those at a lower strain amplitude level (0.4%). Furthermore, the sub-grain size was also observed to decrease. It means that the density of dislocation tends to increase as illustrated in Figs. 10(b), 10(d), and 10(f).

Indeed, the dislocation density of the damaged samples was calculated at different strain amplitudes levels, as shown in Fig. 11. It should be noted that the circle method was used to determine the dislocation density of the samples, and further details of this method can be found elsewhere

[35, 41]. The value of dislocation density was obtained from nine different locations with the same diameter. Consequently, the mean values of dislocation density in BM, HAZ, and WM regions at different strain amplitudes (0.4%–1%) were calculated based on these values of the circle method. The analysis results indicated that the mean dislocation density at 0.4% strain amplitude of BM is 37.331 ± 1.397 lines/μm^2. Similarly, the mean dislocation density at 1% strain amplitude of BM is 48.981± 1.226 lines/μm^2. It can be deduced that the dislocation density tended to increase when the strain amplitude increased in the range of 0.4%–1%. The experimental results confirmed the observation of dislocation structure in Fig. 10.

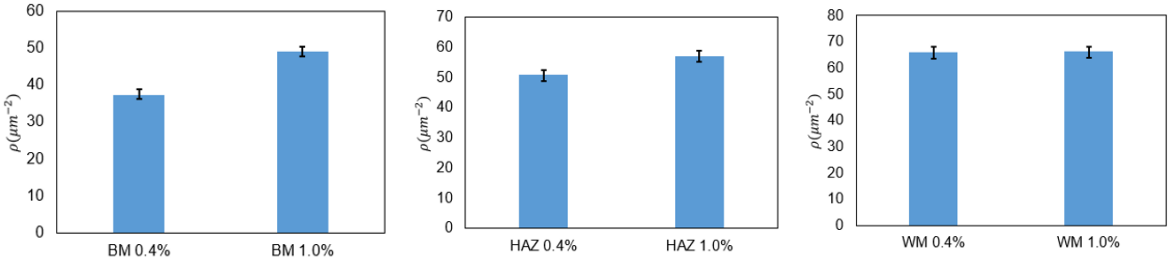

(a) Dislocation density of BM from 0.4% and 1.0%

(b) Dislocation density of HAZ from 0.4% and 1.0%

(c) Dislocation density of WM from 0.4% and 1.0%

Figure 11. Influences of fatigue conditions on dislocation density of BM, HAZ, and WM

Similarly, the microstructure of the HAZ region is at a strain amplitude of 0.4%, and the mean dislocation density of this region is 50.93 ± 1.602 lines/μm^2. When the microstructure of the HAZ region is at a strain amplitude 0.4%, the mean dislocation density of this region is 57.166 ± 2.046 lines/μm^2. The microstructure of the WM region at a strain amplitude of 0.4% , the mean dislocation density of this region is 66.131 ± 2.034 lines/μm^2. The microstructure of the WM region at a strain amplitude of 1%, the mean dislocation density of the region is 66.26 ± 2.244 lines/μm^2. At the same strain amplitude of 0.4%, the mean dislocation density of WM is larger than those in the BM region as observed in Fig. 12(b). Similarly, the mean dislocation density increases from the BM region to the WM region at the same strain applitude of 1% as seen in Fig. 12(a).

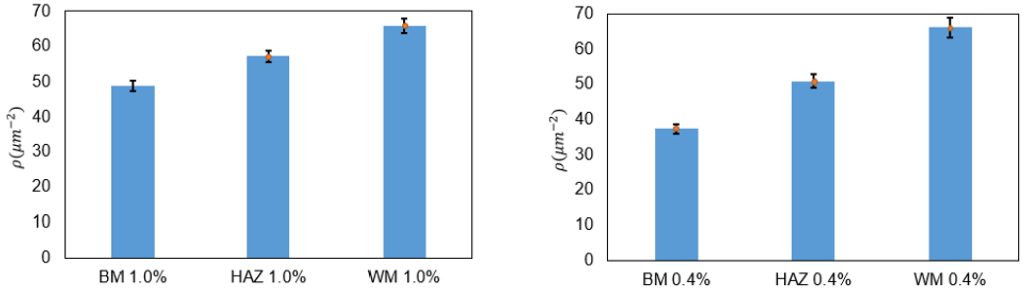

(a) Variation of dislocation density at ε_a = 1%

(b) Variation of dislocation density at ε_a = 0.4%

Figure 12. Dislocation density change of microstructural phases at the same fatigue condition

The relationship between yield stress and dislocation density has been presented through the formula of strain gradient plastic [42]. The formula is built on the dislocation-based Taylor's flow stress

[43], as follows:

$$\sigma = \alpha\mu b\sqrt{\rho_{SSD} + \rho_{GND}} \tag{13}$$

where α is a constant usually assumed to be 0.5 [44]; μ is the shear modulus; b is the magnitude of the Burgers vector; ρ_{SSD} is density Statistically Stored Deviation; ρ_{GND} is density Geometrically Necessary Displacement. In a crystal unit, the GND density is directly related to the plastic strain gradient [45–47]. It can be seen that the yield stress is proportional to the summation of dislocation density since $\alpha\mu b$ is positive for a given material. Indeed, when the strain amplitude increases from 0.4% to 1.0%, the mechanical properties of fatigue specimens increase [48], while the dislocation density tends to increase from 37.331 ± 1.397 lines/μm^2 to 48.981± 1.226 lines/μm^2. It means that the mechanical properties strengthen with the further increase of fatigue condition and yield stress and dislocation density are proportional to each other. This argument confirms the relationship between yield stress and dislocation density as described in Eq. (13).

4. Conclusions

This study provides a simple methodology to estimate the mechanical properties of microstructural phases by constructing the relationship between the yield stress and grain size (strengthening equation). The strengthening equation for SS400 structural steel weld zone was proposed as $\sigma_y = 214.39 + 322.58/\sqrt{d}$. This simple methodology was validated by comparing the yield stress values of SS400 weld zones in the literature. The variation of mechanical properties of SS400 structural steel with the fatigue condition was investigated and discussed. The strain amplitude influences not only the shape but also the magnitude of the loading/unloading curves. When the strain amplitude increased from 0.4% to 1.0%, loading curvature, yield stress, and hardness showed a linear increase while the dislocation density tends to increase from 37.331 ± 1.397 lines/μm^2 to 48.981± 1.226 lines/μm^2.

Acknowledgments

This research has been done under the research project QG.22.25 “Experimental study on the dynamic behavior of microstructural phases in the weld zone under low-cycle fatigue using nanoindentation technology” of Vietnam Nation University, Hanoi.

References

[1] Pham, T.-H., Kim, S.-E. (2015). Nanoindentation for investigation of microstructural compositions in SM490 steel weld zone. *Journal of Constructional Steel Research*, 110:40–47.

[2] Luecke, W. E., McColskey, J. D., McCowan, C. N., Banovic, S. W., Fields, R. J., Foecke, T., Siewert, T. A., Gayle, F. W. (2005). Mechanical properties of structural steel. Technical report.

[3] Pham, T.-H., Kim, S.-E. (2015). Determination of mechanical properties in SM490 steel weld zone using nanoindentation and FE analysis. *Journal of Constructional Steel Research*, 114:314–324.

[4] Nguyen, N.-V., Pham, T.-H. (2020). Experimental study on dynamic nanoindentation on structural weld zone. *IOP Conference Series: Materials Science and Engineering*, 869(3):032027.

[5] Nguyen, N.-V., Pham, T.-H., Kim, S.-E. (2019). Strain rate sensitivity behavior of a structural steel during low-cycle fatigue investigated using indentation. *Materials Science and Engineering: A*, 744:490–499.

[6] Soboyejo, W. (2002). *Mechanical Properties of Engineered Materials*. CRC Press.

[7] Ye, D., Xu, Y., Xiao, L., Cha, H. (2010). Effects of low-cycle fatigue on static mechanical properties, microstructures and fracture behavior of 304 stainless steel. *Materials Science and Engineering: A*, 527 (16-17):4092–4102.

[8] Pham, T.-H., Kim, S.-E. (2017). Characteristics of microstructural phases relevant to the mechanical properties in structural steel weld zone studied by using indentation. *Construction and Building Materials*, 155:176–186.

[9] Nguyen, N.-V., Pham, T.-H., Kim, S.-E. (2019). Microstructure and strain rate sensitivity behavior of SM490 structural steel weld zone investigated using indentation. *Construction and Building Materials*, 206:410–418.

[10] Easterling, K. (1992). *Introduction to the physical metallurgy of welding*. Second edition, Butterworth-Heinemann.

[11] Díaz, M., Madariaga, I., Rodriguez-Ibabe, J. M., Gutierrez, I. (1998). Improvement of mechanical properties in structural steels by development of acicular ferrite microstructures. *Journal of Constructional Steel Research*, 46(1-3):413–414.

[12] Lee, C.-H., Shin, H.-S., Park, K.-T. (2012). Evaluation of high strength TMCP steel weld for use in cold regions. *Journal of Constructional Steel Research*, 74:134–139.

[13] Güral, A., Bostan, B., Özdemir, A. T. (2007). Heat treatment in two phase region and its effect on microstructure and mechanical strength after welding of a low carbon steel. *Materials & Design*, 28(3): 897–903.

[14] Boyer, H. E. (1987). *Atlas of Stress-Strain Curves*. ASM Int. Met. Park. Ohio.

[15] Srinivasan, V., Sandhya, R., Bhanusankararao, K., Mannan, S., Raghavan, K. (1991). Effects of temperature on the low cycle fatigue behaviour of nitrogen alloyed type 316L stainless steel. *International Journal of Fatigue*, 13(6):471–478.

[16] Ye, D., Matsuoka, S., Nagashima, N., Suzuki, N. (2005). Multi-scale deformation behavior investigation of 18Cr–8Ni austenitic steel subjected to low-cycle fatigue loading. *Materials Characterization*, 55(2): 106–117.

[17] Pham, T.-H., Kim, J. J., Kim, S.-E. (2015). Estimating constitutive equation of structural steel using indentation. *International Journal of Mechanical Sciences*, 90:151–161.

[18] Fukumoto, K., Onitsuka, T., Itoh, T., Sakasegawa, H., Tanigawa, H. (2018). Microstructure of fatigue-tested F82H steel under multi-axial loadings. *Nuclear Materials and Energy*, 15:180–184.

[19] Huang, Y. H., Onishi, Y., Hayashi, K. (1996). Inelastic behaviour of HSS with weld connections under cyclic gradient stress. In *11 Th World Conf. Earthq. Eng.*

[20] Park, Y.-S., Park, S.-J., Iwai, S., Kang, S.-H. (2004). Failure and damage of steel thin-plate elements and angle members due to very-low-cycle loading. *Engineering Structures*, 26(11):1623–1632.

[21] Pham, T.-H., Kim, S.-E. (2016). Microstructure evolution and mechanical properties changes in the weld zone of a structural steel during low-cycle fatigue studied using instrumented indentation testing. *International Journal of Mechanical Sciences*, 114:141–156.

[22] Oliver, W. C., Pharr, G. M. (1992). An improved technique for determining hardness and elastic modulus using load and displacement sensing indentation experiments. *Journal of Materials Research*, 7(6):1564–1583.

[23] Nguyen, N.-V., Kim, J. J., Kim, S.-E. (2019). Methodology to extract constitutive equation at a strain rate level from indentation curves. *International Journal of Mechanical Sciences*, 152:363–377.

[24] Nguyen, N.-V., Pham, T.-H., Kim, S.-E. (2019). Microstructure and strain rate sensitivity behavior of SM490 structural steel weld zone investigated using indentation. *Construction and Building Materials*, 206:410–418.

[25] Vinh, N. N., Anh, V. Q., Thang, H. T. (2020). Characterization of strain amplitude-dependent behavior of hardness and indentation size effect of SS400 structural steel. *Journal of Science and Technology in Civil Engineering (STCE) - HUCE*, 14(3):15–25.

[26] Hoan, P. T., Vinh, N. N., Tung, N. T. T. (2019). Indentation for investigation of strain rate effect on mechanical properties in structural steel weld zone. *Journal of Science and Technology in Civil Engineering (STCE) - HUCE*, 13(3):104–112.

[27] Lee, J., Lee, C., Kim, B. (2009). Reverse analysis of nano-indentation using different representative strains and residual indentation profiles. *Materials & Design*, 30(9):3395–3404.
[28] de la Incera, V., Alarcon, R., Cole, P. L., Djalali, C., Umeres, F. (2007). Magnetic Phases in Dense Quark Matter. In *AIP Conference Proceedings*, AIP.
[29] Cheng, Y.-T., Cheng, C.-M. (2004). Scaling, dimensional analysis, and indentation measurements. *Materials Science and Engineering: R: Reports*, 44(4-5):91–149.
[30] Ogasawara, N., Chiba, N., Chen, X. (2006). Measuring the plastic properties of bulk materials by single indentation test. *Scripta Materialia*, 54(1):65–70.
[31] Antunes, J., Fernandes, J., Menezes, L., Chaparro, B. (2007). A new approach for reverse analyses in depth-sensing indentation using numerical simulation. *Acta Materialia*, 55(1):69–81.
[32] Bucaille, J. L., Stauss, S., Felder, E., Michler, J. (2003). Determination of plastic properties of metals by instrumented indentation using different sharp indenters. *Acta Materialia*, 51(6):1663–1678.
[33] Hosseinzadeh, A. R., Mahmoudi, A. H. (2017). Determination of mechanical properties using sharp macro-indentation method and genetic algorithm. *Mechanics of Materials*, 114:57–68.
[34] Truesdell, C. C. *The Pi Theorem of Dimensional Ana sis*. (n.d.).
[35] ASTM E112 (2010). *Standard Test Methods for Determining Average Grain Size E112-10*. ASTM E112-10. 96.
[36] Pham, T.-H., Kim, J. J., Kim, S.-E. (2014). Estimation of microstructural compositions in the weld zone of structural steel using nanoindentation. *Journal of Constructional Steel Research*, 99:121–128.
[37] Kim, J. J., Pham, T.-H., Kim, S.-E. (2015). Instrumented indentation testing and FE analysis for investigation of mechanical properties in structural steel weld zone. *International Journal of Mechanical Sciences*, 103:265–274.
[38] Wikipedia (2019). *Grain boundary strengthening*.
[39] Facchini, D. (2012). Biomedical nanocrystalline metals and alloys: structure, properties and applications. In *Nanomedicine*, Elsevier, 36–67.
[40] Nguyen, N.-V., Pham, T.-H., Kim, S.-E. (2019). Strain rate-dependent behaviors of mechanical properties of structural steel investigated using indentation and finite element analysis. *Mechanics of Materials*, 137: 103089.
[41] Hu, X., Houtte, P. V., Liebeherr, M., Walentek, A., Seefeldt, M., Vandekinderen, H. (2006). Modeling work hardening of pearlitic steels by phenomenological and Taylor-type micromechanical models. *Acta Materialia*, 54(4):1029–1040.
[42] Russo, R., Mata, F. A. G., Forest, S., Jacquin, D. (2020). A Review on Strain Gradient Plasticity Approaches in Simulation of Manufacturing Processes. *Journal of Manufacturing and Materials Processing*, 4(3):87.
[43] Taylor, G. (1938). Plastic strain in metals, Twenty-Eighth May Lect. to Inst. *Met*, 62:307–325.
[44] Nix, W. D., Gao, H. (1998). Indentation size effects in crystalline materials: A law for strain gradient plasticity. *Journal of the Mechanics and Physics of Solids*, 46(3):411–425.
[45] Stölken, J., Evans, A. (1998). A microbend test method for measuring the plasticity length scale. *Acta Materialia*, 46(14):5109–5115.
[46] Nye, J. F. (1953). Some geometrical relations in dislocated crystals. *Acta Metallurgica*, 1(2):153–162.
[47] Ashby, M. F. (1970). The deformation of plastically non-homogeneous materials. *The Philosophical Magazine: A Journal of Theoretical Experimental and Applied Physics*, 21(170):399–424.
[48] Nguyen, N.-V., Pham, T.-H., Kim, S.-E. (2019). Strain rate sensitivity behavior of a structural steel during low-cycle fatigue investigated using indentation. *Materials Science and Engineering: A*, 744:490–499.

Journal of Science and Technology in Civil Engineering, HUCE (NUCE), 2023, 17 (1): 41–57

COMPRESSIBILITY CHARACTERISTICS OF CLAYS IN THE RED RIVER DELTA

Tien Dung Nguyen[a,*], Phyu Sin Khin[a]

[a]*Faculty of Advanced Technologies and Engineering, VNU Vietnam Japan University, Luu Huu Phuoc road, Cau Dien ward, Nam Tu Liem district, Hanoi, Vietnam*

Article history:
Received 17/11/2022, Revised 01/02/2023, Accepted 08/3/2023

Abstract

The Red River Delta (RRD) is the second largest delta in Vietnam and is a significant economic zone in the country, encompassing important cities and economic zones. Geologically, the delta consists of clay layers distributed all over its area, which strongly impact the foundation designs of the infrastructure system (e.g., highways, industrial parks, harbors). However, up to date, there were no comprehensive studies on the compressibility characteristics of the clays in the delta. This study presents a primary study on some compressibility characteristics of clays in the whole delta with an emphasis on the use of CPTu data in the interpretation. For this, high-quality field and laboratory test results obtained from four research test sites and eight project sites were analyzed to depict the characteristics. The results indicate that the clays in the delta are typically soft to medium stiff and normally consolidated to slightly overconsolidated, which represent typical characteristics of young Holocene deposits. The compression index (C_c) of the clays was found to have good correlations with natural water content (W_n) or in-situ void ratio (e_0). The ratio of radial coefficient of consolidation from a consolidation test with a central drain (CD) to the vertical coefficient of consolidation from the standard consolidation test (i.e., $c_{r,CD}/c_v$ from the 4 research test sites is on average 2.76 (log t method) and 2.32 (root t method) and these average ratios are found typical for deltaic soil deposits. The correlations for the remolded samples indicate that the drainage type has a strong influence to the induced coefficients of homogeneously remolded soils. Results from this study help geotechnical engineers have a general view on the compressibility characteristics of the clays in the delta, which in turn helps the engineers secure optimal foundation design solutions.

Keywords: Red River delta; clays; CPTu; compression index; coefficients of consolidation.

https://doi.org/10.31814/stce.nuce2023-17(1)-04

1. Introduction

The Red River Delta (RRD) is the second largest delta in Vietnam, and it plays a significant role in the economics development of the country in both agriculture and industrial sectors. The delta encompasses the capital city of Hanoi, neighbor provinces (e.g., Bac Ninh, Hai Duong, Hung Yen) with important industrial parks, and the port city of Hai Phong. In term of economics, the delta contributes a significant amount over the whole economy of the country. For example, the statistics in 2021 [1] indicated that, with a total area (15,080 km^2) of just 4.5% of the country's area (331,020 km^2), the GDP of the region was up to 26.8 % of that of the country and the contribution rate steadily increases

*Corresponding author. *E-mail address:* nt.dung@vju.ac.vn (Nguyen, T. D.)

further in the coming years. The significant development in economics recently is attributed to the development of the infrastructure system in the delta, which leads to the development of other economic sectors.

For infrastructure projects, such as highways, logistic facilities, harbors, industrial parks, optimal designs of foundation system are highly required since the foundation cost of these project types often accounts for large percent of the total project cost. In securing such optimal designs, properly understanding and using the compressibility characteristics of clayey soils in the designs are crucially important since the characteristics are driving factors for possible excessive deformation of the foundations. In the last two decades, mechanical characteristics of clays (e.g., compression index (C_c), coefficient of consolidation (c_v), and *OCR* value) at some places in Hai Phong city have been reported [2–4]. Geological profiles and physio-mechanical properties from boreholes along some sections of three national highways (NH) in the delta (NH No. 21, NH No. 38B, and NH No. 18) were also analyzed and depicted in Hien [5] and Hien and Giao [6]. The studies above provided us understanding on the characteristics of clays at some specific locations in the delta, however it is still not possible to draw a general picture of the characteristics in the delta, especially the connection between geological and geotechnical features of the delta.

This paper presents a study on some compressibility characteristics of clays in the delta with an emphasis on the use of CPTu data in the interpretation. For this, soil sampling for laboratory tests and CPTu were experimentally carried out at four research sites. In addition, laboratory and field test data at eight additional sites performed by FECON Corp were also used to form a database for the analyses.

2. Geological overview of the RRD

The Red River Delta (RRD) is located on the western coast of the Tonkin Gulf (Gulf of Bac Bo) with an area of about 13,030 km^2. The delta has a triangle shape with its height of about 150 km long from its apex (Viet Tri City at the Northwest) to the Southeast coastline, which is around 146 km from Quang Yen town to Day River mouth. Topographically, the RRD can be divided into three main zones, namely, upper delta, middle delta, and lower delta [7]. The upper delta lies at about 10−15 m above the mean sea level (MSL) and has slightly eroded paleo-terraces at the north side. The middle delta lies at an elevation of 5−6 m above the MSL with gentle wave-shaped in surface and good drainage condition. The lower delta lies near the shoreline with an elevation of 1−2 m above the MSL and composes of coastal flood plain or strand plain, saltwater marshes and sand bars.

Fig. 1 shows a quaternary geological and topographical map of the RRD and adjacent areas [8]. As shown, most of the delta area was formed in the sedimentation process throughout the Holocene period (9 kyr BP to date). Based on the dominated depositional environments, the sediments in the delta can broadly be divided into three main regions: fluvial-dominated, tide-dominated, and wave-dominated. In the north, north-west, west, south-west, the delta plain is surrounded by mountains which are composed of Precambrian crystalline rocks and Paleozoic to Mesozoic sedimentary rocks.

Using the core samples obtained from different locations within the delta, Tanabe et al. [8, 9], Funabiki et al. [10] and among several others, have analyzed and depicted significant findings for the sediments of the delta. Some key points from the studies might be summarized as follows: (1) due to the sea level rise from approximately 100 m below the present MSL (at 15 kyr BP) to the maximum level of about 2−3 m above the present MSL (from 6 kyr to 4 kyr BP), the Quaternary and Holocene sediments in the delta were strongly influenced by both fluvial and marine environments. Stratigraphic cross sections in the delta show the presence of fluvial sediments, estuarine sediments

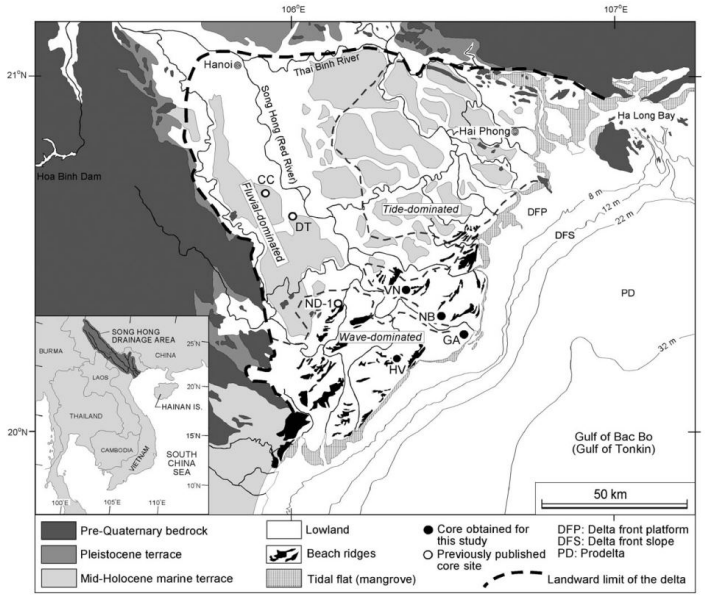

Figure 1. Quaternary geological and topographical map of RRD and adjacent areas [8]

and deltaic sediments [9]; (2) the sediment accumulation curves (attitude vs age) from Tanabe et al. [8] and Funabiki et al. [10] indicate that up to the depth of about 40 m (from the present MSL), all deposits found from the cores are Holocene sediments with the age of less than 10 kyr; (3) from the age of sediments obtained from radiocarbon dating (^{14}C), the progradation of the delta from 9 kyr to present was depicted [8]. The paleogeographic maps of the progradated delta are very helpful to geotechnical engineers to understand the behavior of the deposit regarding the age. It might be deduced from this summary that clay layers in the delta, the target of this study, are typically from the Holocene period.

3. Field and lab test programs

3.1. Study sites

To investigate the compressibility characteristics of the clays in the delta, especially the vertical and horizontal coefficients of consolidation, a research program of field and laboratory tests was carried out recently by the authors. For field tests of this research, soil sampling and cone penetration test with excess pore water pressure measurement (CPTu) were experimentally carried out at four test sites, namely: (1) Dinh Vu Industrial Zone (DVIZ), Hai An Dist., Hai Phong City; (2) Vietnam Singapore Industrial Park (VSIP), Thuy Nguyen Dist., Hai Phong City; (3) Kim Chung – Di Trach Urban Area (KC), Hoai Duc Dist., Hanoi; and (4) Nam Dinh Thermal Power Plant

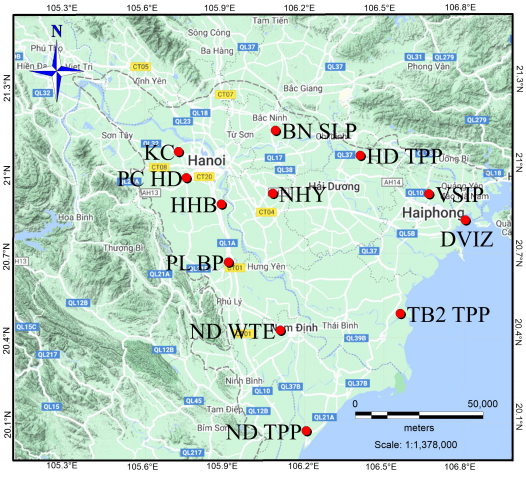

Figure 2. Location of the study sites

(ND TPP), Hai Hau Dist., Nam Dinh Province. Locations of the test sites are marked on the map shown in Fig. 2. Details of the test program are described in next section. Note that these research test sites were also the geotechnical investigation sites of industrial projects where other field tests were also extensively carried out.

Besides test results from the research program, test results from field and lab tests at eight test sites of remarkable industrial projects, which were conducted by FECON Corporation, were selected to make a database of boreholes and soil profiles. The test sites in this collection include: (1) Heineken Hanoi Brewery (HHB), Thuong Tin Dist., Hanoi; (2) Park City Ha Dong (PC HD), Ha Dong Dist., Hanoi; (3) Nestle Hung Yen (NHY), My Hao Dist., Hung Yen Province; (4) Hai Duong Thermal Power Plant (HD TPP), Kinh Mon Dist., Hai Duong Province; (5) Phu Ly Bypass (PL BP), Duy Tien Dist. & Kim Bang Dist., Ha Nam Province; (6) Thai Binh 2 Thermal Power Plant (TB2 TPP), Thai Thuy Dist., Thai Binh Province; (7) Bac Ninh SLP Park (BN SLP), Bac Ninh City, Bac Ninh Province; (8) Nam Dinh Greenity TWE Power Plant (ND WTE), My Loc Dist., Nam Dinh Province. Locations of the test sites are also shown in Fig. 2. The coordinates of all the test sites are given in Table 1.

Table 1. Coordinate of the study sites

No.	Site name	Longitude	Latitude	Province
1	DVIZ	106° 48’ 35.96"	20° 48’ 56.56"	Hai Phong
2	VSIP	106° 40’ 21.79"	20° 54’ 30.67"	Hai Phong
3	KC	105° 43’ 44"	21° 3’ 22.92"	Hanoi
4	ND TPP	106° 12’ 31.21"	20° 4’ 3.11"	Nam Dinh
5	HHB	105° 53’ 22.92"	20° 52’ 15.17"	Hanoi
6	PC HD	105° 45’ 27.86"	20° 57’ 48.38"	Hanoi
7	NHY	106° 5’ 0.96"	20° 54’ 31.5"	Hung Yen
8	HD TPP	106° 24’ 51.8"	21° 2’ 39.62"	Hai Duong
9	PL BP	105° 54’ 58.79"	20° 39’ 54.32"	Ha Nam
10	TB2 TTP	106° 33’ 50.33"	20° 29’ 0.92"	Thai Binh
11	ND WTE	106° 6’ 40.72"	20° 25’ 24.46"	Nam Dinh
12	BN SLP	106° 5’ 39.66"	21° 7’ 56.57"	Bac Ninh

3.2. Field test program

At each test site of the research program, soil boring and sampling were conducted to obtain undisturbed clay samples for laboratory tests, and the CPTu and dissipation test were conducted to study the CPTu-based soil stratification, classification and interpretations. The quantity (i.e., number of borehole and penetration holes) of the tests are listed in Table 2.

For soil boring and sampling, the borehole was advanced by using the rotary wash method with the use of bentonite slurry to stabilize the borehole walls. At a sampling depth, a thin-walled fixed-piston tube sampler of 1.0 m long and 76 mm in inner diameter was hydraulically pushed down to collect undisturbed clay samples. Right after the sample tube was retrieved at the ground surface, the tube ends were cleaned and filled with paraffin and then carefully sealed by tape to preserve water content as well as integrity of the soil sample. All the boring and sampling procedures were carried out in accordance with ASTM D1452–09 [11] and ASTM D1587–09 [12], respectively. When the sampling at the borehole was finished, the sample tubes were then carefully transported to the laboratory for lab tests.

Table 2. Quantity of soil sampling and CPTu test at the four research test sites

No.	Test site	Boring & Sampling			CPTu		
		Number of boreholes	Sampling depths (m)	Number of tubes	Number of Penetration holes	Penetration depths (m)	Number of dissipation points
1	DVIZ	1	8.0–21.0	6	1	0–35	7
2	VSIP	2	6.5–17.5	10	1	0–17.0	5
3	KC	1	7.5–25.5	10	1	0–27.0	9
4	ND TPP	1	2.0–21.0	12	1	0–25.0	7

At each site, the CPTu was conducted nearby the sampling borehole (with a distance of less than 3.0 m). The distance between sampling borehole and penetration hole was strictly controlled to make sure that it is not too close to avoid possible soil disturbance and it is not far to ensure the compatibility of subsoil layers from the two holes. The CPTu was conducted following recommended procedures in ASTM D5778–12 [13]. For each penetration hole, a total of 5 to 6 dissipation test points were conducted to measure the excess pore water press (u_2) dissipated with time, which was then used to estimate the horizontal coefficient of consolidation of the clays. Fig. 3 shows moments of CPTu test at the four test sites.

(a) At DVIZ site

(b) At KC site

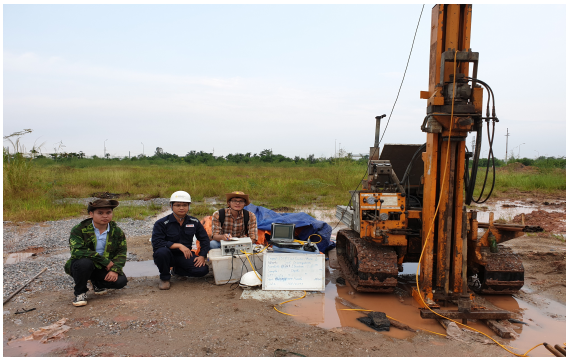

(c) At VSIP site

(d) At ND TPP site

Figure 3. CPTu test at the four research test sites

Besides the field tests purposely conducted in the research program, other field tests, such as boring and sampling, standard penetration test (SPT), CPTu, Downhole seismic test, Field vane shear

(FVS) test, Groundwater level monitoring, were also extensively carried out at the four research test sites as well as at the eight project sites. However, due to space limitation, those field tests are not described in detail herein. Together with the research test results, field and lab test results from the twelve test sites are valuable sources for the analyses in the paper.

3.3. Lab test program

At each test site, standard physical tests and the consolidation test using incremental loading method [14] were carried out on clay specimens to obtain basic physical properties (e.g., unit weight (γ), water content (W_n), particle size (d_p), specific gravity (G_s), liquid and plastic limits (LL and PL), and consolidation properties of clays at the site. In addition to these standard tests, other mechanical (shear) tests such as, unconfined compression (UC) test, unconsolidated undrained triaxial compression (UU) test, consolidated undrained compression (CU) test, and direct shear test (DS) were also carried out for most the sites. All the laboratory tests were carried out at geotechnical laboratory of FECON Corporation (Las XD 442).

In additional to the lab tests described above, pairs of consolidation test with radial drainage using a central drain (CD) and standard consolidation test with vertical drainage (VD) were carried out on clay specimens of the four research sites (i.e., DVIZ, VSIP, KC, ND TPP) to determine radial and vertical coefficient of consolidation (c_r and c_v), respectively. The CD test was performed by using the standard consolidation equipment (i.e., VD) system with the consolidation cell modified to house a central porous stone as graphically illustrated in Fig. 4(a). For the modified consolidation cell, basically, the bottom porous stone (of the standard cell) is replaced by a base steel plate (no. 5 in Fig. 4(a)) with a central hole connected to drainage slots on the bottom face, and the top cap (no. 1 in Fig. 4(a)) is cylindrically hollowed above the central porous stone. The central porous stone was vertically lowed and fit into a central hole of the specimen, which was created by using a mini thin-walled sampler having the same diameter to that of the central porous stone. The verticality and centricity of the central sampled hole was secured by a steel top cap (over the consolidation ring) with a central hole, working as a guide ring. In this study, the central porous stone was manufactured to have a diameter of 29.3 mm, which results in a ratio of diameter of soil specimen (d_e) over the diameter of the central porous stone (d_w) of 2.05 (i.e., $n = d_e/d_w = 2.05$).

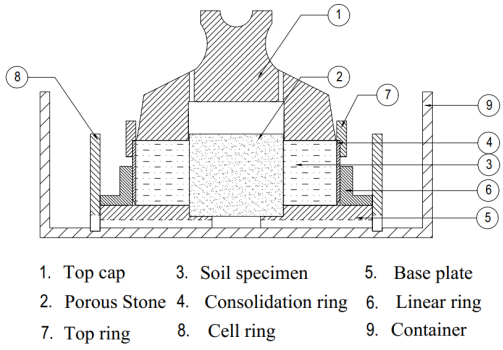

(a) Cell design

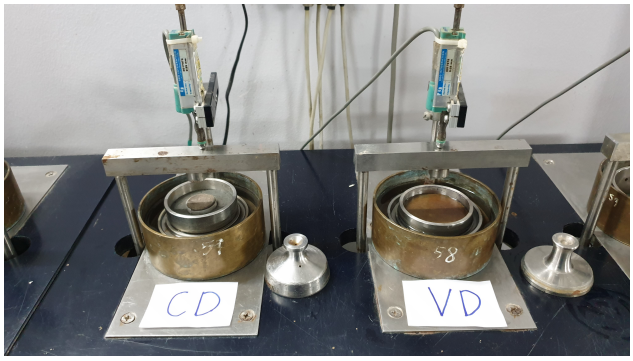

(b) Use of the cell in the laboratory

Figure 4. Consolidation cell of the RCT with a central porous stone

In the laboratory, soil sample were extruded and cut into 10 cm pieces, which were all carefully wrapped in plastic membrane and then waxed to preserve water content of the samples. For a

designated test depth, the 10 cm soil piece was cut into 3 equal parts, one for physical tests, one for the CD test and one for the VD test. It was therefore practically assumed that the soil specimens for the CD and VD had the same characteristics (e.g., homogeneity, compressibility, and permeability). For a typical test pair, seven loading steps of 12.5, 25.0, 50.0, 100.0, 200.0, 400.0, and 800.0 kPa were applied on the specimens. For each loading step, the test method B in ASTM D2435–11 [14] was applied to complete the loading step when 100% primary consolidation is reached. For this, the time – settlement curve of each loading step was observed carefully to make sure that the settlement slightly went beyond the point of 100% primary consolidation. Fig. 4(b) shows an example of the CD and VD tests in the laboratory and Fig. 5 shows an example of time – settlement curves obtained from the two tests at applied pressure σ_v = 800 kPa.

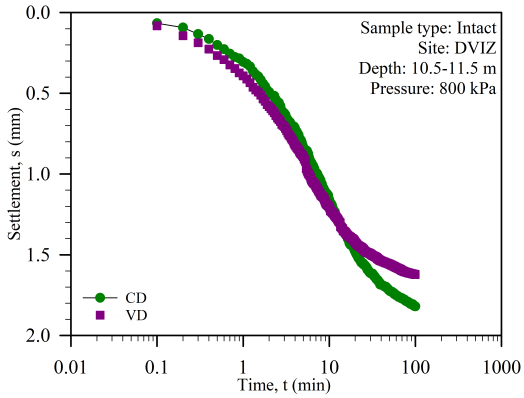

Figure 5. Example of time-settlement curves from CD and VD test

Table 3. Summary of CD and VD tests done for the four research test sites

Test site	Intact soil specimen		Remolded soil specimen	
	CD specimen (test curve)	VD specimen (test curve)	CD specimen (test curve)	VD specimen (test curve)
DVIZ	11 (66)	18 (108)	-	-
VSIP	32 (192)	32 (192)	3 (18)	-
KC	19 (114)	18 (108)	6 (36)	5 (30)
ND TPP	14 (84)	14 (84)	-	-
Total	76 (456)	82 (492)	9 (54)	5 (30)

4. Compressibility characteristics

4.1. CPTu-based stiffness

Stiffness (or consistency) of the clay is an important characteristic that needs to be described in every soil investigation report of sites having clay layers. The feature can be manually assessed in the field by a visual-manual procedure [15] or by the SPT N value (e.g., TCVN 9351:2012 [16], FHWA [17]). Although the CPTu is one of the most versatile field tests described in detail in many references (e.g., Mayne [18], Schnaid [19], Robertson and Cabal [20]), the stiffness classification of clayey soil based on CPTu data has been recommended in a few reports, e.g., Senneset et al. [21], Mayne and Kulhawy [22]. According to Senneset at et al. [21] and Mayne and Kullhawy [22], the stiffness of clayey soil is classified as follows: (*i*) Very soft: $q_t < 0.25$ (MPa); (*ii*) Soft: 0.25 (MPa) $\leq q_t < 0.5$ (MPa); (*iii*) Medium stiff: 0.5 (MPa) $\leq q_t < 1.0$ (MPa); (*iv*) Stiff: 1.0 (MPa) $\leq q_t < 2.0$ (MPa); and Very stiff: $q_t \geq 2.0$ (MPa). This classification is applied to the study sites herein.

Fig. 6 shows q_t profiles in clay layers from 10 sites in the database in which the vertical boundaries of the stiffness ranges described above are given by dashed lines. As shown, a common feature is that the q_t value (or the stiffness) increases rather linearly with depth at all the sites, indicating that the clays are rather homogeneous and were formed under relatively static depositional environments.

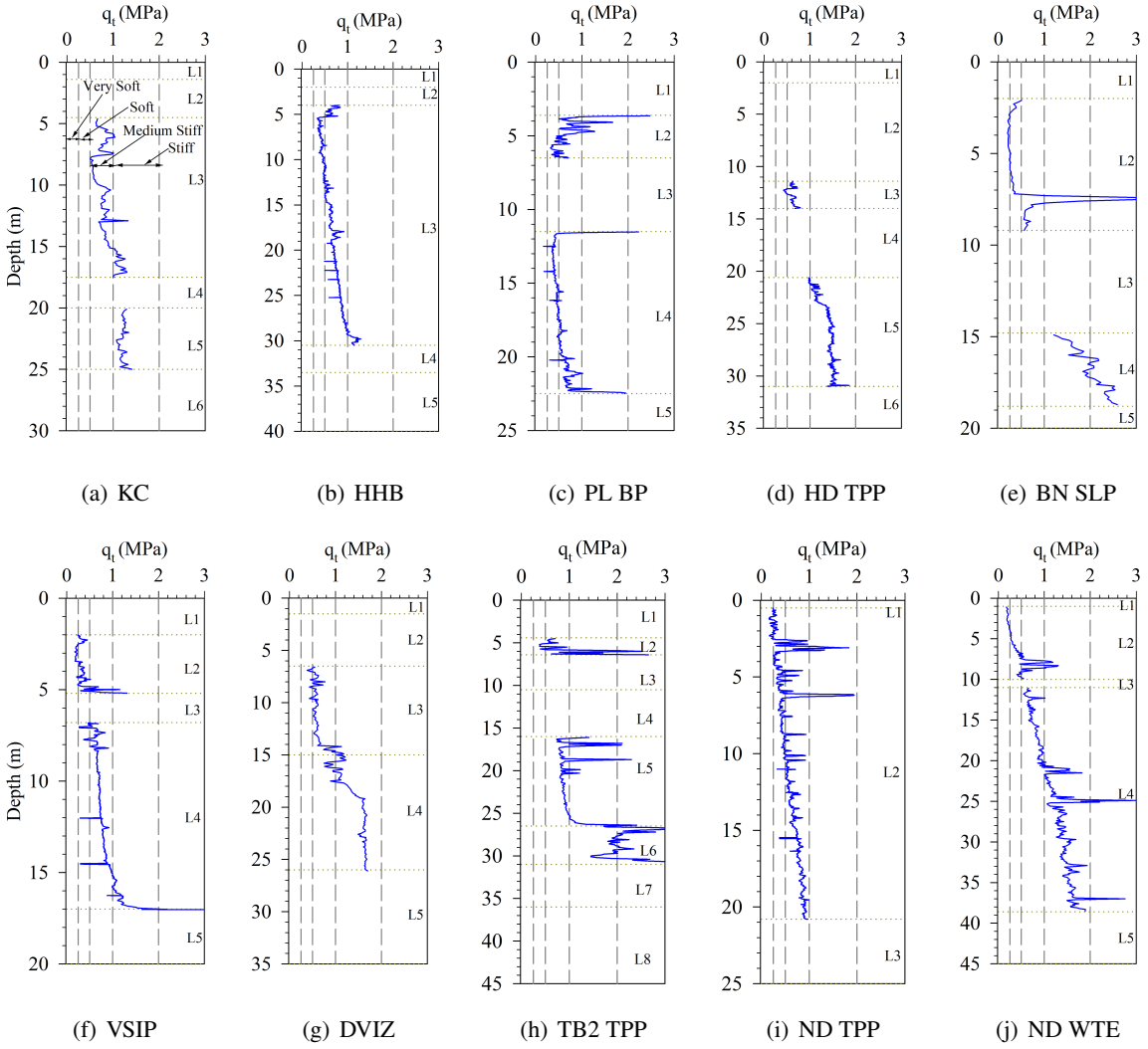

Figure 6. CPTu-based classification of stiffness for clayey soils at the ten test sites

The q_t profiles in Fig. 6 indicate that the clay layers at all depths at some sites (e.g., HHB, PL BP, VSIP, ND TPP) are soft to medium stiff ($0.5 < q_t < 1.0$ MPa) whereas the clay layers at the other sites are soft to medium in the upper depths and medium stiff to stiff in the lower depths, such as KC (20.0–25.0 m), HD TPP (21.0–31.0 m), BN SLP (15.0–20.0 m), DVIZ (19.0–26.0 m), TB 2 TPP (26.5–31.0 m), ND WTE (21.0–39.0 m). The variation of stiffness found in this study reflects typical characteristic of soil stiffness in the deltaic depositional environments: the deeper the soil is the stiffer it becomes. Besides, the stiffness of the soil in the delta can also be inferred from the age of deposits. The accumulation curves (age – depth plots) of soils in the delta [8] show that up to the depth of 20 m the age of the soil deposits is mostly less than 5 kyr (young deposits), and it is found in this study

that the clays in such depths are soft and medium stiff. From depth of 20.0 m to 40.0 m, the age of the soils at some places is up 11 kyr, and logically soils are stiffer as some clay layers found medium stiff to stiff in this study.

4.2. Compression index (C_c)

The compression index (C_c) obtained from the oedometer consolidation test [14] is a key parameter to assess the compressibility of the clayey soil. Based on C_c value, the compressibility of the clayey soil may be classified as follows [23]: (*i*) Slight or low compressibility: $C_c < 0.20$; (*ii*) Moderate or intermediate: $0.2 \leq C_c < 0.4$; and (*iii*) High compressibility: $C_c \geq 0.4$.

The C_c value is typically determined from the $e - \log \sigma'_v$ curve of the test. Besides, the index can also be evaluated by the following equation [24].

$$C_c = (\ln 10)\,(1 + e_0)\,\frac{\sigma'_v}{M} \tag{1}$$

where e_0 is the initial void ratio of the soil specimen; σ'_v is an effective stress value in the range from which C_c is graphically determined; $M$is the constrained modulus at σ'_v.

In this study, the C_c value obtained from the $e-\log \sigma'_v$ curve was compared with that obtained from Eq. (1), for which $\sigma'_v = \sigma'_{v0}$ (the in-situ effective stress at the depth of soil specimen) and the $M = M_0$ (at σ'_{v0}) were simply applied. The M_0 value was obtained from correlations with q_t recommended in Lune et al. [24] as follows: (1) $M_0 = 2q_t$ (for $q_t < 2.5$ MPa) and (2) $M_0 = 4q_t - 5$ (for 2.5 MPa $< q_t <$ 5 MPa).

Fig. 7 shows the variation of C_c values with depth at the same sites (Fig. 6) obtained from the $e - \log \sigma'_v$ and from Eq. (1), in which the vertical dashed lines depict the boundaries of the stiffness ranges described above. It is interesting to note that the C_c values obtained from the $e - \log \sigma'_v$ curve and from Eq. (1) resulted in rather similar trend and values with depth. The figure indicates that most clay layers at the sites are in moderate to high compressibility ($C_c \geq 0.2$) except the clay layers at HD TPP and BN SPL sites. It is interesting that the low compressibility indicated by C_c at HD TPP and NB SLP sites also agree with the stiffness resulted from the q_t profiles shown in Fig. 6. In fact, these two sites are located near the northeast border of the delta, where the clay has been deposited early in the propagation of the delta (Fig. 10 in Tanabe et al. [8]).

Note that the q_t value in Fig. 6 steadily increases rather linearly with depth, indicating that the stiffness of the clays also increases with depth, i.e., the C_c value should theoretically be decreased steadily with depth. However, the C_c values obtained from both the methods in Fig. 7 expose to be relatively constant with depths, except the trend at HD TPP and TB2 TPP. In fact, if a homogeneous clay layer has constant e_0, the $C_c$value by Eq. (1) should be constant with depth (as $\sigma'_v/M = 1/m$ is a constant, where m = modulus number, a constant for a given soil layer), whereas the q_t value should increase linearly due to the influence the total stress level (σ_{v0}) at the test depth. Thus the relatively constant of trend of C_c in Fig. 7 may be attributed to the insignificant variation of e_0 with depth (as the clay layers herein are rather homogeneous), the stress relieve of the soil specimens in the laboratory (i.e. all specimens have $\sigma_{v0} = \sigma_{h0} = 0$ at the beginning of the test) and other possible effects.

The C_c value obtained from all the twelve sites were correlated with the natural water content (W_n) and the in-situ void ratio (e_0). To have more representative correlations, some outliers of C_c/W_n and C_c/e_0 ratios were removed to retain approximately of 68% of the data population under the normal distribution curve [25].That is, the ratios out of the range of $(\mu - \sigma) < C_c/W_n$ (or C_c/e_0) $< (\mu + \sigma)$ were removed, where μ and σ are the mean and standard deviation of corresponding ratio. Fig. 8 shows

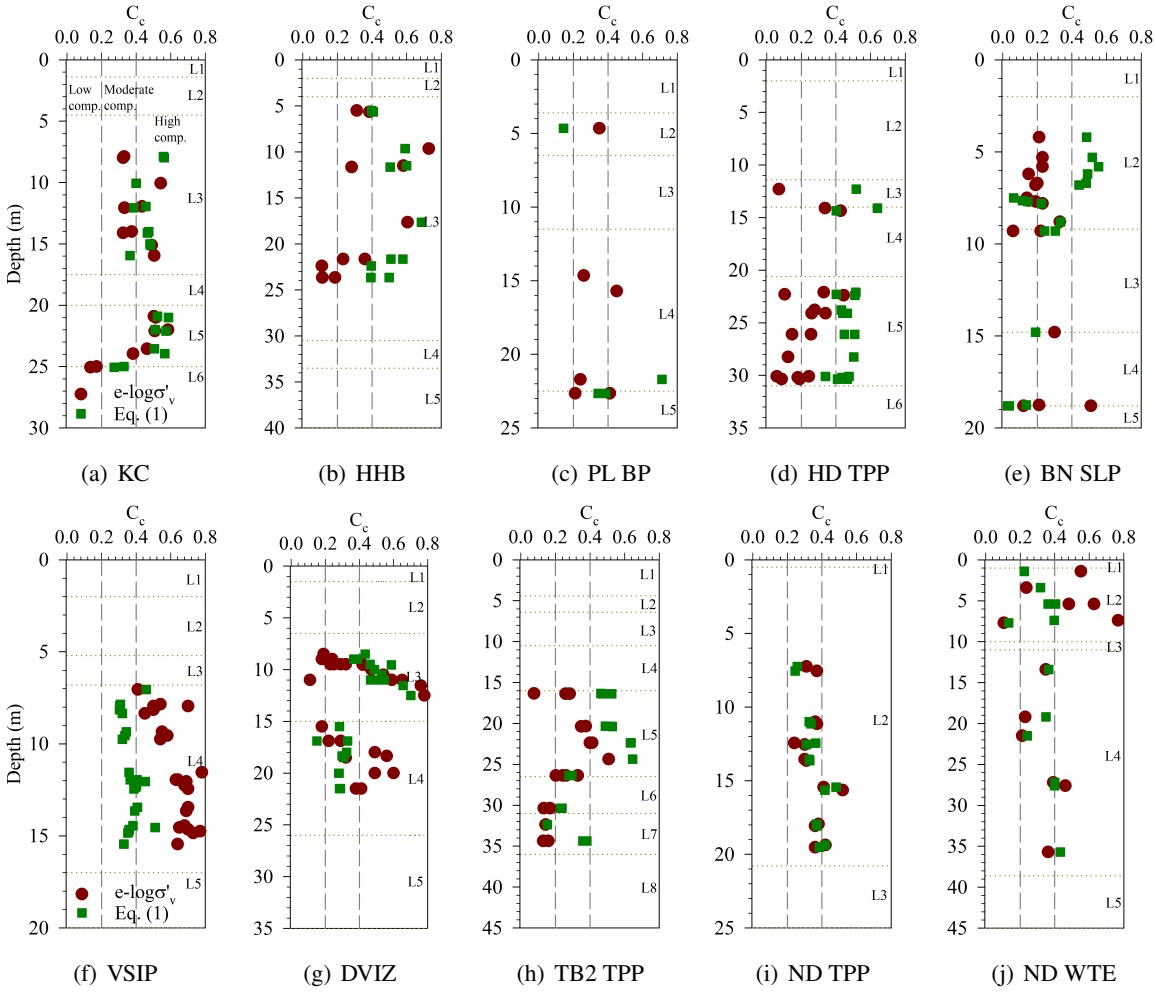

Figure 7. Variation of C_c with depth at the ten test sites

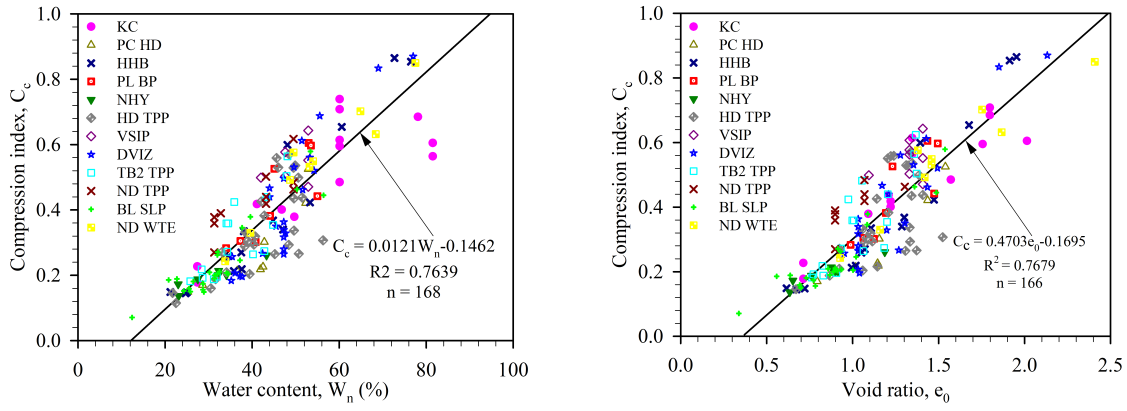

(a) Water content (b) In-situ void ratio

Figure 8. Correlations between C_c and W_n , C_c and e_0

the correlations after such outliers were removed. Note that the correlations shown in Fig. 8 are rather similar to ones summarized in Tables 6.10 and 6.11 in an FHWA report [26] for different clays in the world.

4.3. Overconsolidation ratio (OCR)

The preconsolidation stress (σ'_p) and overconsolidation ratio ($OCR = \sigma'_p/\sigma'_{v0}$) are important compressibility characteristics of clayey soil in estimating settlement of foundations and other behavioral features. In this study, the σ'_p of the clay at the sites were estimated from the $e - \log \sigma'_v$ curve obtained from the 1D consolidation test and from the CPTu data as well.

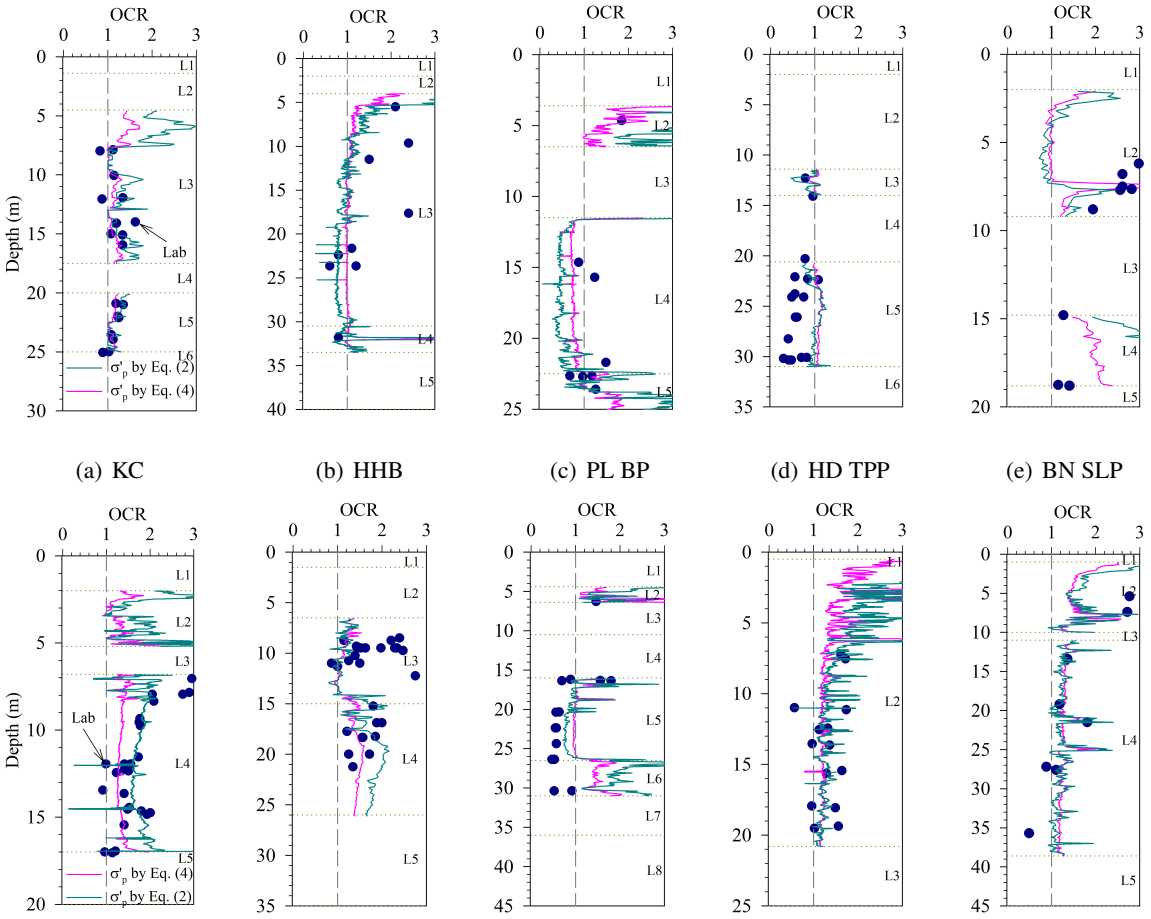

Figure 9. Variation of *OCR* with depth at the ten test sites

From an $e - \log \sigma'_v$ curve, there have been a number of methods proposed to estimate the σ'_p value, which are summarized in some references (e.g., Grozic et al. [27], Dung and Giao [28], Boon [29]). Although Casagrande method [30] has been a traditional one and recommended in many manuals, handbooks and standards (e.g., ASTM D2435-11 [14], CFEM [31], Day [32], FHWA [17]), the method is reported to be operator-dependent and influenced by scale effect [27, 33]. To avoid such

effects and to deal with $e - \log \sigma'_v$ curves showing no distinct curvature around the σ'_p value (for which Casagrande method [30] is difficult to apply), the methods of Silva [34] and Becker et al. [35] are often recommended [33, 36]. In this study both Silva [34] and Becker et al. [35] methods were applied to estimate the σ'_p value of the test specimens from the twelve sites and both methods resulted in similar σ'_p values. Fig. 9 shows the variation of *OCR* with depth at the 10 sites (Figs. 6 and 7), in which the σ'_p value from $e - \log \sigma'_v$ curve was obtained from Becker et al. [35] method.

The σ'_p values at the ten sites were also estimated using CPTu data and compared with that obtained from the $e - \log \sigma'_v$ curve. For this, two CPTu-based recommended equations were applied to estimate the values, of which the first equation is [37]:

$$\sigma'_p = 0.33\,(q_t - \sigma_{v0})^{m'}\,(p_a/100)^{1-m'} \tag{2}$$

where p_a = 101.3 kPa is the atmospheric pressure, m' is an exponent related to soil type.

$$m' = 1 - \frac{0.28}{1 + (I_c/2.65)^{25}} \tag{3}$$

where I_c is soil behavior type index given in detail in [37].

The second equation is for mixed soil types [18, 37]:

$$\sigma'_p = 101\,(p_a)^{0.102}\,(G_0)^{0.478}\left(\sigma'_{v0}\right)^{0.420} \tag{4}$$

where G_0 is the maximum shear modulus of soil (in kPa). In this study, $G_0 = \rho V_s^2$ was applied and the shear wave velocity (V_s, in m/s) of clay was estimated from q_t (in kPa) as follows [18]:

$$V_s = 1.75\,(q_t)^{0.627} \tag{5}$$

The *OCR* values, in which σ'_p was obtained from Eqs. (2) and (4) are also plotted in Fig. 9 for the comparison purpose. It is interesting to note two key features from the Fig. 9: (1) generally, the *OCR* values obtained from the $e - \log \sigma'_v$ curve agree well with the values obtained from CPTu-based methods; (2) *OCR* values from the both approaches indicate that the clay layer in the delta are typically normally consolidated ($OCR \approx 1$, but < 1.5) to slightly overconsolidated ($OCR = 1.5$–4) [38].

Examining closely at the *OCR* profiles one may notice that some *OCR* values from both consolidation test and CPTu data at some depths are less than 1.0. This doesn't mean that the soil at these depths is underconsolidated. In fact, the $OCR < 1$ from the consolidation test (e.g., at HD TPP and TB2 TPP) may come from several reasons such as the heterogeneity (e.g., clay consists of thin lenses of sand or some shell fragments) and unavoidable soil disturbance effect, which led to flatter time – settlement curves. The effect of heterogeneity is clearly indicated in the analysis of coefficient of consolidation in the next section. On the other hand, the $OCR < 1$ from the CPTu data (e.g., at HHB and PL BP sites) may be attributed to the exception of some clays that do not fit to the database used to develop the correlations (i.e., Eqs. (2) and (4)).

4.4. Coefficients of consolidation (c_v and c_r)

In the literature, there are a number of methods proposed to estimate the vertical coefficient of consolidation (c_v) and radial coefficient of consolidation ($c_{r,CD}$) from the time – settlement curves (Fig. 5). For a VD test, the log t and root t methods have been commonly recommended in handbooks and standards (e.g., ASTM D2435-09 [14]) and they are adopted herein. For a CD test, the log t

method [39] and root t method [40, 41] were also adopted for comparable analyses. In fact, log t method (or root t method) for vertical and radial drainage types (i.e., VD and CD tests) uses the same features of the time – settlement curves to derive c_v and $c_{r,CD}$, thus the coefficients from the same method are in principle comparable for the two drainage types. Due to space limitation, detailed procedures of the methods are not described herein.

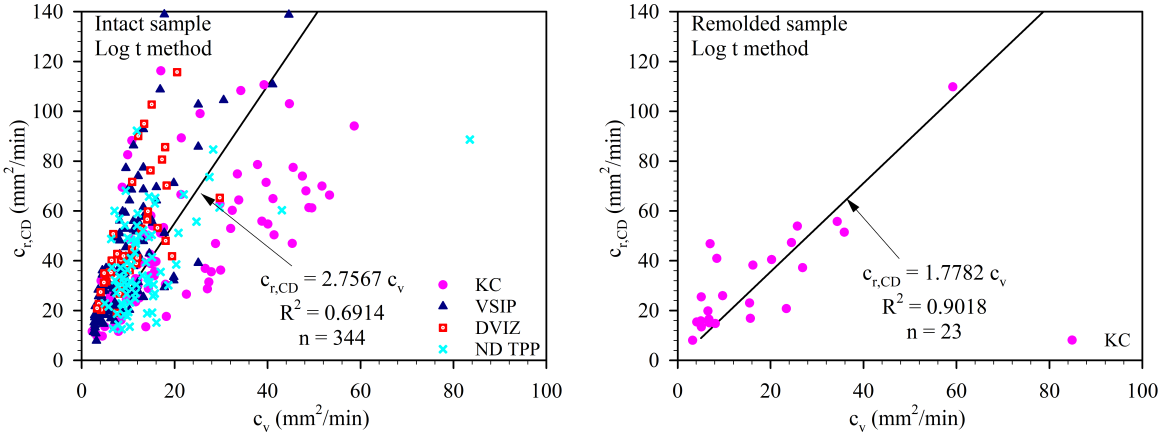

(a) Intact sample (b) Remolded sample

Figure 10. Comparison of $c_{r,CD}$ and c_v for log t method

Following the procedures of the log t and root t methods for VD and CD tests, $c_{r,CD}$ and c_v values were obtained from the time – settlement curves of the test pairs (Table 3) and correlations were developed for the coefficients. Figs. 10, 11, 12, 13 show correlations of the coefficients after outliers, which lie out of the range of $(\mu - \sigma) <$ variable $< (\mu + \sigma)$, were removed as similarly done for the correlations of C_c value shown in Fig. 8.

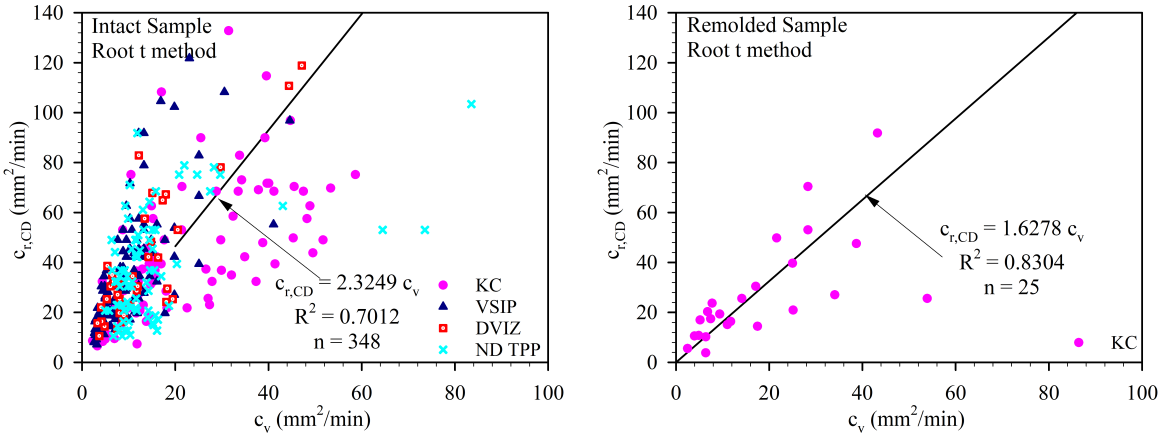

(a) Intact sample (b) Remolded sample

Figure 11. Comparison of $c_{r,CD}$ and c_v for root t method

Figs. 10(a) and 11(a) indicate that although the outliers were removed the data points still distribute quite scatteredly, indicating the strong influence of the heterogeneity of intact soil samples. The correlations in the figures show that on average the ratios of $c_{r,CD}/c_v$ are 2.75 and 2.32 for log t and root t methods, respectively, and these ratios are typically found for many natural soils. For the remolded samples (Figs. 10(b) and 11(b)), one might expect that $c_{r,CD}/c_v$ would be around one since the soil was remolded to be homogeneous. However, it is interesting to note from the figures that on average the $c_{r,CD}/c_v$ ratios are 1.78 and 1.63 for log t and root t methods, respectively, which are larger than one. The ratio of larger than one indicates that, besides the structure of natural soil, the drainage type and drainage length also strongly influence to the induced coefficient of consolidation.

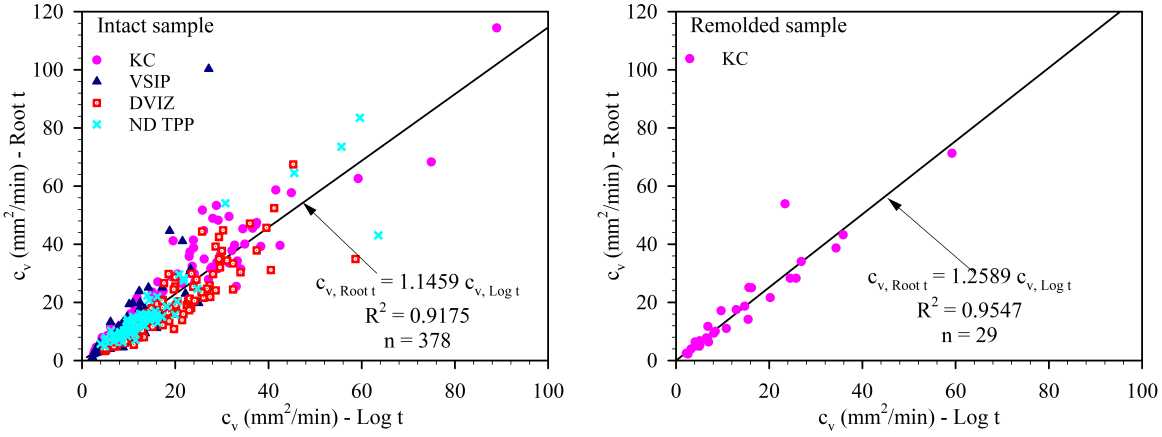

(a) Intact sample (b) Remolded sample

Figure 12. Comparison of c_v from root t and log t methods

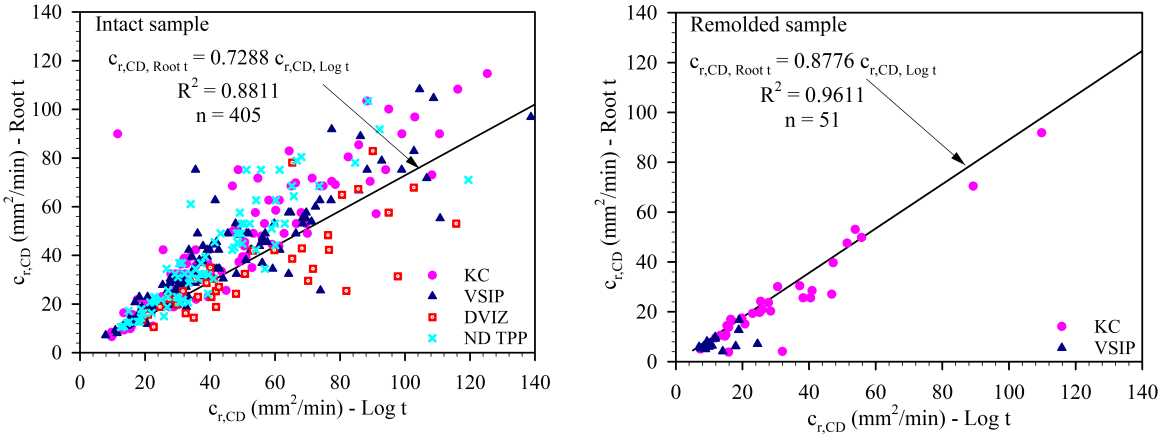

(a) Intact sample (b) Remolded sample

Figure 13. Comparison of $c_{r,CD}$ from root t and log t methods

It is interesting to judge the correlations of the same parameter obtained from different methods. In such an attempt, Fig. 12(a) and 12(b) show correlations of c_v obtained from log t and the value obtained from root t method for intact samples and remolded sample, respectively. Similarly, Figs. 13(a) and 13(b) show the correlations of $c_{r,CD}$ value from the two methods.

Figs. 12(a) and 12(b) indicate that c_v obtained from root t method for the intact and remolded samples is on average 1.15 times and 1.26 times, respectively, the value obtained from log t method. The findings herein agree well with common recommendations that c_v obtained from root t method is slightly larger than that obtained from log t method [42, 43]. Inversely, Figs. 13(a) and 13(b) show that $c_{r,CD}$ obtained from root t method for the intact and remolded samples is on average 0.73 times and 0.87 times, respectively, the value obtained from log t method. The inverse of the $c_{r,CD,Root\ t}/c_{r,CD,Log\ t}$ ratio, which is consistent for intact and remolded samples, implies that not the structure and intactness of soil but the drainage type is the key factor resulting in different ratio of the coefficients from the two methods. Table 4 shows a summary of coefficients obtained from Figs. 12 and 13.

Table 4. Coefficients of correlations shown in Figs. 12 and 13

No.	Correlations	Intact samples			Remolded samples		
		α	R^2	n	α	R^2	n
1	c_v vs $c_{r,CD}$ (Log t)	2.7567	0.6914	344	1.7782	0.9018	23
2	c_v vs $c_{r,CD}$ (Root t)	2.3249	0.7012	348	1.6278	0.8304	25
3	c_v (Root t) vs c_v (Log t)	1.1459	0.9175	378	1.2589	0.9547	29
4	$c_{r,CD}$ (Root t) vs $c_{r,CD}$ (Log t)	0.7288	0.8811	405	0.8776	0.9611	51

5. Conclusions

A database of methodical and well-performed field and laboratory test results from four research test sites and eight project sites over the RRD were analyzed to depict some compressibility characteristics of clays in the delta. The following are key conclusions drawn from this study: (*i*) the corrected cone resistance (q_t) and compression index (C_c) profiles have indicated that clays in the delta are typically soft to medium stiff in the upper depths and medium stiff to stiff in the lower depths at some places. The stiffness increase rather linearly with depth, indicating that the clays are rather homogeneous and were formed relatively static depositional environments; (*ii*) the C_c value of the clays was found to have good correlations with natural water content (W_n) and in-situ void ratio (e_0) and the correlations are similar to ones recommended in manuals and reports; (*iii*) the preconsolidation stress (σ'_p) values obtained from the standard consolidation test as well as from CPTu data (and therefore the overconsolidation ratio, *OCR*) have indicated that the clays in the delta are typically normally consolidated (NC) to slightly overconsolidated with *OCR* mostly from 1.0 to 2.0; (*iv*) the ratio of radial coefficient of consolidation (central drain) to the vertical coefficient of consolidation (i.e., $c_{r,CD}/c_v$) from the 4 research sites is on average 2.76 (log t method) and 2.32 (root t method) and these average ratios are found typical for deltaic soil deposits. For the remolded samples, this ratio is about 1.7 (not 1.0 as one might expect), indicating that the drainage type has strong influence on the induced coefficients.

The findings in this study were obtained from limited test sites in the delta. Since the delta is very large, more test sites with valuable field and lab test data are expected to characterize the compressibility characteristics of the delta more comprehensively.

Acknowledgements

This work was supported by JICA Research Grant of VNU Vietnam Japan University (Grant No. VJU.JICA.21.04). The authors would like to sincerely thank Golden Earth and FECON companies very much for their kind permission to use soil investigation data in the RRD delta.

References

[1] General Statistics Office (2021). *Statistical yearbook of Vietnam*. Statistical Publishing House.

[2] Watanabe, Y., Tanaka, M., Takemura, J. (2004). Field and laboratory tests to evaluate the mechanical characteristics of Hai-Phong clay. In *Proceedings of International Workshop Hanoi GeoEngineering 2003 & 2004*, 27–36.

[3] Takemura, J., Bui, T. M., Watanabe, Y., Tanaka, M. (2004). Consolidation tests on undisturbed Hai Phong clay samples by fixed piston and Shelby tube samplers. In *Proceedings of the Japan National Conference on Geotechnical Engineering, JGS*, volume 39, 155–156.

[4] Phuc, T. T., Giao, P. H. (2019). Geotechnical Properties of Hai Phong and Ninh Binh Clays in the Red River Delta. In *Lecture Notes in Civil Engineering*, Springer Singapore, 751–758.

[5] Hien, D. H. (2006). *A geotechnical-geophysical study of the Red River Delta clay with reference to highway network upgrading*. Master of Engineering, Asian Institute of Technology, School of Civil Engineering, Thailand.

[6] Hien, D. H., Giao, P. H. (2010). *A geotechnical-geophysical study of the Red River Delta clay with reference to highway network upgrading*. LAP LAMBERT Academic Publishing.

[7] Phach, P. V., Lai, V. C., Shakirov, R. B., Le, D. A., Tung, D. X. (2020). Tectonic Activities and Evolution of the Red River Delta (North Viet Nam) in the Holocene. *Geotectonics*, 54(1):113–129.

[8] Tanabe, S., Saito, Y., Vu, Q. L., Hanebuth, T. J. J., Ngo, Q. L., Kitamura, A. (2006). Holocene evolution of the Song Hong (Red River) delta system, northern Vietnam. *Sedimentary Geology*, 187(1-2):29–61.

[9] Tanabe, S., Hori, K., Saito, Y., Haruyama, S., Vu, V. P., Kitamura, A. (2003). Song Hong (Red River) delta evolution related to millennium-scale Holocene sea-level changes. *Quaternary Science Reviews*, 22 (21-22):2345–2361.

[10] Funabiki, A., Haruyama, S., Quy, N. V., Hai, P. V., Thai, D. H. (2007). Holocene delta plain development in the Song Hong (Red River) delta, Vietnam. *Journal of Asian Earth Sciences*, 30(3-4):518–529.

[11] ASTM D1452-09. *Standard practice for soil exploration and sampling by auger borings*. American Society for Testing and Materials.

[12] ASTM D1587-09. *Standard practice for thin-walled tube sampling of soils for geotechnical purposes*. American Society for Testing and Materials.

[13] ASTM D5778-12. *Standard test method for electronic friction cone and piezocone penetration testing of soils*. American Society for Testing and Materials.

[14] ASTM D2435-11. *Standard test methods for one-dimensional consolidation properties of soils using incremental loading*. American Society for Testing and Materials.

[15] ASTM D2488-09. *Standard practice for description and identification of soils (Visual-Manual Procedure)*. American Society for Testing and Materials.

[16] TCVN 9351 (2012). *Soils - field testing method - standard penetration test*.

[17] FHWA-IF-02-03 (2002). *Geotechnical engineering circular No.5: Evaluation of soil and rocks properties*. US Dept. of Transportation, Federal Highway Administration.

[18] Mayne, P. W. (2007). *Cone penetration testing. National Cooperative Highway Research Program (NCHRP)*. Washington, D.C.

[19] Schnaid, F. (2009). *In situ testing in geomechanics*. Taylor & Francis, 270 Madison Ave, New York, NY 10016, USA.

[20] Robertson, P. K., Cabal, K. L. (2015). *Guide to cone penetration testing for geotechnical engineering*. 6th edition, Gregg Drilling & Testing, Inc.

[21] Senneset, K., Sandven, R., Janbu, N. (1989). Evaluation of soil parameters from piezocone tests. *Transportation Research Record*, page 1235.

[22] Kulhawy, F. H., Mayne, P. W. (1990). *Manual on estimating soil properties for foundation design*. Electric Power Research Institute, California 94304, Report No. EL-6800.
[23] Lade, P. V. (2001). Engineering Properties of Soils and Typical Correlations. In *Geotechnical and Geoenvironmental Engineering Handbook*, Springer US, chapter 3, 43–67.
[24] Lunne, T., Robertson, P. K., Powell, J. J. M. (1997). *Cone penetration testing in geotechnical practice*. Blackie Academic & Professional.
[25] Navidi, W. (2019). *Statistics for engineers and scientists*. 5th edition, McGraw-Hill Education.
[26] FHWA-NHI-16-072 (2017). *Geotechnical engineering circular No.5 - Geotechnical site characterization*. US Dept. of Transportation, Federal Highway Administration, Office of Bridge Technology, 400 Seventh Street, SW, Washington, DC 20590.
[27] Grozic, J. L. H., Lunne, T., Pande, S. (2003). An oedometer test study on the preconsolidation stress of glaciomarine clays. *Canadian Geotechnical Journal*, 40(5):857–872.
[28] Dung, N. T., Giao, P. H. (2005). Review of some methods to determine the preconsolidation pressure and application for Mekong soft clay. In *Proceedings of the International Workshop of Hanoi Geoengineering, Hanoi, Vietnam*, 44–54.
[29] Boone, S. J. (2010). A critical reappraisal of "preconsolidation pressure" interpretations using the oedometer test. *Canadian Geotechnical Journal*, 47(3):281–296.
[30] Casagrande, A. (1936). The determination of the preconsolidation load and its practical significance. In *Proceeding of the 1st International Soil Mechanics and Foundation Engineering Conference*, volume 3, Cambridge, Mass., 60–64.
[31] CFEM (2006). *Canadian foundation engineering manual*. 4th edition, Canadian Geotechnical Society, National Research Council of Canada.
[32] Day, R. W. (2010). *Foundation engineering handbook - Design and construction with the 2009 international building code*. 2nd edition, McGraw Hill, USA.
[33] Clementino, R. V. (2005). Discussion of "An oedometer test study on the preconsolidation stress of glaciomarine clays". *Canadian Geotechnical Journal*, 42(3):972–974.
[34] Silva, P. F. (1970). Uma construcao grafica para a determinacao da pressao de pre-adensamento de uma amostra de solo. In *COBRAMSEF*, volume 2, Rio de Janeiro, 219–223.
[35] Becker, D. E., Crooks, J. H. A., Been, K., Jefferies, M. G. (1987). Work as a criterion for determining in situ and yield stresses in clays. *Canadian Geotechnical Journal*, 24(4):549–564.
[36] Holtz, R. D. (1991). Stress Distribution and Settlement of Shallow Foundations. In *Foundation Engineering Handbook*, Springer US, 166–222.
[37] Rix, G. J., Wainaina, N., Ebrahimi, A., Bachus, R. C., Limas, M., Sancio, R., Fait, B., Mayne, P. W. (2019). *Manual on Subsurface Investigations*. Transportation Research Board.
[38] Look, B. G. (2007). *Handbook of Geotechnical Investigation and Design Tables*. Taylor & Francis.
[39] Sridhar, G., Robinson, R. (2011). Determination of radial coefficient of consolidation using log *t* method. *International Journal of Geotechnical Engineering*, 5(4):373–381.
[40] Berry, P. L., Wilkinson, W. B. (1969). The Radial Consolidation of Clay Soils. *Géotechnique*, 19(2): 253–284.
[41] Chaney, R. C., Demars, K. R., Sridharan, A., Prakash, K., Asha, S. R. (1996). Consolidation Behavior of Clayey Soils Under Radial Drainage. *Geotechnical Testing Journal*, 19(4):421.
[42] Das, B. M., Sobhan, K. (2010). *Principles of geotechnical engineering*. Si edition, Cengage Learning.
[43] Leroueil, S., Rowe, R. K. (2001). Embankments Over Soft Soil and Peat. In *Geotechnical and Geoenvironmental Engineering Handbook*, Springer US, 463–499.

Journal of Science and Technology in Civil Engineering, HUCE (NUCE), 2023, 17 (1): 58–66

EFFECTS OF THE SIZE POLYDISPERSITY AND FRICTION COEFFICIENT ON THE COMPRESSIVE STRENGTH OF WET GRANULAR MATERIALS

Vo Thanh Trung[a,b,*], Nguyen Trung Kien[c]

[a]*School of Transportation Engineering, Danang Architecture University, 566 Nui Thanh street, Da Nang city, Vietnam*
[b]*Office of Research Administration, Danang Architecture University, 566 Nui Thanh Street, Da Nang City, Vietnam*
[c]*Faculty of Building and Industrial Construction, Hanoi University of Civil Engineering, 55 Giai Phong road, Hai Ba Trung district, Hanoi, Vietnam*

Article history:
Received 10/10/2022, Revised 06/12/2022, Accepted 12/12/2022

Abstract

We numerically study the effects of the size polydispersity and the friction coefficient on the compressive strength of wet granules under a diametrical compression test by using discrete element simulations. The numerical method is coupled with the capillary cohesion law which is enhanced by the cohesive forces between grains in the pendular regime. The wet granules are composed of primary spherical particles whose size polydispersity is varied from 1 to 10 and the friction coefficient between grains is varied from 0.1 to 1.0. By applying a constant compression velocity on the top plate in quasi-static regime, the granule is deformed but does not abruptly rupture due to the cohesive effects between grains and the rearrangement of primary particles. This no abrupt rupture is characterized by the appearance of the peak compressive stress in a long vertical strain before the onset failure of the granule. The compressive strength of the granule increases with increasing the friction coefficient for all cases of the size polydispersity but seemly declines for low values of the size polydispersity and almost level-off for high-size polydispersity with the friction coefficient larger than 0.5.

Keywords: capillary cohesion, compressive strength, discrete element method, diametrical compression, friction coefficient, size polydispersity.

https://doi.org/10.31814/stce.nuce2023-17(1)-05

1. Introduction

Wet granular materials are omnipresent in nature, industrial processes, and engineering applications [1–3]. In which, wet granules or cohesive power mixtures are known as products of mixing water or adhesives and raw materials with different material properties such as size polydispersity, density, and roughness [4–8]. Basically, the increase of the size polydispersity leads to the enhancement of the granule strength [9, 10]. The grains roughness characterized by their friction coefficient also affects the mechanical properties of wet granular materials. Similar to the size polydispersity of grains, the friction coefficient of grains may help to increase the granule strength due to the enhancement of the frictional forces between grains [11]. However, the increase of the friction coefficient tends

*Corresponding author. *E-mail address:* trungvt@dau.edu.vn (Trung, V. T.)

to reduce the solid fraction of wet granular materials as a consequence of increasing the pore space between grains [12, 13]. This effect may lead to weakening the density of the force network, leading to reducing the compressive strength of granules.

Over the last few decades, the effects of the size polydispersity and the friction coefficient on the behavior of granular materials have been investigated, especially the segregation, mechanical strength, and the rheological properties [11, 14–21]. The increase of the size polydispersity and friction coefficient leads to increase the size segregation of granular materials in different configurations [17, 21–24]. In contrast, the size polydispersity and the friction coefficient of grains represent different effects on the rheological properties of granular materials in the steady flowing state. Meanwhile, the size polydispersity of granular materials is nearly independent to the shear strength of granular flows [10, 25], the friction coefficient of grains lead to a significant increase in the shear strength of granular materials [11, 19, 20, 26]. Recently, Vo et al. numerically reported the mechanical strength of wet agglomerates under the effects of the low size polydispersity of grains and the liquid volume characterized by the rupture distance of capillary bonds between grains [18]. The results showed that the mechanical strength of agglomerates increases with increasing the size span and the rupture distance of the capillary bonds. In order to extend our previous work and also overcome the limitation of experimental investigations due to the difficulty of varying the material properties such as the size polydispersity and the friction coefficient, this numerical work is performed.

In this paper, we report in detail the compressive strength of wet granules under a diametrical compression test by means of the discrete element simulations. The numerical method is coupled with the capillary cohesion law which is enhanced by the cohesive forces between grains having a gap not exceeding a rupture distance. The wet granules are composed of primary particles with different size polydispersity and the friction coefficient between them. By applying a constant downward velocity compression on the top platen, such granules are deformed and their compressive stress changes significantly during the test depending on the values of the size ratio between the largest and smallest particle diameters and their roughness. Remarkably, by normalizing the compressive strength of wet granules by the maximum cohesive stress exerted on the mean particle diameter, it slightly decreases with increasing the size polydispersity of primary particles, but slightly increases with small values of the friction coefficient and almost level-off for the friction coefficient beyond 0.5.

The rest of our paper is arranged as follows. We first introduce shortly the discrete element method and the model preparation with different key parameters in Section 2. The paper then shows the diametrical compression test and the compressive strength of wet granules under the action of the constant downward velocity on the top platen by varying the broad range of values of the size polydispersity and the friction coefficient of grains in Section 3. The conclusion is set in Section 4 with the salient results and further research directions.

2. Numerical simulation

The simulations are performed by using an in-house 3D molecular dynamics DEM program, namely cFGd-3D++code, originally developed by Mutabaruka [27]. This coding program is then improved by the author in order to apply to previous works and also for this current simulation [28–30]. The primary particles are modeled by using spheres as rigid bodies and interacting with others by considering the contact forces law based on a linear spring-dashpot model. The interactions between two primary particles i and j involve the normal contact forces f_n, the tangential contact forces f_t, and capillary cohesion forces f_c [30], as shown in Fig. 1, where f_n is obtained by considering the normal elastic and normal damping components, f_t is determined by the Coulomb friction law [21], and the

capillary cohesion force f_c is proportional to the cohesion pre-factor $\kappa = 2\pi\gamma_s$, where γ_s denotes the liquid-vapor surface tension [30].

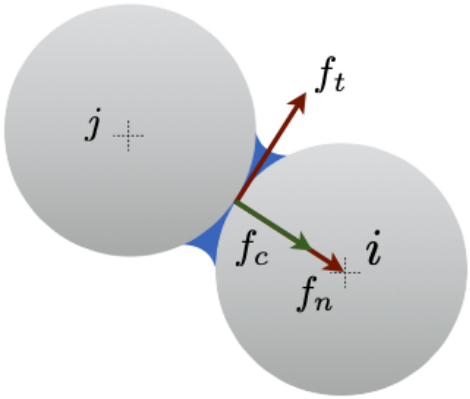

Figure 1. A schematic drawing represents the contact model between two wet particles i and j

The preparation and simulation of this current work involve three different stages: 1) creating assemblies of primary particles with different size polydispersities by using an isotropic compression; 2) extracting granules by applying a spherical probe into the packings of primary particles; 3) applying a constant downward velocity on the top platen to compress the granules. In particular, large samples of granular materials with 10 different size polydispersities ($\alpha = d_{\max}/d_{\min}$) ranging from 1 to 10 were first prepared in a box, then applied isotropic compression to all box walls into reaching a dense packing in the first stage, where $d_{\max}$ is the largest particle diameter, it is kept constant in all simulations, $d_{\min}$ is the smallest particle diameter. In each sample (except $\alpha = 1$), the diameter of primary particles is assumed to be distributed uniformly by particle volume fraction, this means that the particle volume of all size classes of the packing is the same [18, 31]. In the next stage, a spherical probe is then applied to the center of the packing and its radius is increased until exactly reaches 5000 primary particles inside the probe, as shown in Fig. 2(a). In all these steps, the particle gravity and cohesion between grains are absent. After extracting a granule from an assembly, as shown in Fig. 2(b), the cohesion forces between grains are activated. In all simulations, the liquid volume is characterized by the rupture distance, this is set equal 0.1 times to the largest particle diameter ($d_{\text{rupt}}/d_{\max} = 0.1$) and kept constant in all simulations. After reaching a static equilibrium, all granules are compressed by applying a constant downward velocity on the top platen of the model in the third stage, as shown in Fig. 3. The particle gravity is absent in all simulations in order to avoid the local effects during the compression [32]. All values of the other key parameter are given in Table 1.

The wet granules are then subjected to the axial compression by applying a constant velocity v = 0.1 m/s on the top platen, this velocity is slow enough for considering the quasi-static diametrical compression in all simulations. During the compression, the wet granules are deformed, as illustrated in Fig. 3, and the granule stress is changed with different rates and magnitudes depending on the values of the size polydispersity and the friction coefficient between grains. In these simulations, the stress-strain curve for each value of the size polydispersity and friction coefficient between grains is considered. The cumulative vertical strain is determined as a ratio between the cumulative downward displacement Δh of the top platen and the initial diameter D_0 of the wet granules.

$$\varepsilon = \frac{\Delta h}{D_0} = \frac{v \times t}{D_0} \tag{1}$$

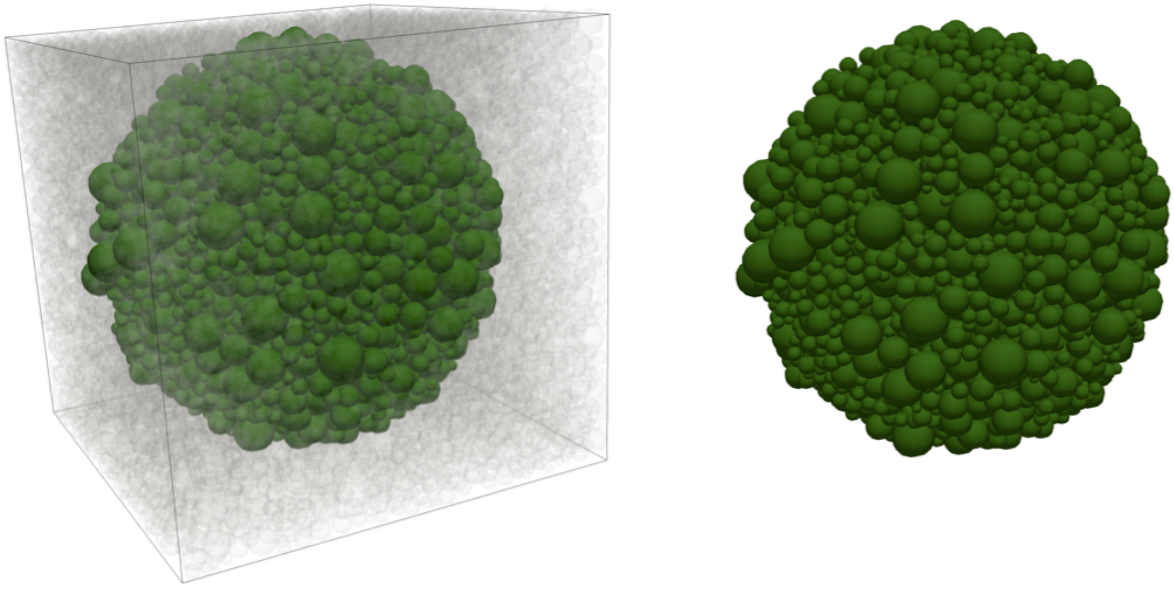

(a) Assembly of granular materials and the setting of a granule inside a box

(b) A granule extracted from the assembly

Figure 2. The numerical preparation of a wet granule with the size polydispersity $\alpha = 6$

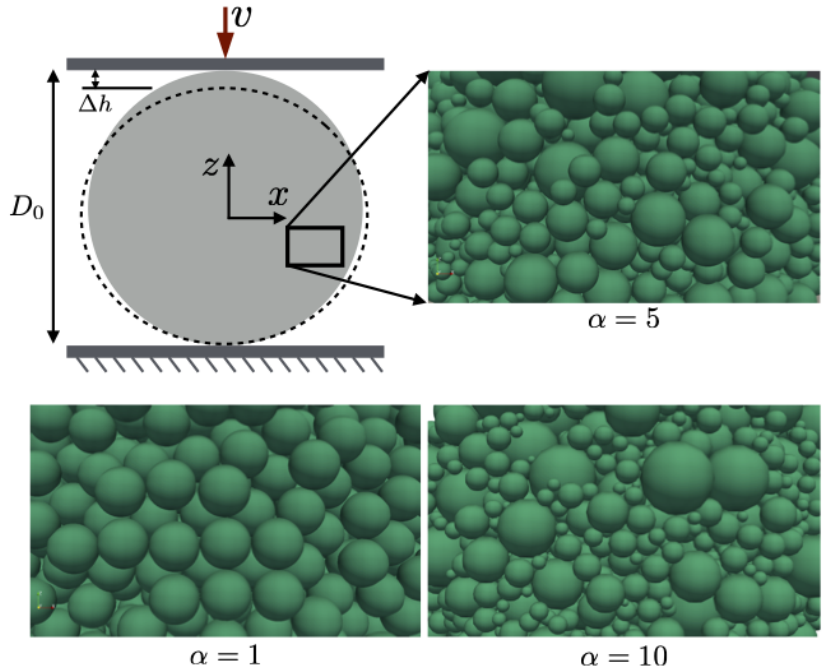

Figure 3. Schematic drawing represents the diametrical compression test of wet granules composed of primary particles with different size polydispersities and friction coefficient by applying a constant downward velocity on the top platen

Table 1. Main parameters and their values in all numerical simulations

Parameter	Symbol	Value	Unit
Largest particle diameter	$d_{\max}$	10	μm
Size polydispersity	α	[1, 10]	-
Density of particles	ρ	2600	kg/m^{-3}
Number of grains	N_p	5000	-
Coefficient of friction	μ	[0.1, 1.0]	-
Normal stiffness	k_n	10^3	N/m
Tangential stiffness	k_t	8×10^2	N/m
Normal damping	γ_n	5×10^{-2}	Ns/m
Tangential damping	γ_t	5×10^{-2}	Ns/m
Cohesion pre-factor	κ	0.47	-
Time step	Δt	1×10^{-9}	sec.
Compression velocity	v	0.1	m/s

In order to analyze the compressive strength of wet granules under the diametrical compression, we calculate the mean vertical stress σ_{zz}, determined by considering the stress tensor of the granules during the test. The mean vertical stress σ_{zz} is obtained by considering z-components of the force vectors that combining all normal contact forces, capillary cohesion forces, and the tangential contact forces and the branch vectors joining centers between two particles in contacts [33], as given by the following expression:

$$\sigma_{zz} = \frac{1}{V_0}\sum_{k=1}^{N_c} f_z^k l_z^k = n_c < f_z^k l_z^k >_k \tag{2}$$

where V_0 is the volume of granules, k is the interaction inside the granules, N_c denotes the number of capillary bonds during the compression, n_c is the density of number of capillary contacts, f_z^k and l_z^k denote the z-components of the force vector and branch vector at the contact k. The stress-strain curve and the compressive strength of wet granules are analyzed in detail below.

3. Results of simulations

Fig. 4 shows the evolution of the mean vertical stress σ_{zz} as a function of the cumulative vertical strain ε for 10 different values of the friction coefficient with the size polydispersity $\alpha = 1$. It is interesting to see that the mean vertical stress for all cases of wet grains first increases rapidly with the rate that increases with increasing the friction coefficient of primary particles. This stress then reaches the peak values in a long range of the cumulative vertical strain ε, implying the wet granules do not abruptly rupture after the stress reaches the peak. This behavior supplies evidence for the ductile properties of the wet granules before the onset failure of such granules. The ductile properties of wet granules may be due to the rearrangement of primary particles and the number of broken capillary bonds are not much with small cumulative vertical strain. The mean vertical stress then declines smoothly but with the rate that nearly increases with increasing the friction coefficient μ. The increase of the declination rate of σ_{zz} may be due to the increase of the number of broken capillary bonds.

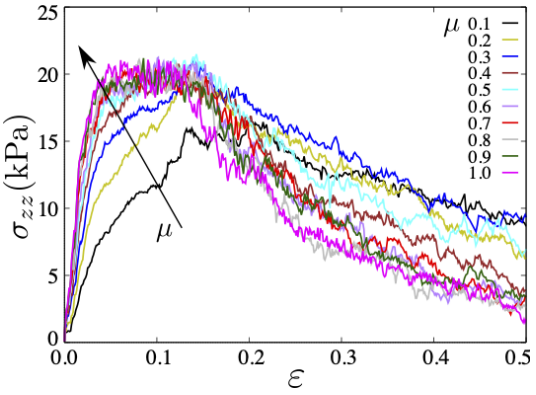

Figure 4. Mean vertical stress σ_{zz} of wet granules as a function of the cumulative vertical strain ε during the compression for different values of the friction coefficient μ of primary particles with the size polydispersity $\alpha = 1$

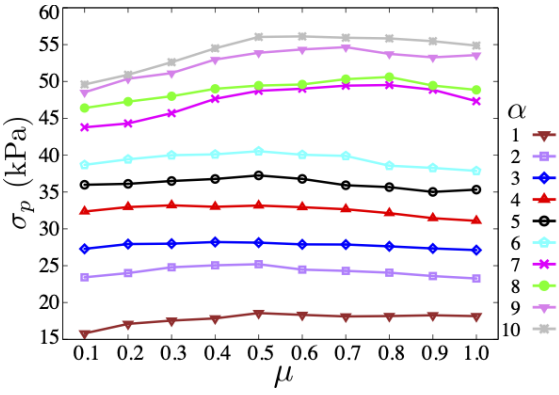

Figure 5. The peak stress σ_p of wet granules composed of primary particles as a function of the friction coefficient μ for 10 different values of the size polydispersity α

In order to highlight the effects of both the size polydispersity and the friction coefficient of primary particles on the compressive strength of wet granules under the diametrical compression test, the peak value σ_p of mean vertical stress σ_{zz} obtained in each simulation when varying α and μ is considered. Fig. 5 displays the evolution of the peak vertical stress σ_p as a function of the friction coefficient for 10 different values of the size polydispersity α. It is remarkable to note that the peak stress σ_p of wet granules increases significantly with increasing the size polydispersity α. In particular, σ_p increases from nearly 19 kPa to approximate 55 kPa when increases the size polydispersity α from 1 to 10 for the case of $\mu = 0.5$. However, the growth rate of the peak vertical stress σ_p is different when increases α in its small range. Furthermore, the friction coefficient also represents different effects on the peak stress of wet granules. However, the common trend of the peak stress is nearly similar for all values of α. Indeed, the peak stress of granules increases slightly when the friction coefficient changes from 0.1 to 0.5. Passing these values of the friction coefficient, σ_p seemly decreases for low size polydispersities ($\alpha \leq 6$) or seemly level-off for higher size spans when $\mu > 0.5$. These differences may be due to the saturated behavior of the friction forces in particle's interactions especially for granules with low size polydispersity and high friction coefficient. These analyses provide evidence for the effects of the size polydispersity and the friction coefficient on the mean vertical stress of wet granules.

To unify the representation of the compressive strength of wet granules under a diametrical compression test as the relationship between dimensionless parameters for all values of the size polydispersity α and the friction coefficient μ of primary particles, we consider the normalization of the peak stress σ_p and the cohesive stress $\sigma_c \sim \kappa/\langle d \rangle$, where κ is the cohesion pre-factor, $\langle d \rangle$ denotes the mean particle diameter which decreases when increasing the size polydispersity α. Fig. 6(a) shows the increase of the cohesive stress σ_c as a function of the size polydispersity α. The increase of σ_c represents the decrease of the mean particle diameter as a consequence of keeping a constant value of the cohesion pre-factor κ. By considering the ratio of the peak stress σ_p and the cohesive stress σ_c, it illustrates the different effects of the size polydispersity and the friction coefficient of grains on the compressive strength of granules. This ratio first increases for all cases of the size polydispersity with small values of the friction coefficient ($\mu \leq 0.5$), σ_p/σ_c then seemingly decreases for higher values of

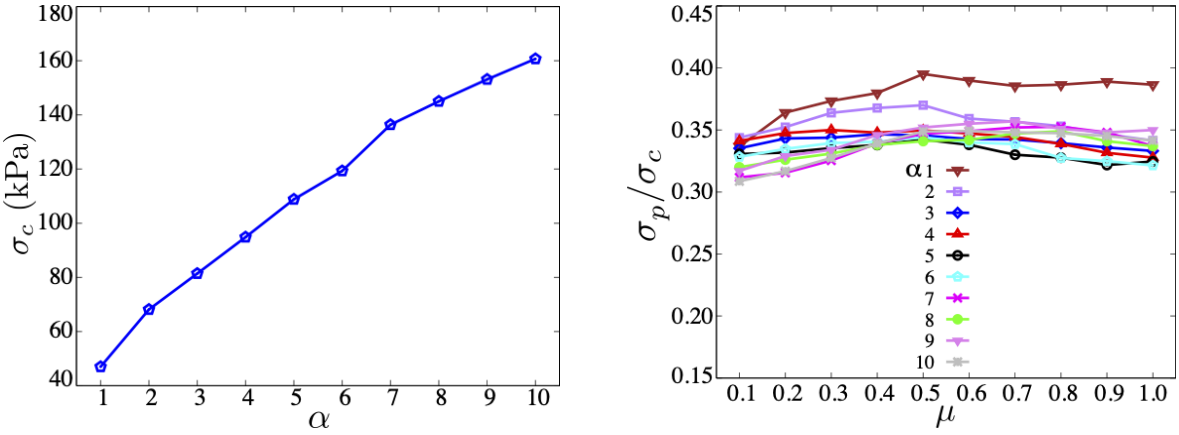

(a) Cohesive stress exerted on particles having mean diameter

(b) Compressive strength of agglomerates

Figure 6. (a) The cohesive stress exerted on particles having mean diameter as a function of the size polydispersity, (b) the peak stress normalized by the cohesive stress as a function of the friction coefficient for different values of the size polydispersity

friction coefficient with low-size polydispersity, as shown in Fig. 6(b). Remarkably, the compressive strength of granules composed of monodisperse primary particles is significantly higher than that for the case of polydisperse spherical particles, especially for high-size polydispersity.

The different effects of the friction coefficient on the compressive strength of wet granules in Fig. 6(b) under the diametrical compression test represent the saturated behavior of the Coulomb frictional interactions. Indeed, the compressive strength of wet granules increases continuously for small values of the friction coefficient. This property provides evidence for the weakness of the frictional forces observed via the material properties as compared to the frictional threshold observed via the Coulomb friction law. Continuously increasing the friction coefficient of granular materials and keeping the external loading (as compression forces), the frictional force may exceed the frictional threshold, leading to reaching a constant compressive strength of granules. These findings observed in the current work show a good agreement with previous investigations on the effects of the friction coefficient of material on the shear strength of the granular samples [34]. The porosity of a granular sample increases with increasing the friction coefficient, meanwhile, its shear strength levels off for high values of the friction coefficient. These observations have important meanings in using raw materials in many engineering applications.

4. Conclusions

As reported in the paper, the mean compressive stress of wet granules evolves differently depending on the size polydispersity and the friction coefficient. In particular, this stress increases rapidly then reaches a peak in a long vertical cumulative strain, this property represents the ductile behavior of wet granules as a consequence of the rearrangement of the primary particles and the cohesive effects of the capillary bonds. Remarkably, by considering the ratio between the peak compressive stress and the cohesive stress exerted on the mean particle diameter, it decreases with increasing the size polydispersity for the whole range values of the friction coefficient. For each case of the size polydispersity, the compressive strength of wet granules increases slightly for low friction coefficient,

this strength then seemly declines with higher friction coefficient for $\alpha \leq 6$ but nearly level-off for the high-size polydispersities. The numerical findings observed in this current work may provide a better understanding of the effects of the polydispersity and friction coefficient of primary particles on the compressive strength of wet granules under diametrical compression. These are clearly difficult to obtain in experimental works, especially for performing with changing the friction coefficient of grains.

Within the scope of the paper research and the limitation of real experiments, it is meaningfully found that the role of friction coefficient has different influences on the mechanical strength of granules or cohesive powder mixtures, leading to providing evidence for using appropriate raw materials in different engineering applications.

Acknowledgements

The authors gratefully acknowledge F. Radjai for his original ideas and helpful discussions.

References

[1] Mikami, T., Kamiya, H., Horio, M. (1998). Numerical simulation of cohesive powder behavior in a fluidized bed. *Chemical Engineering Science*, 53(10):1927–1940.

[2] Herminghaus, S. (2005). Dynamics of wet granular matter. *Advances in Physics*, 54(3):221–261.

[3] Mitarai, N., Nori, F. (2006). Wet granular materials. *Advances in Physics*, 55(1-2):1–45.

[4] Merchant, I. J., Macphee, D. E., Chandler, H. W., Henderson, R. J. (2001). Toughening cement-based materials through the control of interfacial bonding. *Cement and Concrete Research*, 31(12):1873–1880.

[5] Sastry, K. V. S., Dontula, P., Hosten, C. (2003). Investigation of the layering mechanism of agglomerate growth during drum pelletization. *Powder Technology*, 130(1-3):231–237.

[6] Nimmo, J. R. (2005). Aggregation-physical aspects. In *Encyclopedia of Soils in the Environment*, Elsevier, 28–35.

[7] Walker, G. M. (2007). Chapter 4 Drum Granulation Processes. In *Handbook of Powder Technology*, Elsevier, 219–254.

[8] Vo, T. T., Nezamabadi, S., Mutabaruka, P., Delenne, J.-Y., Izard, E., Pellenq, R., Radjai, F. (2019). Agglomeration of wet particles in dense granular flows. *The European Physical Journal E*, 42(9).

[9] Fichtner, F., Rasmuson, Å., Alderborn, G. (2005). Particle size distribution and evolution in tablet structure during and after compaction. *International Journal of Pharmaceutics*, 292(1-2):211–225.

[10] Cantor, D., Azéma, E., Sornay, P., Radjai, F. (2018). Rheology and structure of polydisperse three-dimensional packings of spheres. *Physical Review E*, 98(5):052910.

[11] Badetti, M., Fall, A., Chevoir, F., Roux, J.-N. (2018). Shear strength of wet granular materials: Macroscopic cohesion and effective stress. *The European Physical Journal E*, 41(5).

[12] Salerno, K. M., Bolintineanu, D. S., Grest, G. S., Lechman, J. B., Plimpton, S. J., Srivastava, I., Silbert, L. E. (2018). Effect of shape and friction on the packing and flow of granular materials. *Physical Review E*, 98(5):050901.

[13] Wang, J., Lei, M., Yang, H., Xu, K., Xu, S., Zhao, P., Song, Y. (2021). Effects of coefficient of friction and coefficient of restitution on static packing characteristics of polydisperse spherical pebble bed. *Particuology*, 57:1–9.

[14] Rapaport, D. C. (2002). Simulational studies of axial granular segregation in a rotating cylinder. *Physical Review E*, 65(6):061306.

[15] Félix, G., Thomas, N. (2004). Evidence of two effects in the size segregation process in dry granular media. *Physical Review E*, 70(5):051307.

[16] Arntz, M. M. H. D., Beeftink, H. H., den Otter, W. K., Briels, W. J., Boom, R. M. (2013). Segregation of granular particles by mass, radius, and density in a horizontal rotating drum. *AIChE Journal*, 60(1): 50–59.

[17] Yang, S., Sun, Y., Zhao, Y., Chew, J. W. (2018). A numerical study of the segregation phenomenon of lognormal particle size distributions in the rotating drum. *Physics of Fluids*, 30(5):053301.
[18] Vo, T.-T., Mutabaruka, P., Nezamabadi, S., Delenne, J.-Y., Izard, E., Pellenq, R., Radjai, F. (2018). Mechanical strength of wet particle agglomerates. *Mechanics Research Communications*, 92:1–7.
[19] Tapia, F., Pouliquen, O., Guazzelli, É. (2019). Influence of surface roughness on the rheology of immersed and dry frictional spheres. *Physical Review Fluids*, 4(10):104302.
[20] Shi, H., Roy, S., Weinhart, T., Magnanimo, V., Luding, S. (2019). Steady state rheology of homogeneous and inhomogeneous cohesive granular materials. *Granular Matter*, 22(1).
[21] Vo, T.-T., Vu, T. L., Mutabaruka, P. (2021). Effects of size polydispersity on segregation of spherical particles in rotating drum. *The European Physical Journal E*, 44(6).
[22] Marks, B., Rognon, P., Einav, I. (2011). Grainsize dynamics of polydisperse granular segregation down inclined planes. *Journal of Fluid Mechanics*, 690:499–511.
[23] Deng, Z., Umbanhowar, P. B., Ottino, J. M., Lueptow, R. M. (2019). Modeling segregation of polydisperse granular materials in developing and transient free-surface flows. *AIChE Journal*, 65(3):882–893.
[24] Deng, Z., Fan, Y., Theuerkauf, J., Jacob, K. V., Umbanhowar, P. B., Lueptow, R. M. (2020). Modeling segregation of polydisperse granular materials in hopper discharge. *Powder Technology*, 374:389–398.
[25] Nguyen, D.-H., Azéma, E., Sornay, P., Radjai, F. (2015). Effects of shape and size polydispersity on strength properties of granular materials. *Physical Review E*, 91(3):032203.
[26] Nguyen, T. K. (2013). Modélisation multi-échelle des matériaux granulaires frottant-cohésifs. PhD thesis, Université de Grenoble.
[27] Mutabaruka, P. (2013). Numerical modeling of immersed granular media: initiation and propagation of avalanches in a fluid. PhD thesis, Université Montpellier.
[28] Vo, T. T., Nezamabadi, S., Mutabaruka, P., Delenne, J.-Y., Radjai, F. (2020). Additive rheology of complex granular flows. *Nature Communications*, 11(1).
[29] Vo, T.-T., Nguyen, C. T., Nguyen, T.-K., Nguyen, V. M., Vu, T. L. (2021). Impact dynamics and power-law scaling behavior of wet agglomerates. *Computational Particle Mechanics*, 9(3):537–550.
[30] Vo, T.-T., Nguyen, T.-K. (2022). Unified penetration depth of low-velocity intruders into granular packings. *Physical Review E*, 106(1):014902.
[31] Mutabaruka, P., Taiebat, M., Pellenq, R. J.-M., Radjai, F. (2019). Effects of size polydispersity on random close-packed configurations of spherical particles. *Physical Review E*, 100(4):042906.
[32] Phong, H. V. N., Trung, V. T., Minh, T. D., My, N. V., Lo, V. T. (2022). Effects of lightweight particle content on the mechanical strength of cylindrical aggregates. *Journal of Science and Technology in Civil Engineering (STCE) - HUCE*, 16(2):117–127.
[33] Vo, T.-T., Nguyen, T.-K. (2022). The roles of the reversibility and irreversibility of capillary bonds on the impact dynamics of agglomerates. *Acta Geotechnica*, 18(1):217–233.
[34] Gong, J., Zou, J., Zhao, L., Li, L., Nie, Z. (2019). New insights into the effect of interparticle friction on the critical state friction angle of granular materials. *Computers and Geotechnics*, 113:103105.

Journal of Science and Technology in Civil Engineering, HUCE (NUCE), 2023, 17 (1): 67–78

MACHINE LEARNING-BASED PEDO TRANSFER FUNCTION FOR ESTIMATING THE SOIL COMPRESSION INDEX

Pham Nguyen Linh Khanh[a,*], Nguyen Huu Bao Ngan[a]

[a]*School of Civil Engineering and Management, International University, Vietnam National University HCM City, Quarter 6, Linh Trung Ward, Thu Duc District, Ho Chi Minh City, Vietnam*

Article history:
Received 17/11/2022, Revised 12/02/2023, Accepted 21/02/2023

Abstract

Soil compression index (C_c) plays a vital role in describing the settlement behaviors of geotechnical infrastructures. The conventional Oedometer test broadly used to determine C_c is time-consuming and expensive, which challenges incorporating the high spatial variability of C_c. Alternatively, this study utilized the pedo transfer function (PTF) concept to develop a predictive model on the extreme gradient boosting (XGB) framework for estimating C_c with high accuracy and low effort. The presented XGB-PTF implemented on the database is acquired from 40 boreholes in Ho Chi Minh city and its vicinity to learn and recognize the correlation patterns of C_c and the easily-obtainable soil parameters (i.e., grain size distribution, unit density, moisture content, Atterberg limits). Rigorous evaluation with standard regression metrics demonstrated the efficiency and excellent performance of the XGB-PTF (e.g., low root-mean-squared error of 0.089 and a high coefficient of determination of 0.903). Furthermore, the presented framework showed its superiority over the current empirical equations in estimating C_c by higher prediction accuracy and applicability to the broader range of soil types. Given efficiency, flexibility, and dynamics, the presented model is expected to be a versatile approach to quantizing and advancing the knowledge of soil characteristics over a regional area.

Keywords: compression index; pedo transfer function; extreme gradient boosting; soil mechanics.

https://doi.org/10.31814/stce.nuce2023-17(1)-06

1. Introduction

Accuracy estimate of ground settlement is a typical geotechnical problem that has drawn massive attention during the history of soil mechanics. In practice, the state-of-the-art Terzaghi approach linearizes the correlation between void ratio (e) and effective stress to approximately describe the primary soil settlement behaviors with a certain degree of success. Given the increased effective stress, the expected settlement can be sufficiently estimated utilizing the compression index (C_c) with acceptable accuracy for engineering applications. However, the Oedometer experiment for determining C_c is time-consuming and labor-intensive, which challenges incorporating the high spatial variability of C_c.

Several experimental studies have been carried out to explore the variation patterns of C_c concerning different soil types. Closed-form equations have been proposed to estimate C_c based on fitting the obtained experimental data [1, 2]. Those published equations generally relate C_c in terms

*Corresponding author. *E-mail address:* pnlkhanh@hcmiu.edu.vn (Khanh, P. N. L.)

of liquid limit (LL), water content (w), and void ratio (e_0) (e.g., $C_c = 0.009(LL - 10)$ for clays [3]; $C_c = 0.011wC_c = 0.54e - 0.19$ for peat [4]; $C_c = 0.54e - 0.19$ for clays [5]). However, despite the practicality, merely being suitable for some specific soil texture restrains the generalized capacity of those empirical models.

In this regard, machine learning (ML) based pedo transfer function (PTF) is a promising alternative to the generic PTF. For details, PTF contributes as mathematical links between the easily-obtainable parameters (i.e., basic soil properties [6]) and the parameter of interest (e.g., C_c) that later allows exploiting the ML advantages in data mining to increase the model performance. Furthermore, the potential of ML-PTF has been accredited in describing various geotechnical applications ([7–10]). Recently, Zhang [11] developed the Bayesian Neural network-based model to forecast soil compressibility and undrained shear strength of clayey. Similarly, Scott Kirts et al. [12] utilized the support vector machine (SVM) model to predict the soil compressibility for coarse-grained, fine-grained, and organic peat. The obtained results once demonstrated the great potential of this approach in geotechnical design. Yet proper academic attention is required to enhance the practical applications of this approach further, as well as advance the knowledge of the correlation between given attributes and soil compressibility behaviors.

The primary objective of this research is to develop an ML-PTF on the extreme gradient boosting (XGB) framework [13] capable of estimating soil compression index with high precision and low effort. Furthermore, advancing the quantitative knowledge of which soil structural indicators determine soil compressibility using correlation analysis. The XGB-PTF was implemented on the Ho Chi Minh (HCM) soil database based on 40 boreholes system collected from different projects in HCMC and its vicinity.

2. Database and Correlation Analysis

2.1. Compression Index Database

This study developed the ML-PTF model for forecasting the C_c value base on the database of boreholes investigated in Ho Chi Minh city and its vicinity. Fig. 1 presents the approximate position of the boreholes. The soil specimen was collected at every 2 m to 3 m of the borehole, whose depth ranges from 30 m to 50 m, for determining the fundamental soil parameters. Consequently, the database of interest contains 600 data points with 13 attributes.

Data validity is utilized to eliminate errors that are likely to occur during measuring or documenting. The data points are expected to satisfy: (i) the particle size criterion and (ii) the physical relationship between soil parameters. The validity process resulted in a clean dataset containing 433 data points.

Moreover, the database includes features directly extracted from grain size distribution (fine gravel (FG), medium gravel (MG), coarse gravel (CG), very fine sand (VFS), fine sand (FS), medium sand (MS), coarse sand (CS), very coarse sand (VCS), fine silt (FS) and coarse silt (CS), fraction of clay (Fclay), silt (Fsilt) and sand (Fsand), natural moisture content (w), natural gravity of soil (γ), dry unit weight (γ_d), degree of saturation (S_r), the specific gravity of soil (G_s), void ratio (e_0), liquid limit (LL), plastic limit (PL), compression index (C_c). The secondary features were estimated based on interpreting the particle size distribution (i.e., D_{10} and D_{60} are grain sizes of 60% and 10% passing the sieved soil, respectively, C_u is a measure of the uniformity of grain size in the soil).

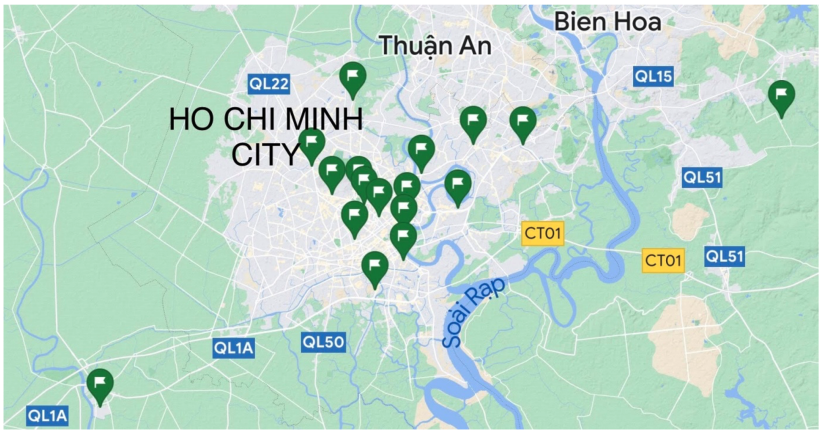

Figure 1. Approximate locations of 40 boreholes

2.2. *Data Properties*

Table 1 summarizes the statistical descriptions of primary indicators in the database.

Table 1. Statistical descriptions of data attributes

Statistical description	w (%)	γ (g/cm^3)	γ_d (g/cm^3)	G_s (g/cm^3)	S_r (%)	e	LL (%)	PL (%)	C_c (cm^2/kG)
Number	433	433	433	433	433	433	433	433	433
Mean	36.7	1.86	1.42	2.68	90.9	1.05	42.4s_r	24.0	0.27
Std.	26.2	0.22	0.35	0.04	6.25	0.68	18.5	10.9	0.40
Min	12.5	1.37	0.64	2.51	53.9	0.40	19.8	9.57	0
Q_1 (25%)	19.3	1.66	1.2	2.66	87.0	0.60	27.2	16.9	0.06
Median	24.1	1.95	1.57	2.69	91.8	0.72	38.5	20.1	0.10
Q_3 (75%)	42.5	2.01	1.69	2.72	96	1.19	48.1	27.4	0.20
Max	117	2.15	1.89	2.75	99.8	3.17	103	73.3	2.41
(Q_1 and Q_3 are first and third quartiles)									

As shown in Fig. 2, the water content had the broadest range among the other factors, which slanted toward the smaller value in the 19.3 - 42.53% range. Moreover, the degree of saturation had an extent from 53.9 to 99.8%, which slanted toward the larger value varying between 87 and 96%. In particular, 75% of the data had a degree of saturation higher than 87%. The natural gravity of soil showed a possible bimodal distribution, varying between 1.37 and 2.15 g/cm^3, which was primarily centered in the range of 1.66 - 2.01 g/cm^3. Similarly, the dry unit weight of soil also performed a possible bimodal distribution, varying between 0.64 and 1.89 g/cm^3, which was primarily centered in the range of 1.2 - 1.69 g/cm^3. The specific gravity indicates the lowest standard deviation, only 0.04, with a narrow range from 2.51 to 2.75 g/cm^3. The soil's void ratio ranged from 0.4 to 3.17, which slanted toward the smaller value varying between 0.6 and 1.19. Only 25% of the data had a void ratio higher than 1.19. The liquid limit had a high standard deviation value (18.54%) compared to other factors and has a broad range from 19.8 to 103.4%, which is slanted toward the smaller value in the range of 27.21 - 48.12%. Only 25% of the data had a liquid limit higher than 48.12%. The plastic limit

also had a broad vary from 9.57 to 73.3%, which slanted toward the smaller value varying from 16.9 - 27.4%. The compression index ranged from 0 to 2.41 cm^2/kG, which slanted toward the smaller value varying from 0.06 to 0.2 cm^2/kG.

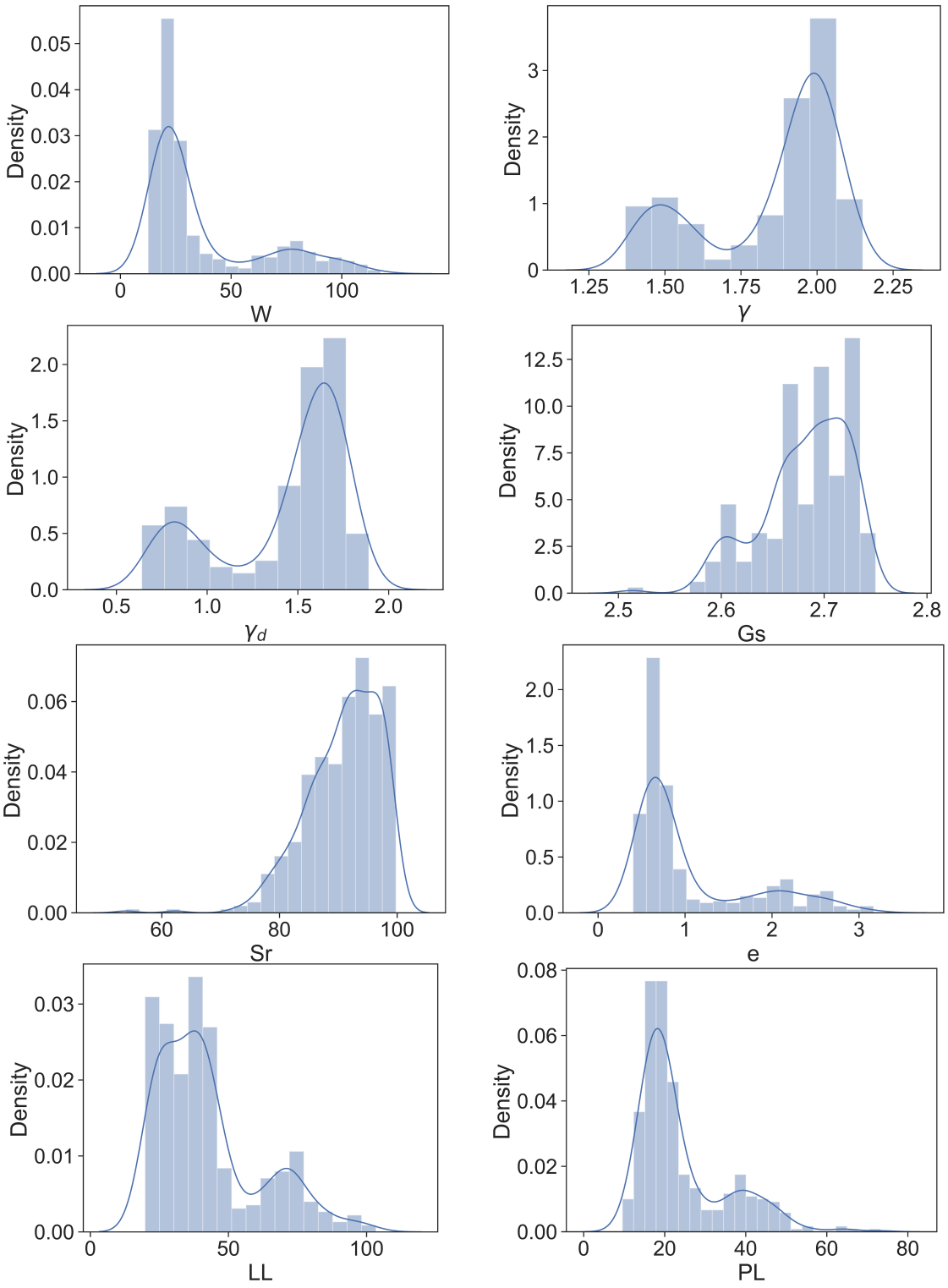

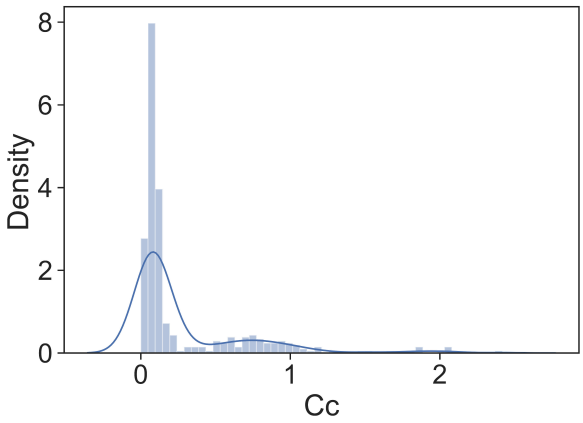

Figure 2. Distribution of factors on their ranges

2.3. Data Analysis

The Pearson correlation coefficient (R) was concisely utilized to estimate the correlation between each couple of input factors:

$$R = \frac{\sum_{i=1}^{n}(x_i - \overline{x})(y_i - \overline{y})}{\sqrt{\sum_{i=1}^{n}(x_i - \overline{x})^2}\sqrt{\sum_{i=1}^{n}(y_i - \overline{y})^2}} \quad (1)$$

The perfectly positive linear correlation gets the absolute R-value of 1; meanwhile, for two factors with no linear relationship, R equals 0. Fig. 3 shows the scatter plot for the correlation of C_c with the most relevant features (i.e., W, e, γ_d, and γ). A relatively strong correlation was observed in the pair of C_c with W (R = 0.861) and e (R = 0.859). These observations are consistent with the empirical equations proposed in the literature. In contrast, in the case of γ_d, and γ the negative R values were obtained, indicating the negative correlation with C_c of these parameters, expressed in the downward trend of the scatterplot.

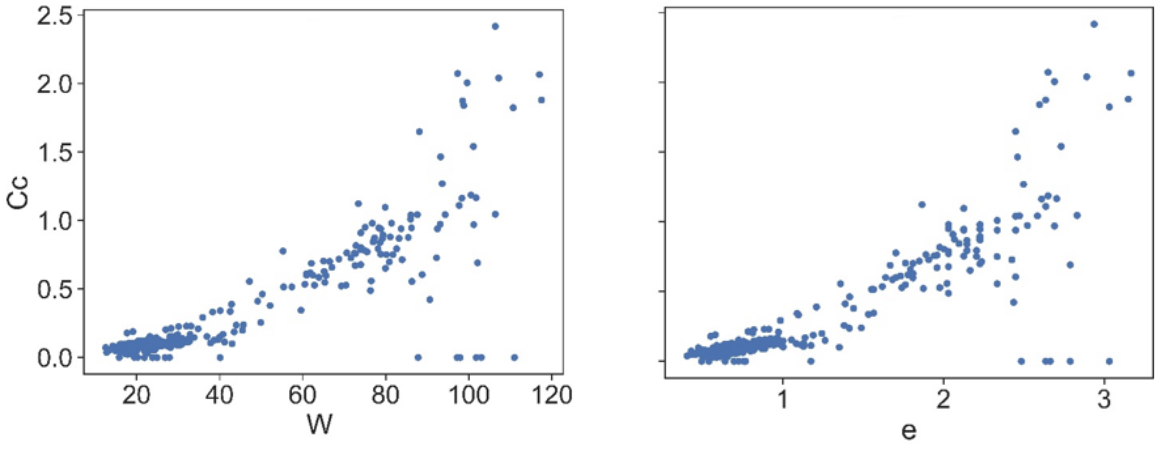

(a) (b)

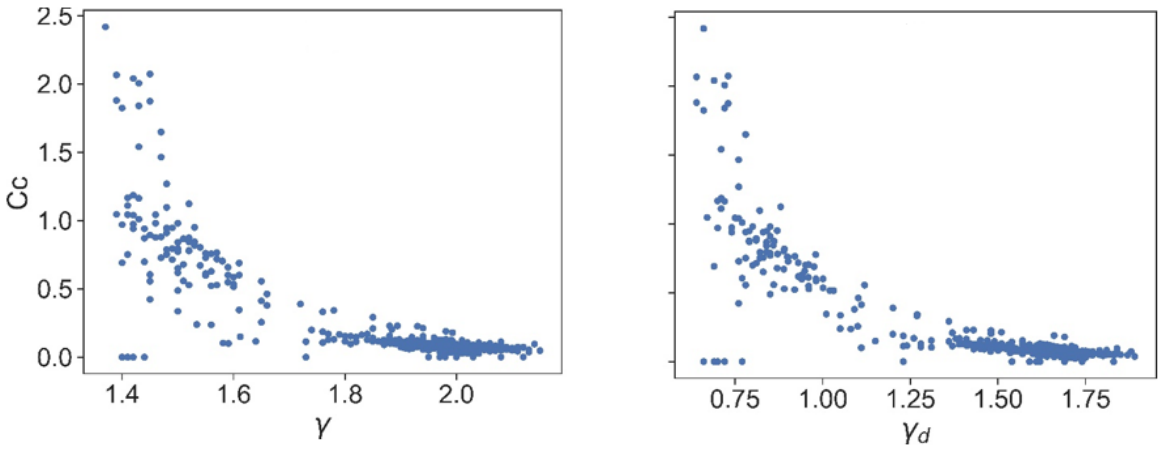

(c) (d)

Figure 3. Geographical scatterplots in pairs: (a) C_c and W (P = 0.86); (b) C_c and e (P = 0.86); (c) C_c and γ_d (P = -0.82); (d) C_c and γ (P = -0.80)

3. Methodology

3.1. Boosting learning

Boosting is a well-known branch of ensemble learning used to improve model performance. A chain of "weak" learners is sequentially added to the ensemble in a stepwise fashion to yield a potentially better one (as presented in Fig. 4).

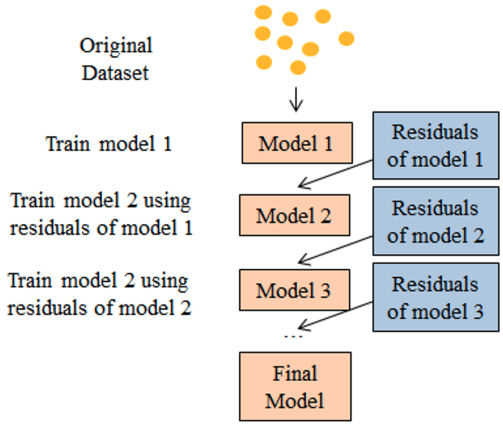

Figure 4. Boosting learning concepts

3.2. Extreme Gradient Boosting (XGB)

Extreme gradient boosting is engineered from the well-known boosting algorithm, especially emphasized in [13] for decreasing the great amount of risk of overfitting problems and enhancing model efficiency. Overfitting is a state-of-the-art issue to all the machine learning models, in which the model performs excellently on the training data but poorly on the previously unseen data (i.e., test set).

Owing to the simplicity, the Decision tree (DT) is chosen as the weak learner that is sequentially added to the ensemble stepwise fashion to enhance the overall performance. Given an instance x_i, the prediction $\hat{y}_i$ of the target y_i is obtained by utilizing predetermined K DTs as below:

$$\hat{y}_i = \sum_{k=1}^{K} \hat{f}_k(x_i) = \sum_{k=1}^{K} \hat{f}_k(x_i) + \rho_K \hat{f}_K(x_i) \tag{2}$$

where $F = \left\{\mathrm{f(x)} = \mathrm{w}_{q(x)} | q : R^m \rightarrow T; \mathrm{w} \in R^T\right\}$ is the family of DT f(x), q is the structure of each tree that represents an instance to the corresponding leaf index. T represents the number of leaves in the tree; each leaf contains a continuous score w; ρ represents the learning rate.

Chen & Guestrin resettled the high risk of overfitting issue inherent in boosting models by regularizing the original objective functions (Eq. (3)) to favor the less complexity model (e.g., simple DT structure with low w on each leaf)

$$L(\hat{y}) = \sum_{i=1}^{n} l(y_i, \hat{y}_i) + \sum_{k=1}^{K} \Omega(\hat{f}_k)$$

where

$$\Omega(f) = \gamma T + \frac{1}{2}\lambda \sum_{j=1}^{T} \mathrm{w}_j^2 \tag{3}$$

Here l is a differentiable convex loss function that computes the difference between and y_i; n is the number of data; γ and λ are regularized hyperparameters; $\Omega(f)$regularized functions.

During the training process, the new DTs are added to the ensemble in the direction determined by the gradient descent concept to minimize the objective function (Eq. (3)). For details, the $k^{th}\hat{f}_k$ is trained with the pseudo database $\left\{x_i, r_{ik} = \frac{\partial L^k}{\partial \hat{f}(x)} \middle| \hat{f}(x) = \hat{f}_k(x)\right\}$ to focus on specific rows. The objective function becomes as follows:

$$L^k = \sum_{i=1}^{n} l(y_i, \hat{y}^{(k-1)} + \rho_k \hat{f}_k(x_i)) + \gamma T_k + \frac{1}{2}\lambda \sum_{j=1}^{T^k} (\mathrm{w}_j^k)^2 \tag{4}$$

3.3. Hyperparameter tuning

The hyperparameters are used to manage the distance between the testing and training errors and enhance model performance. Considering the computational expense, the Bayesian optimization [14] coupled with the K-fold cross-validation was adopted to tune the hyperparameters of the XGB. Table 2 summarizes the XGB hyperparameters.

3.4. Train-Test set

Machine learning models conduct specific tasks in accordance with the patterns extracted from the databases. The training or learning process is the procedure of identifying the regularity and pattern of the database. Once the learning phase is finished, the trained model can appropriately execute a given task on the formerly unseen inputs, and this capability is experienced as generalization. This study utilized 80% of the database (i.e., training data) for training the model, and the remaining 20% (i.e., test set) was to evaluate the model's generalized capacity.

4. Results and Discussion

4.1. Evaluation metrics

Standard evaluation metrics for regression models, including root mean squared error (RMSE), mean absolute error (MAE), coefficient of determination (R^2), and coefficient of determination (R),

Table 2. A summary of the hyperparameters of XGB

Hyperparameters	Descriptions	Search space/ Distribution	XGB
Number of estimators (K)	Determine the number of DTs	[10, 500]/ Uniform	162
Regularized parameters (λ, γ)	Penalty the model complexity	$[1 \times 10^{-5}, 5]$/ Log-Uniform	0.427 0.168
Learning rate (ρ)	Adjust the generalization capacity	[0.01, 1]/ Log-Uniform	0.3
Maximum depth	Control the maximum depth of DT	[1, 20]/ Uniform	4
Subsample ratio	Subsample ratio of training instances	[0, 1]/ Uniform	0.912
Column subsample by tree	Subsample ratio of columns when constructing each DT	[0, 1]/ Uniform	0.683

were utilized to evaluate predictive performance. The high R-values, accompanied by low RMSE and MAE values, prove the outstanding presentation of the developed XGB.

$$RMSE = \sqrt{\frac{1}{n}\sum_{i=1}^{n}(y_i^{obs.} - y_i^{pred.})^2}$$
$$R^2 = 1 - \frac{\sum_{i=1}^{n}\left(y_i^{pred.} - y_i^{obs.}\right)^2}{\sum_{i=1}^{n}\left(y_i^{obs.} - \bar{y}^{obs.}\right)^2}; MAE = \frac{1}{n}\sum_{i=1}^{n}\left|y_i^{obs.} - y_i^{pred.}\right| \quad (5)$$

where n is data samples; $y_i^{pred.}$ and $y_i^{obs.}$ are observed and predicted C_c.

In addition, five empirical equations for predicting C_c in terms of LL, w, or in-situ void ratio (e_0) [15] were utilized to validate the XGB model performance.

4.2. Results

Table 3 and Fig. 5 summarize the evaluation results for the performance of the presented XGB-PTF, along with the broadly used empirical equations. The RMSE and MAE values of XGB were the lowest in comparison with all empirical models on the same dataset, whereas the R^2 value of XGB was higher than all empirical models that demonstrate the superior performance of the developed XGB.

Further elaboration on the model performance was carried on by analyzing the residual errors $y^{pred.} - y^{obs.}$ of the presented models. In Table 4, the mean value of residual error in the case of XGB is -0.006, and the standard deviation is 0.09, which is relatively low compared to the remaining. This means the predicted value of XGB does not fluctuate greatly and is adaptable to many types of soils. Furthermore, the interquartile range ($Q_3 - Q_1$) of the residual error distribution of XGB was close to the zeros line, ranging from -0.045 to 0, as shown in Fig. 6. The amplitude obtained in the case of XGB is smaller than the rest, especially box D, which ranges from -0.197 to -0.55. Box D has a large

Table 3. RMSE, R^2, MAE comparison between XGB and five empirical equations

Regression Metrics	Criteria	XGB	A	B	C	D	E
RMSE	RMSE → 0	0.089	0.106	0.111	0.575	0.636	0.095
R^2	R > 0.8	0.903	0.864	0.849	0.749	0.796	0.891
MAE	MAE → 0	0.055	0.087	0.092	0.563	0.474	0.072

Note: A: $C_c = 0.37(e_0 + 0.003LL - 0.34)$ [16]; B: $C_c = 0.009w + 0.002LL - 0.10$ [16]; C: $C_c = 0.141G_s(\frac{\gamma_w}{\gamma_d})^{\frac{12}{5}}$; D: $C_c = 1.15(e_0 - 0.35)$ [5]; E: $C_c = -0.156 + 0.411e_0 + 0.00058LL$ [17].

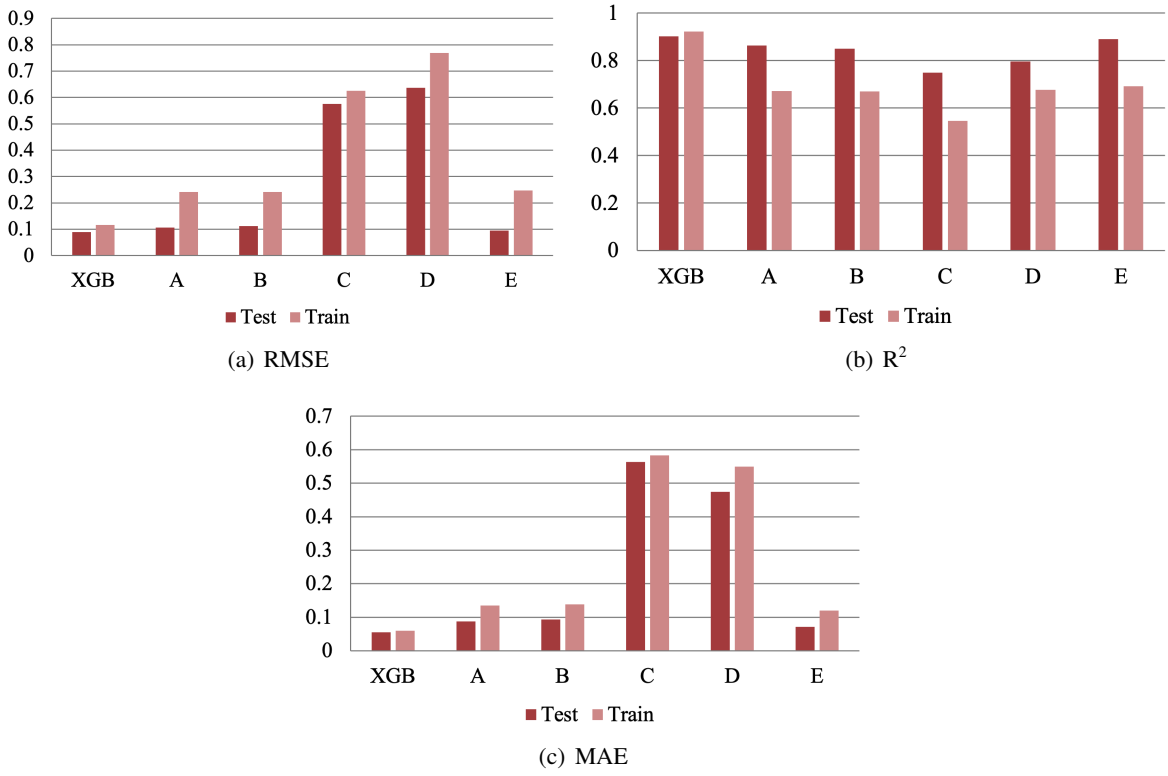

(a) RMSE

(b) R^2

(c) MAE

Figure 5. Comparison between XGB and empirical equations

amplitude because it only considers one factor, e_0, which will lead to low performance compared to other models. Consequently, these results again show the predictive ability of the XGB model.

In Table 5, the XGB model, which applies to various types of soil, performs better values of RMSE and R^2 than SVM, which present inconsistent results. In particular, SVM models have a grateful prediction only for coarse-grained, whereas the prediction for fine-grained and organic peat is not good at all. It is acceptable that XGB is a preeminent model for prediction C_c.

Fig. 7 indicates the impact on the expected accuracy of given features on the model. Among them, the moisture content showed the most substantial influence, expressed by the highest value of feature importance. This is supported by the experimental results reported in the literature, which were later developed into the empirical equation describing the linear correlation between C_c and W.

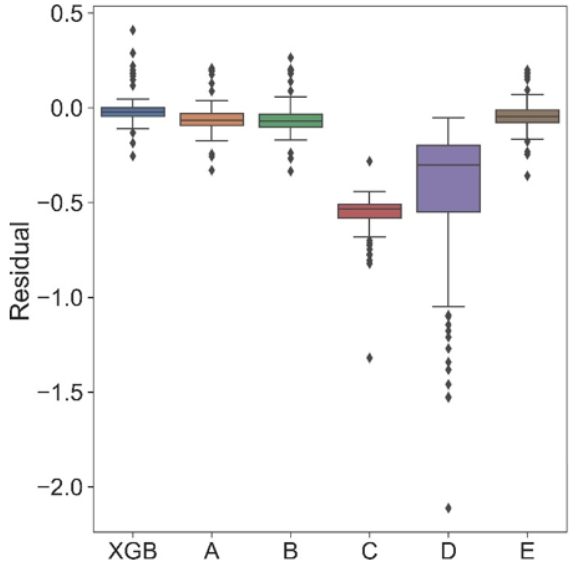

Figure 6. Residuals comparison between XGB and empirical equations

4.3. Discussion

The evaluation results demonstrated that the presented XGB-PTF outperformed the empirical formulas broadly used for predicting C_c. Note that the XGB-PTF consistently performed excellently on various soil types. The flexibility in considering multiple input features for predicting C_c of the XGB-PTF, instead of one or two independent variables like those empirical equations, responds to the improvement in the prediction accuracy. Also, the remarkable capacity to learn complex data patterns allows the XGB-PTF to be workable on a wide range of soil types.

The feature importance indicates the critical role of W in predicting C_c. This obtained result is supported by the theoretical interpretation from soil mechanics and experimental results reported in the literature. Nevertheless, limited in the relatively small database may mislead the understanding of the impacts of the remaining features (such as Atterberg limits and attributes describing grain size distributions). Therefore, further studies should be carried on to explore the potential influence of those relevant factors.

Table 4. Residuals statistical summarization on the test set

	XGB	A	B	C	D	E
Mean	-0.006	-0.053	-0.056	-0.563	-0.474	-0.041
Std	0.090	0.092	0.097	0.117	0.427	0.086
Min	-0.255	-0.330	-0.335	-1.320	-2.113	-0.359
Q_1	-0.045	-0.093	-0.102	-0.581	-0.550	-0.078
Median	-0.023	-0.067	-0.071	-0.534	-0.301	-0.047
Q_3	0.000	-0.031	-0.034	-0.508	-0.197	-0.012
Max	0.410	0.209	0.264	-0.282	-0.052	0.200

Table 5. RMSE and R^2 comparison between XGB and SVM model used in predicting compression index C_c (Scott Kirts et al., 2017)

	XGB		SVM		
	Train	Test	Coarse grained	Fine grained	Organic peat
RMSE	0.117	0.089	0.111	0.391	1.090
R^2	0.923	0.903	0.910	0.650	0.770

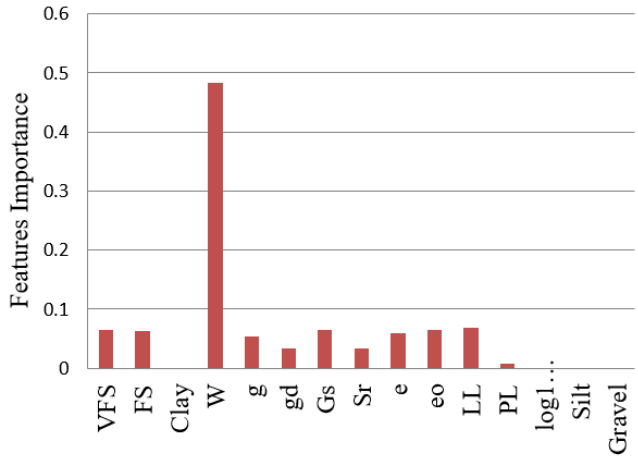

Figure 7. Features Importance of model

5. Conclusions

This study developed the XGB-PTF for predicting compression index. The XGB-PTF was implemented on the geological data from a system of boreholes around Ho Chi Minh city and its vicinity. Also, the hyperparameters of XGB were tunned with the aid of Bayesian optimization coupled with the K-fold cross-validation. Standard evaluation metrics (RMSE, MAE, and R^2) were utilized to evaluate the performance of the developed model. For comparison, five empirical formulas were utilized to evaluate the performance of XGB. The statistical metrics demonstrated excellent performance of the model over the empirical formulas in predicting the compression index of soil (e.g., $RMSE = 0.089$ and $R^2 = 0.903$). Consequently, using machine learning models, especially XGB-PTF, is highly suggested to develop reliable models for identifying the compression index C_c and for advanced application in geotechnical infrastructures.

Acknowledgment

This research is funded by Vietnam National University Ho Chi Minh City (VNU-HCM) under grant number DS2022-28-01.

References

[1] Jefferson, I., Smalley, I. (1997). Soil mechanics in engineering practice. *Engineering Geology*, 48(1-2): 149–150.

[2] Einav, I. (2007). Soil mechanics: breaking ground. *Philosophical Transactions of the Royal Society A: Mathematical, Physical and Engineering Sciences*, 365(1861):2985–3002.
[3] Terzaghi, K., Peck, R. B., Mesri, G. (1996). *Soil mechanics in engineering practice*. John Wiley & Sons.
[4] Cook, P. M. (1956). Consolidation characteristics of organic soils. In *Proc. of 9th Canadian Soil Mechanics Conf*, volume 41, 82–87.
[5] Nishida, Y. (1956). A Brief Note on Compression Index of Soil. *Journal of the Soil Mechanics and Foundations Division*, 82(3).
[6] Looy, K. V., Bouma, J., Herbst, M., Koestel, J., Minasny, B., Mishra, U., Montzka, C., Nemes, A., Pachepsky, Y. A., Padarian, J., Schaap, M. G., Tóth, B., Verhoef, A., Vanderborght, J., Ploeg, M. J., Weihermüller, L., Zacharias, S., Zhang, Y., Vereecken, H. (2017). Pedotransfer Functions in Earth System Science: Challenges and Perspectives. *Reviews of Geophysics*, 55(4):1199–1256.
[7] Pham, K., Kim, D., Yoon, Y., Choi, H. (2019). Analysis of neural network based pedotransfer function for predicting soil water characteristic curve. *Geoderma*, 351:92–102.
[8] Pham, K., Won, J. (2022). Enhancing the tree-boosting-based pedotransfer function for saturated hydraulic conductivity using data preprocessing and predictor importance using game theory. *Geoderma*, 420:115864.
[9] Hung, D. V., Thang, N. T. (2022). Predicting dynamic responses of frame structures subjected to stochastic wind loads using temporal surrogate model. *Journal of Science and Technology in Civil Engineering (STCE) - HUCE*, 16(2):106–116.
[10] Doan, Q. H., Thai, D.-K., Tran, N. L. (2020). A hybrid model for predicting missile impact damages based on k-nearest neighbors and Bayesian optimization. *Journal of Science and Technology in Civil Engineering (STCE) - HUCE*, 14(3):1–14.
[11] Zhang, P., Yin, Z.-Y., Jin, Y.-F. (2022). Bayesian neural network-based uncertainty modelling: application to soil compressibility and undrained shear strength prediction. *Canadian Geotechnical Journal*, 59(4): 546–557.
[12] Kirts, S., Panagopoulos, O. P., Xanthopoulos, P., Nam, B. H. (2018). Soil-Compressibility Prediction Models Using Machine Learning. *Journal of Computing in Civil Engineering*, 32(1).
[13] Chen, T., Guestrin, C. (2016). XGBoost. In *Proceedings of the 22nd ACM SIGKDD International Conference on Knowledge Discovery and Data Mining*, ACM.
[14] Snoek, J., Larochelle, H., Adams, R. P. (2012). Practical bayesian optimization of machine learning algorithms. *Advances in neural information processing systems*, 25.
[15] Al-Khafaji, A. W. N., Andersland, O. B. (1992). Equations for Compression Index Approximation. *Journal of Geotechnical Engineering*, 118(1):148–153.
[16] Azzouz, A. S., Krizek, R. J., Corotis, R. B. (1976). Regression Analysis of Soil Compressibility. *Soils and Foundations*, 16(2):19–29.
[17] Rendon-Herrero, O. (1980). Universal Compression Index Equation. *Journal of the Geotechnical Engineering Division*, 106(11):1179–1200.

Journal of Science and Technology in Civil Engineering, HUCE (NUCE), 2023, 17 (1): 79–93

EVALUATING THE PERFORMANCE OF THE RANS TURBULENCE MODELS FOR SIMULATING WAVE PROPAGATION OVER A SUBMERGED BREAKWATER USING OPENFOAM

Luong Cao Linh[a,*], Mai Cao Tri[a]

[a]*Faculty of Coastal and Offshore Engineering, Hanoi University of Civil Engineering, 55 Giai Phong road, Hai Ba Trung district, Hanoi, Vietnam*

Article history:
Received 21/02/2023, Revised 20/3/2023, Accepted 21/3/2023

Abstract

The present work is to evaluate the performance of the RANS turbulence models for simulating regular wave propagation over a submerged breakwater using the open-source Computational Fluid Dynamics (CFD) software OpenFOAM. The present numerical results of four turbulence models ($k-\varepsilon$ model, $k-\omega$ *SST* model, buoyancy-modified $k-\omega$ *SST* model, and stabilized $k-\omega$ *SST* model) are compared with published experimental data for free surface elevations and velocities at gauges. Moreover, the results of the turbulent kinetic energy (TKE) are compared and assessed between the turbulence models. Results show that the buoyancy-modified $k-\omega$ *SST* model and the stabilized $k-\omega$ *SST* model predictions agree very well with the experimental data, although the turbulence kinetic energy is still significant differences between the two models. Therefore, these two models should be used in the future for simulating the interaction between waves and submerged breakwaters.

Keywords: submerged breakwater; turbulence models; OpenFOAM/waves2foam; CFD, RANS; VOF.

https://doi.org/10.31814/stce.nuce2023-17(1)-07

1. Introduction

Submerged breakwater is an effective solution for beach protection or restoring beaches. The wave-structure interaction processes change the parameters of the wave and those are very complex. Understanding the parameters of the wave field around the submerged breakwater is essential for the design of the structure. The research method of physical models using wave flume has been applied by many authors [1–7]. The main results often are empirical formulas, the most common of which are the wave transmission coefficient formulas. The experiment's research is often not very informative about hydrodynamic characteristics and wave fields around the submerged breakwater.

In recent years, with the development of computers and software, Computational Fluid Dynamics (CFD) has become an effective tool to supplement and partially replace experimental research. Many numerical models have been developed to simulate wave-submerged structure interactions by the research of the authors such as Shen et al. [8], Peng and Zou ([9], Rahman [10], Kamath et al. [11], Liang et al. [12], Ning et al. [2], Liu et al. [4], Li and Zhang [13], Srineash et al. [14], Abdullah et al.

*Corresponding author. *E-mail address:* linhlc@huce.edu.vn (Linh, L. C.)

[15], Xu et al. [16], Kamath et al. [6]. The Reynold-Averaged Navier-Stokes (RANS) equations model can simulate well nonlinear waves and flow fields around the structure.

The turbulence models are used in the numerical models to more accurately simulate wave-submerged structure interactions, most commonly two-equation RANS turbulence models, e.g. $k-\varepsilon$ model [8], $k-\omega$ model [11], $k-\omega$ *SST* model [13]. These standard turbulence models have been demonstrated to be unconditionally unstable, and the turbulent kinetic energy (TKE) is predicted large to be excessive and might cause a significant decrease in wave height over the length of the numerical wave flume. Recently, several authors have proposed modified turbulence models to solve this problem. Devolder et al. [17, 18] proposed buoyancy-modified turbulence models that use a buoyancy term added to the TKE equation. Larsen and Fuhrman [19] proposed stabilized-modified turbulence models that use the addition of stress-limiting modification. OpenFOAM is an open-source software popular among researchers and industry, across many areas of offshore, and coastal [13, 17–19]. The library waves2foam is a plug-in toolbox to OpenFOAM [20]. Waves2foam is used to generate and absorb free surface water waves with the possibility of modeling the interaction between free surface waves and a permeable medium such as breakwaters and scour protection [19, 21–23].

Previous studies have shown that using different turbulence models will greatly affect the results in numerical models, especially for nonlinear wave problems such as breaking waves or wave-structures interaction [23, 24]. The interaction between waves and submerged breakwaters changes the parameters of the wave and those are very complex. Therefore, it is necessary to evaluate the performance of different turbulence models on wave propagation over a submerged breakwater.

In this paper, we present a study to evaluate the performance of the RANS turbulence models for simulating wave propagation over a submerged breakwater. The study uses open-source software OpenFOAM with the toolbox waves2foam [20]. The two-dimensional numerical simulation cases with four turbulence models ($k-\varepsilon$ model, $k-\omega$ *SST* model, buoyancy-modified $k-\omega$ *SST* model, and stabilized $k-\omega$ *SST* model). The paper is organized as follows. First is the introduction section. In Section 2, the governing equations for the numerical model are presented. Section 3 includes a description of the computational domain and the convergency studies of the numerical model. Subsequently, the present numerical results are compared with published experimental data and discussed in detail in Section 4. Finally, the main conclusions are drawn in Section 5.

2. Numerical method

2.1. Governing equations

The numerical model uses the incompressible RANS equations:

Mass conservation equation:

$$\frac{\partial u}{\partial x}+\frac{\partial v}{\partial y}+\frac{\partial w}{\partial z}=0 \tag{1}$$

x-component of momentum equation:

$$\begin{aligned}\frac{\partial u}{\partial t}+\frac{\partial}{\partial x}(uu)+\frac{\partial}{\partial y}(vu)+\frac{\partial}{\partial z}(wu)=&-\frac{1}{\rho}\frac{\partial p}{\partial x}+g_x+\frac{1}{\rho}\mu\left(\frac{\partial^2 u}{\partial x^2}+\frac{\partial^2 u}{\partial y^2}+\frac{\partial^2 u}{\partial z^2}\right)\\&-\left(\frac{\partial}{\partial x}\left(\overline{u'u'}\right)+\frac{\partial}{\partial y}\left(\overline{v'u'}\right)+\frac{\partial}{\partial z}\left(\overline{w'u'}\right)\right)\end{aligned} \tag{2}$$

y-component of momentum equation:

$$\frac{\partial v}{\partial t}+\frac{\partial}{\partial x}(uv)+\frac{\partial}{\partial y}(vv)+\frac{\partial}{\partial z}(wv)=-\frac{1}{\rho}\frac{\partial p}{\partial y}+g_y+\frac{1}{\rho}\mu\left(\frac{\partial^2 v}{\partial x^2}+\frac{\partial^2 v}{\partial y^2}+\frac{\partial^2 v}{\partial z^2}\right)-\left(\frac{\partial}{\partial x}\left(\overline{u'v'}\right)+\frac{\partial}{\partial y}\left(\overline{v'v'}\right)+\frac{\partial}{\partial z}\left(\overline{w'v'}\right)\right) \tag{3}$$

z-component of momentum equation:

$$\frac{\partial w}{\partial t}+\frac{\partial}{\partial x}(uw)+\frac{\partial}{\partial y}(vw)+\frac{\partial}{\partial z}(ww)=-\frac{1}{\rho}\frac{\partial p}{\partial z}+g_z+\frac{1}{\rho}\mu\left(\frac{\partial^2 w}{\partial x^2}+\frac{\partial^2 w}{\partial y^2}+\frac{\partial^2 w}{\partial z^2}\right)-\left(\frac{\partial}{\partial x}\left(\overline{u'w'}\right)+\frac{\partial}{\partial y}\left(\overline{v'w'}\right)+\frac{\partial}{\partial z}\left(\overline{w'w'}\right)\right) \tag{4}$$

where u, v, w are the Cartesian components of the fluid velocity, ρ is the fluid density, p is the pressure, g_x, g_y, g_z is the gravitational acceleration in x, y, z direction, μ is the kinematic viscosity.

The Reynolds stress tensor $\bar{\sigma}_t$ is defined as:

$$\bar{\sigma}_t=-\rho\begin{bmatrix}\overline{u'u'} & \overline{v'u'} & \overline{w'u'}\\ \overline{u'v'} & \overline{v'v'} & \overline{w'v'}\\ \overline{u'w'} & \overline{v'w'} & \overline{w'w'}\end{bmatrix} \tag{5}$$

2.2. Turbulence modeling

a. The $k-\varepsilon$ model

Turbulent kinetic energy k equation:

$$\frac{\partial k}{\partial t}+u_j\frac{\partial k}{\partial x_j}=\frac{\partial}{\partial x_j}\left[\left(\frac{\nu_t}{\sigma_k}+\nu\right)\frac{\partial k}{\partial x_j}\right]+\overline{u_i'u_j'}\frac{\partial u_i}{\partial x_j}-\varepsilon \tag{6}$$

Turbulent kinetic energy dissipation rate ε equation:

$$\frac{\partial \varepsilon}{\partial t}+u_j\frac{\partial \varepsilon}{\partial x_j}=\frac{\partial}{\partial x_j}\left[\left(\frac{\nu_t}{\sigma_\varepsilon}+\nu\right)\frac{\partial \varepsilon}{\partial x_j}\right]+C_{1\varepsilon}\frac{\varepsilon}{k}\nu_t\left(\frac{\partial u_i}{\partial x_j}+\frac{\partial u_j}{\partial x_i}\right)\frac{\partial u_i}{\partial x_j}-C_{2\varepsilon}\frac{\varepsilon}{k} \tag{7}$$

where ν_t is the turbulent kinematic viscosity, the constants for this model are: σ_k = 1.0, σ_ε = 1.3, $C_{1\varepsilon}$ = 1.44, $C_{2\varepsilon}$ = 1.92.

b. The $k-\omega$ *SST* model

In the $k-\omega$ *SST* model, the turbulence kinetic energy k and the turbulence specific dissipation rate ω are solved using two additional transport equations defined as:

$$\frac{\partial k}{\partial t}+\frac{\partial u_j k}{\partial x_j}-\frac{\partial}{\partial x_j}\left[(\nu+\sigma_k\nu_t)\frac{\partial k}{\partial x_j}\right]=P_k-\beta^*\omega k \tag{8}$$

$$\frac{\partial \omega}{\partial t}+\frac{\partial u_j \omega}{\partial x_j}-\frac{\partial}{\partial x_j}\left[(\nu+\sigma_\omega\nu_t)\frac{\partial \omega}{\partial x_j}\right]=\frac{\gamma}{\nu_t}G-\beta\omega^2 k+2(1-F_1)\frac{\sigma_{\omega 2}}{\omega}\frac{\partial k}{\partial x_j}\frac{\partial \omega}{\partial x_j} \tag{9}$$

where P_k is the production term of k, ν_t is the turbulent kinematic viscosity.

$$\begin{aligned} P_k &= \min\left(G, 10\beta^*\omega k\right) \\ G &= \nu_t \frac{\partial u_i}{\partial x_j}\left(\frac{\partial u_i}{\partial x_j} + \frac{\partial u_j}{\partial x_i}\right) \\ \nu_t &= \frac{a_1 k}{\max\left(a_1\omega, S F_2\right)} \end{aligned} \tag{10}$$

The constants of α_k, α_ω, α and β are blended using the equation:

$$\varphi = F_1\varphi_1 + (1 - F_1)\varphi_2 \tag{11}$$

The constants for this model are: $\beta^* = 0.09$, $\alpha_1 = 5/9$, $\beta_1 = 0.075$, $\sigma_{k1} = 0.85$, $\sigma_{\omega 1} = 0.5$, $\alpha_2 = 0.44$, $\beta_2 = 0.0828$, $\sigma_{k2} = 1$, $\sigma_{\omega 2} = 0.856$.

c. The buoyancy-modified $k - \omega$ *SST* model

The buoyancy-modified $k - \omega$ *SST* model was proposed by Devolder et al. [17, 18]. The density ρ is included in two equations of the standard $k - \omega$ *SST* model and the buoyancy term G_b is added to the TKE equation.

$$\frac{\partial \rho k}{\partial t} + \frac{\partial \rho u_j k}{\partial x_j} - \frac{\partial}{\partial x_j}\left[\rho\left(\nu + \sigma_k \nu_t\right)\frac{\partial k}{\partial x_j}\right] = \rho P_k + G_b - \rho\beta^*\omega k \tag{12}$$

$$\frac{\partial \rho \omega}{\partial t} + \frac{\partial \rho u_j \omega}{\partial x_j} - \frac{\partial}{\partial x_j}\left[\rho\left(\nu + \sigma_\omega \nu_t\right)\frac{\partial \omega}{\partial x_j}\right] = \frac{\gamma}{\nu_t}\rho G - \rho\beta\omega^2 + 2\left(1 - F_1\right)\rho\frac{\sigma_{\omega 2}}{\omega}\frac{\partial k}{\partial x_j}\frac{\partial \omega}{\partial x_j} \tag{13}$$

$$G_b = -\frac{\nu_t}{\sigma_t}\frac{\partial \rho}{\partial x_j}g_j \tag{14}$$

where the buoyancy term G_b is treated implicitly, the scalar $\sigma_t = 0.85$.

d. The stabilized $k - \omega$ *SST* model

The stabilized $k - \omega$ *SST* model was proposed by Larsen and Fuhrman [19]. The buoyancy term G_b is added to the TKE equation and stress-limiting modifications to the standard $k - \omega$ *SST* model.

$$\frac{\partial \rho k}{\partial t} + \frac{\partial \rho u_j k}{\partial x_j} - \frac{\partial}{\partial x_j}\left[\rho\left(\nu + \sigma_k \nu_t\right)\frac{\partial k}{\partial x_j}\right] = \rho P_k + G_b - \rho\beta^*\omega k \tag{15}$$

$$\frac{\partial \omega}{\partial t} + \frac{\partial u_j \omega}{\partial x_j} - \frac{\partial}{\partial x_j}\left[\left(\nu + \sigma_\omega \nu_t\right)\frac{\partial \omega}{\partial x_j}\right] = \frac{\gamma}{\nu_t}G - \beta\omega^2 k + 2\left(1 - F_1\right)\frac{\sigma_{\omega 2}}{\omega}\frac{\partial k}{\partial x_j}\frac{\partial \omega}{\partial x_j} \tag{16}$$

$$\nu_t = \frac{a_1 k}{\max\left(a_1\omega, F_2\sqrt{p_0}, a_1\lambda_2\frac{\beta}{\beta^*\alpha}\frac{p_0}{p_\Omega}\omega\right)} \tag{17}$$

where λ_2 is an additional stress limiter coefficient, and the default value is 0.05.

2.3. Free surface capture

The interface between the water and the air is tracked using the volume of fluid (VOF) method [25]. The method is based on a volume fraction coefficient α, which is 0 for air and 1 for water. The volume fraction is solved by an advection equation:

$$\frac{\partial \alpha}{\partial t} + \frac{\partial\left(\alpha u_i\right)}{\partial x_i} + \frac{\partial\left[\alpha\left(1 - \alpha\right)u_{ir}\right]}{\partial x_i} = 0 \tag{18}$$

where u_{ir} is the relative velocity between the water phase and the air phase.

The density and kinematic viscosity at the interface is obtained by a weighted value based on the volume fraction coefficient.

$$\begin{aligned} \rho &= \alpha\rho_w + (1-\alpha)\rho_a \\ \nu &= \alpha\nu_w + (1-\alpha)\nu_a \end{aligned} \tag{19}$$

where ρ_w and ρ_a are the densities of water and air, $\nu_w$and ν_a are the kinematic viscosity coefficients of water and air.

2.4. Relaxation method

The wave relaxation zone technique was presented by Jacobsen et al. [20] in the waves2foam toolbox. Relaxation zones are implemented to avoid wave reflection at the inlet and outlet boundaries. The relaxation function is in the following way:

$$\varphi = \gamma_R\varphi_{computed} + (1-\gamma_R)\varphi_{\text{target}} \tag{20}$$

where φ is either velocity u_i or volume fraction α, γ_R is the weighting factor defined as:

$$\gamma_R(\chi_R) = 1 - \frac{\exp\left(\chi_R^{3.5}\right) - 1}{\exp(1) - 1} \quad for \quad \chi_R \in [0,\ 1] \tag{21}$$

3. Numerical implementation

3.1. Computational domain

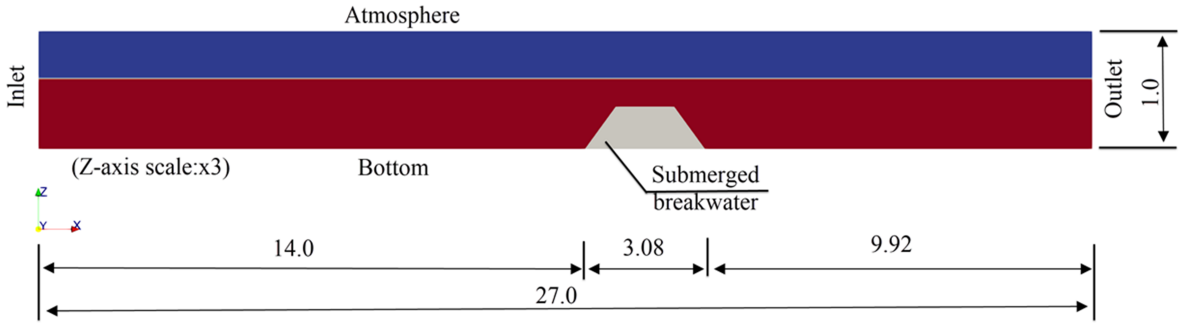

Figure 1. The dimensions of the numerical wave tank, units (m)

The numerical model setup is accorded to the setup from the physical experiment conducted by Liu et al. [4]. The dimensions of the numerical wave tank (NWT) are shown in Fig. 1. The length of NWT is reduced compared to those of the physical wave flume to decrease the computational domain. The water depth of the NWT is 0.6 m. A regular wave test case is selected from experimental data with a wave height of 0.1 m and a wave period of 2.2 s, and 2^{nd} order Stokes theory is used for all the simulation cases presented. A relaxation zone of approximately one wavelength, L, is applied at the inlet and outlet boundary. Six wave gauges (W1-6) and three velocity gauges (V1-3) are placed at the same locations as the experimental, as shown in Fig. 2.

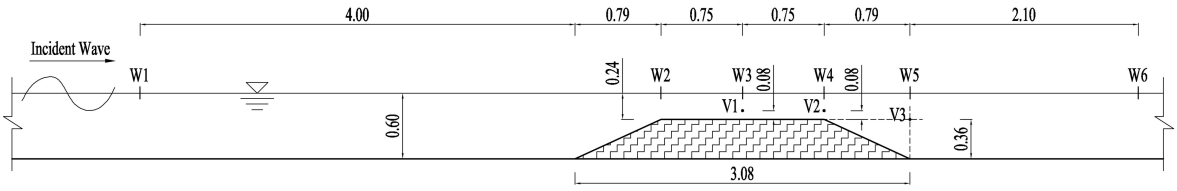

Figure 2. Locations of gauges, units (m)

3.2. *Boundary conditions*

The types of boundary conditions for this simulation are given in Fig. 1: inlet on the left, outlet on the right, and atmosphere on the top. The bottom and the structure's surface are modeled as smooth solid walls. The no-slip condition for velocity and zero gradient condition for pressure is employed in the front, back, bottom, and structure's surface boundaries. The velocity is specified based on the 2nd order Stokes wave theory at the inlet boundary. At the outlet boundary, both the water and air velocities are set to zero. At the atmosphere boundary, the *pressureInletOutletVelocity* is applied to the velocity.

3.3. *Convergence study*

This study performs spatial and temporal convergence studies for the numerical wave tank without structure. All the present simulations are performed for 50 seconds. The free surface elevations at the six probes are used as metrics in the convergence studies.

For the spatial convergence study, the grid size in the free surface region is refined, as shown in Fig. 3. The vertical cell size is normalized by the wave height, and the horizontal cell size ensures an aspect ratio of 1. In this study, three size options are chosen: 5, 10, and 20 cells per wave height (CPH) [26].

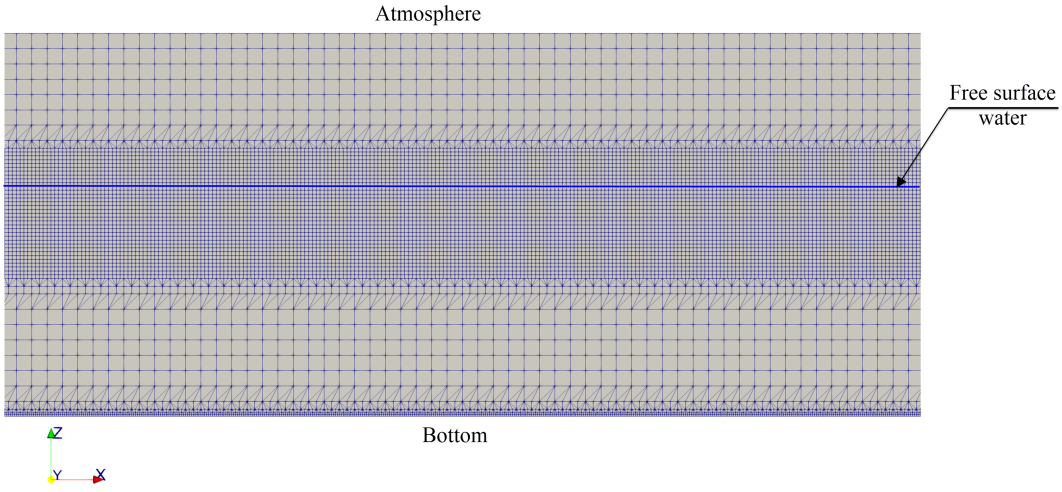

Figure 3. The mesh around the free surface

For the temporal convergence study, the time step is varied by controlling the maximum Courant number ($Co_{\max}$). In this study, three $Co_{\max}$ are used: 0.25, 0.50, and 1.00. Thus, different meshes and $Co_{\max}$ cases are shown in Table 1.

Table 1. Parameters of convergence study cases

Cases	Mesh 1	Mesh 2	Mesh 3
Minimum vertical cell size Δz (m)	0.020	0.010	0.005
CPH	5	10	20
Number of Cells	97852	190350	519075
Co_{max}	0.5	0.25/0.5/1.0	0.5

Simulation results corresponding to three mesh sizes with $Co_{\max}$ of 0.5 are shown in Fig. 4. Free surface elevations at six gauges (W1-W6) are shown as full-time simulations and magnified views. The results show good agreement with comparing three mesh sizes, only differences can be observed in the magnified view versions. The relative errors of peak free surface elevations (averaged over the last ten wave periods of simulation) are shown in Fig. 6(a), where, ε_{12} is the relative error between Mesh 1 and Mesh 2, ε_{23} is the relative error between Mesh 2 and Mesh 3. The results show that the mesh size option of 10CPH is sufficient for accuracy for spatial convergence.

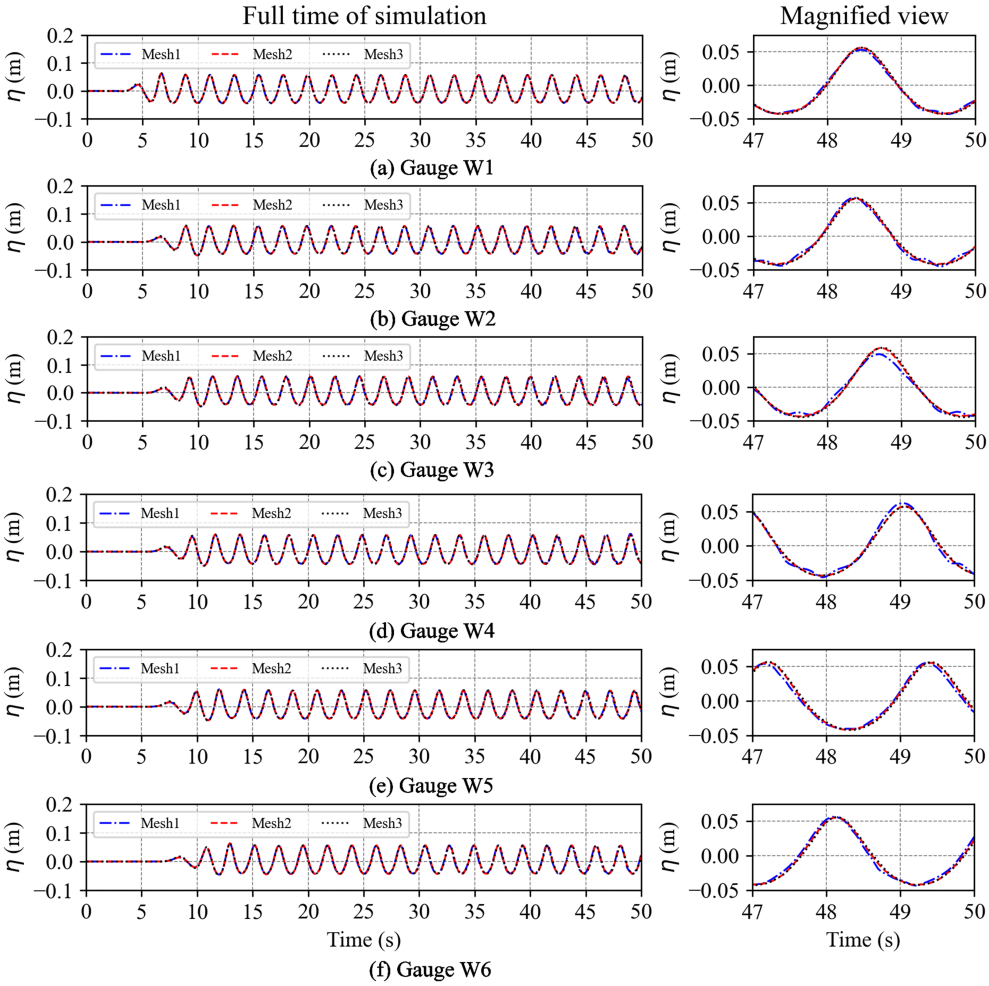

Figure 4. Free surface elevations at wave gauges with three mesh cases

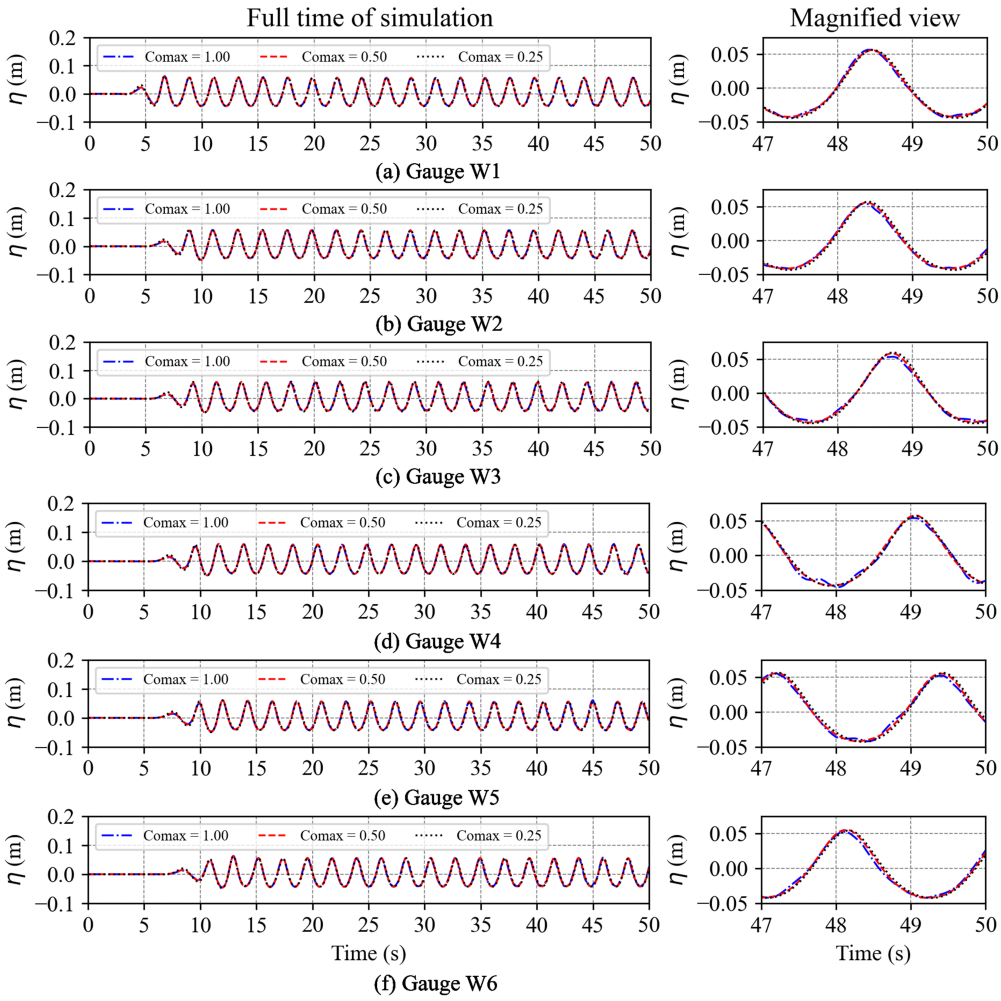

Figure 5. Free surface elevations at wave gauges with three Courant number

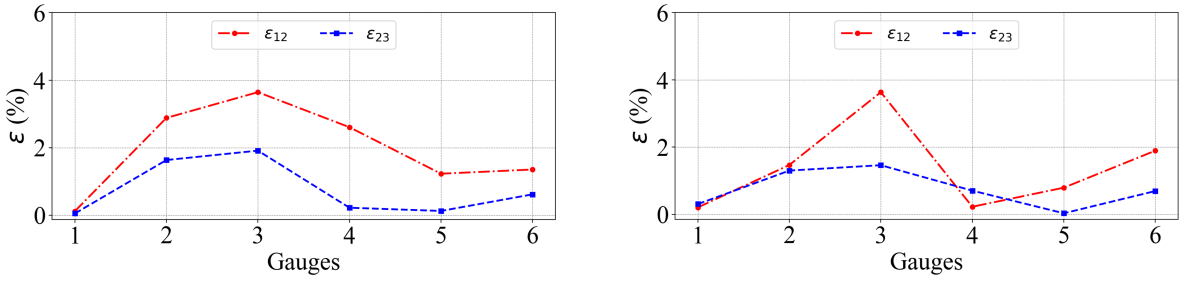

(a) Spatial convergence study

(b) Temporal convergence study

Figure 6. The relative error between the results of the convergence study cases

Similarly, the results corresponding to three $Co_{\max}$ cases with Mesh 2 option are shown in Fig. 5. The relative errors of peak free surface elevations are shown in Fig. 6(b), where, ε_{12} is the relative error between $Co_{\max}$ = 1.0 and $Co_{\max}$ = 0.5, ε_{23} is the relative error between $Co_{\max}$ = 0.5 and $Co_{\max}$

= 0.25. The results show only small differences with $Co_{\max}$ = 1.0 case, and good agreement between the other two maximum Courant number cases. Thus, $Co_{\max}$ = 0.5 case is sufficient for accuracy for temporal convergence.

Therefore, the mesh size option of 10CPH and an aspect ratio of 1 (in the free surface region) with a maximum Courant number of 0.5 is chosen and will be used in subsequent simulations.

4. Results and discussion

In this study, four simulations corresponding to four turbulence models are conducted. The numerical results of free surface elevations and velocities at gauges are compared with experimental data from Liu et al. [4]. Moreover, the results of the turbulent kinetic energy (TKE) are compared and assessed between the turbulence models. All the present simulations are performed for 50 seconds. The simulation time is chosen to ensure that the waves in the NWT fully develop and become stable, and the results after that point have a sufficiently long time interval corresponding to the experimental data, for free surface elevations of 10 seconds and the horizontal velocity of 5 wave periods.

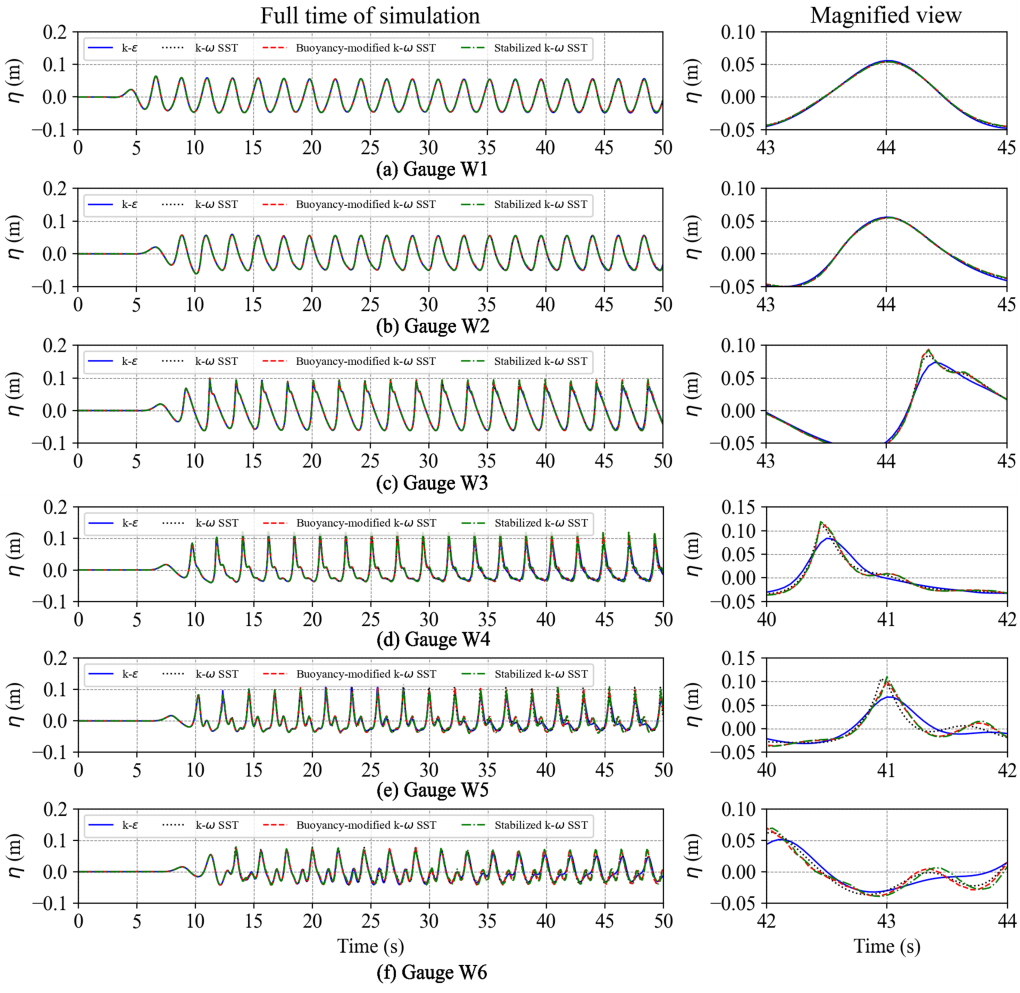

Figure 7. Free surface elevations at wave gauges with four turbulence models

The root means square error (RMSE) for free surface elevations and horizontal velocities is used to compare the performance of the various turbulence models.

$$RMSE = \sqrt{\frac{\sum_{i=1}^{n}\left(X_{num} - X_{exp}\right)^2}{n}} \tag{22}$$

where n is the number of data, X_{num} is the numerical model results, and X_{exp} is the experimental value.

4.1. Free surface elevation

Fig. 7 presents the comparison of free surface elevations at six wave gauges (W1-W6) between four numerical simulations corresponding to four turbulence models. The results are shown as full-time simulations and magnified views.

It is seen that good agreement between all numerical models at the two first probe locations (Fig. 7(a) and (b)), at the remaining four probe locations, shows the significant discrepancy between the $k-\varepsilon$ model and the other three turbulence models (Fig. 7(c), (d), (e) and (f)).

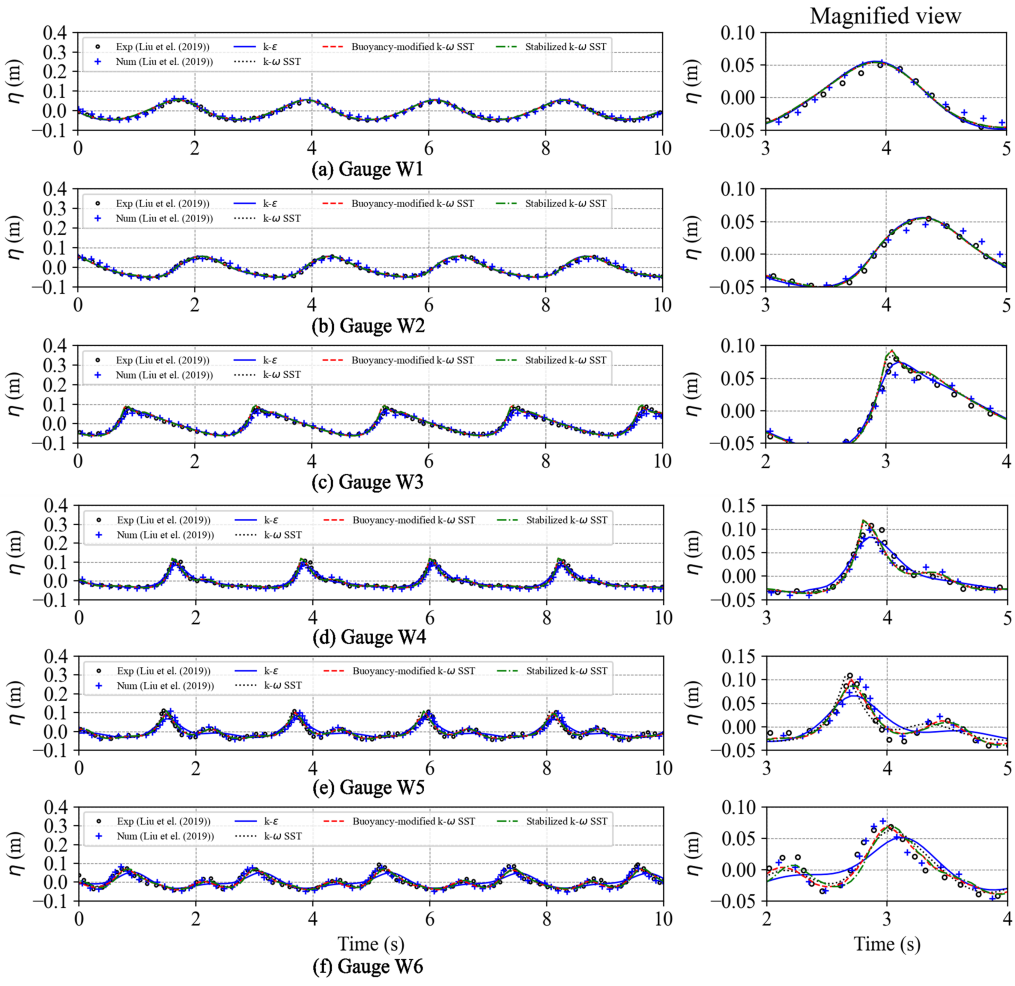

Figure 8. Comparison of free surface elevation between numerical models and experimental data

Fig. 8 shows the numerical results and the corresponding experimental data in ten seconds at six wave gauges. Note, for experimental data, $t = 0$ s is defined as after the wave has fully developed and becomes stable, for present numerical models, results obtained in ten seconds near the end of the simulation time are used for comparison.

Prediction of all the numerical models shows good agreement in the free surface compared to experimental data at two wave probes in front of the submerged breakwater. However, the $k-\varepsilon$ model predicted was poorly accurate at four other wave probes, especially the last two (Fig. 8(e) and (f)). Three other turbulent models generally show reasonably well with experimental data. The $k-\omega$ *SST* model predicted a significantly different secondary wave at the fifth wave gauge (W5).

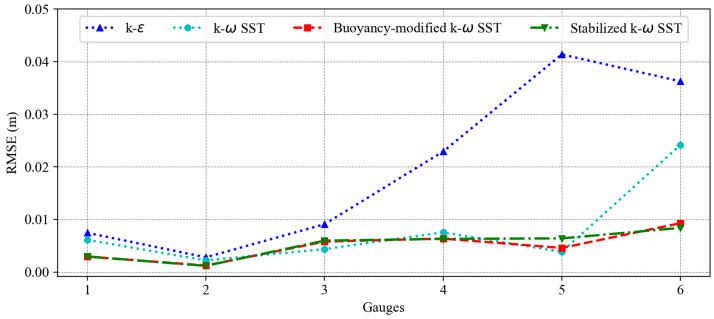

Figure 9. RMSE of peak free surface elevations with four turbulence models

Fig. 9 shows RMSE results of peak free surface elevations at six gauges. The buoyancy-modified $k-\omega$ *SST* and the stabilized $k-\omega$ *SST* models are almost the same at all wave gauges and agree best with the experimental data.

4.2. Velocity

Fig. 10 and Fig. 11 compare horizontal and vertical velocities at three gauges (V1-V3) between four turbulence models. The results are shown as full-time simulations and magnified views. The results show that, similar to the free surface elevation, the $k-\varepsilon$ model has a significant discrepancy compared to the three other turbulence models.

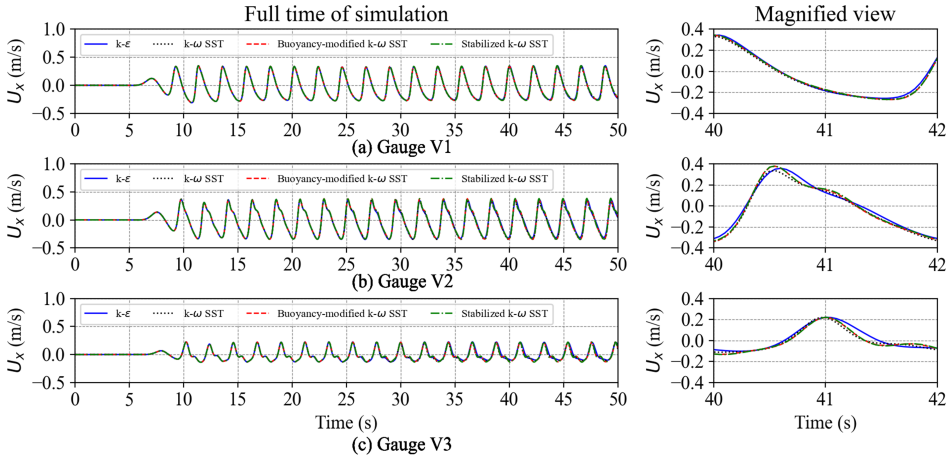

Figure 10. Time series of horizontal velocities with four turbulence models

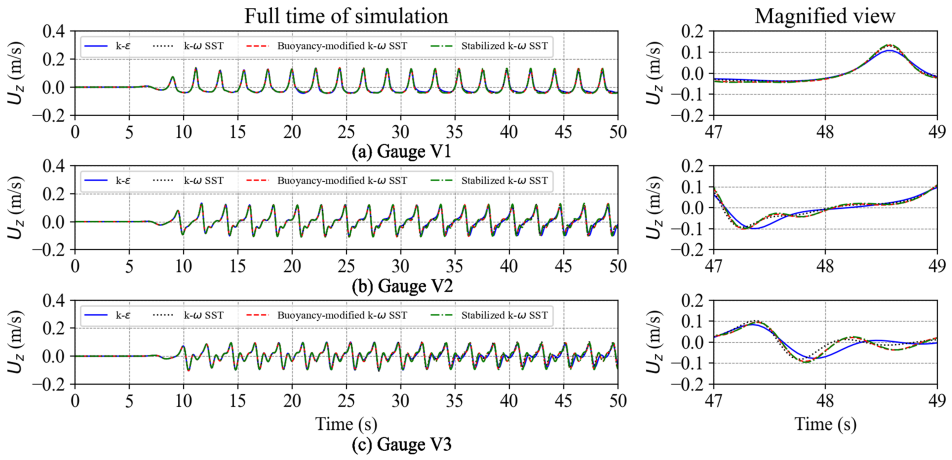

Figure 11. Time series of vertical velocities with four turbulence models

Fig. 12 presents the comparison of horizontal velocities between numerical models and experimental data in five wave periods, where t/T is the normalized time.

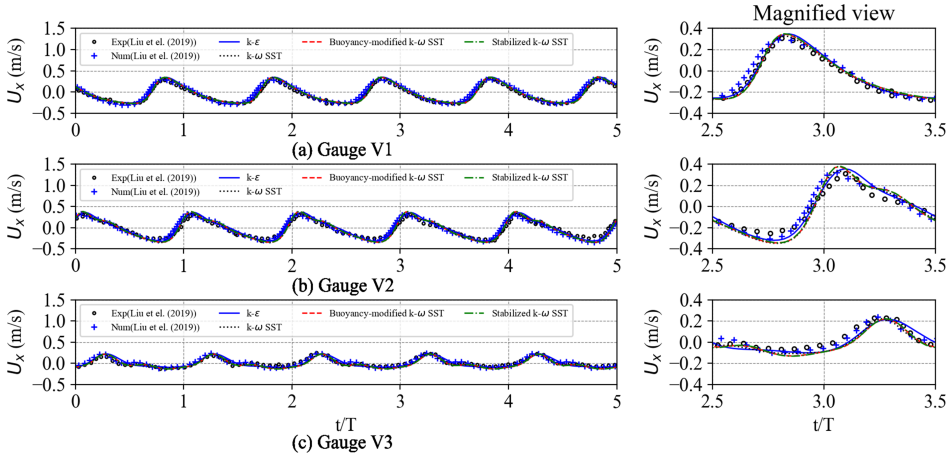

Figure 12. Comparison of horizontal velocities between numerical models and experimental data

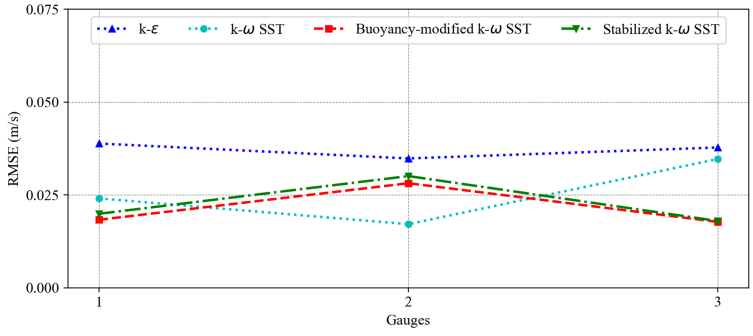

Figure 13. RMSE of peak horizontal velocities with four turbulence models

Fig. 13 shows RMSE results of peak horizontal velocities at three gauges. It is seen that the three turbulence models ($k-\omega$ *SST*, buoyancy-modified $k-\omega$ *SST* and stabilized $k-\omega$ *SST*) agree well with the experimental data at all probes.

4.3. Turbulent behavior

The turbulent behavior of turbulence models is judged through TKE k analysis. Fig. 14 shows the contour plot of the TKE of the four turbulence models. It is seen that the $k-\varepsilon$ model predicted the TKE largest, followed by the $k-\omega$ *SST* model and buoyancy-modified $k-\omega$ *SST*, and the stabilized $k-\omega$ *SST* model predicted the TKE smallest.

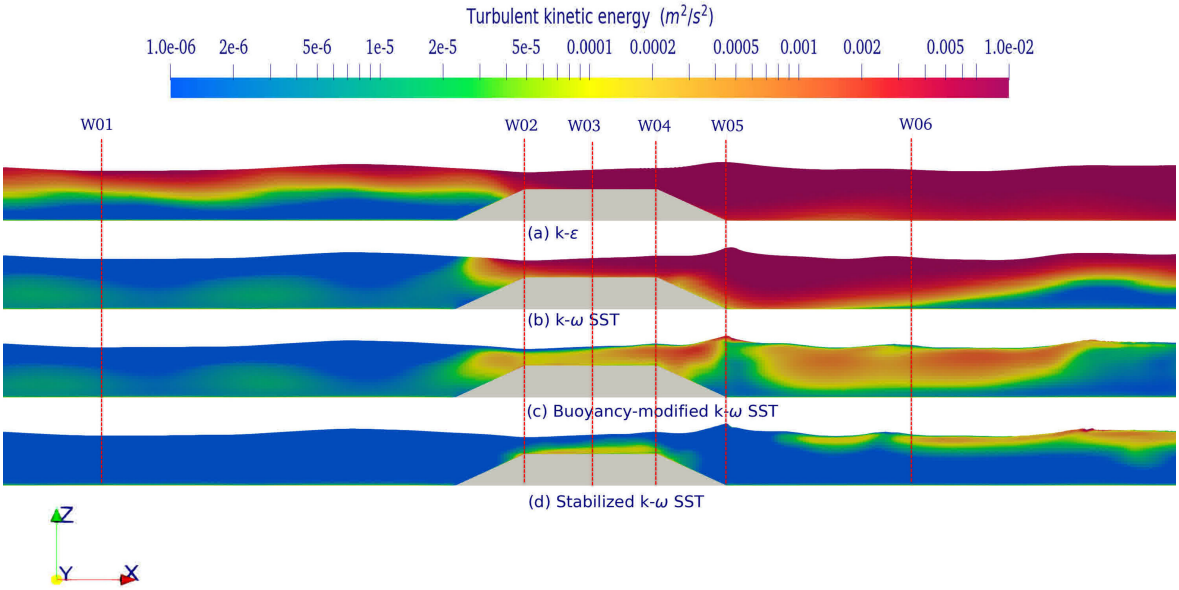

Figure 14. Snapshots of the turbulent kinetic energy k (m^2/s^2) with four turbulence models

As can be seen, the $k-\omega$ *SST* model and the buoyancy-modified $k-\omega$ *SST* model give almost the same results in the wave propagating zone in front of the structure. For the $k-\omega$ *SST* model, the TKE is pretty large in the above and behind the dike, which does not affect the prediction results of the prime wave much but significantly affects the prediction results of the secondary wave. This is improved when using the buoyancy-modified $k-\omega$ *SST* or the stabilized $k-\omega$ *SST* model. There is a significant difference in TKE prediction between the buoyancy-modified $k-\omega$ *SST* model and the stabilized $k-\omega$ *SST* model, but it does not affect the results of free surface elevations and the velocity results at gauges, the results are almost the same between the two turbulence models.

Numerical models give results consistent with previous studies. The standard turbulent models ($k-\varepsilon$, $k-\omega$ *SST*) are demonstrated which results in the exponential growth of the TKE and eddy viscosity [19]. The modified turbulent models (buoyancy-modified $k-\omega$ *SST*, stabilized $k-\omega$ *SST*) significantly reduce the TKE [17–19].

The turbulent kinetic energy is a component of total kinetic energy that will be diffused and dissipated by viscous forces during wave propagation. Therefore, the larger the turbulent kinetic energy, the faster the total kinetic energy decreases, leading to the corresponding decrease in potential energy. As a result, the free surface elevations also decrease [23]. For the $k-\varepsilon$ model, the TKE phenomenon

large to excessive is the cause of wave height decline as discussed in free surface elevations. Consequently, there was no wave breaking as observed in the three other numerical models.

5. Conclusions

In this paper, we analyzed four RANS turbulence models that predicted waves through submerged breakwater using open-source CFD software OpenFOAM with the toolbox waves2foam. In the present study, the results of numerical models are compared to published experimental data, from this, the main conclusions are drawn as follows:

(i) The $k-\varepsilon$ model over-predicts turbulent kinetic energy leading to wave height attenuation during wave propagation through the submerged breakwater.

(ii) The $k-\omega$ *SST* model predicts free surface elevations and velocities pretty well, although the turbulent kinetic energy is still quite large, especially at the fluid field behind the dike, the significant error is the result of the prediction of the secondary wave.

(iii) The buoyancy-modified $k-\omega$ *SST* model and the stabilized $k-\omega$ *SST* model predict free surface elevations and velocities almost the same and agree well with the experimental data, although the turbulence kinetic energy is still significant differences between the two models.

Thus, open-source CFD software OpenFOAM/waves2foam with turbulent models, i.e. the buoyancy-modified $k-\omega$ *SST* and stabilized $k-\omega$ *SST* models, can be applied to simulate the interaction of waves and submerged breakwaters.

Acknowledgments

The author sincerely thanks the financial support of the Hanoi University of Civil Engineering for the research "Study on the wave reduction efficiency of submerged breakwater using numerical method", number 31-2022/KHXD.

References

[1] Lokesha, Kerpen, N. B., Sannasiraj, S. A., Sundar, V., Schlurmann, T. (2015). Experimental Investigations on Wave Transmission at Submerged Breakwater with Smooth and Stepped Slopes. *Procedia Engineering*, 116:713–719.

[2] Ning, D., Chen, L., Zhao, M., Teng, B. (2016). Experimental and Numerical Investigation of the Hydrodynamic Characteristics of Submerged Breakwaters in Waves. *Journal of Coastal Research*, 320: 800–813.

[3] Kubowicz-Grajewska, A. (2016). Experimental investigation into wave interaction with a rubble-mound submerged breakwater (case study). *Journal of Marine Science and Technology*, 22(2):313–326.

[4] jin Liu, B., Cheng, D., chen Sun, Z., zeng Zhao, X., Chen, Y., dong Lin, W. (2019). Experimental and numerical study of regular waves past a submerged breakwater. *Journal of Hydrodynamics*, 31(4):641–653.

[5] Jafarzadeh, E., Kabiri-Samani, A., Mansourzadeh, S., Bohluly, A. (2020). Experimental modeling of the interaction between waves and submerged flexible mound breakwaters. *Proceedings of the Institution of Mechanical Engineers, Part M: Journal of Engineering for the Maritime Environment*, 235(1):127–141.

[6] Kamath, A., Roy, T., Seiffert, B. R., Bihs, H. (2022). Experimental and Numerical Study of Waves Breaking Over a Submerged Three-Dimensional Bar. *Journal of Waterway, Port, Coastal, and Ocean Engineering*, 148(2).

[7] Tuan, V. M., Duong, B., Hung, V. Q., Manh, N. D., Linh, N. M. (2022). Experimental study on the wave dissipation performance of a perforated semi-circular floating breakwater. *Journal of Science and Technology in Civil Engineering (STCE) - HUCE*, 16(3):59–70.

[8] Shen, Y. M., Ng, C. O., Zheng, Y. H. (2004). Simulation of wave propagation over a submerged bar using the VOF method with a two-equation k–ϵ turbulence modeling. *Ocean Engineering*, 31(1):87–95.

[9] Peng, Z., Zou, Q. (2008). Numerical analysis of wave transformation over low-crested impermeable breakwater. In *The Eighteenth International Offshore and Polar Engineering Conference*, OnePetro, 672–677.

[10] Rahman, M. A. (2013). Experimental and Numerical Investigation on Wave Interaction with Submerged Breakwater. *Journal of Water Resources and Ocean Science*, 2(6):155.

[11] Kamath, A., Bihs, H., Chella, M. A., Arntsen, Ø. A. (2015). CFD Simulations of Wave Propagation and Shoaling over a Submerged Bar. *Aquatic Procedia*, 4:308–316.

[12] Liang, B., Wu, G., Liu, F., Fan, H., Li, H. (2015). Numerical study of wave transmission over double submerged breakwaters using non-hydrostatic wave model. *Oceanologia*, 57(4):308–317.

[13] Li, X., Zhang, W. (2019). 3D numerical simulation of wave transmission for low-crested and submerged breakwaters. *Coastal Engineering*, 152:103517.

[14] Srineash, V. K., Kamath, A., Murali, K., Bihs, H. (2020). Numerical Simulation of Wave Interaction with Submerged Porous Structures and Application for Coastal Resilience. *Journal of Coastal Research*, 36 (4):752.

[15] Abdullah, S. F., Fitriadhy, A., Desa, S. M. (2021). Numerical and experimental investigations of wave transmission behind a submerged WABCORE breakwater in low wave regime. *Journal of Ocean Engineering and Marine Energy*, 7(4):405–420.

[16] Xu, T.-J., Wang, X.-R., Guo, W.-J., Dong, G.-H., Hou, H.-M. (2020). Numerical simulation of combined effect of pneumatic breakwater and submerged breakwater on wave damping. *Ships and Offshore Structures*, 17(2):242–256.

[17] Devolder, B., Rauwoens, P., Troch, P. (2017). Application of a buoyancy-modified k-ω SST turbulence model to simulate wave run-up around a monopile subjected to regular waves using OpenFOAM ®. *Coastal Engineering*, 125:81–94.

[18] Devolder, B., Troch, P., Rauwoens, P. (2018). Performance of a buoyancy-modified k-ω and k-ω SST turbulence model for simulating wave breaking under regular waves using OpenFOAM®. *Coastal Engineering*, 138:49–65.

[19] Larsen, B. E., Fuhrman, D. R. (2018). On the over-production of turbulence beneath surface waves in Reynolds-averaged Navier–Stokes models. *Journal of Fluid Mechanics*, 853:419–460.

[20] Jacobsen, N. G., Fuhrman, D. R., Fredsøe, J. (2011). A wave generation toolbox for the open-source CFD library: OpenFoam®. *International Journal for Numerical Methods in Fluids*, 70(9):1073–1088.

[21] Kazakis, I., Karambas, T. V. (2023). Numerical Simulation of Hydrodynamics and Sediment Transport in the Surf and Swash Zone Using OpenFOAM®. *Journal of Marine Science and Engineering*, 11(2):446.

[22] Jin, H., Liu, Y., He, S.-y., Li, H.-j. (2014). Numerical study on the wave dissipating performance of a submerged horizontal plate breakwater using OpenFOAM. In *The Eleventh ISOPE Pacific/Asia Offshore Mechanics Symposium*, OnePetro.

[23] Qu, S., Liu, S., Ong, M. C. (2021). An evaluation of different RANS turbulence models for simulating breaking waves past a vertical cylinder. *Ocean Engineering*, 234:109195.

[24] Brown, S. A., Greaves, D. M., Magar, V., Conley, D. C. (2016). Evaluation of turbulence closure models under spilling and plunging breakers in the surf zone. *Coastal Engineering*, 114:177–193.

[25] Hirt, C. W., Nichols, B. D. (1981). Volume of fluid (VOF) method for the dynamics of free boundaries. *Journal of Computational Physics*, 39(1):201–225.

[26] Schmitt, P., Windt, C., Davidson, J., Ringwood, J. V., Whittaker, T. (2020). Beyond VoF: alternative OpenFOAM solvers for numerical wave tanks. *Journal of Ocean Engineering and Marine Energy*, 6(3): 277–292.

Journal of Science and Technology in Civil Engineering, HUCE (NUCE), 2023, 17 (1): 94–110

UTILIZATION OF ARTIFICIAL LIGHTWEIGHT AGGREGATE AND UNGROUND RICE HUSK ASH AS INTERNAL CURING AGENTS TO MODIFY PERFORMANCE OF SUPER-SULFATED CEMENT MORTAR

Vu-An Tran[a], Hoang-Anh Nguyen[b,*], Bui Le Anh Tuan[a], Duy-Hai Vo[c]

[a]*College of Engineering Technology, Can Tho University, Ninh Kieu district, Can Tho city, Vietnam*
[b]*College of Rural Development, Can Tho University, Ninh Kieu district, Can Tho city, Vietnam*
[c]*Department of Civil Engineering, University of Technology and Education, The University of Danang, Hai Chau district, Danang city, Vietnam*

Article history:
Received 13/01/2023, Revised 19/02/2023, Accepted 16/3/2023

Abstract

This study attempts to utilize cold-bonded fly ash based artificial lightweight aggregate (ALWA) and retrieved unground rice husk ash (URHA) as internal curing (IC) agents for improving performance of typical super-sulfated cement (SSC) mortar fabricated with ternary mixture of 85% slag, 10% gypsum, and only 5% blended Portland cement (PCB). The ALWA partially replacing fine aggregate (FA) at four values of 25, 50, 75, and 100 vol.% was used. For evaluating impact of using hybrid addition of IC agents on performances of SSC mortars, the ALWA amount after being optimized was partially replaced by URHA at four levels of 25, 50, 75, and 100 vol.%. Experimental results showed that, ALWA partially replacing FA up to 50 vol.% led to the SSC mortars with remarkably increased workability and uncompromised impacts on the strengths and durability. Addition of URHA partially replacing ALWA significantly improved the fresh properties and flexural strength but it negatively impacted the durability performances of the resultant SSC mortars in terms of increased water absorption, decreased UPV, and increased drying shrinkage.

Keywords: super-sulfated cement; unground rice husk ash; internal curing; engineering properties; durability

https://doi.org/10.31814/stce.nuce2023-17(1)-08

1. Introduction

Super-sulfated cement (SSC), being typically produced with minuscule content of ordinary Portland cement (OPC) has been used as an alternative binder to the ordinary Portland cement (OPC) in Europe and India due to beneficial effects of simple manufacture, little consumption of natural material and energy and low carbon dioxide emissions [1–4]. In general, the proportions of the SSCs include 80–85% ground granulated blast furnace slag (GGBFS/slag), 10-15% calcium sulfate under different chemical formations and only about 5% OPC/lime serving as the alkaline activator [1, 4]. For formulating the commercial SSCs with adequately high quality, using primary powder, i.e., slag, with sufficiently large amount of alumina has been quintessential, which is possibly unavailable in

*Corresponding author. *E-mail address:* hoanganh@ctu.edu.vn (Nguyen, H.-A.)

widespread areas [5, 6]. Consequently, most of the commercial SSCs has been superseded due to a lack of slag with appropriate chemical composition as aforementioned and/or extra cost induced by advanced chemical treatment applied for raw material [7].

Recently, productions of environmentally friendly SSCs containing calcium sulfate derived from various industrial by-products such as flue gas desulfurization gypsum and circulating fluidized bed combustion ashes receive a serious consideration from the modern cement/concrete industries to persuade the sustainability development [8]. But, the mechanical properties of the low energy SSCs were obviously unsatisfactory to be widely applied for construction fields where the OPC has been properly used [9–11] For enhancing the SSC performance, instead of adapting physicochemical treatment, lowering water content in the SSC proportions seems to be the most preferable consideration to minimize the cost [11], which possibly led to increased risk of shrinkage issue induced by self-desiccation phenomenon as subsequently described [12].

Proper curing regime including appropriate temperature and adequate water supply over certain period of time is significant for hydration of cementitious binder in concrete. Traditional concrete is cured by applying external curing (EC) methods where the water supply coming from surrounding environment plays an important role in maintaining the hydration process of the binder. Currently, high performance concretes become gradually dominant in construction sectors due to a growing focus on durability. By using low water content accompanying with workability modifying chemical admixture, the concrete structure becomes more condensed, which resists water penetration from surrounding environment and thus lowers the efficiency of the EC. As such, continuous hydration of cementitious binder induces reduction of water from capillary pores and thus results in increased internal stress, which is known as self-desiccation phenomenon increasing risk of shrinkage. For overcoming the problem, mitigating reduction of internal humidity in concrete mixture is a quintessential consideration.

Internal curing (IC) has been developed to maintain proper hydration process of cementitious binder by supplying internal water reservoirs in concrete mixture without impacts on the workability and hardened performance of the resultant concrete. Therefore, IC is considered as an effective technique to resolve the issue related to high autogenous shrinkage of concrete, especially the high performance concrete. In general, tremendous types of appropriate porous materials such as superabsorbent polymer (SAP) [13], wood fibers [14], rice hush ash (RHA) [15], mixture of aerated concrete blocks (ACB) and sintered clay bricks (SCB) [16], and lightweight fine aggregate (LWFA) derived from either natural [17, 18], or artificial productions [19–21] have been successfully applied for IC concretes. Among the aforementioned IC agents, LWFA seems to be a preferable choice due to the specialized benefits of simple manufacture and easy quality control. Since the 1950s, excellent effect of utilizing saturated LWFA based IC agent as partial replacement of conventional fine aggregate (FA) has been identified [22, 23]. Apparently, commercially available expanded shale, clay, and slate based LWFAs have been widespread used for improving shrinkage of ultra-high performance concrete [24, 25]. In addition, LWFA produced with compaction of alkali-activated bottom coal ash [26] was also utilized in IC concrete. Currently, cold-bonded fly ash based artificial lightweight aggregate (ALWA) with low energy consumption could be a promising alternative IC agent to ramp up sustainability concept, but its' applicability seems to be limited as coarse aggregate fraction in concrete productions [27, 28].

According to above review points, although beneficial effects of different IC agents on enhanced performance of concrete have been well-understood, an existing gap associated with impact of IC on performance of modified green cement, particularly emphasizing on SSC, is still unaware. Moreover,

applicability of simultaneous using of cold-bonded fly ash LWFA and URHA as the IC agents has been also unexplored. Therefore, this study attempts to initially evaluate comprehensive performance of the SSC mortars modified with hybrid utilization of these two IC agents in order to fulfill the database related to IC modified low energy binder. Alternately, the significance of the current study is also expanded to lay an essential foundation for persuading concept of sustainability development by maximizing additions of low energy materials such as cold-bonded fly ash LWFA and URHA in concrete/mortar productions which were effectively applied for construction fields where the superior resistance to sulfate attach was seriously required.

2. Experimental program

2.1. Materials

Commercial products of blended Portland cement (PCB) and gypsum and industrial by-products of low calcium Class F fly ash (FFA) and ground granulated blast furnace slag (GGBFS/slag) were used for manufacturing the ALWA and SSC binder. The physicochemical properties and mineral compositions of the raw materials were detected using X-ray fluorescence (XRF) and X-ray powder diffraction as shown in Table 1 and Fig. 1, respectively. Accordingly, PCB was primarily comprised of CaO rich alite and belite crystals. On the other hand FFA was mostly comprised of mullite and quartz crystals which were rather stable in low to mid concentration of alkali. Different from FFA, GGBFS mostly contained calcium and magnesium oxides and tremendous amount of amorphous silica and alumina, which was assigned to the high reactive pozzolanic material (Table 1 and Fig. 1). The features of the raw materials' particles were shown in Fig. 2. Accordingly, the FFA particles were mostly spherical shapes when compared with the irregular shapes of the others. For manufacturing control SSC mortar, natural fine aggregate (FA) with specific gravity of 2.68, fineness modulus (FM) of 1.32 and water absorption of 1.5% was used. The particle size distribution of FA was conducted based on TCVN 7572-2 [29] as shown in Table 2, illustrating that the FA contained rather high fraction of fine particles. For evaluating effect of internal curing (IC) on SSC mortar performance, both cold-bonded fly ash artificial light weight aggregate (ALWA) and retrieved unground rice husk

Table 1. Physical properties and chemical compositions of the raw materials

	Slag	Class F fly ash	Portland cement	Gypsum	URHA
Specific gravity	2.86	2.13	3.05	2.68	1.28
Water absorption, %					44
SiO_2, %	38.01	58.77	22.45	-	> 95%
Al_2O_3, %	13.13	26.11	6.81	-	
Fe_2O_3, %	0.55	5.61	3.15	-	
CaO, %	36.80	2.07	60.03	-	
MgO, %	5.77	1.66	2.08	-	
SO_3, %	1.36	0.21	2.77	-	
Na_2O, %	0.13	0.27	0.55	-	
K_2O, %	0.78	1.48	0.79	-	
TiO_2, %	0.45	0.66	0.41	-	
L.O.I, %	3.01	3.11	0.95	-	

ash (URHA) were also used. The manufacturing process applied for ALWA was just subsequently described.

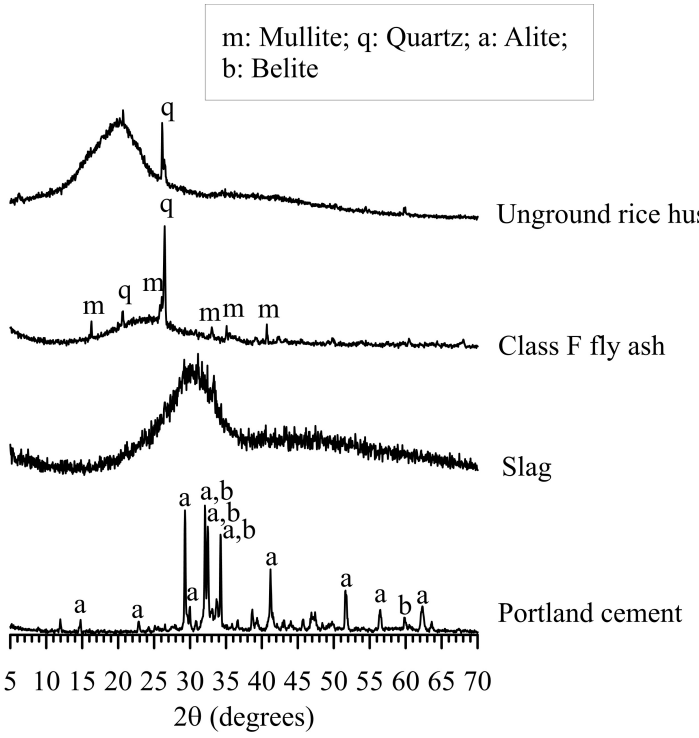

Figure 1. XRD patterns of raw materials

Table 2. Particles size distributions of fine aggregate (FA)

Sieve size (mm)	Retaining amount (%)	Accumulated retaining amount (%)	Limit ranges suggested by TCVN 7572-2	
			Coarse FA	Fine FA
5	0	0	-	-
2.5	0.05	0.05	0-20	0
1.25	0.1	0.15	15-45	0-15
0.630	0.5	0.65	35-70	0-35
0.315	34.15	34.8	65-90	5-65
0.140	61.95	96.75	90-100	65-90
Bottom	3.25	100	90-100	65-100

2.2. Preparation and characteristics of the ALWA

The ALWA proportion was comprised of 90% FFA and 10% OPC by mass. The fundamental manufacturing process of ALWA was based on the cold-bonded agglomeration as previously described [27, 28] as shown in Fig. 3. After being agglomerated, the ALWA products were suffered from a curing regime of temperature of 27°C and RH of 95% for 28 days. After that, the hardened

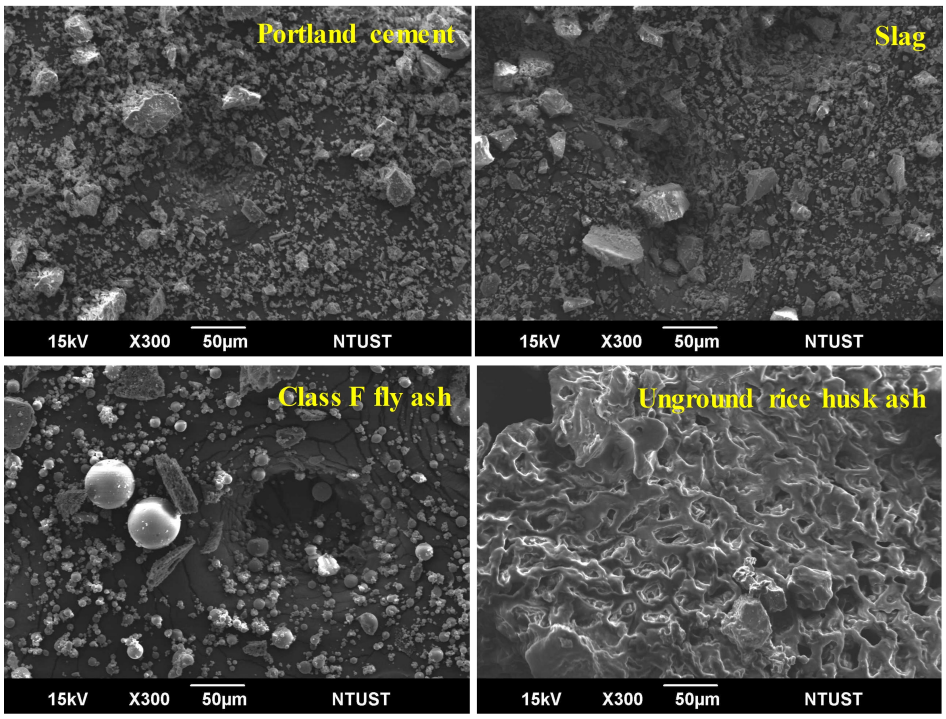

Figure 2. SEM images of the raw materials

ALWA particles were sieved to remove the particles with the sizes larger than 5 mm, and then used for producing mortars. In this study, the dried density of the ALWA being conducted according to TCVN 6221 [30] was 943 kg/m^3 which was in range of 500-1000 kg/m^3 normally assigned to the aggregates used for concrete productions as suggested by TCVN 6220. The particle size distribution of the ALWA was conducted in accordance to TCVN 6221 [30] and shown in Table 3, indicating its' applicability for only nonstructural insolating concretes as suggested by TCVN 6220. The fineness modulus (FM) of the ALWA was 4.86. In addition the water absorption of the ALWA complying with TCVN 7572-4:2006 [31] was 18% which was in range of 6-31% assigned to satisfactory IC agent as previously suggested [25]. As such, instead of being suffered a suitable surface treatment for improving water absorption as previously reported [27], the untreated ALWA was directly used for mortar manufacture in order to cut the cost.

Figure 3. Manufacture process of ALWA

2.3. Mix proportions

The binding powders of all SSC mortars were comprised of 5% PCB, 10% gypsum, and 85% slag by mass. The water-to-powder ratio (w/p) fixed at 0.4 was used for all SSC mortars. To produce the reference SSC mortar, mass ratio of FA to binder was fixed at 2.0. For evaluating effect of internal curing (IC) on SSC mortar performance, ALWA was used as partial replacement of FA at four values of 25, 50, 75, and 100% by volume. In this study, the dried density as mentioned in Section 2.2 was used to identify the volume of the ALWA. After being optimized based on mechanical strengths, the ALWA amount was partially replaced by URHA at four values of 25, 50, 75, and 100% by volume to assess the synergistic impact of binary addition of the IC agents on the properties of the SSC mortars.

In this study, ALWA was firstly soaked in water for 30 min to reach the stage of saturated surface dry before being used as previous suggestion [27]. The proportions of the SSC mortars are shown in Table 4.

2.4. Specimen preparation and test methods

Immediately after being mixed, the fresh SSC mortars were tested for the slump flow by applying flow table equipment and unit weight in accordance to TCVN 3121-3 [32] and TCVN 3108 [33], respectively. To estimate the hardened properties of the SSC mortars, the tests on dried density complying with TCVN 3121-10 [34], compressive and flexural strengths according to TCVN 3121-11 [35], UPV complying with TCVN 9357:2012 [36], and water absorption according to TCVN 3121-18 [37] using the prismatic specimens with dimensions of 40×40×160 mm^3. At the ages of testing, each mortar sample used for the dried density test was dried in oven to reach a so-called stable weight and identified the volume based on measuring the samples' dimensions. The dried density then calculated as ratio of the stable weight to the volume. For the test of water absorption, the stable weight of the sample under saturated state obtained by water immersion was used. The samples applied for testing on the flexural and compressive strengths were suffered from 3-point bending and compressing processes. The strengths were defined as the failure stresses acting on the cross sections of the tested samples. The UPV was identified by dividing length of tested sample by time detected by the commercial ultrasonic transducer. On the other hand, the prisms with dimensions of 25×25×285 mm^3 were cast for the test on drying shrinkage according to TCVN 8824:2011 [38]. After being cast and

Table 3. Particles size distribution of ALWA

Sieve size (mm)	Retaining amount (%)	Accumulated retaining amount (%)	Limit ranges suggested by TCVN 6220 for different applications		
			Load bearing	Load bearing and heat and acoustic isolation	Heat and acoustic isolation
5	0	0	0-10	0-10	-
2.5	89.8	89.8	-	-	-
1.25	8.3	98.1	20-60	30-50	-
0.630	0.95	99.05	-	-	-
0.315	0.3	99.35	45-80	65-90	-
0.160	0.15	99.5	70-90	90-100	-
Bottom	0.5	100	-	-	-

Table 4. Mix proportions of SSC mortars with different ingredients

Mixes	Slag	Gypsum	Portland cement	Sand	ALWA	URHA	Water
L0	566	67	33	1333	-	-	267
L25	566	67	33	1000	211	-	267
L50	566	67	33	667	421	-	267
L75	566	67	33	333	632	-	267
L100	566	67	33	-	843	-	267
L50R25	566	67	33	667	316	80	267
L50R50	566	67	33	667	211	159	267
L50R75	566	67	33	667	105	239	267
L50R100	566	67	33	667	-	318	267

Note: ALWA = Artificial lightweight aggregate; URHA = Unground rice husk ash.

cured at ambient temperature for 24 hours, the hardened mortar samples were removed and cured in air at 27±2 °C and 65% RH until the ages of tests.

3. Results and discussions

3.1. Workability

The workability of the fresh SSC mortars was summarized and feasibly illustrated in Table 5 and Figs. 5–5, respectively.

Table 5. Fresh properties of SSC mortars with different ingredients

Mixes	ALWA:Sand	URHA:Sand	Flow diameter, cm	Unit weight, kg/m^3
L0	0:100	-	14	2123
L25	25:75	-	16	2009
L50	50:50	-	16	1975
L75	75:25	-	14.5	1694
L100	100:0	-	14.5	1637
L50R25	-	25:75	18	1864
L50R50	-	50:50	16.5	1811
L50R75	-	75:25	17	1694
L50R100	-	100:0	17	1669

Note: ALWA = Artificial lightweight aggregate; URHA = Unground rice husk ash.

Accordingly, flowing diameters of the fresh SSC mortars with/without the IC agents consisting of ALWA and URHA were in range of 14-18 cm. Addition of ALWA partially replacing FA in range of 0-50 vol.% increased the flowing diameters of the fresh SSC mortars, which was possibly attributed to both the improved grading of particle size distribution and the reduced interfacial friction induced by spherical shapes of the ALWA particles. But, further increase of the ALWA partially replacing FA in range of 75-100 vol.%, slightly decreased the workability of the fresh SSC mortars due to minor decrease in flowing diameter. Such result was possibly due to excessive amount of coarser ALWA

(a) L0 mix

(b) L25 mix

(c) L50 mix

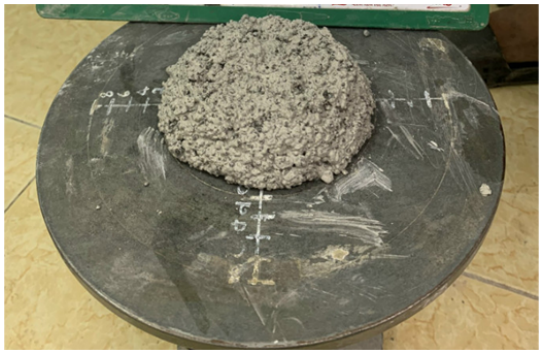

(d) L75 mix

(e) L100 mix

Figure 4. Effect of ALWA on workability of fresh SSC mortars

when compared with FA particles resulted in increasing paste demand for achieving the workability of the fresh SSC mortars. In this study, ALWA partially replacing FA in range of 25-50 vol.% induced the fresh mortars with the best flowing ability due to the highest flowing diameters. By fixing amount of ALWA at desired value of 50 vol.% as partial replacement of FA, addition of URHA partially replacing FA in range of 25-100 vol.% decreased the flowing diameters of the fresh SSC mortars. Such result was primarily attributed to the irregular shapes of the URHA in comparison with the spherical shapes of the ALWA. In addition, the severely rough surface of the porous URHA particles was also a considerable factor inducing the reduction on workability of the fresh SSC mortars due to

an increased interfacial friction among ingredients. However, when compared with the reference SSC mortar without IC agents, the IC-SSC with various amount and ingredients of the IC agents still had the better workability due to the higher values of flowing diameters, which was just opposite to the performance of the fresh IC mortar containing recycling aerated concrete block (ACB) and sintered clay brick (SCB) as previously shown [16]. Accordingly, the incorporation of ACB and SCB agents resulted in the reduced workability of the fresh IC mortars, which was possibly due to irregular shapes of these two materials. In addition, as suggested by the authors, the reduced workability of the fresh IC mortars was also attributed to the fast initial absorption of the fine particles with increases in surface area and porosity.

(a) L50 mix

(b) L50R25 mix

(c) L50R50 mix

(d) L50R75 mix

(e) L50R7100 mix

Figure 5. Effect of URHA on workability of fresh SSC mortars

3.2. Unit weight and dried density

The properties including unit weight and dried density of the fresh SSC mortars are shown in Fig. 6. As illustrated from the figure, the unit weight and the dried density of the fresh and hardened SSC mortars were in the ranges of 1637-2123 kg/m^3 and 1605-1926 kg/m^3, respectively. The ALWA partially replacing FA respectively significantly decreased the unit weight and dried density of the fresh and hardened SSC mortars. Such result was possibly due to the fact that the specific gravity of the ALWA was 0.943 as shown in Section 2.2 lower than the value of 2.68 of the FA as shown in Section 2.1. Especially, utilization of URHA as partial replacement of ALWA further decreased the unit weight and dried density of the fresh and hardened SSC mortars, respectively, which was primarily attributed to the porous structure of URHA particles. The obtained experimental result apparently indicated a beneficial effect of using the IC agents, particularly URHA, on reducing self-weight of the construction structures and thus reducing the construction cost. Obviously, the degrees of porosity of the IC agents was the crucial factor affecting the density of the resultant mortars, which was also mentioned in the previous publication [16].

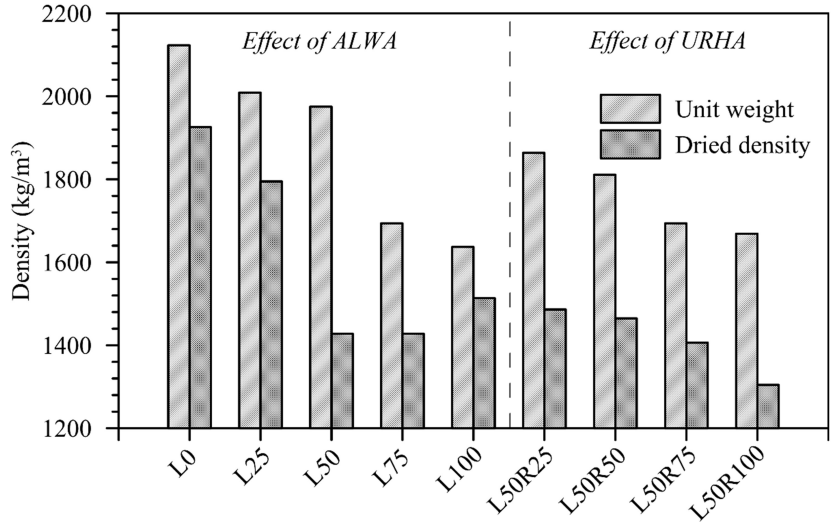

Figure 6. Dried density of the hardened super-sulfated cement

3.3. Compressive strength

The compressive strengths of the hardened SSC mortars was shown in Fig. 7. As being expected, the compressive strengths increased with the curing ages due to the enhanced degree of binder hydration. Generally, the compressive strengths of the SSC mortars decreased with the increased amount of ALWA partially replacing FA in range of 0-100 vol.%, which was primarily attributed to the lower mechanical performance of the ALWA particles in comparison with the FA particles. However, the observed result in Fig. 7 indicated that the SSC mortar containing ALWA partially replacing FA at 25 vol.% had the compressive strengths comparable to those of the reference SSC mortar without addition of IC agents at all ages of curing. At 28 days of curing, when compared with the reference SSC mortar, ALWA partially replacing FA at up to 50 vol.% insignificantly impacted the compressive strength of the IC modified SSC mortar due to minor strength reduction of 10.7%. Increased amount of ALWA addition at 75-100 vol.% replacing FA was associated with excessive amount of coarser

ALWA and thus resulted in lack of binder volume to fill the voids generated by poor packed aggregates. On the other hand, by fixing the ALWA amount at 50 vol.% as partial replacement of FA, using URHA as partial replacement of ALWA in range of 0-100 vol.% continuously decreased the compressive strengths of the hardened SSC mortars. Such result was attributed to the porous structure skeleton of the URHA particles.

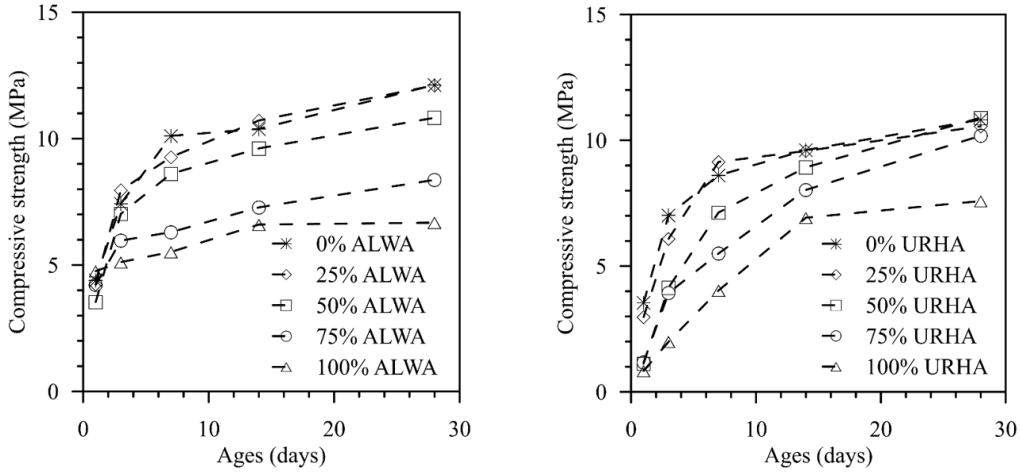

(a) 0% URHA (b) 50% ALWA

Figure 7. Compressive strengths of the hardened super sulfated cement mortars

But, addition of URHA replacing ALWA at up to 75 vol.% unremarkably influenced 28-day compressive strength of the hardened SSC mortars as shown in Fig. 7(b), possibly due to the improved packing condition of the aggregates induced by filling effect of the URHA particles. Further increased addition of URHA replacing ALWA at 100 vol.% dramatically decreased the compressive strengths of the hardened SSC mortars, particularly at 28 days, due to excessive amount of fine particles led to lack of binding paste volume. As results, in this study, to produce the IC-SSC mortars with compromised 28-day compressive strength, the volume of IC agents replacing FA needed to be limited at 50 vol.% in which the volume ratio of URHA: ALWA was possibly varied at values from 0:100 to 75:25. Obviously, the suggested amount of the IC agents, i.e., up to 50 vol.% replacing FA, as obtained in this study was farther from the optimum around 10 vol.% of IC mortars containing aerated concrete block (ACB) and sintered clay brick (SCB) as suggested in previous studies [16], probably due to the differences in the binder and IC based aggregates usages. Probably, the SSC demanded more water for maintaining continuous hydration when compared with various SCM binders. However, as commercial ALWA was applied for IC concrete production [24], the optimum of IC agents replacing FA was even as high as 60 vol.% which was higher than value of 50 vol.% as obtained in this study, possibly due to the better physical properties of the commercial ALWA.

3.4. Flexural strength

The flexural strengths of the hardened SSC mortars with/without IC agents including ALWA and URHA at 28 days are shown in Fig. 8. In consistence with the compressive strength result, ALWA addition partially replacing FA at up to 50 vol.% insignificantly impacted 28-day flexural strength of the hardened IC-SSC mortar, but further increased amount of ALWA replacing FA at 75-100 vol.%

induced the IC-SSC mortars with significant fluctuation on the 28-days flexural strengths. On the other hand, when the ALWA amount was fixed at 50 vol.% as partial replacement of FA, the addition of URHA substituting ALWA at up to 100 vol.% gradually increased the 28-day flexural strengths of the hardened IC-SSC mortars. Particularly, the highest 28-day flexural strength of the hardened IC-SSC mortar was observed as URHA was set at 50 vol.% as a partial replacement of the ALWA. The result was possibly explained based on the improvement on interfacial transition zone (ITZ) attributed to the IC effect. As previously clarified [24], the presence of ALWA led to maintaining the internal relative humidity, which was favorable to the processing hydration of the binders and thus contributed to the pore refinement induced by higher polymerization degree of C-S-H precipitation.

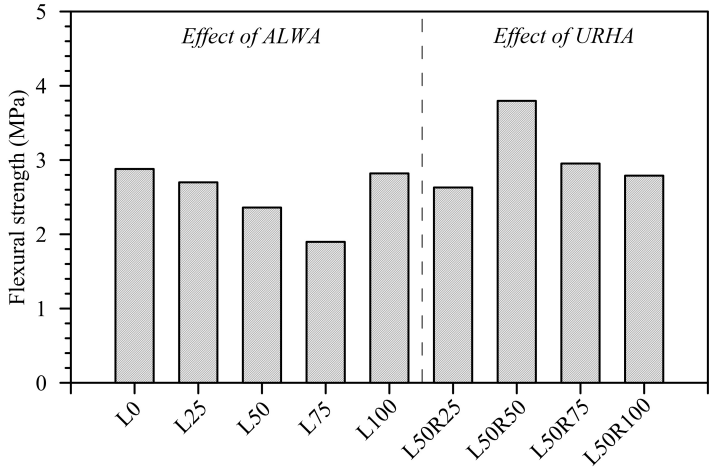

Figure 8. Flexural strengths of the hardened super sulfated cement mortars at 28 days

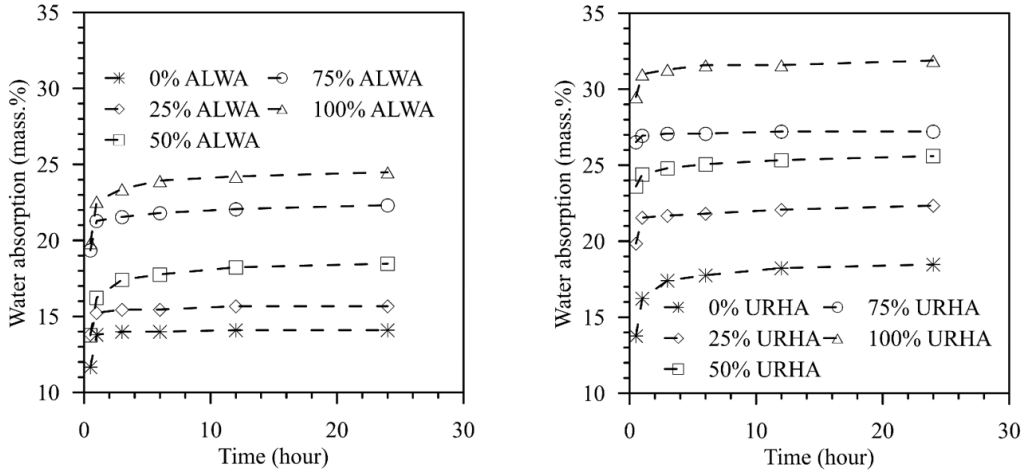

(a) 0% URHA (b) 50% ALWA

Figure 9. Water absorption performances of the hardened super sulfated cement mortars

3.5. Water absorption

The water absorption performances of the hardened SSC mortars are shown in Fig. 9. The figure indicated that water absorption rates of the hardened SSC mortars with/without IC agents consisting of ALWA and URHA primarily gained during initial 6 hours. In general, addition of IC agents including either sole amount of ALWA or mixture of ALWA and URHA dramatically increased the water absorption of the hardened SSC mortars. Such result was possibly attributed to the high absorptivity of the IC agents. According to the previous study [16], incorporation of the porous IC agents resulted in the resultant mortars with increased porosity, which also corresponded to the mortar specimens with increased water absorption. As such, addition of the porous structure URHA particles was more favorable to the generation of porosity and thus more severely increased the water absorption of the IC-SSC mortars when compared with the effect of using ALWA in IC-SSC mortars. For alleviating the water absorption increment, the IC agent amount should be limited at 25 vol.% as partial substitution of FA. In addition, using URHA was improper for improving the water absorption of the IC-SSC mortars.

3.6. UPV

Effects of adding IC agents on the UPV of the hardened SSC mortars are illustrated in Fig. 10. Accordingly, the obtained UPV result was in good consistence to the observation on the water absorption performance as previously discussed. Indeed, the UPV values of the hardened SSC mortars significantly decreased with increased amount of the IC agents including ALWA and URHA. Such result was due to the decreased dried density of the mortar samples induced by the porous structures of the IC agents, which was clarified in the UPV-dried density relationship as shown in Fig. 11.

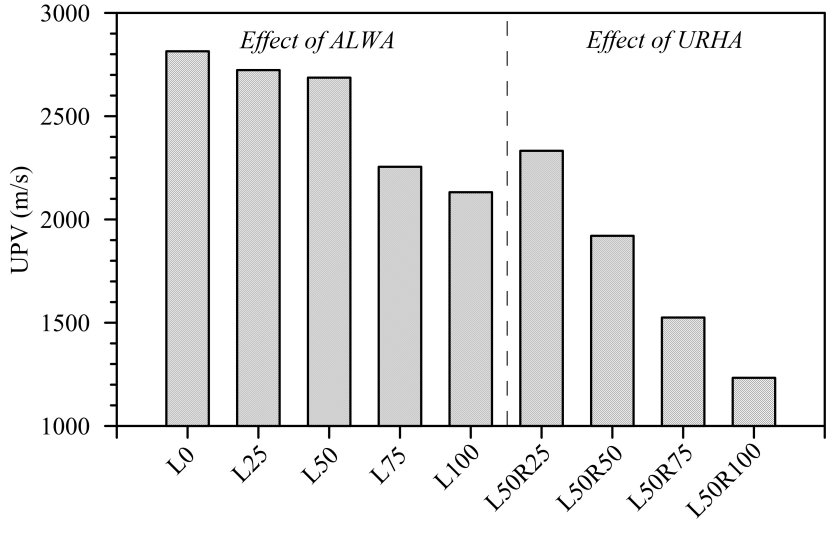

Figure 10. UPV of the hardened super sulfated cement mortars at 28 days

Accordingly, Fig. 11 showed that generally the higher value of dried density was associated with the specimen with the higher UPV value. Particularly, more negative impact on UPV of the hardened mortar samples on addition of URHA when compared with the ALWA addition was obviously obtained. Reasonably, the URHA particles owned porous structure being unfavorable to the ultrasonic

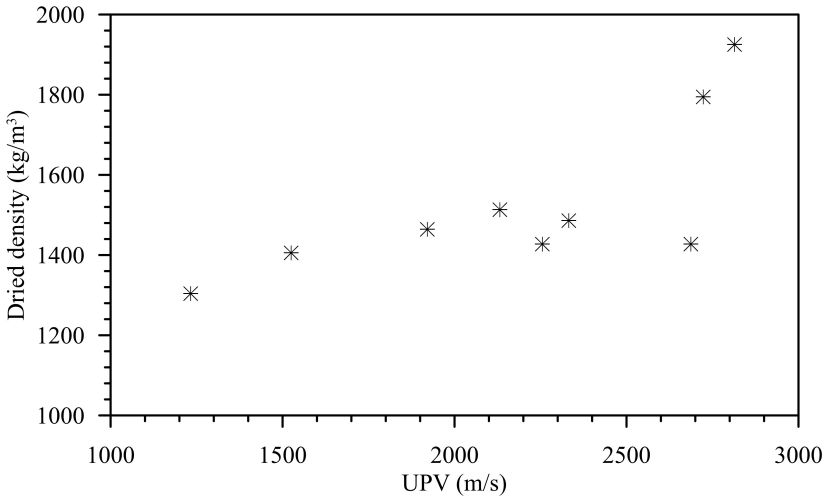

Figure 11. Relationship between UPV and dried density of the hardened super sulfated cement mortars

pulse transmission and thus illustrated a negative influence on the UPV value of the hardened IC-SSC mortars. For producing the IC-SSC mortars without compromised UPV values, sole addition of ALWA partially replacing FA at up to 50 vol.% should be considerably used. Such result was probably due to the pozzolanic reaction between the IC agents and alkali pore solution tended to reduce the porosity in the interfacial transition zones as previously suggested [16] and thus improved the UPV transmission.

3.7. Drying shrinkage

The drying shrinkage of the hardened SSC mortars with/without the IC agents is shown in Fig. 12. In general, the drying shrinkage values increased with increased ages of curing due to an accumulated evaporation of water from the mortar specimens into air. As being expected, the addition of the ALWA at saturated state alleviated the self-desiccation effect and thus decreased the drying shrinkage of the hardened SSC mortars at early. At later, increase of the ALWA replacing FA in range of 25-75 vol.% capriciously affected the drying shrinkage of the hardened IC-SSC mortars but the shrinkage discrepancy between the reference and IC-SSC mortars was just minor, which was probably attributed to self-assembling effect on aggregate mixture [16]. But, further increase of ALWA replacing FA at 100 vol.% slightly reduced drying shrinkages of the IC-SSC mortars when compared with the reference mortar, which was probably due to the pozzolanic activity of the ALWA tended to reduce the porosity in the interfacial transition zones and thus lowered the shrinkage observations [16]. On the other hand, when the ALWA amount was set at 50 vol.% as partial substitution of FA, increased addition of URHA partially replacing ALWA resulted in the hardened IC-SSC mortars with increased drying shrinkage, which was due to the lower elastic moduli and volume stability of the porous URHA in comparison with the ALWA [16]. In addition, the URHA with porous structures seemed to be vulnerable to the self-assembling effect. Moreover, the pozzolanic reactivity of URHA was normally too low, as clarified in the previous publication [39], to sufficiently compensate the long-term drying shrinkage of the mortar samples. For alleviating the drying shrinkage increment of the mortar specimens, addition of URHA as partial replacement of ALWA should be limited at 25 vol.%. In the previous study [16], aerated concrete blocks (ACB) and sintered clay bricks (SCB) with high water absorption were explored to serve as IC agents in mortars. Accordingly, hybrid addition of ACB and SCB considerably

compensated the negative effect of sole addition of ACB on the drying shrinkage of the hardened mortars, which was obviously different from the result observed from the current study. Such result was possibly due to the stronger structural skeletons of the ACB-SCB mixture when compared with those of ALWA-URHA mixture.

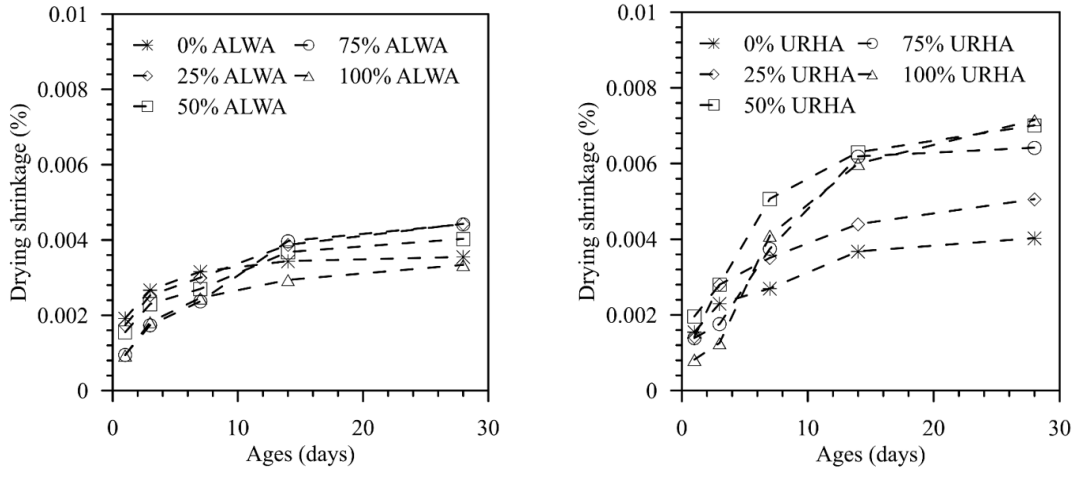

(a) 0% URHA (b) 50% ALWA

Figure 12. Drying shrinkage of the hardened super sulfated cement mortars

4. Conclusions

Effects of cold-bonded fly ash agglomeration based artificial lightweight aggregate (ALWA) and retrieved unground rice husk ash (URHA) acting as internal curing (IC) agents on the engineering and durability performances of a typical super-sulfated cement (SSC) mortars have been explored. According to the observed experimental results, the following conclusions should be drawn:

1. The workability, unit weight, and dried density of the SSC mortars containing various amount and ingredients of IC agents partially replacing fine aggregate (FA) in range of 25-100 vol.% were significantly improved, particularly as URHA was used.

2. The increased amount of the IC agents including ALWA and URHA decreased compressive strengths of the hardened SSC mortars. The hardened SSC mortars containing ALWA as partial substitution of FA up to 50 vol.% had the 28-day compressive strength unremarkably reduced when compared with the reference mortar without IC agents. Addition of URHA partially substituting ALWA gradually reduced the compressive strength of the hardened SSC mortars. The URHA addition was possibly considered at lower than 50 vol.% for alleviating the compressive strength reduction.

3. The flexural strengths of the hardened SSC mortars decreased with increased amount of ALWA partially replacing FA in range of 0-100 vol.%. By fixing amount of ALWA at selected value of 50 vol.% partially replacing FA, addition of URHA partially replacing ALWA in range of 25-100 vol.% positively improved the flexural strength of the hardened SSC mortars. 50 vol.% of URHA replacing ALWA was the optimum value due to the maximum flexural strength of the hardened IC-SSC mortars.

4. The increase of ALWA addition replacing FA in range of 0-100% unremarkably impacted or slightly improved drying shrinkage but significantly decreased the durability performances in terms of increased water absorption and decreased UPV. The URHA addition partially replacing ALWA

negatively impacted the durability performances of the hardened SSC mortars in terms of decrease in UPV and increases in drying shrinkage and water absorption. The utilization of URHA replacing ALWA should be limited at 25 vol.% for alleviating the durability issues.

Acknowledgement

The authors would like to acknowledge the financial aid from Can Tho University, through research grant of T2021-106, for this investigation.

References

[1] Dutta, D. K., Borthakur, P. C. (1990). Activation of low lime high alumina granulated blast furnace slag by anhydrite. *Cement and Concrete Research*, 20(5):711–722.

[2] Gruskovnjak, A., Lothenbach, B., Winnefeld, F., Figi, R., Ko, S.-C., Adler, M., Mäder, U. (2008). Hydration mechanisms of super sulphated slag cement. *Cement and Concrete Research*, 38(7):983–992.

[3] Midgley, H. G., Pettifer, K. (1971). The micro structure of hydrated super sulphated cement. *Cement and Concrete Research*, 1(1):101–104.

[4] Singh, M., Garg, M. (2002). Calcium sulfate hemihydrate activated low heat sulfate resistant cement. *Construction and Building Materials*, 16(3):181–186.

[5] Juenger, M. C. G., Winnefeld, F., Provis, J. L., Ideker, J. H. (2011). Advances in alternative cementitious binders. *Cement and Concrete Research*, 41(12):1232–1243.

[6] da Luz, C. A., Hooton R., D. (2015). Influence of curing temperature on the process of hydration of supersulfated cements at early age. *Cement and Concrete Research*, 77:69–75.

[7] Imbabi, M. S., Carrigan, C., McKenna, S. (2012). Trends and developments in green cement and concrete technology. *International Journal of Sustainable Built Environment*, 1(2):194–216.

[8] Chen, C.-T., Nguyen, H.-A., Chang, T.-P., Yang, T.-R., Nguyen, T.-D. (2015). Performance and microstructural examination on composition of hardened paste with no-cement SFC binder. *Construction and Building Materials*, 76:264–272.

[9] Nguyen, H.-A., Chang, T.-P., Lee, P.-H., Shih, J.-Y. (2020). Experimental Investigation of Bond-Slip Performance of Reinforcement in Two Green Concretes. *Journal of Materials in Civil Engineering*, 32 (3).

[10] Nguyen, H.-A., Chang, T.-P., Shih, J.-Y., Chen, C.-T., Nguyen, T.-D. (2016). Sulfate resistance of low energy SFC no-cement mortar. *Construction and Building Materials*, 102:239–243.

[11] Chang, T.-P., Nguyen, H.-A., Chen, C.-T., Yang, T.-R., Nguyen, T.-D. (2015). Physical-chemical characteristics of an eco-friendly binder using ternary mixture of industrial wastes. *Materiales de Construcción*, 65(319):e064.

[12] Nguyen, H.-A., Tran, V.-A. (2022). Influence of artificial lightweight aggregate on property modification of unfired brick with low energy super-sulfated cement. *Journal of Science and Technology in Civil Engineering (STCE) - HUCE*, 16(1):126–137.

[13] Wang, F., Yang, J., Hu, S., Li, X., Cheng, H. (2016). Influence of superabsorbent polymers on the surrounding cement paste. *Cement and Concrete Research*, 81:112–121.

[14] Mohr, B., Premenko, L., Nanko, H., Kurtis, K. (2005). Examination of wood-derived powders and fibers for internal curing of cement-based materials. In *Proceedings of the 4th Interntational Seminar: Self-Desiccation and Its Importance in Concrete Technology*, 229–244.

[15] Tuan, N. V., Ye, G., van Breugel, K. (2010). Internal curing of ultra high performance concrete by using rice husk ash. In *International RILEM Conference on Material Science, RILEM Publications SARL Paris, France*, 265–274.

[16] Liu, Q., Singh, A., Xiao, J., Li, B., Tam, V. W. Y. (2020). Workability and mechanical properties of mortar containing recycled sand from aerated concrete blocks and sintered clay bricks. *Resources, Conservation and Recycling*, 157:104728.

[17] Zhutovsky, S., Kovler, K., Bentur, A. (2002). Efficiency of lightweight aggregates for internal curing of high strength concrete to eliminate autogenous shrinkage. *Materials and Structures*, 35(2):97–101.
[18] Alaskar, A., Alshannag, M., Higazey, M. (2021). Mechanical properties and durability of high-performance concrete internally cured using lightweight aggregates. *Construction and Building Materials*, 288:122998.
[19] Lura, P., Wyrzykowski, M., Tang, C., Lehmann, E. (2014). Internal curing with lightweight aggregate produced from biomass-derived waste. *Cement and Concrete Research*, 59:24–33.
[20] Cusson, D., Hoogeveen, T. (2008). Internal curing of high-performance concrete with pre-soaked fine lightweight aggregate for prevention of autogenous shrinkage cracking. *Cement and Concrete Research*, 38(6):757–765.
[21] Bentur, A., ichi Igarashi, S., Kovler, K. (2001). Prevention of autogenous shrinkage in high-strength concrete by internal curing using wet lightweight aggregates. *Cement and Concrete Research*, 31(11): 1587–1591.
[22] Klieger, P. (1969). *Early high-strength concrete for prestressing*.
[23] Bloem, D. L., Gaynor, R. D. (1965). Concrete strength measurement-cores versus cylinders. In *Aterials Research and Standards, Materials Research Society 506 Keystone DR, Warrendale, PA*, volume 5, page 258.
[24] Shen, P., Lu, J.-X., Lu, L., He, Y., Wang, F., Hu, S. (2021). An alternative method for performance improvement of ultra-high performance concrete by internal curing: Role of physicochemical properties of saturated lightweight fine aggregate. *Construction and Building Materials*, 312:125373.
[25] Castro, J., Keiser, L., Golias, M., Weiss, J. (2011). Absorption and desorption properties of fine lightweight aggregate for application to internally cured concrete mixtures. *Cement and Concrete Composites*, 33(10):1001–1008.
[26] Balapour, M., Zhao, W., Garboczi, E., Oo, N. Y., Spatari, S., Hsuan, Y. G., Billen, P., Farnam, Y. (2020). Potential use of lightweight aggregate (LWA) produced from bottom coal ash for internal curing of concrete systems. *Cement and Concrete Composites*, 105:103428.
[27] Hwang, C.-L., Tran, V.-A. (2015). A study of the properties of foamed lightweight aggregate for self-consolidating concrete. *Construction and Building Materials*, 87:78–85.
[28] Hwang, C.-L., Tran, V.-A. (2016). Engineering and Durability Properties of Self-Consolidating Concrete Incorporating Foamed Lightweight Aggregate. *Journal of Materials in Civil Engineering*, 28(9).
[29] TCVN 7572-2 (2006). *Aggregates for concrete and mortar - Test methods - Part 2: Determination of partical zise distribution*.
[30] TCVN 6221 (1997). *Lightweight aggregates for concrete - Expanded clay, gravel and sand - Test methods*.
[31] TCVN 7572-4 (2006). *Aggregates for concrete and mortar - Test methods - Part 4: Determination of apparent specific gravity, bulk specific gravity and water absorption*.
[32] TCVN 3121-3 (2003). *Mortar for masonry - Test methods - Part 3: Determination of consistence of fresh mortar (by flow table)*.
[33] TCVN 3108 (1993). *Heavyweight concrete compounds - Method for determination of density*.
[34] TCVN 3121-10 (2003). *Mortar for masonry - Test methods - Part 10: Determination of dry bulk density of hardened mortars*.
[35] TCVN 3121-11 (2003). *Mortar for masonry - Test methods - Part 11: Determination of flexural and compressive strength of hardened mortars*.
[36] TCVN 9357 (2012). *Normal concrete - Nondestructive methods - Assessment of concrete quality using ultrasonic pulse velocity*.
[37] TCVN 3121-18 (2003). *Mortar for masonry - Test methods - Part 18: Determination of water absorption of hardened mortars*.
[38] TCVN 8824 (2011). *Cements - Test method for drying shrinkage of mortar*.
[39] Van, V.-T.-A., Rößler, C., Bui, D.-D., Ludwig, H.-M. (2013). Mesoporous structure and pozzolanic reactivity of rice husk ash in cementitious system. *Construction and Building Materials*, 43:208–216.

Journal of Science and Technology in Civil Engineering, HUCE (NUCE), 2023, 17 (1): 111–124

A STUDY ON THE PROBABILISTIC SAFETY ASSESSMENT OF THE TRUSS STRUCTURE DESIGNED BY THE LRFD CODE

Nhu Son Doan[a,*]

[a]*Faculty of Civil Engineering, Vietnam Maritime University, 484 Lach Tray street, Le Chan district, Haiphong*

Article history:
Received 12/12/2022, Revised 11/01/2023, Accepted 16/01/2023

Abstract

The probabilistic analyses provide a more rational approach for the safety assessment of structures since they consider the uncertainties in the calculations. Consequently, the design specifications of engineering structures are gradually transformed from the allowable stress design to the reliability-based specifications such as load and resistance factors design (LRFD) or partial safety factor design. The partial safety factors and the load and resistance factors provided in the reliability-based design codes are successfully determined from probabilistic frameworks. However, these specifications are classified into semi-probabilistic-based codes because no probabilistic analysis is required in the design practice. Thus, the actual reliability index of the design solutions may not be as close to the target value as expected. This study employs the fully probabilistic analysis as an additional analysis to examine the reliability index of an LRFD-based design of the truss structure. A planar truss, which is designed following the semi-probabilistic code, is thoroughly examined. Several feasible sections are first designed using the LRFD code. Then, the actual reliability indexes of truss structures are evaluated to check if they meet the target reliability index specified in the reliability-based design codes. The tension and compression members concerning the strength limit state and the maximum deflection presenting for serviceability are investigated as representative performances. The results of the probabilistic analyses indicate that the reliability indexes for the strength limit state are higher than the target value stipulated in the LRFD code. Compared to the tension members, more redundancy in terms of reliability index is observed for compression elements, although they are both designed at the limit state. Moreover, the reliability index obtained for the serviceability limit state is strongly dependent on the component (i.e., floor or roof) where the truss is utilized.

Keywords: reliability analysis; fully probabilistic analysis; Monte-Carlo simulation; truss structure; LRFD.

https://doi.org/10.31814/stce.nuce2023-17(1)-09

1. Introduction

The probabilistic analyses appear to be efficient and rational methods for assessing safety structures considering uncertainties [1–3]. Particularly, the uncertainties that are inherently involved in the operation loads or the strength properties of materials built in the structures are considered in the probabilistic analysis. This feature set the foundation for probabilistic-based design specifications such as the partial safety method or load and resistance factor design (LRFD) [4, 5]. The uncertainties in load and resistance components are examined and considered during the calibration of the factors specified in the design codes. Moreover, the applications of the probabilistic-based design codes are also

*Corresponding author. *E-mail address:* vanson.ctt@vimaru.edu.vn (Doan, N. S.)

similar to those of the allowable stress design. These two features make the probabilistic-based design codes more efficient and widely applied. Particularly, the applications of the probabilistic-based design codes intend to provide a uniform and consistent design class. However, these probabilistic-based design codes above mentioned are identified as semi-probabilistic analyses since no risk analysis is performed during the design phase [6, 7]. That means the probabilistic quantities such as the reliability index (RI) or probability of failure are not determined for the designed solutions. Therefore, the satisfaction in terms of probabilistic quantities becomes questionable [8].

The MVFOSM (mean value first-order second-moment method) or FORM (first-order reliability method) were prevailingly conducted to determine the resistance factors in most of the reliability-based codes. For example, MVFOSM was applied to evaluate the resistance factors in some American specifications, such as AASHTO 2017 [6] or AISC 360-16 [7]. Alternatively, FORM was performed during the development of the design code of the harbor facilities in Japan [9]. However, it was reported that the MVFOSM and FORM could not produce good results if the performance function is highly nonlinear or when the input variables have high variations [3, 5]. That means the use of the resistance factors recommended in the above specifications may not result in solutions that have the RIs close enough to the target values. Contrastingly, Monte-Carlo simulation (MCS) - a fully probabilistic approach [3, 10], which does not require any assumption on the distribution properties of the performance functions is reported as the most accurate method. Thus, MCS is utilized in this work for validation purposes.

Recently, probabilistic analyses have been recommended to be performed to check if the actual RIs of the designed solutions meet the target values specified in the reliability-based codes. Several studies indicated that the actual RI is not always as close to the targets as expected. Some reasons were indicated, such as the differences between the wide uncertainty range of site conditions and the applied range of testing methods, or the different transformations utilized [11, 12]. The additional reliability analysis aims to provide rational insights into the design solutions. In addition, the reliability calculations help to compare different design solutions which are designed following the same specifications. Based on that the most suitable solution can be identified.

Based on the discussions above, this study applies the fully probabilistic analysis to investigate the probabilistic results of the truss structures designed using LRFD code. Namely, the MCS is combined with the finite element method (FEM) to evaluate the failure probability of the truss structure. For this purpose, based on MATLAB [13], a MATLAB program was first developed for FEM-based analysis of truss structures. Then, the MCS technique is adopted to generate the sampling set of the uncertain input variable. The data from MCS are then driven into the MATLAB program to evaluate the performance functions. The strength limit states concerning tension and compression behaviors of the truss members, and the deflection representing the serviceability limit state are thoroughly examined.

2. Deterministic analysis and LRFD-based design of truss members

FEMs were widely utilized in most engineering problems, and their applications to structural problems were well presented in many studies [14, 15]. Several important steps are summarized in Fig. 1. A MATLAB program (*FEM-Truss*) is developed following Fig. 1 for analyzing truss problems. A truss structure shown in Fig. 2(a), adapted from Blum [16] and Packer et al. [17], is used to validate the developed MATLAB program. The i^{th} nominal (unfactored) dead load, D_i is 18 kN; and the i^{th} nominal live load, L_i is 54kN ($i = 1 - 7$) [16]. The resultants of axial forces are calculated for the load combination of 1.2D + 1.6L [18] and reported in Fig. 2(b). The maximum tension load of 1215

kN, and the most critical compression load of 1147kN are determined. The results obtained from the program are identical to those reported in the two previous studies [16, 17]. This comparison confirms the accuracy of the MATLAB program.

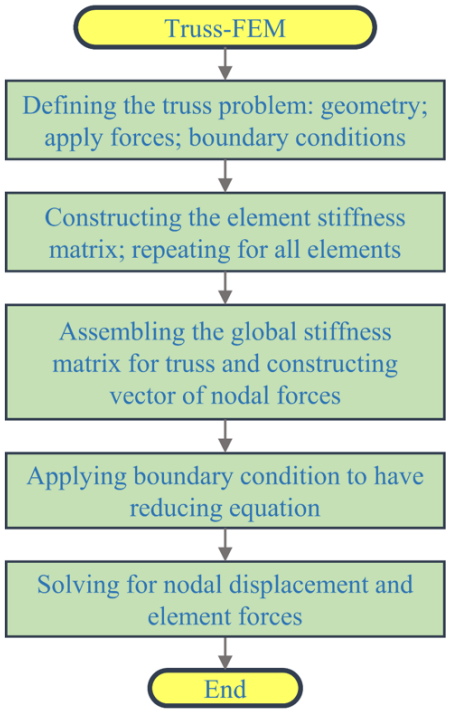

Figure 1. Flowchart for FEM-based analysis of truss structures

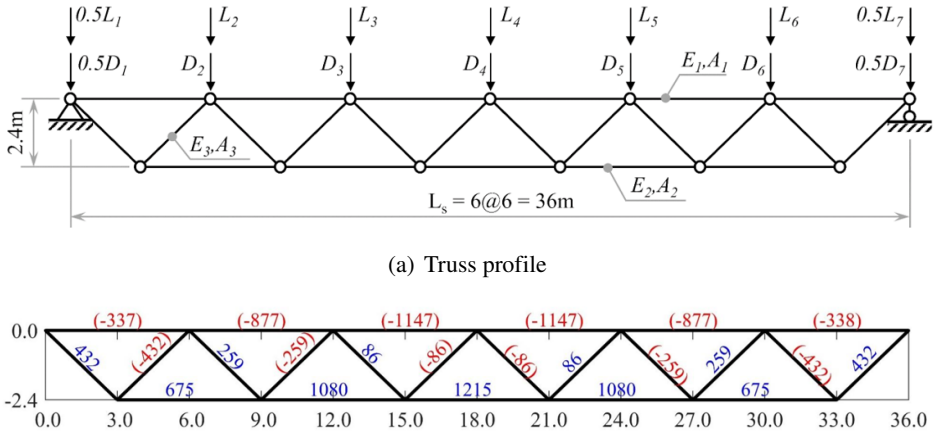

(a) Truss profile

(b) Resultant axial forces obtained from load combination of 1.2D+1.6L

Figure 2. Example of Warren truss

The sections of the truss members are then designed following the Specification for Structural Steel Building of American Institute of Steel Construction (AISC 360-16) [7]. The truss bars are

classified into three different groups for simplicity, i.e., tension bars in the lower chord; compression bars in the upper chord; and web bars. Noticeably, AISC 360-16 provides both ASD (Allowable Strength Design) and LRFD approaches to designing steel structures. This study focuses on the LRFD approach to designing element sections. The sections of truss members were provided in Packer [17] and adapted in Blum [16]. However, the two previous studies used the same sections for the tension and the compression members. On the contrary, this study investigates the probabilistic results when using different sections, and only sections of the web members are kept as $120 \times 120 \times 4$ mm of square hollow section (SHS) following Blum [16]. Then, the tension bars are designed following Chapter D, and the compression bars are designed based on Chapter E of AISC 360-16. Finally, the vertical deflection is checked with the specified value of $L_s/360$ (i.e., 10 cm) assuming for floor members (where L_s is the span length of the truss).

The typical sections of the cold-formed SHS of SSAB (Svenska Aeroplan Aktie Bolag) Domex Tube (provided on www.ssab.com for steel sections) are chosen for the design process in this study. The yield strength of 350 kPa and Young's modulus of 200 GPa are utilized for the steel material. The strength of tension and compression elements are then verified following AISC 360-16 with the most critical axial forces reported in Fig. 2(b). The procedure for checking tension and compression members is briefly summarized in Fig. 3. The width of the SHS sections is chosen from 120 mm to 220 mm for the chord members. Notably, the same resistance factors of 0.9 (i.e., ϕ_t, ϕ_c) specified in AISC 360-16 are used for designing both tension and compression members.

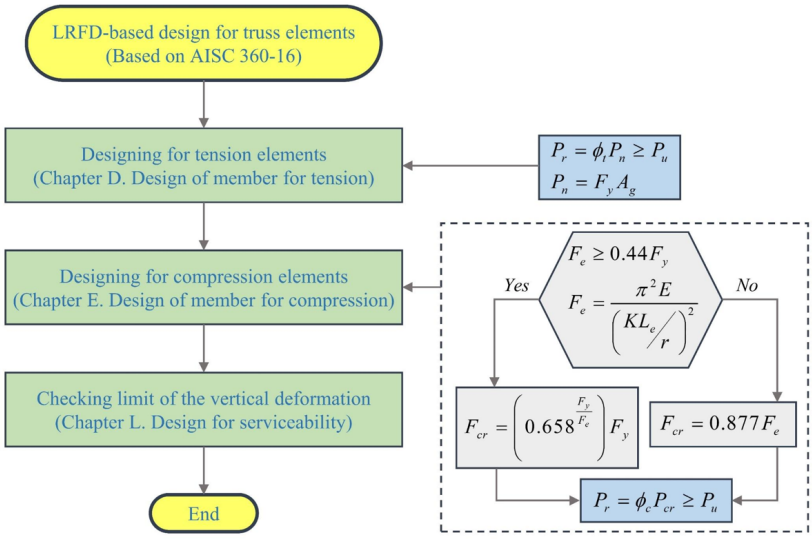

Figure 3. Strength checking for tension and compression members

In Fig. 3, P_u is the axial force in the truss bars. P_r and P_n correspond to the factored and nominal resistances. F_y, E, A_g are yield strength, Elastic modulus, and cross-section area, respectively. The critical stress (F_{cr}) in compression bars is determined based on the elastic buckling stress (F_e), the effective length factor (K), and the element length (L_e). The results computed from all considered sections are summarized in Fig. 4 for tension bars and Fig. 5 for compression bars. The circle markers and the associated numbers in the figures indicate reasonable sections, which are within 5% of redundancy. It is seen that there are three suitable sections for tension bars ($120 \times 120 \times 10$ mm; $140 \times 140 \times 8$ mm; and $150 \times 150 \times 7.1$ mm); and three feasible sections for compression bars ($180 \times 180 \times$

8.8 mm; 200 × 200 × 7.1 mm; and 220 × 220 × 6.0 mm). Here, it is worth noting that the sections for compression bars are much bigger than those for tension members, although the compression force is smaller than the tension force.

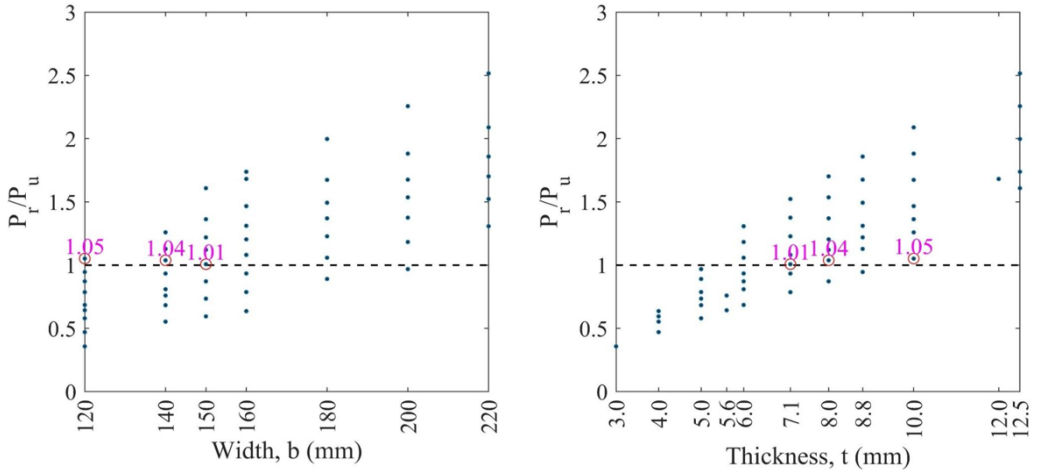

Figure 4. Strength checking for tension members

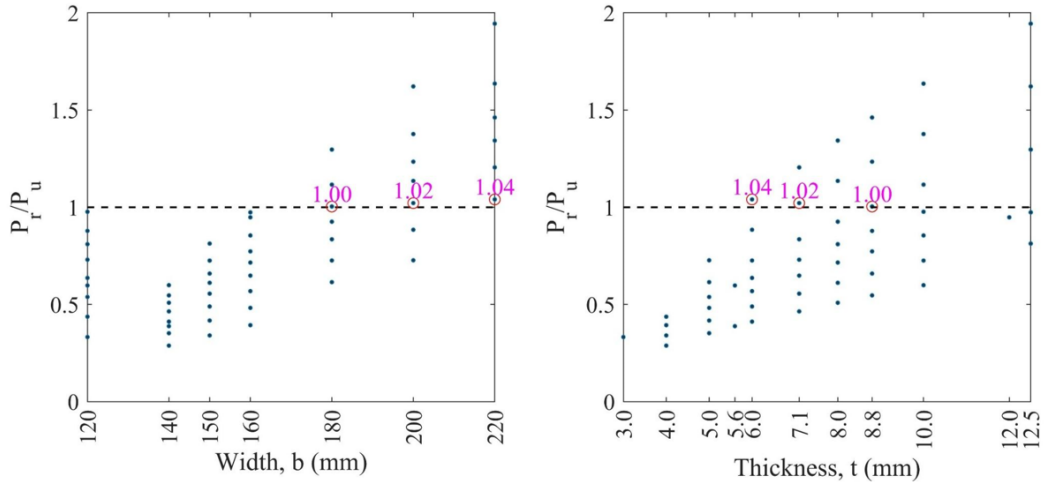

Figure 5. Strength checking for compression members

The chosen sections, which have the ratio between P_r and P_u close to unity aim to achieve the LRFD limit state. The LRFD limit state implies that the RI of the structure is expected to be close to the target value. Then, the slenderness ratio limitation (300 for tension bars and 200 for compression bars) is determined based on the effective length of the components. The effective length factor (K) of 0.9 is selected for the compression bars [16, 17]. The slenderness ratios are shown in Fig. 6 for all SHS sections of SSAB considered in this study. Moreover, the limiting width-thickness ratios for compression elements are checked to desire the compact sections, i.e., protecting local buckling (Table 4.1 of AISC 360-16 [7]). The summarizations are illustrated in Fig. 7.

Based on the buckling conditions, it is seen that all sections satisfy the global buckling condition (Fig. 6). However, the 220 × 220 × 6 mm section is not desired for local buckling checks (Fig. 7).

Thus, two sections for compression and three sections for tension bars (among the six sections above mentioned) are suitable for the probabilistic analysis.

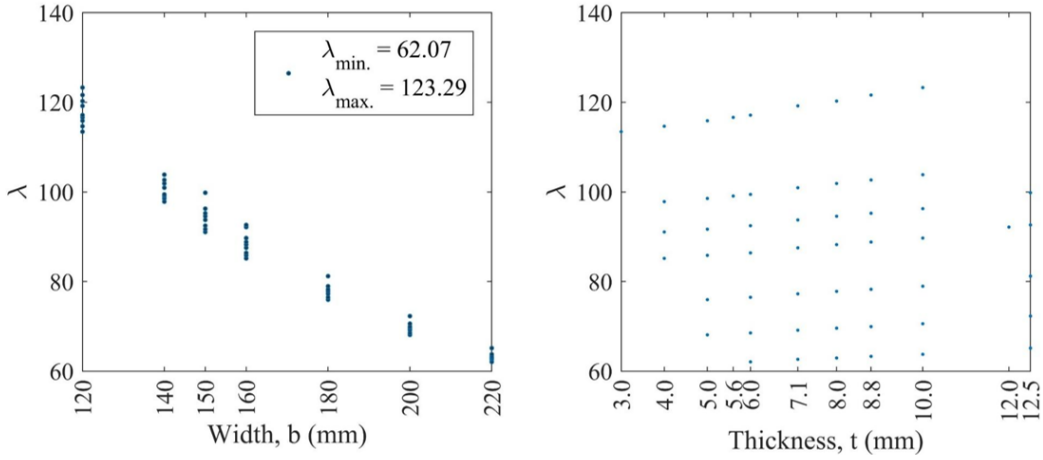

Figure 6. Global buckling of chord bars ($\lambda = KL_s/r$)

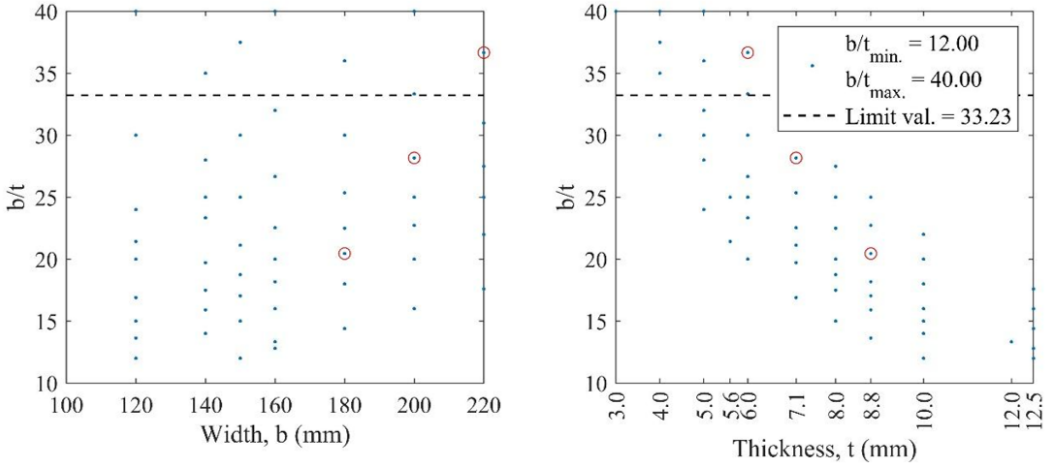

Figure 7. Local buckling limitation of compression sections

3. Fully probabilistic analysis for truss structure

The reliability analysis methods have been presented in the literature [3, 19]. Three different reliability analysis methods were applied to evaluate the overall stability of vertical breakwaters [10]. It was proven that the Monte Carlo simulation is a straightforward and robust approach to probabilistic analysis. The MCS provides not only the failure probability but also the statistical information on the performance functions. Moreover, MCS is the most suitable approach for nonlinear and high-dimension problems. Therefore, MCS is stated to be superior to the point estimate methods. The most critical disadvantage of MCS is the computing time and effort required since a huge number of calculations is needed [20]. However, the integration of the MCS with FEM has been more convenient with the aid of the computer recently. The conjunction of the FEM with MCS is presented in Fig. 8.

The truss problem is defined in the first step, in which the truss profile, applied load, and boundary conditions are provided. The uncertainties considered in the truss problem are also defined in this step. In this work, the truss profile and boundary conditions are treated deterministically. The uncertainty variables are referred from previous studies [16, 21–23] relating to AISC 360-16 and summarized in Table 1. It is seen in the table that the first five random variables are from steel sections and material properties. Meanwhile, the last two random variables are taken from excitation loads. The COV defined in the table is the coefficient of variation, which is the ratio between the standard deviation and the mean value μ. μ is the mean of the bias factors that is defined as the ratio between the mean and the nominal values [4].

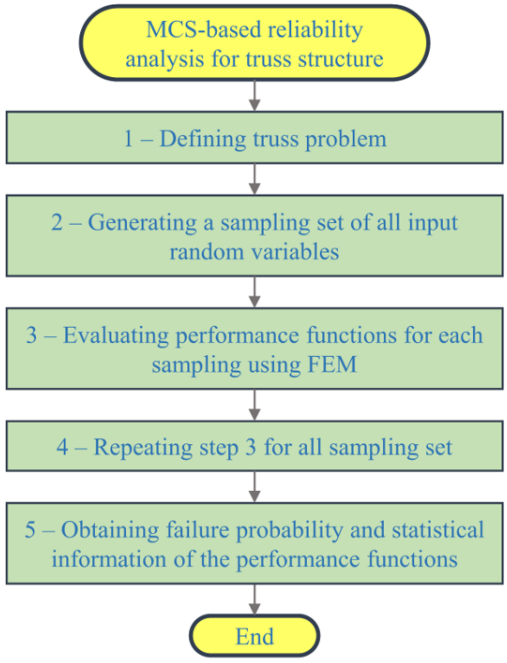

Figure 8. Integration of MCS and FEM for reliability analysis of truss structures

Table 1. Random variables considered

No.	Symbol	Description	Nominal	μ	COV	Distribution
1	t_c	Thickness of comp. bars	7.1 or 8.8 mm	0.964	0.04	Normal
2	t_t	Thickness of tension bars	7.1; 8.0; 10.0 mm	0.964	0.04	Normal
3	t_w	Thickness of web members	4.0 mm	0.964	0.04	Normal
4	E	Young's modulus	200 GPa	1.00	0.06	Normal
5	F_y	Yield strength	350 MPa	1.10	0.10	Normal
6	D	Dead load	18 kN	1.05	0.10	Normal
7	L	Live load	54 kN	1.00	0.25	Extreme type 1

In Step 2, MCS is performed to generate a sampling set of all random input variables using the statistics defined in the first step. The size of the MCS (N_{MCS}), which strongly influences the calculation performance, is recommended in previous studies [3, 20]. In this study, the size of MCS

is chosen as 1 million so that the COV of the failure probability is not higher than 0.18 (assuming the RI is about 4.0). The histograms of Young's modulus, yield strength, dead load, and live load are illustrated in Fig. 9.

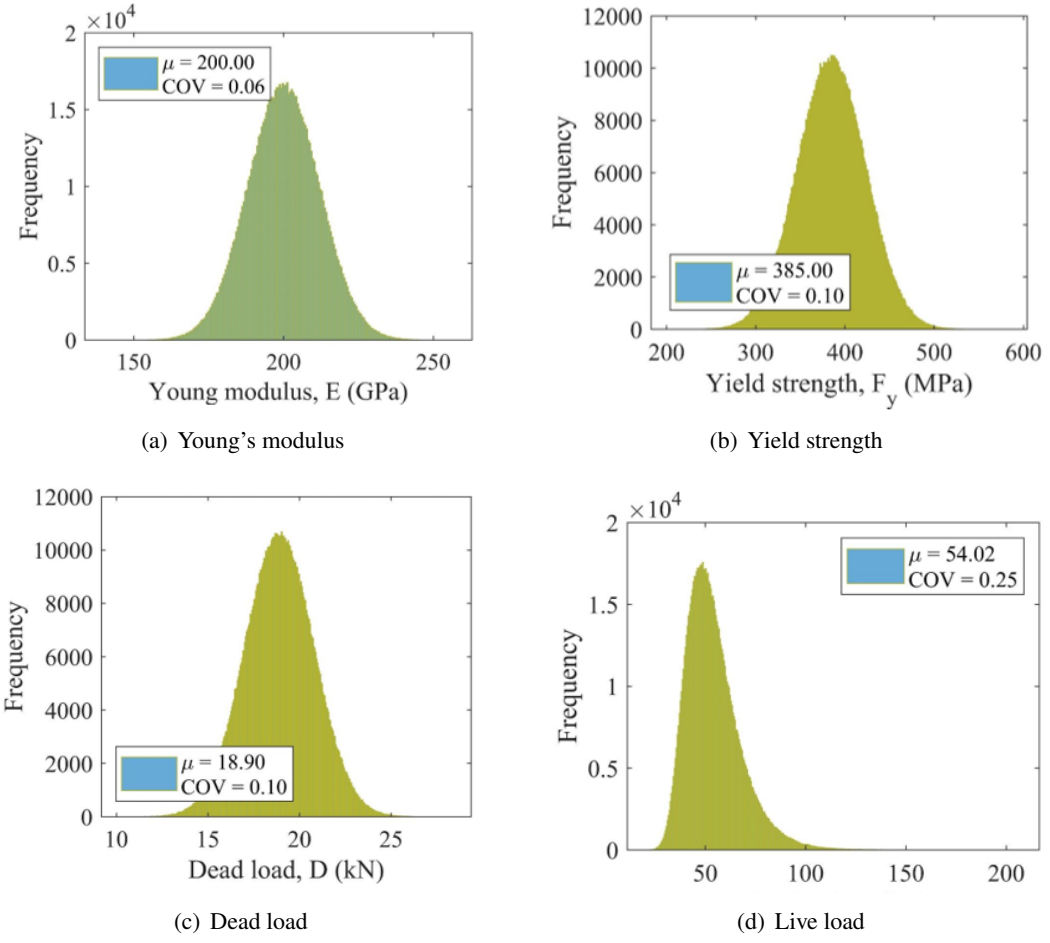

(a) Young's modulus

(b) Yield strength

(c) Dead load

(d) Live load

Figure 9. Illustrations of several histograms of random variables considered in MCS

In Step 3, *FEM-Truss* program is employed to evaluate the performance functions associated with each sample including all considered variables. The performance functions associated with the critical forces in the tension and compression bars are shown in Eq. (1). In Eq. (1), Q is the axial forces (tension or compression), and R is the corresponding strength of the member of interest. In addition, the performance associated with the maximum deflection of the structure is shown in Eq. (2). The limitation of the deflection, y_{LS} is L_s/360 (assuming floor structure), and y is the maximum deflection due to the live load. The routine is repeatedly executed for the entire sampling set generated in Step 4.

$$g = R - Q \tag{1}$$

$$g = y_{LS} - y = \frac{L_s}{360} - y \tag{2}$$

Finally, the probability of failure (P_f) in MCS can be evaluated using Eq. (3). In the equation, N^{fail} is the number of failure events recorded among the N_{MCS} simulations. The reliability index, β

can be converted from P_f using Eq. (4). The statistical information, i.e., the mean, standard deviation, and COV of the performance functions are also determined in this step [3, 24].

$$P_f = \frac{N^{fail}}{N_{MCS}} \tag{3}$$

$$\beta = \Phi^{-1}\left(1 - P_f\right) \tag{4}$$

4. Results and discussions

There are three different feasible sections for tension and two for compression members as selected in Section 2. Noticeably, these sections are designed at the LRFD limit states of interest as discussed in Section 2. This section investigates safety from the probabilistic point of view as presented in Section 3. The tension behaviors are examined for the three feasible sections and reported in Fig. 10. Similarly, the results of the compression bars are captured in Fig. 11 for two chosen sections. It is worth noting that the considered truss is a statistically determinate structure. Therefore, the resultants (i.e., the axial forces Q) are not dependent on the sections designed, whereas the resistances (R) strongly depend on the specific sections designed. Consequently, the statistical properties of Q are observed similarly in Fig. 10 for tension behavior and Fig. 11 for compression cases.

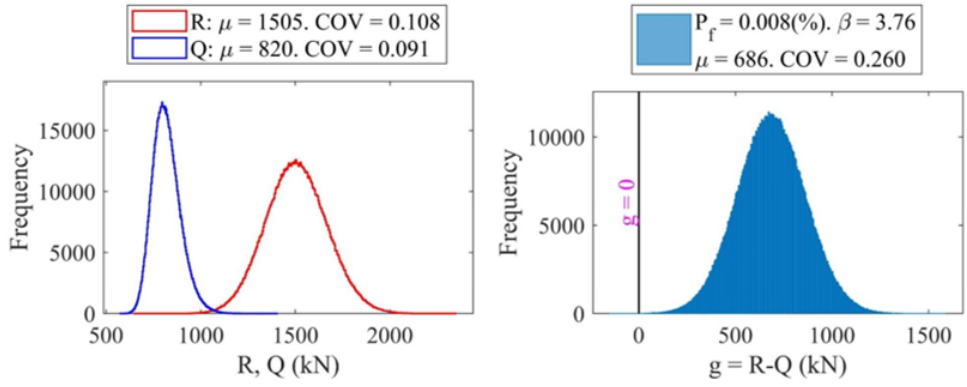

(a) RHS Section of 120 × 120 × 10 mm

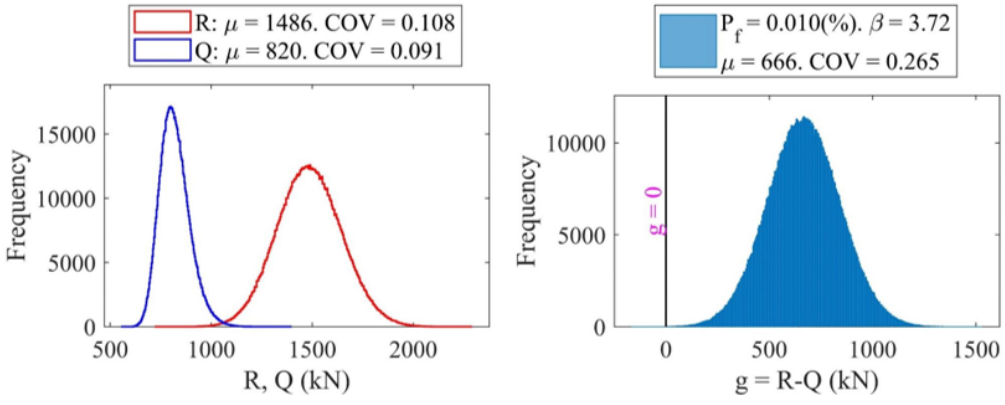

(b) RHS Section of 140 × 140 × 8.0 mm

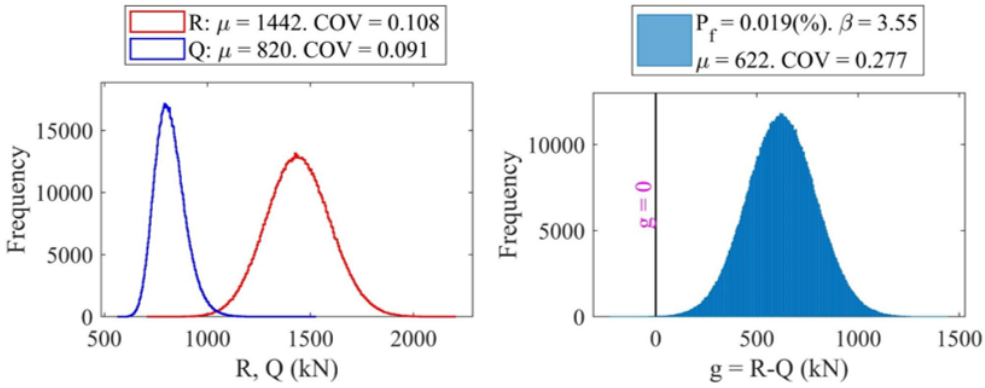

(c) RHS Section of 150 × 150 × 7.1 mm

Figure 10. Results of MCS for tension bar

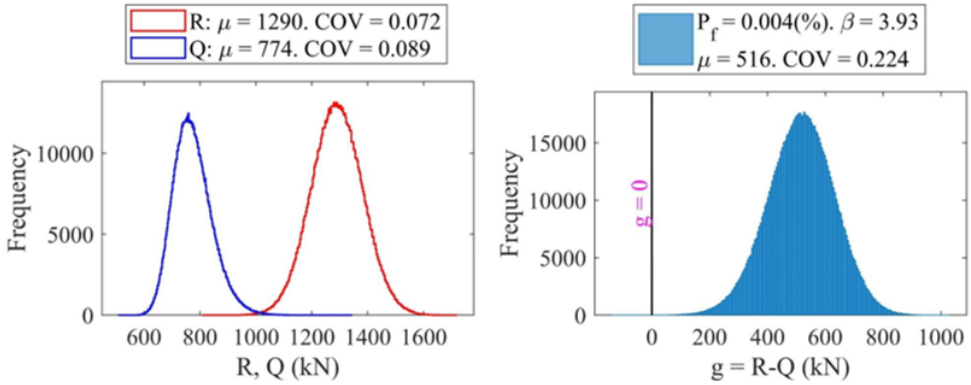

(a) RHS Section of 180 × 180 × 8.8 mm

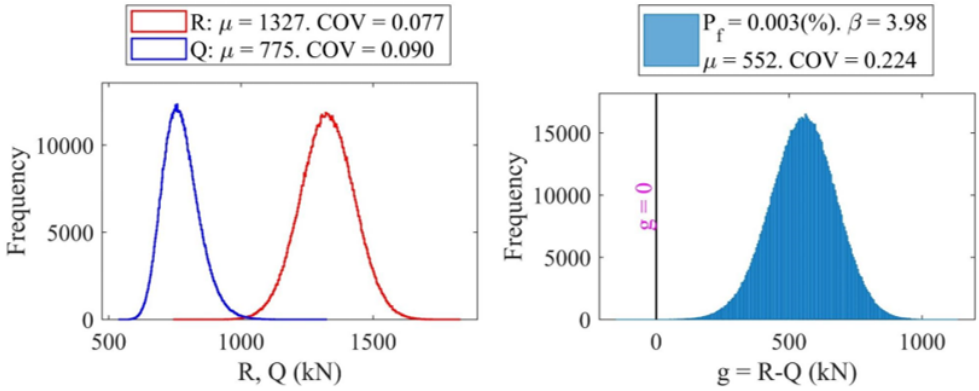

(b) RHS Section of 200 × 200 × 7.1 mm

Figure 11. MCS results for compression bar

It is seen in Fig. 10 and Fig. 11 that all RIs relating to the strength limit states are all higher than the target value of 3.0, which is specified in AISC 360-16 and ASCE/SEI 7-16 [7, 18]. In addition, the RIs for compression members are much higher than the target value. Moreover, the RIs for compression are also higher than those for tension behaviors. Here, it can be stated that the compression behavior is specified with more redundancy in the current codes, although they are designed at the limit states as indicated by the ratio between the P_r and P_u. These observations imply that the resistance factors for tension and compression designs in AISC 360-16 are conservatively specified for truss members. In other words, the resistance factors specified in the current design code can be increased to make the actual RI meet the target value. In this context, the MCS-based framework proposed in this study is recommended for reliability analyses.

The COV terms reflect the uncertainty levels of the variables. The COVs of both load and resistance are summarized in Fig. 10 and Fig. 11 for tension and compression, respectively. It is seen that the COVs of axial loads are the same at about 0.09. However, the COVs of tension resistances are observed higher than those for compression. Thus, the COVs of the performance functions relating to tension are also higher than those for the compression, as depicted in the right panels of Fig. 10 and Fig. 11. As a result, the RIs for the tension are lower than those for compression behaviors. Moreover, the different COVs of the performance function relating to tensions are also captured although the uncertainties in the material are similar for the two behaviors. These observations illustrate that the MCS can reflect the feature of uncertainties more accurately than the point estimate method, which was performed in the development of current design codes.

The comparisons of the design solutions are summarized in Table 2. It is seen that the RIs for each behavior (compression or tension) are relatively identical when the sections are sized at the LRFD limit state (indicated by the unity ratios of P_r and P_u).

Table 2. Comparison of the feasible sections

No.	Behavior	Section (mm)	Weight (kg/m)	P_r/P_u	RI
1	Compression	$180 \times 180 \times 8.8$	45.2	1.00	3.93
2	Compression	$200 \times 200 \times 7.1$	41.6	1.02	3.98
3	Tension	$120 \times 120 \times 10$	40.57	1.05	3.76
4	Tension	$140 \times 140 \times 8$	40.04	1.04	3.72
5	Tension	$150 \times 150 \times 7.1$	38.85	1.01	3.55

Based on the comparison table, the sections are chosen as $200 \times 200 \times 7.1$ mm for compression and $150 \times 150 \times 7.1$ mm for tension members. Although the reliability index of the tension behavior is not the highest, the weights of the selected tension chords are the lowest and this size combination helps to easily connect members in the truss structure.

Next, the deflection of the structure is investigated for the chosen sections. The results of MCS are captured in Fig. 12 assuming the maximum deflection at the middle of the span. The RI of 0.95 is assessed for deflection performance considering floor structures, as shown in Fig. 12(a). This value is much lower than those obtained for strength limits shown in Table 2. The target RI under the serviceability was not specified in AISC 360-16. However, it is observed that the RI under the serviceability (e.g., deflection in this study) is commonly lower than that of the strength limit state [25, 26]. Particularly, the RI regarding the deflection was reported as about zero in the previous study [27]. This is because the consequences of failures concerning the serviceability limit states are minor or moderate

in comparison with those relating to the strength limit states [28].

Alternatively, if the truss structure is designed for the roof members, then the limiting deflection of L_s/240 needs to be applied as specified in AISC 360-16. In this context, the RI of 3.66 is obtained in the MCS as shown in Fig. 12(b). That means the RI increases about four times when the same structure is used from the floor to the roof member. This observation indicates that the different limiting of deflections will result in very different RIs of floor or roof members in the same building.

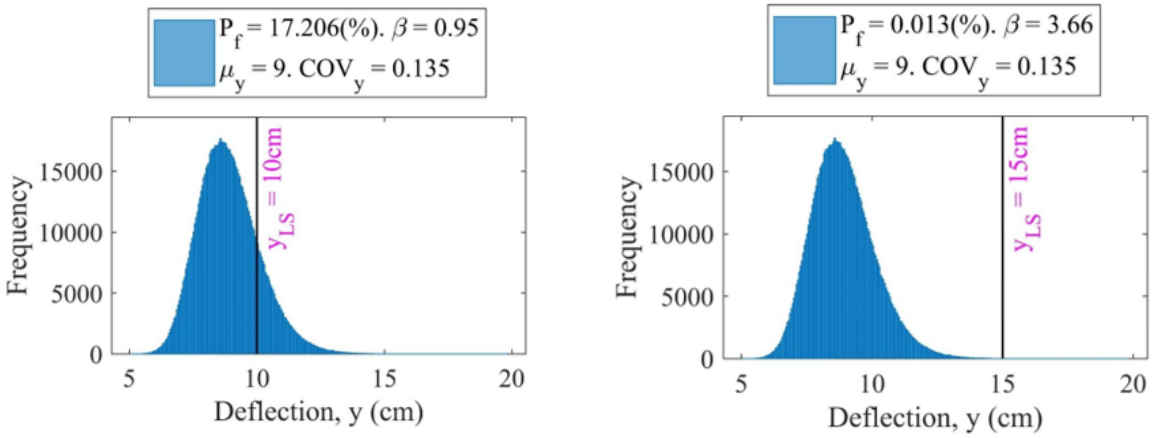

(a) For limiting deflection (y_{LS}) of L_s/360

(b) For limiting deflection of L_s/240

Figure 12. Results from MCS concerning deflection limit state

5. Conclusions

This study investigates the safety of the truss structure from a probabilistic point of view. The limit states concerning the strength and serviceability are handled. The sections of the truss members are first designed using the LRFD specification. Then, the MCSs are performed to evaluate the failure probabilities and the reliability indexes for the considered performances. Several conclusions are established as follows.

A procedure for applying MCS as additional analyses is presented to elicit insight into the LRFD-based design solutions. The results of the examined truss demonstrate that all of the strength limit states are redundantly satisfied with the target value specified in the current design codes, although the sections are designed at the limit state (depicted by the most likely unity ratio of P_r and P_u).

The excess of safety in terms of RI for both tension and compression bars demonstrates that the resistance factors specified in the current codes are overestimated since they are obtained from the MVFOSM. Thus, if the resistance factors are specifically calibrated for individual problems with the aid of MCS, using them might then provide more uniform design solutions as the main purpose of the reliability-based design codes. Consequently, more economical design solutions will be achieved.

Pertaining to the serviceability limit state, the RI is much lower than those estimated for the strength limit states. Furthermore, the RI for the serviceability limit state (i.e., deflections in this study) strongly depends on the limiting values specified in the design codes. It is also observed that the RI is different about four times when the same structure is applied to the floor or the roof members.

Acknowledgments

This research is funded by Vietnam Maritime University under grant number: DT22-23.73.

References

[1] Ditlevsen, O., Madsen, H. O. (2007). *Structural reliability methods*. Department of Mechanical Engineering Technical University of Denmark: Denmark.

[2] Ang, A. H., Tang, W. H. (1984). *Probability concepts in engineering planning and design, Vol. 2: decision, risk, and reliability*. John Wiley & Sons: New York, USA.

[3] Haldar, A., Mahadevan, S. (2000). *Probability, reliability and statistical methods in engineering design*. John Wiley: Hoboken, NY, USA.

[4] Allen, T. M., Nowak, A. S., Bathurst, R. J. (2005). *Calibration to determine load and resistance factors for geotechnical and structural design*. Transportation Research Circular: Washington, DC, USA.

[5] Nowak, A. S., Collins, K. R. (2000). *Reliability of structures*. McGraw-Hill: New York.

[6] AASHTO (2017). *LRFD Bridge Design Specifications*. AASHTO: Washington, DC, USA.

[7] AISC 360-16 (2016). *Specification for structural steel buildings*. American Institute of Steel Construction: Chicago, USA.

[8] Phoon, K.-K., Ching, J. (2018). *Risk and reliability in geotechnical engineering*. CRC Press: New York, USA.

[9] MLIT (2009). *Technical standard and commentaries for port and harbor facilities in Japan*. Ministry of Land, Infrastructure, Transport and Tourism (MLIT): Ports and Harbors Bureau: Tokyo, Japan.

[10] Doan, N. S., Huh, J., Mac, V. H., Kim, D., Kwak, K. (2020). Probabilistic risk evaluation for overall stability of composite caisson breakwaters in Korea. *Journal of Marine Science and Engineering*, 8(3): 148.

[11] Phoon, K.-K. (2016). Role of reliability calculations in geotechnical design. *Georisk: assessment and management of risk for engineered systems and geohazards*, 11(1):4–21.

[12] Low, B. K., Phoon, K.-K. (2015). Reliability-based design and its complementary role to Eurocode 7 design approach. *Computers and Geotechnics*, 65:30–44.

[13] MATLAB. *MATLAB (2020b)*. The Mathworks Inc., Natick, Massachusetts, USA.

[14] Cook, R. D., Malkus, D. S., Plesha, M. E., Witt, R. J. (2002). *Concepts and applications of finite element analysis*. 4th edition, Willey: New York.

[15] Logan, D. L. (2010). *A first course in the finite element method*. 5th edition.

[16] Blum, H. B. (2013). *Reliability-based design of truss structures by advanced analysis*. Research Report R936, The University of Sydney, Sydney, Australia.

[17] Packer, J. A., Wardenier, J., Zhao, X.-L., van der Vegte, G. J., Kurobane, Y. (2009). *Design guide for rectangular hollow section (RHS) joints under predominantly static loading*. 2nd edition, CIDECT: Germany.

[18] ASCE/SEI 7-16 (2016). *Minimum design loads for buildings and other structures*. American Society of Civil Engineers: Reston VA.

[19] Nowak, A. S., Collins, K. R. (2012). *Reliability of structures*. 2nd edition, CRC Press: Boca Raton, FL, USA.

[20] Doan, N. S., Dang, P. V., Huh, J., Mac, V. H., Haldar, A. (2022). Efficient approach for calibration of load and resistance factors in the limit state design of a breakwater foundation. *Ocean Engineering*, 251: 111170.

[21] Ellingwood, B., Galambos, T. V., MacGregor, J. G., Cornell, C. A. *Development of a Probability Based Load Criterion for American National Standard A58 - Report 577*. 1st edition, National Bureau of Standards: Washington D. C., USA.

[22] Galambos, T. V., Ravindra, M. K. (1981). Load and resistance factor design. *Engineering Journal, AISC*, 18(3):78–84.

[23] Zhang, H., Liu, H., Ellingwood, B. R., Rasmussen, K. J. R. (2018). System reliabilities of planar gravity steel frames designed by the inelastic method in AISC 360-10. *Journal of Structural Engineering*, 144 (3).

[24] Doan, N. S., Huh, J., Mac, V. H., Kim, D. H., Kwak, K. (2021). Calibration of Load and Resistance Factors for Breakwater Foundations under the Earthquake Loading. *Sustainability*, 13(4):1730.

[25] CAN/CSAS614:2014 (2014). *Canadian highway bridge design code*. Canadian Standards Organization: Mississauga, Ontario, Canada.

[26] Galambos, T. V., Ellingwood, B. (2013). Serviceability limit states. In *Design of Steel-Concrete Composite Bridges to Eurocodes*, CRC Press, 442–465.

[27] Ghasemi, S. H. (2015). Target reliability analysis for structures. PhD thesis, Graduate Faculty of Auburn University.

[28] Bhattacharya, B., Basu, R., tung Ma, K. (2001). Developing target reliability for novel structures: the case of the Mobile Offshore Base. *Marine Structures*, 14(1-2):37–58.

Journal of Science and Technology in Civil Engineering, HUCE (NUCE), 2023, 17 (1): 125–136

AN ANALYSIS OF THE RELATIVE VARIABLE IMPORTANCE TO FLOOD FATALITY USING A MACHINE LEARNING APPROACH

Luu Thi Dieu Chinh[a], Ha Thi Hang[b,*]

[a]*Faculty of Hydraulic Engineering, Hanoi University of Civil Engineering, 55 Giai Phong road, Hai Ba Trung district, Hanoi, Vietnam*
[b]*Faculty of Bridges and Road, Hanoi University of Civil Engineering, 55 Giai Phong road, Hai Ba Trung district, Hanoi, Vietnam*

Article history:
Received 19/12/2022, Revised 16/02/2023, Accepted 08/3/2023

Abstract

Vietnam is regularly and severely affected by flood events and there were nearly 14,000 dead people in 200 separate floods from 1989 to 2015. However, there have been limited studies specifically on flood-related mortality in Vietnam. This paper presents a longitudinal investigation of flood fatalities in Vietnam. More specifically, we use the available national disaster database and machine learning techniques to investigate the importance of different attributes of flood damage to the attribute of flood fatalities. The results show that the housing damage attribute significantly influences the fatality attribute, of which the weights are 0.45, 0.62, and 0.36 for the random forest, boosting, and multiple linear regression techniques, respectively. Thus, it is recommended that the proper policy prioritize housing improvements, establish evacuation plans, and develop a strategy for temporary flood shelters in flood-prone areas. Understanding how various components of flood damage are more likely to lead to fatalities analyzed in this study is critical for developing risk reduction strategies.

Keywords: flood fatalities; national disaster database; machine learning; variable importance; disaster risk reduction; Vietnam.

https://doi.org/10.31814/stce.nuce2023-17(1)-10

1. Introduction

According to the Global Disaster Database, Asia is the region most at risk from natural disasters like floods and storms since 3,620 such events occurred there between 1900 and 2016 and caused at least 8,085,516 deaths (Fig. 1). Natural hazards almost often have the greatest impact on developing economies [1–3]. The potential for human casualties is important to consider when assessing flood risk [4]. In contrast to the substantial research conducted on flood-related mortality in developed countries [5–9], very few studies have been conducted on the topic in developing countries [10], despite their higher fatality rates [11]. Several approaches were used to study flood-related mortality.

Penning-Rowsell et al. [12] developed a model to forecast flood-related deaths and injuries using flood hazard and exposure aspects. Jonkman and Vrijling [13] presented a technique to estimate the death toll in flood occurrences by analyzing flood hazard characteristics, evaluating the exposed

*Corresponding author. *E-mail address:* hanght@huce.edu.vn (Hang, H. T.)

population, and assessing the fatality rate. Many other studies examined the context and root causes of flood-related mortality [14–16]. These studies were conducted for particular places or events and needed information such as the reason for death, evacuation condition, gender, age, time of day, and coping ability. Studying the causes of flood-related deaths is also possible via the use of prediction models [17–19]. It is hard to apply these models in data-poor regions because of the exact input parameters they need when paired with hydraulic models. A lack of precise data for analysis contributes to the paucity of research on mortality caused by floods in developing nations.

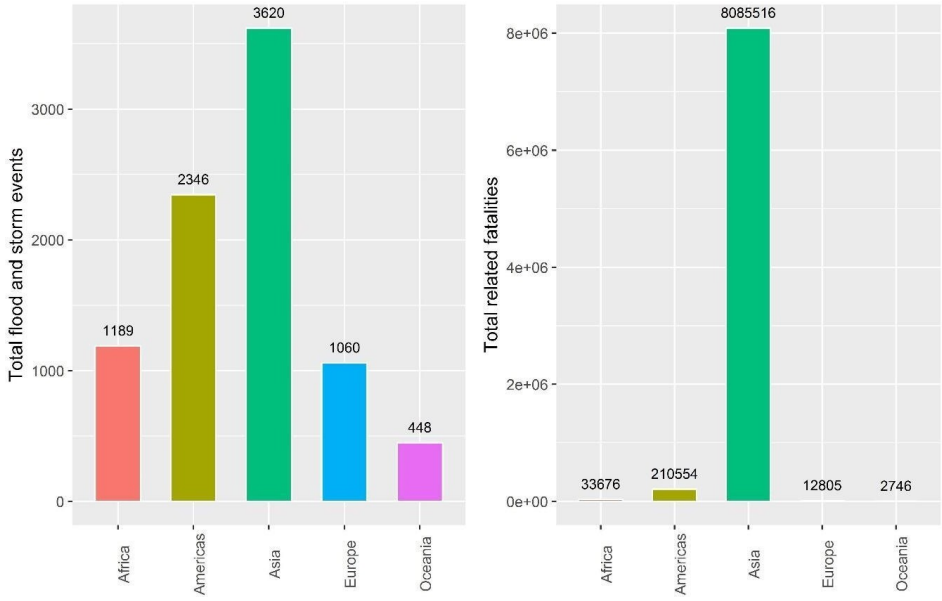

Figure 1. Worldwide flood and storm occurrences and fatalities from 1900 to 2016 (information retrieved on April 20, 2017, from http://emdat.be)

Analyzing disaster damage data may give important information for policy development and decision-making in disaster management [20, 21]. Disaster databases that are available for public access are grouped and aggregated in the publications of Simpson et al. [22] and Grasso and Dilley [23], such as the global disaster database (www.emdat.be) and national disaster databases (www.desinventar.net). These databases can be used for flood studies in which the data are analyzed and converted into useful information for disaster management. In addition, we also need to focus on research on data recording standards to improve the quality of disaster databases and to provide diverse and accurate databases for analysis [23].

Vietnam is significantly influenced by flood hazards, being the ninth most severely affected by extreme weather events [24] and the fourth most vulnerable to river flood danger by the percentage of the population [25]. Thus, there has been a significant growth in research on flood risk in Vietnam. Tran et al. [26] analyzed how rural Thua Thien Hue province people deal with the threat of flooding. Chau et al. [27] analyzed the impacts of flood hazards on the agriculture sector in Quang Nam province using GIS techniques. Chinh et al. [28] had a survey with households and small private businesses in Can Tho city on flood preparedness, response, and recovery. The machine learning method was utilized to model the vulnerability of the Tuong Duong district [29]. Luu et al. [30] used spatial analysis techniques to evaluate the risk of flooding in Quang Nam province. On the other hand, there have been no studies conducted thus far on the deaths caused by floods in Vietnam.

DANA (Damage Assessment and Needs Analysis) is the acronym for the Vietnam national disaster database. It was developed by the government commissioner of the Department of Dyke Management, Flood and Storm Control under the support of the United Nations Development Programme [23]. Since 1989, damages from disaster events have been recorded [31, 32]. Machine learning algorithmic models have been more and more popular in natural hazard assessment, including floods [33]. Machine learning techniques are very useful to solve complicated problems with multiple interacting factors and can analyze the importance of attended variables in flood studies [34, 35]. Besides, ML techniques can be arranged according to a diverse classification to denote the desired results of the modeling procedure [36]. Thus, this study aimed to analyze the DANA data (documented from 1989-2015) to assess the influencing attributes on fatality attributes. We used advanced machine learning techniques of random forest, multiple linear regression, and boosting. The result may help define flood risk management strategies and relevant measures to reduce mortality from future floods.

2. Material and Methods

2.1. Data used

Data on flood damage had been compiled by the National Steering Committee for Flood and Storm Control via the DANA system [31, 37, 38]. Like many other international, regional, and national disaster databases, DANA does not include data on the physical exposure of buildings and infrastructure [22]. DANA compiles information about disaster-related losses by classifying them according to many different attributes, such as the number of people killed or injured, the number of houses destroyed, the area of rice and crop lost, the amount of soil washed away, and the aquaculture areas [32]. However, the DANA database only records the values lost due to business interruption, not the indirect losses resulting from the recovery and restoration of destroyed properties and infrastructure [39].

We collected more than 200 flood and storm data cards between 1989 and 2015 from the DANA database. After that, the data are compiled for 63 provinces of Vietnam, as shown in Fig. 2.

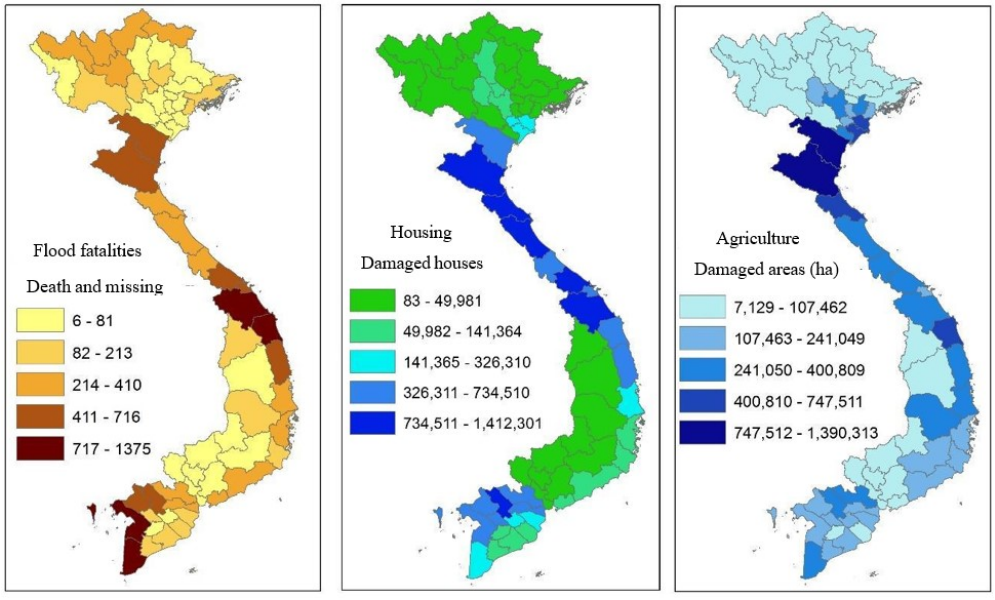

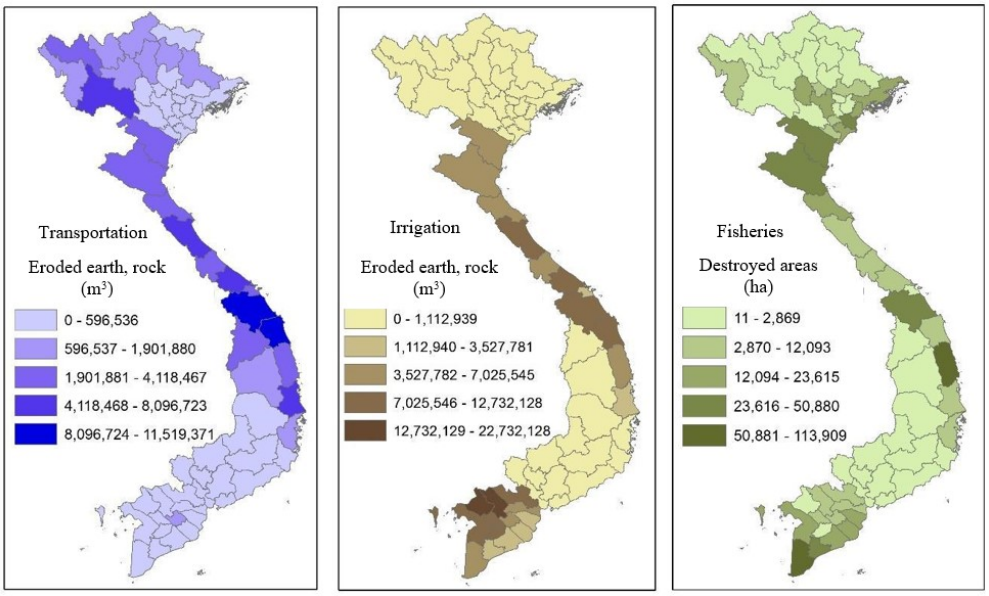

Figure 2. The spatial distribution of flood impacts at the provincial level

Flood fatality is a key indicator in risk analysis. The number of confirmed fatalities from a flood is known as the death toll [31]. The Vietnamese people have suffered greatly as a result of flood and storm disasters, particularly in terms of mortality. Between 1989 and 2015, there were at least 14,927 flood fatalities documented (Fig. 3).

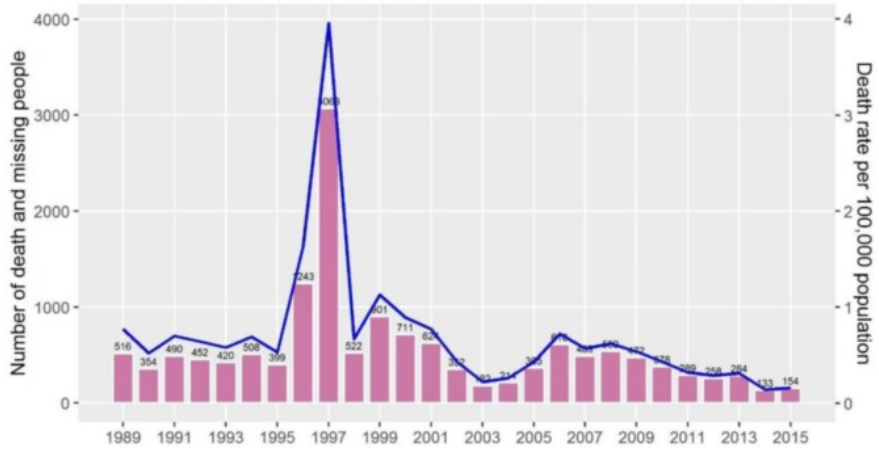

Figure 3. Temporal distribution of flood-related fatalities and death rate per 100,000 population in Vietnam, 1989-2015

The following flood damage attributes are considered for analysis: death toll, house damage, agriculture loss, transportation damage, irrigation damage, and fisheries loss (as shown in Fig. 2). The six variables of the flood damage attributes are collected for 63 provinces from 1989 to 2015. There are a total of 1,701 observations, one for every year for each province.

2.2. *Method used*

This study aims to examine the relationship between different flood damage qualities and the mortality attribute using the DANA database. We focus on measuring the variable importance using statistical machine learning models. Statistical tools in R software are used to analyze the relationship between flood fatality attribute and other flood damage attributes [40]. Fig. 4 details the analytic approach used in this study. There are five steps to this process: (1) collecting a sample data set, (2) splitting randomly the sample data set into training data set and testing data set, (3) constructing a training model, (4) applying it to a testing model for model validation, and (5) measuring model performance via an index, Mean Squared Error (MSE).

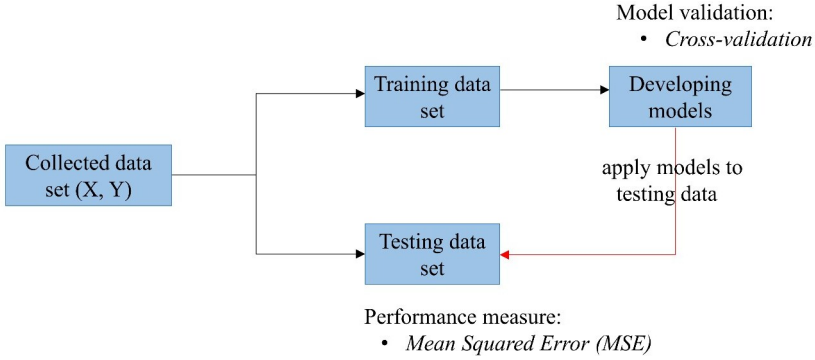

Figure 4. The machine learning framework applied in this study

We calculated the mean, median, range, minimum, and maximum for examining the statistical distributions of variables. Similar to the characteristic of data in the study of Zhou et al. [41], our flood damage data have a large variation. Therefore we applied log transformation for all six flood damage categories to better fit the normal distribution. We applied the machine learning framework in Fig. 4. The sample data is randomly split into training and testing data sets at a ratio of 70% and 30%, respectively, using the 'caTools' package in R software [42]. To verify the model, we used the cross-validation technique. In this procedure, the training data set was used to create the model and the testing data set to verify it.

We used three advanced machine learning models of random forest, boosting, and multiple linear regression to investigate the relationship between flood damage attributes and fatality attributes. These methods provide a simple and natural justification for how each variable affects the whole. The following sections elaborate on each of these models.

a. Multiple linear regression

A typical statistical modeling method known as multiple linear regression may be found in any modeling book, for example, the book [43]. The research uses multiple linear regression to model flood mortality as a linear function of other damage attributes. Assumed is the absence of any variable interactions. After that, we used LMG measure (the abbreviation of Lindeman, Merend, and Gold [44]) to compute the variable importance in the linear model. The LMG measure is based on the proportional contribution of the total R-squared of each variable in the linear model [44, 45].

b. Random forest

Random forest for regression is another method that is used on the same data. Random forest is a method for improving prediction accuracy by combining numerous separate weak regression models,

such as decision trees, which often have high bias and low variance, into a single ensemble model [46]. This study establishes the random forest model using the 'randomForest' package in R software [47]. The random forest algorithm is based on Breiman et al. [46] 's classification and regression tree or CART.

c. Boosting

The boosting method, like the random forest method, combines many separate, weak regression models to create a more robust and precise ensemble model. Contrary to the random forest, boosting is a sequential strategy in which each weak model is introduced to improve the performance of the prior group of weak models. This research used the R 'gbm' package to construct a boosting model from decision trees [47].

3. Results

3.1. Variable importance measures using multiple linear regression

We conducted an analysis of the correlation between the log-transformed flood mortality attribute and other flood damage variables [40]. The machine learning framework in Fig. 4 was applied for data analysis. The residual standard error of the training model is 0.856, and its multiple coefficient of determination is 0.5932. The MSE of the model under testing is 0.674. The 'relaimpo' package is then used to create relative variable importance based on the LMG indicator [48].

The linear regression model was used to examine the correlation between the flood damage attributes and the flood death attribute. Training data sets are used to develop the model, while test data sets are used to test model performance. The model of the training data set has a defined coefficient (squared R) of 0.5932, and the remaining standard error is 0.856. Next, we calculated the forecasted value of the test data set model. The average square error (MSE) of the test model is 0.674. We then ran the 'relaimpo' package in R software to create significant change measures based on the LMG indicator [48].

According to the findings shown in Table 1, the feature representing housing damage is the most significant factor to consider since it has a relative importance of 0.3642. The significance of the other factors is not as great. The *P* value for each variable comes in at less than 0.05.

Table 1. Variable importance from multiple linear regression modeling

Damage attributes	Relative variable importance	*P*-value
Housing	0.3642	< 0.0001
Agriculture	0.1791	0.0468
Transportation	0.1548	< 0.0001
Irrigation	0.1527	< 0.0001
Fisheries	0.1492	0.0221

3.2. Variable importance measures using random forest

The influence of flood damage variables on the mortality attribute is quantified using a random forest regression model. The random forest model is constructed using the 'randomForest' package in R software [49]. The input parameters are set for the modeling, with 500 for the number of trees and

15 for the maximum number of terminal nodes. The mean of squared residuals for the training model is 0.687, and the percentage variance explained is 61.64%. The MSE of the testing model is 0.612.

Table 2 displays the random forest model's variable importance measures. The variable importance results of the random forest modeling show that housing damage is the most important variable, while other factors have a limited influence, which is consistent with the finding from the multiple linear regression modeling.

Table 2. Variable importance from random forest modeling

Damage attributes	Relative variable importance
Housing	0.4546
Irrigation	0.2438
Agriculture	0.1260
Fisheries	0.0906
Transportation	0.0848

3.3. Variable importance measures using boosting

We fitted the boosted regression model using the training data set and the 'gbm' package in R software [47]. The input parameters are set for the modeling with 10,000 for the number of trees, 4 for the maximum depth of variable interactions, and Gaussian for the distribution assumption. The performance of the boosting model is evaluated using the cross-validation method. Its MSE is 0.638 for the test data set. It is compatible with the results of the multiple linear regression model (0.674) and the random forest model (0.612). Small variations in MSEs among methods suggest the used models are accurate and well-validated.

Table 3 displays the outcomes of the boosting model's variable importance measurements. We also discover that the mortality attribute is most heavily influenced by the flood housing damage attribute and is only somewhat influenced by the other damage characteristics. The three used models all arrive at similar conclusions throughout the analysis.

Table 3. Variable importance from boosting modeling

Damage attributes	Relative variable importance
Housing	0.6191
Irrigation	0.1372
Agriculture	0.0959
Fisheries	0.0845
Transportation	0.0633

4. Discussion

Table 4 summarizes the findings of variable significance measurements for three applicable models. There is consensus between the models that the house damage attribute has the greatest impact on the flood fatality attribute, whereas other damage qualities have considerably less impact. The outcomes of the boosting and random forest models are comparable for all variables. The linear regression model and several other models have somewhat different rankings for some aspects of

damage. The variations may be traced back to the underlying assumptions of the statistical methods used. In contrast to the random forest and boosting models, which are done under the premise of interaction between variables, the multiple linear regression model assumes that there are no such interactions [43].

Table 4. Comparison of variable importance measures between used models

Damage attribute/ Statistical model	Relative importance measures					
	Multiple linear regression		Random forest		Boosting	
	Weight	Rank	Weight	Rank	Weight	Rank
Housing	0.3642	1	0.4546	1	0.6191	1
Irrigation	0.1527	4	0.2438	2	0.1372	2
Agriculture	0.1791	2	0.1260	3	0.0959	3
Fisheries	0.1492	5	0.0906	4	0.0845	4
Transportation	0.1548	3	0.0848	5	0.0633	5

Our findings show the high significance of the flood housing damage attribute in relation to the fatality attribute. This result is supported by the observation of De Bruijn and Klijn [50]. Collapsing buildings were noted as one of the major causes of mortality during floods by De Bruijn and Klijn [50]. However, a significant number of deaths involving vehicles have been associated with flood occurrences in several developed countries [6, 7, 9]. In Europe and the US, automobiles were determined to be responsible for 38.5% of fatalities, whereas buildings only accounted for 9.3% [13]. 63% of flood-related deaths in the United States were found to be vehicle-related [6, 9]. 48.5% of flood-related deaths in Australia included vehicles [7]. As a result, economic, social, and income situations are probably connected to variables determining flood fatalities. The quality of housing stock in developing countries is a massive risk to life. The current research could provide a more robust basis for Vietnam's flood risk reduction decision-making procedures.

The results are a true reflection of Vietnamese dwelling conditions in flood-prone locations. As shown in some representative instances in Fig. 5, the majority of the dwellings in the rural region are single-story and in bad condition. They are often severely damaged or destroyed by storms or heavy rain events. Flood depths of more than two meters are common in many floodplain areas in central Vietnam [30]. Residents in floodplains susceptible to high flood depth levels should not live in single-story homes. Several appropriate measures can be applied to these situations, such as amphibious houses [51] and evacuation plans [52].

The most vulnerable populations in rural Vietnam are those who are impoverished or marginalized. They struggle greatly because they have limited access to public resources like insurance and emergency assistance [53]. Under Decree 67/2007/ND-CP, the affected families sometimes get financial assistance from the government; nonetheless, this financing is very little compared to the demand. As is customary worldwide, the effect of disasters is inextricably related to the poverty rate. Addressing societal vulnerability, and therefore flood risk and mortality tolls requires more focus.

Consideration must be given to potential solutions to reduce flood-related fatalities. These actions should reduce flood risk throughout the long period of growth and in the near term. Three policy implications are suggested based on the current study findings to provide decision-makers with something to consider when prioritizing flood risk control operations and appropriately allocating resources.

(a) A house collapsed in 2006 Typhoon Xangsane [54]

(b) Houses in Central Vietnam were inundated in November of 2016 [55]

Figure 5. Some typical dwellings in flood-prone areas in Vietnam

First, it is crucial to improve the house quality in flood-prone regions of Vietnam, as shown by the strong influence of the flood dwelling damage attribute on the mortality attribute. Therefore, assistance for the poor to modify their homes for flood risk adaptation should be given top priority in government programs on disaster risk reduction. The government should work with the locals on the rehabilitation project and take solutions such as amphibious houses [51] and 2-floor resistant dwellings [54].

Second, flood deaths might be considerably decreased with proper evacuation arrangements [56]. To reduce damage from catastrophes, communities' capacity to evacuate during storm and flood events has to be strengthened [52, 57]. It is vital to create evacuation plans for dangerous regions based on integrating flood hazard assessments with data on housing and population since the housing factor substantially impacts flood fatalities in Vietnam.

Third, in low-income nations with subpar engineering building performance and maintenance, flood shelter is one of the most effective methods to prevent flood-related mortality after evacuation preparations [52]. Under the funding of NGOs, flood shelters have been built in a number of flood-prone localities in Vietnam [58, 59]. Government strategies on disaster risk mitigation should prioritize building flood shelters in flood-affected regions due to the important impact of flood home damage on fatality and the efficacy of flood shelters.

Since the advent of big data, machine learning methods have been widely used in academia and industry. This is the first time that machine learning techniques and a national catastrophe database have been used to conduct longitudinal research on the correlation between flood damage and fatalities. Our analysis provides a more detailed picture of flood fatalities. It is possible that this research, which uses a machine learning approach, may strengthen the machine-learning approach for flood risk management and encourage the use of disaster databases for policy applications.

5. Conclusions

Based on data from Vietnam's national disaster database, this report offers an informative analysis of flood mortality in Vietnam from 1989 to 2015. Relative predictor relevance is calculated using statistical machine learning methods. The flood housing damage attribute has the greatest relevance on the flood mortality attribute in Vietnam, according to the findings of variable importance measurements. Our results have applications for governmental initiatives that aim to reduce human casualties.

Some policy suggestions include raising the standard of poor people's homes, creating evacuation plans for places with a high danger of flooding, and building flood shelters in flood-prone areas. Using national and regional catastrophe datasets, where damages are classified by characteristics and recorded for a long time, machine learning techniques may be used to investigate the variable importance measures in different nations and areas.

This research is restricted to looking at how flood damage characteristics compare to mortality attributes in the national disaster database of Vietnam. This restriction relates to the recorded national disaster database, which is not equipped with the data to represent physical damage. To decrease fatalities in future flood occurrences, government strategies in flood risk management may benefit from knowing the relative impact measurements of flood damage attributes to fatality attributes. Future studies should make an effort to include additional predictor factors, such as flood hazard type, exposure, and demographic data (victim age and gender), to better understand the causes of flood deaths in Vietnam.

6. Acknowledgments

We sincerely thank the Central Steering Committee for Natural Disaster Prevention and Control in Vietnam for providing the flood damage data.

References

[1] Kahn, M. E. (2005). The Death Toll from Natural Disasters: The Role of Income, Geography, and Institutions. *Review of Economics and Statistics*, 87(2):271–284.

[2] Hansson, K., Danielson, M., Ekenberg, L. (2008). A framework for evaluation of flood management strategies. *Journal of Environmental Management*, 86(3):465–480.

[3] Jongman, B., Winsemius, H. C., Aerts, J. C. J. H., de Perez, E. C., van Aalst, M. K., Kron, W., Ward, P. J. (2015). Declining vulnerability to river floods and the global benefits of adaptation. *Proceedings of the National Academy of Sciences*, 112(18).

[4] Chinh, L. T. D., Hằng, H. T., Linh, T. H., Quỳnh, B. D. (2022). Assessing flood impacts for Quang Binh province using Google Earth Engine and spatial analyses. *Journal of Science and Technology in Civil Engineering (STCE) - HUCE*, 16(5V):101–113.

[5] Coates, L. (1999). Flood Fatalities in Australia, 1788-1996. *Australian Geographer*, 30(3):391–408.

[6] Ashley, S. T., Ashley, W. S. (2008). Flood Fatalities in the United States. *Journal of Applied Meteorology and Climatology*, 47(3):805–818.

[7] FitzGerald, G., Du, W., Jamal, A., Clark, M., Hou, X.-Y. (2010). Flood fatalities in contemporary Australia (1997-2008). *Emergency Medicine Australasia*, 22(2):180–186.

[8] Sharif, H. O., Jackson, T. L., Hossain, M. M., Zane, D. (2015). Analysis of Flood Fatalities in Texas. *Natural Hazards Review*, 16(1).

[9] Terti, G., Ruin, I., Gourley, J. J., Kirstetter, P., Flamig, Z., Blanchet, J., Arthur, A., Anquetin, S. (2017). Toward Probabilistic Prediction of Flash Flood Human Impacts. *Risk Analysis*, 39(1):140–161.

[10] Paul, B. K., Mahmood, S. (2016). Selected physical parameters as determinants of flood fatalities in Bangladesh, 1972–2013. *Natural Hazards*.

[11] Jonkman, S. N. (2005). Global Perspectives on Loss of Human Life Caused by Floods. *Natural Hazards*, 34(2):151–175.

[12] Penning-Rowsell, E., Floyd, P., Ramsbottom, D., Surendran, S. (2005). Estimating Injury and Loss of Life in Floods: A Deterministic Framework. *Natural Hazards*, 36(1-2):43–64.

[13] Jonkman, S., Vrijling, J. (2008). Loss of life due to floods. *Journal of Flood Risk Management*, 1(1): 43–56.

[14] Jonkman, S. N., Kelman, I. (2005). An Analysis of the Causes and Circumstances of Flood Disaster Deaths. *Disasters*, 29(1):75–97.

[15] Jonkman, S. N., Maaskant, B., Boyd, E., Levitan, M. L. (2009). Loss of Life Caused by the Flooding of New Orleans After Hurricane Katrina: Analysis of the Relationship Between Flood Characteristics and Mortality. *Risk Analysis*, 29(5):676–698.

[16] Haynes, K., Coates, L., van den Honert, R., Gissing, A., Bird, D., de Oliveira, F. D., D'Arcy, R., Smith, C., Radford, D. (2017). Exploring the circumstances surrounding flood fatalities in Australia—1900–2015 and the implications for policy and practice. *Environmental Science & Policy*, 76:165–176.

[17] Zhai, G., Fukuzono, T., Ikeda, S. (2006). An empirical model of fatalities and injuries due to floods in Japan. *Journal of the American Water Resources Association*, 42(4):863–875.

[18] Mauro, M. D., de Bruijn, K. M. (2012). Application and validation of mortality functions to assess the consequences of flooding to people. *Journal of Flood Risk Management*, 5(2):92–110.

[19] Mauro, M. D., Bruijn, K. M. D., Meloni, M. (2012). Quantitative methods for estimating flood fatalities: towards the introduction of loss-of-life estimation in the assessment of flood risk. *Natural Hazards*, 63 (2):1083–1113.

[20] UNISDR (2015). *Global Assessment Report on Disaster Risk Reduction 2015*.

[21] IRDR (2014). *IRDR Peril Classification and Hazard Glossary*. Integrated Research on Disaster Risk (IRDR), Beijing.

[22] Simpson, A., Murnane, R., Saito, K., Phillips, E., Reid, R., Himmelfarb, A. (2014). *Understanding Risk in an Evolving World: Emerging Best Practices in Natural Disaster Risk Assessment. Washington DC*. Washington DC: Global Facility for Disaster Reduction and Recovery, the World Bank.

[23] Grasso, V. F., Dilley, M. (2013). *A Comparative Review of Country-Level and Regional Disaster Loss and Damage Databases*. United Nations Development Programme Bureau for Crisis Prevention and Recovery, New York.

[24] Kreft, S., Eckstein, D., Melchior, I. (2016). *Global climate risk index 2017*. Berlin: Germanwatch e.V.

[25] Luo, T., Maddocks, A., Iceland, C., Ward, P., Winsemius, H. (2015). *World's 15 countries with the most people exposed to river floods*.

[26] Tran, P., Marincioni, F., Shaw, R., Sarti, M., An, L. V. (2007). Flood risk management in Central Viet Nam: challenges and potentials. *Natural Hazards*, 46(1):119–138.

[27] Chau, V. N., Holland, J., Cassells, S., Tuohy, M. (2013). Using GIS to map impacts upon agriculture from extreme floods in Vietnam. *Applied Geography*, 41:65–74.

[28] Chinh, D. T., Bubeck, P., Dung, N. V., Kreibich, H. (2016). The 2011 flood event in the Mekong Delta: preparedness, response, damage and recovery of private households and small businesses. *Disasters*, 40 (4):753–778.

[29] Bui, D. T., Pradhan, B., Nampak, H., Bui, Q.-T., Tran, Q.-A., Nguyen, Q.-P. (2016). Hybrid artificial intelligence approach based on neural fuzzy inference model and metaheuristic optimization for flood susceptibilitgy modeling in a high-frequency tropical cyclone area using GIS. *Journal of Hydrology*, 540: 317–330.

[30] Luu, C., Meding, J. V., Kanjanabootra, S. (2017). Assessing flood hazard using flood marks and analytic hierarchy process approach: a case study for the 2013 flood event in Quang Nam, Vietnam. *Natural Hazards*, 90(3):1031–1050.

[31] Below, R., Vos, F., Guha-Sapir, D. (2010). *Moving towards harmonization of disaster data: a study of six Asian databases*. Brussels: Centre for Research on the Epidemiology of Disasters.

[32] Hughey, E., Bell, H., Chatman, M. (2011). Who Needs What? A Case Study of Post-disaster Damage and Needs Assessment (DANA) in Vietnam. *Risk, Hazards & Crisis in Public Policy*, 2(4):1–24.

[33] Tehrany, M. S., Jones, S., Shabani, F. (2019). Identifying the essential flood conditioning factors for flood prone area mapping using machine learning techniques. *CATENA*, 175:174–192.

[34] Wang, Z., Lai, C., Chen, X., Yang, B., Zhao, S., Bai, X. (2015). Flood hazard risk assessment model based on random forest. *Journal of Hydrology*, 527:1130–1141.

[35] Zhao, G., Pang, B., Xu, Z., Yue, J., Tu, T. (2018). Mapping flood susceptibility in mountainous areas on a national scale in China. *Science of The Total Environment*, 615:1133–1142.

[36] Rahmati, O., Yousefi, S., Kalantari, Z., Uuemaa, E., Teimurian, T., Keesstra, S., Pham, T., Bui, D. T. (2019). Multi-Hazard Exposure Mapping Using Machine Learning Techniques: A Case Study from Iran. *Remote Sensing*, 11(16):1943.

[37] MARD (2006). *Guideline on Natural Disaster Damage and Needs Assessment*. UNDP Project VIE/01/014 - Capacity Building for Disaster Mitigation in Vietnam.

[38] Bollin, C., Khanna, S. (2007). *Review of Post Disaster Recovery Needs Assessment and Methodologies: Experiences from Asia and Latin America*. International Recovery Platform.

[39] Wang, X., Mahul, O., Stutley, C. (2010). *Weathering the Storm: Options for Disaster Risk Financing in Vietnam*. Washington, DC: Global Facility for Disaster Reduction and Recovery, the World Bank.

[40] R Core Team. *R: A language and environment for statistical computing*. R Foundation for Statistical Computing, Vienna, Austria.

[41] Zhou, Q., Leng, G., Feng, L. (2017). Predictability of state-level flood damage in the conterminous United States: the role of hazard, exposure and vulnerability. *Scientific Reports*, 7(1).

[42] Tuszynski, J. (2014). *caTools: Tools: moving window statistics, GIF, Base64, ROC AUC, etc.. R package version 1.17.1*.

[43] James, G., Witten, D., Hastie, T., Tibshirani, R. (2013). *An Introduction to Statistical Learning*. Springer New York.

[44] Lindeman, R. H., Merenda, P. F. (1980). *Introduction to bivariate and multivariate analysis*. The USA: Scott, Foresman and Company.

[45] Grömping, U. (2015). Variable importance in regression models. *Wiley Interdisciplinary Reviews: Computational Statistics*, 7(2):137–152.

[46] Breiman, L., Friedman, J., Stone, C. J., Olshen, R. A. (1984). *Classification and regression trees*. Monterey: Wadsworth.

[47] Ridgeway, G. (2015). *gbm: generalized boosted regression models. R package version 2.1.1*.

[48] Grömping, U. (2006). Relative Importance for Linear Regression in R: The Package relaimpo. *Journal of Statistical Software*, 17(1).

[49] Liaw, A., Wiener, M. (2002). Classification and regression by randomForest. *R news*, 2(3):18–22.

[50] de Bruijn, K. M., Klijn, F., van de Pas, B., Slager, C. T. J. (2015). Flood fatality hazard and flood damage hazard: combining multiple hazard characteristics into meaningful maps for spatial planning. *Natural Hazards and Earth System Sciences*, 15(6):1297–1309.

[51] English, E. C., Friedland, C. J., Orooji, F. (2017). Combined Flood and Wind Mitigation for Hurricane Damage Prevention: Case for Amphibious Construction. *Journal of Structural Engineering*, 143(6).

[52] Masuya, A., Dewan, A., Corner, R. J. (2015). Population evacuation: evaluating spatial distribution of flood shelters and vulnerable residential units in Dhaka with geographic information systems. *Natural Hazards*, 78(3):1859–1882.

[53] Chau, V. N., Holland, J., Cassells, S. (2014). Institutional structures underpinning flood management in Vietnam. *International Journal of Disaster Risk Reduction*, 10:341–348.

[54] Tran, T. A. (2016). *Developing Disaster Resilient Housing in Vietnam: Challenges and Solutions*. Springer International Publishing.

[55] Luu, C., Meding, J. V., Kanjanabootra, S. (2017). Analysing flood fatalities in Vietnam using national disaster database and tree-based methods.

[56] Coppola, D. P. (2015). *Introduction to International Disaster Management*. Boston: Butterworth-Heinemann.

[57] Liu, D., Li, Y., Fang, S., Zhang, Y. (2017). Influencing factors for emergency evacuation capability of rural households to flood hazards in western mountainous regions of Henan province, China. *International Journal of Disaster Risk Reduction*, 21:187–195.

[58] Anh, T. T., Phong, T. V. G., Mulenga, M. (2014). Community consultation for climate resilient housing: A comparative case study in Vietnam. *International Journal of Disaster Risk Reduction*, 10:201–212.

[59] Tran, T. A. (2015). Post-disaster housing reconstruction as a significant opportunity to building disaster resilience: a case in Vietnam. *Natural Hazards*, 79(1):61–79.